Biophysical Characterisation of Self-assembling Nanoparticles



Henry L. D. Sawczyc

Exeter College

University of Oxford

A thesis submitted for the degree of

Doctor of Philosophy

Trinity 2020

Acknowledgements

Whilst the words, data, and conclusions in the following pages are the result of four years of individual work, this thesis would not exist without the help of several people.

Firstly, I must thank Tony for the opportunity to pursue a DPhil in the lab. I have thoroughly enjoyed the independence and freedom during my time at Oxford, as well as the challenge of learning so many techniques as part of my four years in your lab. I must also thank my industrial supervisor, Dr Max Ryadnov, for the opportunity of this DPhil and for welcoming me to the NPL in my final year.

Thanks also to the EPSRC, whose funding has made this DPhil possible, and to Exeter College, both for the travel grants and for the experiences as a member of the College.

I would like to thank the members of the Watts lab, both past and present for their company and advice throughout the years. To Dr Javier Vinals Camallonga and Dr Steven Lavington, my fellow inmates of DPhil life. It has been a pleasure getting to know you both during our shared time in the lab, and a greater pleasure getting to know you both in our shared time in the pub. Javi, I can not thank you enough for your help, humour, and chilled nature you brought to everything you did. Steve, your encyclopaedic knowledge of all topics and music taste was fantastic company in the lab, and I am sure you will go on to do a great many things. To Owen Crowther, thanks for the good company, both in the lab and as my College son, and for listening to my many rants over the years. To Dr Jason Yau, thank you for your unending patience for my questions about all things NMR, even after you had left the lab! To Dr Juan Francisco Bada Juarez; thank you for the warm welcome to the lab, the supervision in my first year, and good laughs throughout. I am still scared of how you managed to find papers the very second they were released. Thank you also to Dr Felipe Santos Mendes and Natalia Fontana, our Brazilian contingent, for the great company over the time you both shared with us. Thanks also to Dr Xiaoyan Ding for her knowledge and help in the lab. To my two students, official or not, Constanze Cavalier and Tongran Zhang, it was a pleasure to show you the wonders -and difficulties- of lab-based work, and thank you for teaching me in return.

To the patient experts; Dr David Staunton, Dr William Myers, Tina Jackson, and Professor Tim Claridge, thank you for all of your expertise and time in

training me in biophysical techniques, EPR, and NMR. Thank you also to my collaborators; Professor Gerhard Gröbner, Dr Sabine Heit, Dr Juliette Devos, thank you for collecting some of the data in this thesis, and answering my numerous questions on how to best analyse it.

I would also like to thank the people at the NPL for their help and company during my time there. Most notably I would like to thank Dr Emiliana de Santis for her unending help, guidance, and kindness during my time at the NPL. I would also like to thank Dr Erol Hasan for his help in teaching me both solid phase peptide synthesis and HPLC methods, as well for the frequent coffee breaks. Secondary thanks goes to my induction buddy Ilyas Roble, for the good company and assistance in the G8 lab. Thank you also to Kate Hammond, Purnank Aggarwal, Dr James Noble, Dr Ibolya Kepiro and Dr Jascindra Ravi for their respective help, and collective company at cake club.

A massive thanks also to my friends and family for being there for me throughout these past four years. Thank you to my parents for their unending love and support both during my time at Oxford, and the many years before. I would not be the person I am today without that love, and I am very lucky to have them. A special mention to Elaine, for her un-ending patience and kindness, and more importantly for putting up with the terrible humour of my dad and I. To my sister, Rachael, for the shared jokes, hi-jinks, and games of tri-ominoes over the years - long may they continue. Thank you to my grandma, the strongest person I've ever known, for the impossible stories as a child, and as an adult. Thank you also for telling everyone who would listen that her grandchild is going to be a doctor (albeit not the type she wanted).

Finally, this DPhil would not have been completed, written, or submitted if it was not for the amazing love and support from my partner, Joe. He has been my rock across the four years I have known him, supporting me, helping me, and making me laugh throughout the ups and the downs of both of our DPhils. I can not thank him enough for everything - including proofreading all 200 something pages of this thesis. I will, however, blame him for any typos that are found...

Abstract

Biophysical characterisation of membrane proteins has been revolutionised through the development of membrane protein extraction with the use of a random co-polymer of styrene:maleic acid (SMA). Since the development of SMA, several novel polymers have been developed, in addition to modifications to the original SMA structure. However, a rigorous comparative characterisation of these polymers is missing.

This thesis presents the development of novel, high-throughput, solubilisation assays that can be used for the direct comparison of membrane solubilisation. These assays allow for the determination of optimal solubilisation conditions using the four polymers tested (SMA 3:1, SMA 2:1, DIBMA, and PMA). In addition, the effects of pH, ionic strength and divalent cation presence on the solubilisation of membranes by these polymers to form lipid-polymer nanoparticles was probed.

Characterisation of DMPC-polymer nanoparticles formed in 'ideal' conditions (pH 7.4, 100 mM NaCl) was performed to ascertain the lipid environment within these extracted bilayers. This showed that all lipid-polymer nanoparticles possess a higher lipid order than that observed in large unilamellar vesicles (LUVs) and further the thermal phase transition of the lipids within these nanoparticles is altered.

A previously discovered novel property of lipid-polymer nanoparticles, collisional lipid transfer, was also explored. Through the novel use of asymmetric membrane models it was found that lipid mixing occurs during membrane solubilisation. The rate of this mixing is variable according to the temperature and polymer used, and is a native property of lipid-polymer nanoparticles. This thesis goes on to apply this novel property for the specific titration of lipids into protein containing SMA-nanoparticles (Lipodisqs), using the well characterised cytochrome oxidase c dependence on cardiolipin as a test case. This is the first recorded instance of specific lipid:protein titration without the use of detergent or organic solvent addition.

Finally, the thesis explores the generation of a self-assembling peptide, ST1-QAA, which has been designed to spontaneously form viral-like particles for the purpose of gene transfection. It present a robust, optimised, purification protocol for synthesised ST1-QAA and biophysical characterisation of peptide self-assembly to form viral-like particles.

Contents

List of Figures xi

List of abbreviations xv

1 Introduction 1

1.1 Biological membranes . . . 2
1.1.1 Lipids . . . 2
1.1.2 Membrane asymmetry . . . 5
1.1.3 Lipid phases and domains . . . 7
1.1.4 Membrane proteins . . . 9
1.1.5 Lipid-protein interactions . . . 11
1.2 Reconstitution of membrane proteins . . . 14
1.3 Model membranes . . . 16
1.3.1 Liposomes . . . 16
1.3.2 Bicelles . . . 18
1.3.3 Nanodiscs . . . 18
1.4 Polymer-based nanoparticles . . . 19
1.4.1 Amphipols . . . 19
1.4.2 Lipid-polymer nanoparticles . . . 19
1.4.3 Styrene-maleic acid copolymers (SMA) . . . 21
1.4.4 Diisobutylene-maleic acid (DIBMA) . . . 23
1.4.5 Polymethacrylate copolymer (PMA) . . . 24
1.5 Biophysical techniques for nanoparticle characterisation . . . 24
1.5.1 Spectrophotometry . . . 24
1.5.2 Dynamic light scattering (DLS) . . . 27
1.5.3 Förster resonance energy transfer (FRET) . . . 29
1.5.4 Electron paramagnetic resonance (EPR) . . . 31
1.5.5 Principles of solid phase peptide synthesis (SPPS) . . . 39
1.6 Aims of the thesis . . . 42

2 Characterising the formation of lipid-polymer nanoparticles 45

2.1 Introduction . . . 45

2.1.1 Aims . . . 49

2.2 Materials & methods . . . 49

2.2.1 Preparation of polymer . . . 49

2.2.2 Preparation of lipid dispersion (MLVs) . . . 50

2.2.3 Initial solubilisation assay by spectrophotometry . . . 50

2.2.4 High-throughput spectrophotometry (96-well plate) . . . 51

2.2.5 Dynamic light scattering (DLS) . . . 52

2.3 Results & discussion . . . 52

2.3.1 Development of solubilisation assay by optical density (OD) 53

2.3.2 Formation of lipid-polymer nanoparticles across pH range . . 58

2.3.3 Formation of lipid-polymer nanoparticles across NaCl concentration . . . 60

2.3.4 Formation of lipid-polymer nanoparticles across divalent cation (Mg^{2+}, Ca^{2+}) concentration . . . 63

2.4 Summary and Conclusions . . . 66

3 Biophysical characterisation of DMPC-polymer nanoparticles 71

3.1 Introduction . . . 71

3.1.1 Aims . . . 72

3.2 Materials & methods . . . 73

3.2.1 Polymer preparation . . . 73

3.2.2 Transmission electron microscopy (TEM) . . . 73

3.2.3 Differential scanning calorimetry (DSC) . . . 74

3.2.4 Laurdan fluorescence . . . 75

3.2.5 Continuous wave electron paramagnetic resonance (cw-EPR) 76

3.3 Results & Discussion . . . 80

3.3.1 Negative stain transmission electron microscopy (TEM) . . . 80

3.3.2 EM particle analysis . . . 83

3.3.3 Thermotropic characterisation . . . 85

3.3.4 Differential scanning calorimetry (DSC) . . . 86

3.3.5 cw-EPR . . . 92

3.4 Summary and conclusions . . . 97

4 Investigations into lipid mixing of lipid-polymer nanoparticles 99
4.1 Introduction . . . 99
4.1.1 Aims . . . 100
4.1.2 Asymmetric model membranes . . . 101
4.2 Materials & methods . . . 102
4.2.1 aLUV generation . . . 102
4.2.2 FRET & TR-FRET measurements . . . 104
4.2.3 NMR . . . 106
4.2.4 Cytochrome oxidase c (CcO) and cardiolipin titration . . . 106
4.3 Results & discussion . . . 110
4.3.1 Measurement of LUV and LQ asymmetry by FRET . . . 110
4.3.2 Kinetics of lipid mixing by TR-FRET . . . 115
4.3.3 Unlabelled lipid mixing as measured by NMR . . . 121
4.3.4 Titration of cardiolipin into CcO-Lipodisqs . . . 126
4.4 Summary and conclusions . . . 131

5 Purification and biophysical characterisation of self-assembling viral-like capsules 133
5.1 Introduction . . . 133
5.1.1 Aims . . . 136
5.2 Materials & methods . . . 136
5.2.1 Peptide synthesis . . . 136
5.2.2 High Pressure Liquid Chromotography (HPLC) . . . 137
5.2.3 Mass spectrometry . . . 138
5.2.4 Transmission Electron Microscopy . . . 138
5.2.5 Circular dichroism (CD) . . . 139
5.2.6 Fourier transform infra-red spectroscopy (FTIR) . . . 139
5.3 Results & discussion . . . 140
5.3.1 Purification of synthesised ST1-QAA . . . 140
5.3.2 ST1-QAA self-assembly . . . 144
5.4 Conclusions and future works . . . 152

6 Summary 155

Appendices

A Appendix for Chapter 2 **161**
A.1 Buffers used for OD_{350} assay development . . . 161
A.2 Concentration control for lipid concentration *vs* OD_{350} . . . 163
A.3 Raw OD_{350} values for spectrophotometry . . . 164
A.3.1 OD_{350} for pH range . . . 164
A.3.2 OD_{350} for NaCl titration . . . 166
A.3.3 OD_{350} for Mg^{2+} titration . . . 168
A.3.4 OD_{350} for Ca^{2+} titration . . . 171
A.4 Raw DLS histograms . . . 173
A.5 Current solubilisation conditions in literature . . . 182

B Appendix for Chapter 3 **187**
B.1 EM particle eccentricity . . . 187
B.2 Aligned TEMPO spectra . . . 188
B.3 5-PCSL spectra . . . 188

C Appendix for Chapter 4 **195**
C.1 Development of FRET assay for aLUV and supposed aLQ . . . 195
C.2 Development of EPR assay for aLUV and supposed aLQ . . . 197
C.3 Development of ^{31}P NMR assay to determine level of mixing in LQ systems . . . 201
C.4 TR-FRET data for additional polymers . . . 205

D Appendix for Chapter 5 **209**
D.1 Additional HPLC purification attempts . . . 209
D.2 ST1-QAA T0 EM image . . . 214
D.3 Additional characterisation assays . . . 215
D.3.1 Dynamic light scattering (DLS) . . . 216
D.3.2 CD melt . . . 217

References **219**

List of Figures

1.1 Chemical structures of the major membrane forming lipid types, and common phospholipid head group structures . . . 3
1.2 Effect of overall lipid shape and distribution on membrane organisation, and asymmetric bilayer distribution of common phospholipid head groups . . . 5
1.3 Diagram of lipid phases and the effect of cholesterol on membrane organisation . . . 7
1.4 Examples of membrane-protein interactions . . . 9
1.5 Structure of selected detergent molecules, and diagram of detergent action on a membrane . . . 15
1.6 Example of commonly used membrane mimetics, and generalised workflow for membrane protein solubilisation and preparation . . . 17
1.7 Chemical structures of currently available polymers used for forming polymer-lipid nanoparticles. . . . 20
1.8 Diagram of spectrophotometry principles for both optical density (OD) and absorbance . . . 25
1.9 Principles of dynamic light scattering (DLS) measurement . . . 28
1.10 Diagram of FRET principles . . . 29
1.11 Diagram of EPR magnetisation principles in EPR spectra generation 32
1.12 EPR spectra and measurement positions for the calculation of lipid order (S) used in this thesis. . . . 36
1.13 Spin-labelled lipid probes used within this thesis. . . . 38
1.14 Principles of TEMPO partitioning. . . . 39
1.15 Stages of solid phase peptide synthesis . . . 40

2.1 Chemical structures of polymers used for forming polymer-lipid nanoparticles. . . . 46
2.2 Initial OD_{350} measurements of DMPC membrane solubilisation . . . 55
2.3 Formation of nanoparticles across pH range as measured by light scattering (OD_{350}) and DLS . . . 58
2.4 Formation of nanoparticles across an ionic strength gradient (NaCl) as measured by light scattering (OD_{350}) and DLS . . . 61

2.5 Formation of nanoparticles across a Mg^{2+} concentration gradient as measured by light scattering (OD_{350}) and DLS . . . 64
2.6 Formation of nanoparticles across a Ca^{2+} concentration gradient as measured by light scattering (OD_{350}) and DLS . . . 65

3.1 Negative stain transmission electron microscopy (TEM) images . . . 81
3.2 Negative stain TEM particle analysis . . . 83
3.3 Differential scanning calorimetry (DSC) data of DMPC-polymer nanoparticles . . . 87
3.4 Laurdan measurements for DMPC membranes . . . 90
3.5 Laurdan measurements for DMPC and DLPC composed membranes 91
3.6 f-plot of TEMPO partitioning *vs* temperature . . . 93
3.7 EPR spectra of TEMPO-labelled POPC (POPTC) and stearic acid spin label (SASL) probes in DMPC nanoparticles. . . . 94
3.8 Order parameter (S) of lipid membrane generated from cw-EPR measurements over a temperature range. . . . 96

4.1 Method of asymmetric LUV generation through MβCD lipid exchange 103
4.2 NBD-PE and Rho-PE fluorescence and FRET in LUV and LQ samples 112
4.3 FRET efficiency of NBD-PE and Rho-PE labelled lipids in aLUV and polymer nanoparticles . . . 114
4.4 Rate of lipid mixing as measured by TR-FRET for SMA 3:1 nanoparticles across a temperature range . . . 117
4.5 Rate of lipid mixing as measured by TR-FRET for SMA 3:1 nanoparticles before and after SEC . . . 119
4.6 Rate of lipid mixing as measured by TR-FRET of lipid-polymer nanoparticles for various polymer types . . . 120
4.7 ^{31}P solution NMR spectra of SMA 3:1-DMPC and SMA 3:1-DMPG Lipodisqs . . . 123
4.8 Lipid mixing of SMA 3:1-DMPC and SMA 3:1-DMPG nanoparticles as measured by ^{31}P NMR . . . 124
4.9 Activity assay of CcO in DDM micelles pre- and post-delipidation . 127
4.10 Activity assay of CcO in POPC-LQs with and without CL . . . 129

5.1 Sequence and rational design of ST1-QAA . . . 135
5.2 Initial purification attempt of ST1-QAA . . . 141
5.3 Sixth attempt of purification of ST1-QAA by HPLC . . . 143
5.4 Negative stain TEM images showing nanoparticle macromolecular structure of ST1-QAA at 3 hours. . . . 145
5.5 Negative stain TEM images showing nanoparticle macromolecular structure of ST1-QAA at 24 hours. . . . 146

5.6 Dimensional analysis of particles imaged by EM 148
5.7 Particle eccentricity of particles imaged by EM 149
5.8 Circular dichroism (CD) spectra of ST1-QAA over time (0-48 hours) 150
5.9 Fourier transform infra-red (FTIR) spectroscopy spectra of ST1-QAA at 0 and 24 hours incubation 151

A.1 Concentration control of lipid concentration *vs* Od_{350} 163
A.2 Initial OD_{350} measurements of DMPC membrane solubilisation (full range) 164
A.3 Raw OD_{350} measurements for pH 165
A.4 Raw OD_{350} measurements for NaCl 166
A.5 Raw OD_{350} measurements for NaCl for POPC:POPE membranes . 167
A.6 Raw OD_{350} measurements for Mg^{2+} 168
A.7 DLS measurements for polymers tested throughout Mg^{2+} concentration 170
A.8 Raw OD_{350} measurements for Ca^{2+} 171
A.9 DLS measurements for polymers tested throughout Ca^{2+} concentration 172
A.10 Original DLS histograms for polymer solubilisation of DMPC membranes across pH range 174
A.11 Original DLS histograms for polymer solubilisation of POPC:POPG (3:1) membranes across pH range 175
A.12 Original DLS histograms for polymer solubilisation of DMPC membranes across pH range 176
A.13 Original DLS histograms for polymer solubilisation of POPC:POPG (3:1) membranes across pH range 177
A.14 Original DLS histograms for polymer solubilisation of DMPC membranes across pH range 178
A.15 Original DLS histograms for polymer solubilisation of POPC:POPG (3:1) membranes across pH range 179
A.16 Original DLS histograms for polymer solubilisation of DMPC membranes across pH range 180
A.17 Original DLS histograms for polymer solubilisation of POPC:POPG (3:1) membranes across pH range 181

B.1 Diagram showing how eccentricity was measured per TEM particle and calculated for individual polymer variants. 188
B.2 TEMPO partitioning measurement of DMPC and DLPC LUVs . . 189
B.3 Annotated EPR spectra of 1% (molar) 5-PCSL label within a 400 nm DMPC LUV 190
B.4 Annotated EPR spectra of 1% (molar) 5-PCSL label within a SMA 3:1-DMPC nanoparticle. 191

B.5 Annotated EPR spectra of 1% (molar) 5-PCSL label within a SMA 2:1-DMPC nanoparticle. 192
B.6 Annotated EPR spectra of 1% (molar) 5-PCSL label within a DIBMA-DMPC nanoparticle. 193
B.7 Annotated EPR spectra of 1% (molar) 5-PCSL label within a PMA-DMPC nanoparticle. 194

C.1 Fluorescence spectra for Cy3 and Cy5 labelled lipids in LUV and LQ systems 196
C.2 EPR spectra of aLUV and supposed aLQ with leaflet-selective labelled AR3 and POPTC 199
C.3 EPR subtraction spectra of aLUV and supposed aLQ with leaflet-selective labelled AR3 and POPTC 200
C.4 ^{31}P NMR spectra for pre-mixed PC:PG standards and asymmetric DMPC /DMPG samples 203
C.5 Lipid mixing of asymmetric (DMPC/DMPG) SMA 3:1 nanoparticles as measured by ^{31}P NMR 204
C.6 Rate of lipid mixing as measured by TR-FRET for SMA 2:1 nanoparticles across a temperature range 206
C.7 Rate of lipid mixing as measured by TR-FRET for DIBMA nanoparticles across a temperature range 207
C.8 Rate of lipid mixing as measured by TR-FRET for PMA nanoparticles across a temperature range 207

D.1 Second attempt at purification of ST1-QAA by HPLC 210
D.2 Third attempt at purification of ST1-QAA by HPLC 211
D.3 Fourth attempt of purification of ST1-QAA by HPLC 212
D.4 Fifth attempt of purification of ST1-QAA by HPLC 213
D.5 Negative stain EM image of ST1-QAA 0 hours after incubation . . 215
D.6 Formation of ST1-QAA nanoparticles by DLS 216
D.7 Circular dichroism (CD) melt spectra of ST1-QAA from 20°C-90°C 218

List of abbreviations

ACN . . . . . Acetronitrile

ASCII . . . . . American standard code for information interchange

AR3 . . . . . Archaerhodopsin 3

aLUV . . . . . Asymmetric large unilamellar vesicle

aLQ . . . . . Asymmetric Lipodisq

BCA . . . . . Bicinchoninic acid

Boc . . . . . Tert-butyloxycarbonyl

cbc . . . . . Critical bilayer concentration

CcO . . . . . Cytochrome oxidase c

CD . . . . . Circular dichromism

Chol . . . . . Cholesterol

Cy3 . . . . . Cyanine 3

Cy3-PE . . . . Cyanine 3-DLPE

Cy5 . . . . . Cyanine 5

Cy5-PE . . . . Cyanine 5-DLPE

DCM . . . . . Dichloromethane

DDM . . . . . n-Dodecyl-B-D-maltoside

dH_2O . . . . . Distilled H_2O

D_H . . . . . Hydrodynamic diameter

DIBMA . . . . Di-isobutylene-*alt*-maleic acid

DIPEA . . . . N,N-Diisopropylethylamine

DLPE 1,2-dilauroyl-*sn*-glycero-3-phosphoethanolamine

DLS . . . . . Dynamic light scattering

DMF . . . . . Dimethylformamide

DMPC 1,2-dimyristoyl-*sn*-glycero-3-phosphocholine

DTT . . . . . Dithiothreitol

ESI-MS . . . . Electrospray ionisation mass spectrometry

FRET . . . . . Förster resonance energy transfer

FTIR . . . . . Fourier transform infra-red spectroscopy

HBTU . . . . . Hexafluorophosphate benzotriazole tetramethyl uronium

HEPES . . . . 4-(2-hydroxyethyl)-1-piperazineethanesulfonic acid

HPLC . . . . . High pressure liquid chromotography

LC-MS . . . . Liquid chromotography mass spectrometry

LUV . . . . . Large unilamellar vesicle

LQs . . . . . Lipodisqs

NBD-PE . . . 1,2-dipalmitoyl-*sn*-glycero-3-phosphoethanolamine-N-(7-nitro-2-1,3-benzoxadiazol-4-yl)

Rho-PE . . . . 1,2-dioleoyl-*sn*-glycero-3-phosphoethanolamine-N-(lissamine rhodamine B sulfonyl)

M . . . . . Molar

MALDI . . . . Matrix-assisted laser desorption/ionisation (time of flight)

MβCD . . . . . Methyl-β-cyclodextrin

MLV . . . . . Multilamellar vesicles

MOPS . . . . . 3-morpholinopropane-1-sulfonic acid

$\mathbf{M_R}$ . . . . . Relative molecular mass

MTSL . . . . . (1-oxyl-2,2,5,5-tetramethylpyrroline-3-methyl)methanethiosulfonate

$\mathbf{M_w}$ . . . . . (Average) molecular weight

MWCO . . . . Molecular weight cut off

NPL . . . . . National Physical Laboratory

OD . . . . . Optical density

PA . . . . . Phosphatidic acid head group

Pbf 2,2,4,6,7-pentamethyidlhydrobenzofuran-5-sulfonyl

PC . . . . . Phosphatidylcholine head group

PE . . . . . Phosphatidylethanolamine head group

PG . . . . . Phosphatidylglycerol head group

PI . . . . . Phosphatidylinositol head group

PLA2 . . . . . Phospholipase A2

PMA . . . . . Polymethacrylate polymer

PCSL . . . . . Phosphatidylcholine spin label

POPC 1-palmitoyl-2-oleoyl-*sn*-glycero-3-phosphocholine

POPG . . . . . 1-palmitoyl-2-oleoyl-*sn*-glycero-3-phospho-(1'-rac-glycerol)

POPTC . . . . 1,2-dipalmitoyl-*sn*-glycero-3-phospho(tempo)choline

R_H . . . . . Hydrodynamic radius

PS . . . . . Phosphatidylserine head group

RT . . . . . Room temperature

SASL . . . . . Stearic acid spin label

SEC . . . . . Size exclusion chromatography

SM . . . . . Sphingomyelin

SMA . . . . . Styrene-maleic acid copolymer

SMALP(s) . . SMA-lipid particle(s)

SPPS . . . . . Solid-phase peptide synthesis

TEMPO . . . 2,2,6,6-tetramethyl-1-piperidinyloxy

TFA . . . . . Trifluoroacetic acid

TFE . . . . . Tetrafluoroethylene

TIS . . . . . Triisopropylsilane

TR-FRET . . Time-resolved Förster resonance energy transfer

UA . . . . . Uranyl acetate

UV . . . . . Ultraviolet

(v/v) . . . . . Volume/volume ratio

(w/v) . . . . . Weight/voume ratio

(w/w) . . . . . Weight/weight ratio

Biology is the search for the chemistry that works...

R.J.P Williams

1 Introduction

Contents

1.1 Biological membranes 2
1.1.1 Lipids 2
1.1.2 Membrane asymmetry 5
1.1.3 Lipid phases and domains 7
1.1.4 Membrane proteins 9
1.1.5 Lipid-protein interactions 11
1.2 Reconstitution of membrane proteins 14
1.3 Model membranes 16
1.3.1 Liposomes 16
1.3.2 Bicelles 18
1.3.3 Nanodiscs 18
1.4 Polymer-based nanoparticles 19
1.4.1 Amphipols 19
1.4.2 Lipid-polymer nanoparticles 19
1.4.3 Styrene-maleic acid copolymers (SMA) 21
1.4.4 Diisobutylene-maleic acid (DIBMA) 23
1.4.5 Polymethacrylate copolymer (PMA) 24
1.5 Biophysical techniques for nanoparticle characterisation 24
1.5.1 Spectrophotometry 24
1.5.2 Dynamic light scattering (DLS) 27
1.5.3 Förster resonance energy transfer (FRET) 29
1.5.4 Electron paramagnetic resonance (EPR) 31
1.5.5 Principles of solid phase peptide synthesis (SPPS) . . . 39
1.6 Aims of the thesis 42

1.1 Biological membranes

Biological membranes are a fundamental, ubiquitous, component of life allowing compartmentalisation of individual cells in a vast abiotic world. This compartmentalisation allows for the concentration of essential materials for life-sustaining processes, along with spatial separation of processes within eukaryotic cells.[1] These membranes are composed of molecules called lipids which, due to their amphipathic nature, spontaneously form bilayers in aqueous solutions. In addition to the lipid component of biological membranes, membrane proteins -both integral and peripheral- play an important role in both membrane function and content. The exact content percentage of protein in biological membranes varies, with a typical membrane containing approximately 50% membrane protein by mass. However this value is known to vary depending on the exact functional role of the membrane.[2]

1.1.1 Lipids

Lipids are small hydrophobic or amphiphilic molecules that have a range of uses in biological systems. In eukaryotic organisms, an average of 5% of genes encode for proteins involved in lipid biosynthesis.[3] Across all organisms, there are more than 44,000 individual molecules classified as lipids to date.[4] These lipids have diverse roles, and can broadly be categorised into three primary roles in biology; energy storage,[5] cell signalling,[6] and as the main structural component of biological membranes.[7] The membrane forming lipids are the main focus of this thesis.

Biological membranes are most commonly formed by phospholipids in a bilayer structure, which are composed of, on average, two hydrophobic fatty acid chains ('tails') and a hydrophilic phosphate group ('head'), bound together through a glycerol (Figure 1.1 A). This class of phospholipid is also known as a glycerophospholipid. Another important class of phospholipid are the sphingolipids (Figure 1.1 C, left) which possess a sphingosine linker group in place of the glycerol group in phospholipids. Aromatic sterols, such as cholesterol (Figure 1.1 C,

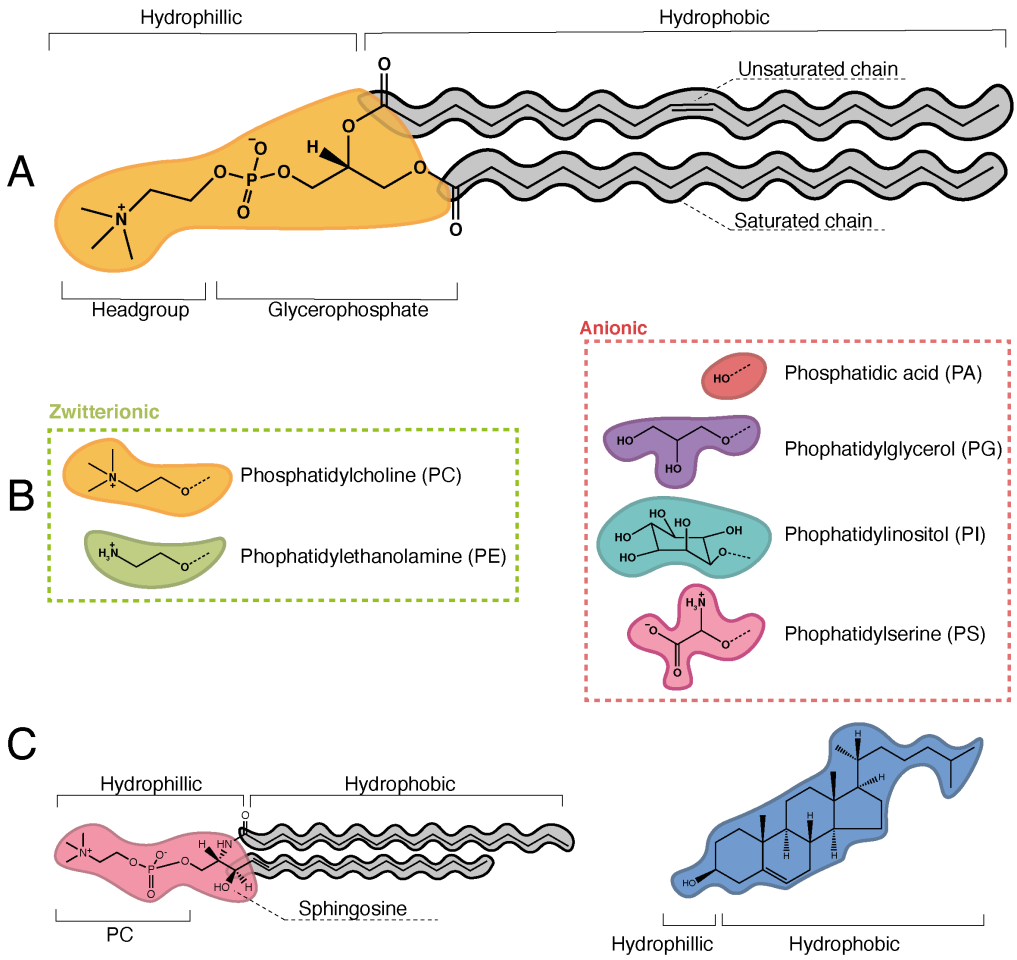


Figure 1.1: Chemical structures of the major membrane forming lipid types, and common phospholipid head group structures. (A) Chemical structure of an example phospholipid, 1-palmitoyl-2-oleoyl-sn-glycero-3-phosphocholine (POPC). (B) Chemical structures of common phospholipid head groups, (with repeating phosphate group omitted) separated into overall zwitterionic (left, green box) and anionic (right, red box) charge when found as a phospholipid. (C) Chemical structure of phosphatidylcholine sphingolipid (Shingomyelin, left), and cholesterol (right).

right) are also present in most biological membranes, and aid in their structural stability and homogeneity of complex lipid mixtures. Together, these lipids form bilayers spontaneously in aqueous solutions due to the combination of hydrophobic exclusion of aliphatic or aromatic groups and the favourable interactions of the hydrophilic groups.

Phospholipid diversity occurs in either the fatty acid tail, or head group regions. Fatty acid tails possess varying degrees of unsaturated bonds, and have varied chain lengths (Figure 1.1 A).[7] Biological membrane lipids typically have one unsaturated

Table 1.1: Phospholipid head groups present (as total %) in bacterial (*E. coli*, inner membrane),[8] mammalian (human erythrocyte),[7] and yeast (*S. cerevisiae*)[9] plasma membranes. Where PC = phosphatidylcholine, PE = phosphatidyletholamine, PG = phosphatidylglycerol, PI = phosphatidylinositol, PS = phosphatidylserine. Trace lipids (<1% total lipid) are not shown for clarity.

Lipid type	***E. coli***	**Human erythrocyte**	***S. cerevisiae***
PC	-	40	18
PE	75	25	14
PG	19	-	-
PI	-	2.5	28
PS	-	7.5	5
Sphingolipid	-	25	31
Sterol (mol/mol)	-	0.85	0.5
Others	6% DPG	-	4% CL

chain and one saturated chain, as shown in Figure 1.1 A. The unsaturated chain aids in increasing lipid diffusion within the membrane, called 'membrane fluidity', at physiological temperatures.[10] The lipid head groups are similarly diverse, with common head groups shown in Figure 1.1 B and the overall distribution of these head groups in example organisms shown in Table 1.1. Phosphatidylcholine head groups are the most abundant, accounting for approximately 50% the total phospholipid content in most eukaryotic cells.[7] Some head group moieties are charged, with negatively charged groups generating an overall negative lipid charge (Figure 1.1 B, anionic). Positively charged headgroup moieties neutralise the negative charge of the phosphate group, leading to a net neutral charge (Figure 1.1 B, zwitterionic).

In addition to charge variation, lipid shape can vary depending on the head group and tail variation, which can cause spontaneous curvature of the membrane (Figure 1.2 A).[11] The overall shape of a lipid can be defined by the packing parameter, P, where P = 1 indicates a cylindrical lipid shape within a bilayer (no curvature), P < 1 generates a negative curvature, and P > 1 generates a positive curvature (Figure 1.2 A).[12]

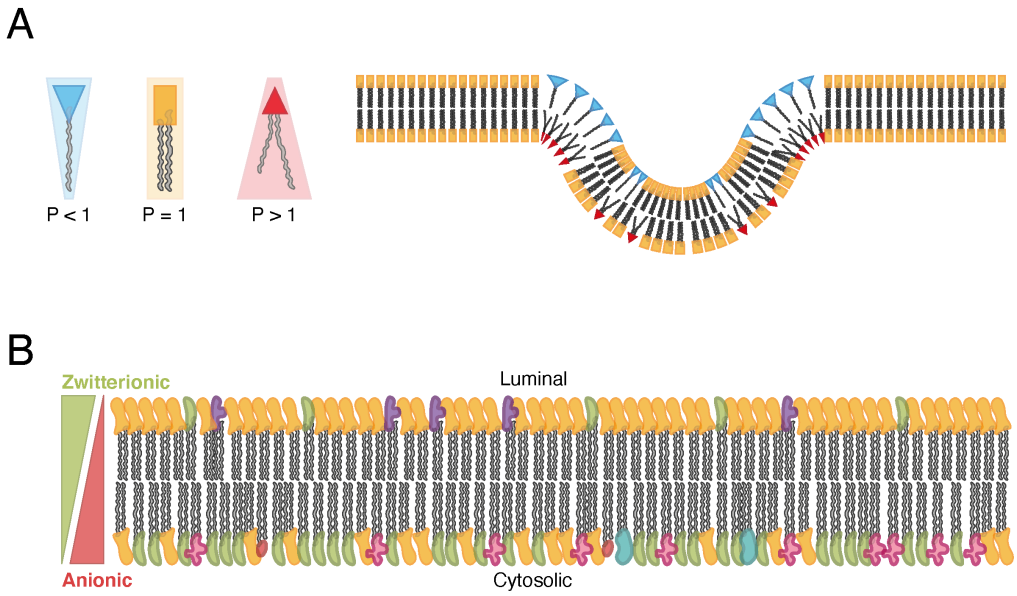


Figure 1.2: Effect of overall lipid shape and distribution on membrane organisation, and asymmetric bilayer distribution of common phospholipid head groups. (A) Overall shape of lipid molecules, and their effect on membrane structure. Showing positive curvature (P $>$ 1, blue), no curvature (P $=$ 1, yellow), and negative curvature (P $<$ 1, red) and the common local distribution in the membrane during spontaneous membrane curvature. (B) Representative cartoon of asymmetric lipid head distribution in mammalian plasma membrane, showing a net zwitterionic charge for luminal (extracellular) facing leaflets, and overall anionic charge for cytosolic leaflets.

1.1.2 Membrane asymmetry

Biological membranes are rarely a single species of lipid, but instead a complex mixture of different lipids within a membrane as a whole.[7] To add to the complexity, each leaflet of the bilayer generally contains different lipid species, leading to asymmetry across the membrane (Figure 1.2 B).[13] This was famously observed initially in the plasma membrane of red blood cells,[14] but has since been shown to be present in all organisms.[15] In eukaryotic plasma membranes, the luminal (outward-facing) leaflet is largely composed of zwitterionic lipids, with the cytosolic leaflet (inward-facing) possess a majority of anionic lipids (Figure 1.2 B).[13] Lipid saturation has also been shown to be asymmetric,[16] with predominantly polyunsaturated lipids on the cytosolic leaflet, and saturated or mono-unsaturated lipids on the outer leaflet.

Table 1.2: Asymmetric distribution of phospholipid head groups in human erythrocyte plasma membranes shown as % weight of total lipid type.[14, 19] Where PC = phosphatidylcholine, PE = phosphatidyletholamine, PS = phosphatidylserine. Trace lipids (<1% total lipids) are not shown for clarity.

Lipid type	Outer leflet	Inner leaflet
PC	70	30
PE	20	80
PS	5	95
Sphingolipid	80	20

This membrane asymmetry, whilst ubiquitous, is not a passive state. Asymmetry is actively achieved through the use of lipid transporter proteins (flippases and floppases) within the membrane,[17] using energy in the form of ATP to maintain order.[18] If not constantly maintained, passive lipid flip-flop between bilayers slowly occurs, ablating membrane asymmetry. The rate of this flip-flop is dependant on many factors, such as the lipid head group and membrane fluidity. For example, the rate of flip-flop for phosphatidylcholine lipids can range from hours to days.[7]

Asymmetry is clearly important for biological membranes due to its ubiquity in natural membranes, despite the energy expenditure it requires to maintain.[20] It is known that loss of asymmetry membrane is a signal for cell degradation.[21, 22] With exposure of the normally inward-facing phosphatidylserine (PS) to the outer leaflet, by scramblase activation,[22] being shown to be an essential factor in the recognition and clearance of apoptotic cells.[23] PS exposure is also a regulator of platelet activation, leading to blood clotting.[17] However, it remains unclear why all cells possess membrane asymmetry outside specific examples. It has proven difficult to fully elucidate the biological relevance of asymmetric membranes, due to the difficulty in the production of asymmetric model membranes. However, recent advances in the production of asymmetric membrane models,[24] in-depth biophysical characterisation of asymmetric membranes has now become a possibility.

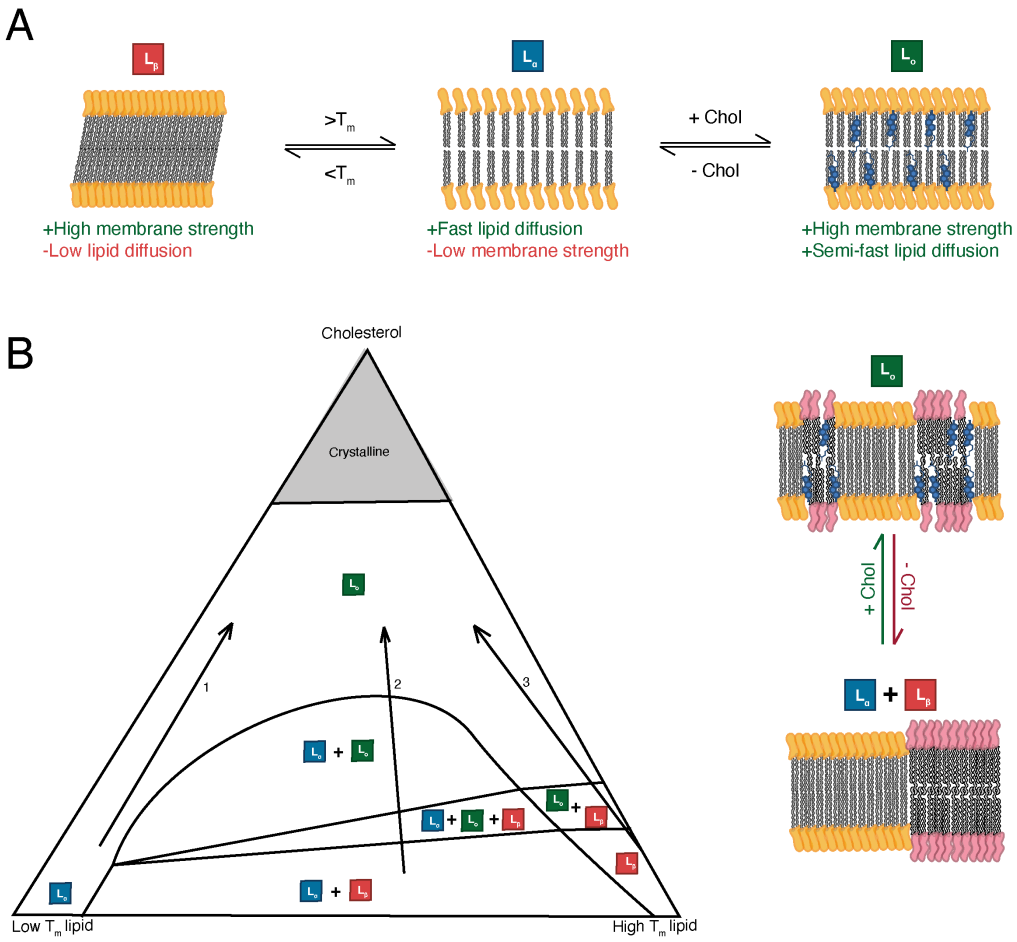


Figure 1.3: (A) Diagram of different lipid phases from the rigid gel phase (L_β) below the transition temperature, and the mobile fluid phase (L_α, also referred to as the liquid-crystalline phase) above the transition temperature. Addition of cholesterol allows for the benefits of both phase states over abroad temperature range, leading to the liquid-ordered (L_O) state. (B, left) Ternary phase diagram showing effect of cholesterol on a lipid mixture of two different melting temperatures. (B, right) effect of cholesterol on a representative SM/POPC bilayer, showcasing the phase separation into L_α and L_β forms without cholesterol, and the L_O form with cholesterol.

1.1.3 Lipid phases and domains

Most simple membranes of a single lipid species have a well defined melting temperature (T_m), below which the lipid is tightly packed with reduced motion, known as the gel phase (L_β, Figure 1.3 A). The L_β form is structurally very rigid, however there is little to no diffusion of lipids within the membrane. Above the T_m, the lipid exists in a fluid state (L_α, Figure 1.3 A). The L_α phase is highly fluid in terms of lipid diffusion, however possesses less structural stability than the gel phase,

or L_β form. In mixed membrane systems (2 or more lipid species), a significant difference in T_m can lead to the separation of lipids in the membrane, leading to distinct regions of L_α and L_β forms. This is known as lateral phase separation.

However, biological membranes are not composed of a single lipid species, but instead are a diverse mixture of lipids with a wide range of melting temperatures. As membranes are often physical as well as chemical barriers, organisms must balance the structural requirements of a membrane against physical stress, as well as maintaining lipid diffusion within the membrane. Eukaryotic organisms maintain this balance through the use of sterol lipids, with the most abundant sterol being cholesterol in animals (Figure 1.1 A, right),[25] ergosterol in fungi,[26] and stigmasterol in plants.[27] These sterol lipids can not form bilayers independently, but instead intercalate between phospholipids in a membrane (Figure 1.3 A). Intercalation prevents tight association between individual phospholipids below the T_m, and provides structural support to the disordered acyl chains of the lipid above the T_m. The addition of sterol lipids combines the benefits of the structural stability in the L_β phase, whilst retaining the lipid fluidity in the L_α phase. This modulated state is known as liquid-ordered phase (L_O).

Without sterol modulation the complexity of lipid membranes would lead to uncontrolled phase separation, leading to a structurally compromised membrane. This has been shown to significantly affect membrane morphology in synthetic vesicles with induced lateral phase separation.[28] The presence of cholesterol allows for the coexistence of lipids with a wide range of melting temperatures, into a near homogenous bilayer (Figure 1.3 B). Studies with model membranes have shown that sterol lipids preferentially associate with longer, more unsaturated acyl chains, such as sphingomyelin (Figure 1.1 C, left).[29] This partitioning leads to the presence of micro-domains, possessing a larger hydrophobic thickness and tighter lipid packing than the surrounding membrane, and are sometimes referred to as 'lipid-rafts'.[30–32] It it thought that the difference in hydrophobic thickness and lipid packing can allow for the passive sorting of membrane proteins into these micro-domains, which has been implicated in numerous cellular signalling

pathways,[33, 34], and even in certain disease states.[35] Whilst there is a good deal of evidence of micro-domain formation in model membranes,[36] capture of these rafts in natural systems by direct imaging or other biophysical techniques has proven difficult, due to their predicted small size (<10 nm) and transient nature.[37] This has led to the dispute of lipid rafts as a biologically relevant phenomenon.[38] Recent advances in fluorescent microscopy techniques and generation of more native-like model membranes have reignited this debate.[39]

1.1.4 Membrane proteins

Membrane proteins are a major constituent of cellular membranes, with a average plasma membrane being approximately 50% membrane proteins by mass.[2] In addition to their large number, membrane proteins play a vital role in cellular processes, such as signalling,[40] transport,[41] and energy production.[42] The sheer number and diversity of membrane proteins in these processes mean that membrane protein encoding genes account for approximately 20% of the eukaryotic genome,[43] and account for 60% of all current drug targets.[44]

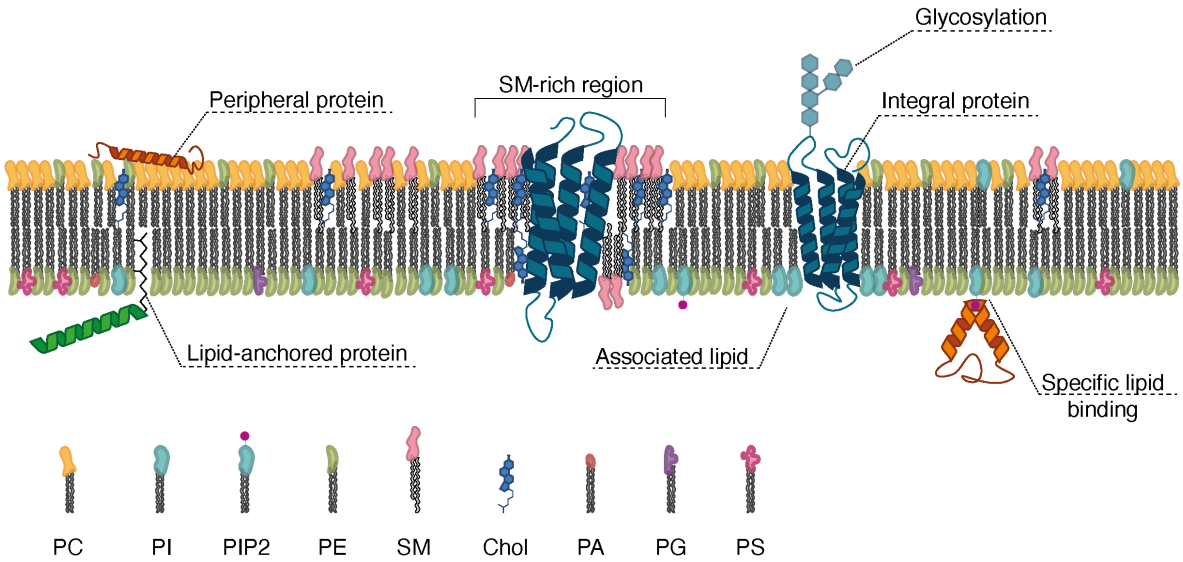


Figure 1.4: Examples of membrane-protein interactions, showing integral membrane proteins (blue), peripherally associated proteins (orange) and lipid-anchored proteins (green).

Membrane proteins can either be integral, peripheral, or lipid-anchored within the membrane. Integral membrane proteins (Figure 1.4, blue) are permanently embedded within the lipid membrane, with portions of the amino acid chain exposed on one - or both - sides of the bilayer. Integral membranes can either be inserted into the membrane without traversing the entire bilayer (monotopic), possess only one transmembrane domain with exposed protein regions on either side of the membrane (bitopic), or possess multiple transmembrane domains (polytopic).[45] The majority of integral membrane proteins are bi- or poly-topic. The transmembrane domains have, to-date, only included α-helical or β-barrel secondary structures,[45] with the membrane spanning regions being enriched in hydrophobic amino-acid residues. Numerous studies have shown that the hydrophobic residues (Ala, Ile, Leu, Val) are particularly enriched in the mid-bilayer region, while the aromatic residues (Trp, Tyr) are more enriched at the bilayer-water interface. It it thought that the aromatic residues aid correct insertion into the membrane and prevent tilting of the integral protein, through interactions of the rigid aromatic groups with the acyl core of the lipid bilayer.[46] The enrichment in aromatic residues is especially observed in β-barrel transmembrane proteins.[46] The hydrophobic residues primarily face into the bilayer, with the more hydrophilic amino acid groups of the main backbone being shielded within the secondary structure. Charged residues are often observed immediately adjacent to transmembrane domains, with some evidence suggesting that this is to aid in lipid-protein interactions.[47] As observed in lipid asymmetry, membrane proteins are similarly asymmetric in charge distribution, with a higher propensity of cationic amino acids observed on the cytoplasmic facing side of the protein (the 'positive-inside rule').[16]

Peripheral proteins (Figure 1.4, orange) transiently associate with the membrane, often binding in a reversible or transient manner. They bind through either interactions with integral membrane proteins,[48] through association with lipids within the membrane directly,[6, 49] or sometimes a combination of the two.[11, 50] These interactions are typically electrostatic in nature, and are often non-specific interactions (between cationic residues and anionic lipids).[51] Some peripheral

membrane proteins have also been shown to specifically bind lipids through the use of lipid binding domains.[52] An example of this is the specific recognition and binding of pleckstrin homology domains to the lipid headgroup phosphatidylinositol4,5-bisphosphate (PIP2) in cellular signalling processes.[6]

Lipid-anchored proteins (Figure 1.4, green) are soluble proteins tethered to the lipid bilayer through post-translational addition of hydrophobic groups, such as an aliphatic chain.[53] The most common lipid modification is the addition of a glycosylphosphatidylinositol (GPI) link, accounting for 0.5% of all eukaryotic proteins.[54] These GPI-linked, or GPI-anchored, proteins are almost exclusively located on the exterior leaflet of the plasma membrane.[55] These modifications are highly conserved, and are often used to localise signalling molecules in developmental processes.[55, 56] They play a wide variety of physiological roles, such as signalling receptors,[57] cell adhesion,[58] and surface antigens.[59]

Another lipid modification, prenylation, is more transient. Prenylation involves the addition of a 15-carbon (farnesyl) or a 20-carbon (geranyl) isoprenoid lipid to the Cys residue of a C-terminal CAAX motif.[60] It is is often reversibly applied to signalling proteins, again to aid in their localisation in cellular processes such as growth, cellular movement, and protein trafficking.[61] One family known to be commonly prenylated is the Ras superfamily GTPases, where loss of prenylation has been implicated in abhorrent signalling cascades, leading to cancer.[62, 63]

In addition to lipid-based modifications, both soluble and membrane proteins can be glycosylated.[64] Glycosylated proteins have diverse functions,[65] however the most well characterised role of glycosylation is in cellular recognition and adhesion. This recognition has been shown to be vital in development and immunology,[66, 67] with altered glycosylation being shown in various disease states.[68, 69]

1.1.5 Lipid-protein interactions

It is known that membrane proteins are not inert within the lipid bilayer, but actively interact with the lipids in their local environment.[70] This was first shown through electron paramagnetic resonance (EPR) experiments, which indicated

that lipids adjacent to the protein do not readily exchange with those in the bulk membrane.[71] These 'motionally restricted' lipids have been proven to be part of a lipid 'annulus' surrounding the membrane protein,[72] which are restricted enough to be resolved in techniques such as X-ray crystallography.[73] Solved X-ray structures indicate that the association of lipids to these membrane proteins is localised only to those in direct contact, with EPR experiments showing the lipid exchange between the lipid bulk and annulus is on the scale of 10^6-10^7 s^{-1}.[71]. More recently, high-resolution (< 2 Å) cryo-EM images -most notably on the human $GABA_A$ receptor- of membrane proteins have allowed for the direct observation of both non-specific and specific lipid-protein interactions.[74, 75] These recent works highlight not only the developing power of cryo-EM as in structural biology, but also the developing field of protein-lipid interactions as more delicate techniques become available.[76, 77]

A key aspect of these lipid-protein interactions is the shielding of the hydrophobic residues on the protein by the associated lipids.[78] In biological membranes, the exact bilayer thickness varies depending on the specific membrane, but on average has been conserved across all organisms to be between 25-30 Å. Similarly, the average hydrophobic thickness of an integral membrane protein is between 25-30 Å. Discrepancy between the hydrophobic thickness of the bilayer and the membrane protein can lead to distortion of the lipid and/or protein. This discrepancy is called 'hydrophobic mismatch', and can lead to numerous outcomes for both protein and bilayer, such as protein aggregation,[78] refolding,[79] or lipid reorganisation.[80] For example, it has been shown that acyl chain length can modulate the ATPase activity of the Ca^{2+}-ATPase, with a maximal activity rate shown to be at a bilayer thickness of 27 Å.[81] It it thought that the bilayer thickness leads to an altered mechanism of action, due to reorganisation of key residues along the ATPase backbone.[82] Additionally, a systematic review of transmembrane domains of eukaryotic membrane proteins has indicated specificity of membrane protein composition for different organelle membranes, through modification of the hydrophobic thickness and the presence of specific amino acid residues.[83]

Proteins have also been shown to preferentially interact with lipids dependent on head group type, through electrostatic interactions.[84, 85] Numerous EPR-based studies have shown that many proteins preferentially interact with negatively charged lipids (PG, PS, PA) over zwitterionic lipids (PC).[71] However, it is difficult to fully delineate bulk lipid effects and specific binding interactions for individual lipid-protein combinations.[86, 87]

Specific lipid-protein interactions are also important to protein activity, with numerous examples in the literature of lipids affecting ion transport rates,[88] protein oligomerisation,[89] ligand binding affinity,[90, 91] and signalling cascades.[50] The earliest, and perhaps the most famous, example of lipid-mediated protein activity is the dependance of the mitochondrial electron transport protein cytochrome oxidase c (CcO) on cardiolipin (CL).[92] Cardiolipin constitutes approximately 15-20% of the total lipid content of the mitochondrial inner membrane,[93] with various acyl chain length and compositions in a tissue specific manner.[94, 95] Loss of bound CL results in approximately a two-thirds decrease in electron transport activity by CcO.[96] Titration of other phospholipids in place of CL has been shown to be ineffective in restoring native-like activity, with only the addition of CL regenerating the fully-active complex.[92] Additionally, it has been shown that just 3-4 bound CL molecules are required for full electron transport activity of CcO,[97] indicating that the activity enhancement is due to specific interactions rather than bulk lipid effects.

Historically, the separation of specific *vs* non-specific lipid-protein interactions has been challenging, primarily due to the required use of detergent based extraction methods. The use of detergent based extraction methods has often limited examination of lipid-protein interactions to tightly bound complexes, such as CL and CcO. However, the recent development in detergent-free extraction methods,[98] and the advancement of native mass spectrometry techniques,[99] has led to expansion of lipidomics and the development of 'native-omics'.[100] This field is highly promising for the elucidation of the looser lipid-protein interactions that have previously been overlooked.[101]

1.2 Reconstitution of membrane proteins

Due to the complexity of biological membranes, it is common to extract, purify, and reconstruct membrane proteins of interest for isolated biochemical and biophysical characterisation.[102] These model membrane systems are often a far more simple analog to the native membrane system, containing a singular species of membrane protein in a simple binary or ternary lipid membrane.[103] The simple membrane model is due to both the high complexity of the biological membranes being difficult to fully mimic, and a desire to study homogenous systems for biochemical and biophysical assays. As membrane proteins are diverse, numerous reconstitution and extraction methods have been developed for different protein and assay requirements.[104–106]

Historically, the majority of membrane protein extractions have been performed through the use of detergents. Detergents are water-soluble amphiphilic molecules, which possess similar structural motifs as seen in lipids -possessing a charged, hydrophilic, headgroup with a non-polar, hydrophobic, tail (Figure 1.5 A). However, unlike lipids, detergents do not spontaneously form bilayers but instead form micelles above a critical concentration in water (Figure 1.5 B).[107]

When introduced into bilayer systems, detergent molecules preferentially insert into the bilayer, shielding the hydrophobic tails in the acyl core of the lipid bilayer. Due to the overall detergent shape, this introduces packing defects into the membrane.[102] Above the critical micellar concentration (cmc) of the detergent, the lipid bilayer is dissolved, with membrane lipids and proteins being incorporated into the detergent micelles (Figure 1.5 B).

Detergent solubilisation often leads to destabilisation of native protein activity and stability, primarily through a loss of lateral pressure supplied by the lipid bilayer,[102] and through detrimental detergent-protein interactions.[108] The extent of this destabilistion is somewhat detergent dependant, with non-ionic detergents shown to have a generally more mild effect on protein stability than ionic detergents. Similarly, long hydrocarbon chains, such as those observed in SDS and DDM, have been shown to directly interact with α-helical secondary structure motifs on

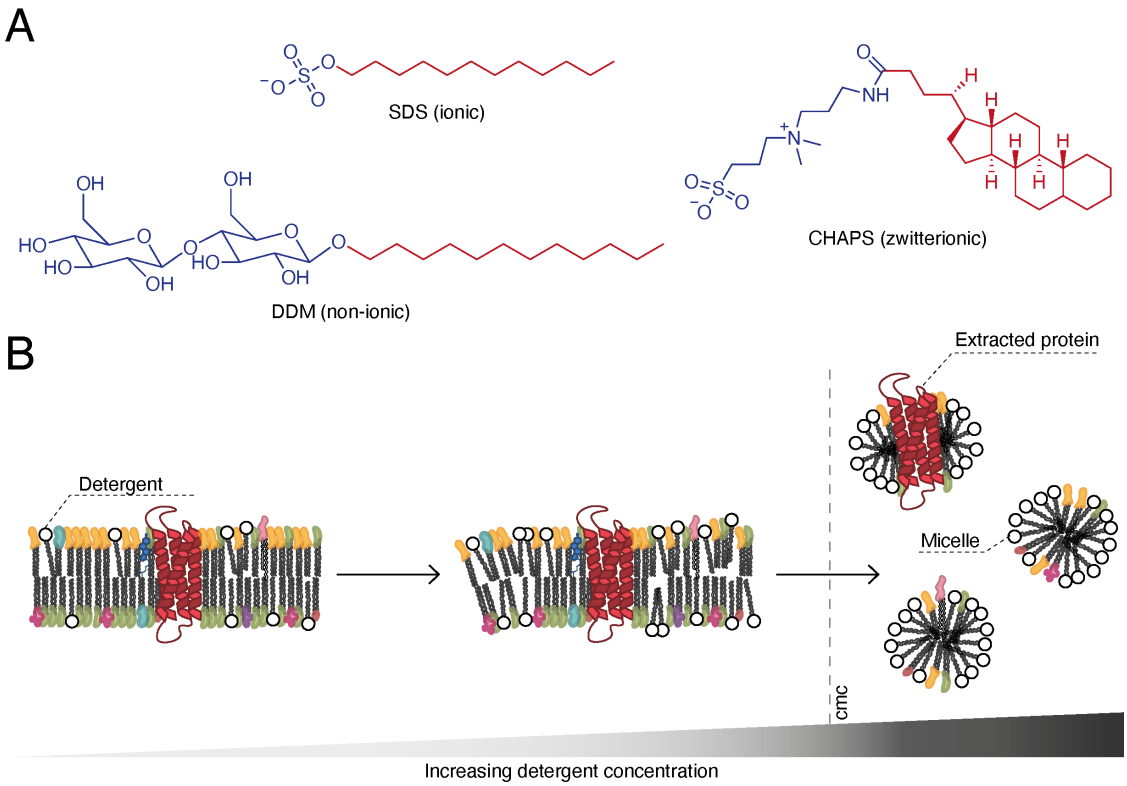


Figure 1.5: Detergent structure and mechanism of action. (A) Example structures of ionic detergents (SDS), non-ionic (DDM), and zwitterionic detergents (CHAPS). (B) Cartoon diagram of detergent-membrane interaction with increasing detergent concentration. Increasing membrane destabilisation occurs as detergent concentration increases. Above the critical micelle concentration (cmc) bilayer is dissolved and detergent-lipid and detergent-protein micelles are formed.

membrane proteins causing a loss of protein stability when compared to native bilayers.[108] Detergent choice is therefore often a balance between the efficiency of membrane solubilisation by the detergent compared to the destabilisation of the desired membrane protein once extracted.[102]

Because of the destabilising effect of detergents as a whole, it is common that detergent extraction is quickly followed by reconstitution of membrane proteins into various lipid environments, after which the denaturing detergent is removed (Figure 1.6 B).[109] Due to the varied nature of membrane proteins and their accompanying assays, a plethora of model membranes have been developed (Figure 1.6 A).

1.3 Model membranes

Native biological membranes are extremely complex, which causes difficulties in the generation of native-like membranes for *in vitro* studies. In contrast, detergent-protein micelles are extremely simple, but proteins in these systems are unstable and degrade quickly over time.[108] Model membrane systems are a compromise between the simplicity of detergent-protein micelles, and the stability of biological membranes. These models often mimic one or two important features of a membrane bilayer as required for the assay in use, i.e. the replication of bacterial membrane charge with the use of POPC:POPG (3:1).[110] These models are simplistic when compared to biological membranes, but have been shown to be effective in mimicking basic membrane functions required for membrane protein characterisation.[99, 111] The commonly used model membranes are shown in Figure 1.6 A.

1.3.1 Liposomes

Liposomes are enclosed vesicles of bilayer, containing an inner aqueous volume (lumen). Liposomes spontaneously form upon hydration of dried phospholipids, initially as multilamellar vesicles (MLVs), but can be extruded through polycarbonate filters to form unilamellar vesicles. Liposomes can be generated in various sizes and are classified by their average diameter. The smallest liposomes are called small unilamellar vesicles (SUVs) and average 20-50 nm in diameter, and can be formed by sonication. SUVs are highly curved, and are not often used in combination with membrane proteins.[112] Large unilamellar vesicles (LUVs, Figure 1.6 A) are the most commonly used in general membrane protein research, and can range in size from 100 nm to 1 μm. Due to the ease of generation with respect to complex lipid mixtures,[113] and the low curvature of the bilayer at this diameter range, they are often the default membrane model for membrane protein research. This is particularly true of membrane proteins that require different aqueous environments across the bilayer such as ion channels,[114] or transporters[115] due to the entrapped aqueous volume in the lumen. Giant unilamellar vesicles (GUVs) are >1 μm in diameter, and can be formed through controlled hydration of dried lipid films.[36]

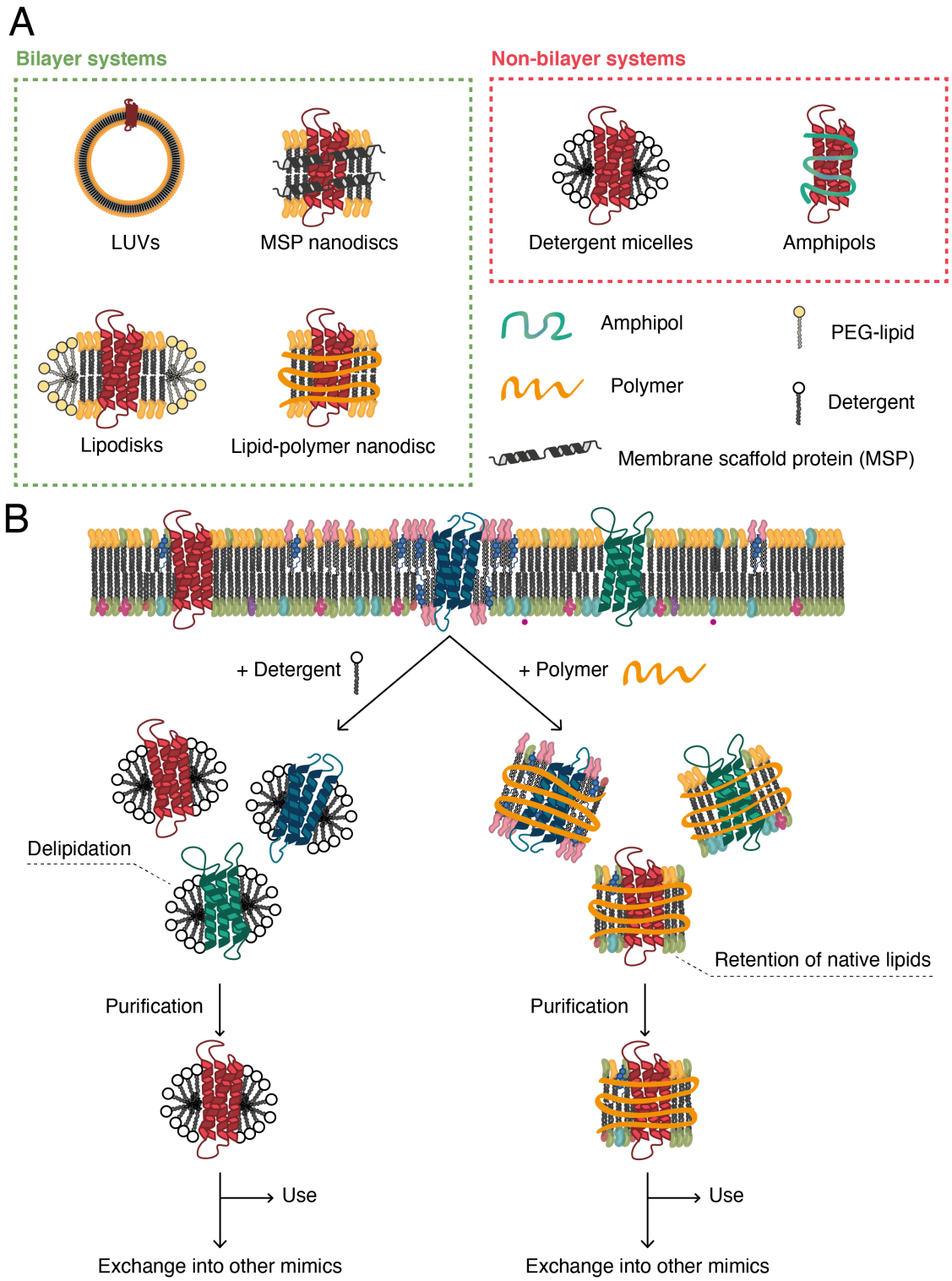


Figure 1.6: Example of commonly used membrane mimetics (A) separated into bilayer (left, green), and non-bilayer systems (right, red). (B) A generalised workflow for membrane protein extraction into membrane mimetics through the use of detergents (left) and polymer based approaches (right).

Their large size limits their use in general membrane protein research, however they are often used in optical microscopy techniques.[116]

Asymmetric LUVs (aLUVs) have also been developed to enable the addition of membrane asymmetry to these model membrane systems. Whilst other asymmetric model membranes have been developed,[117, 118] the generation of asymmetry in the commonly used LUV system has enabled broad biochemical and biophysical techniques to be used on these more complex systems. There are various methods of aLUV generation, with the most recent (and widely applicable) being the use of metyl-β-cyclodextrin (MβCD) to facilitate lipid exchange between donor vesicles to acceptor LUVs (Figure 4.1).[119] As of yet, these asymmetric systems have not been used in conjunction with integral membrane proteins, but have shown promise in the generation of more suitable membrane models for antimicrobial peptides.[120]

1.3.2 Bicelles

Bicelles are coin-shaped nanoparticles formed of a bilayer forming lipid with a 'belt' of detergent or modified lipid in a defined ratio (Figure 1.6 A).[121] Unlike liposomes, both sides of the bilayer are exposed to the same aqueous condition, which can be beneficial to some assays. Bicelles are preferentially used in NMR experiments, as their elongated structure allows them to align in an applied magnetic field.[121, 122]

1.3.3 Nanodiscs

Nanodiscs are similar to bicelles, in that they form coin-shaped nanoparticles. However, the 'belt' of detergent or modified lipid is instead a belt of amphipathic protein (Figure 1.6 A). The protein belt is most often a modified version of human Apoplipoprotein A1, otherwise known as membrane scaffold protein (MSP).[123] Nanodiscs can be generated through removal of detergent in the presence of MSPs at a defined ratio. The MSPs form a dimer, entrapping a disc of lipid at a defined size dependant on the MSP length. Different mutants have been developed to generate a range of nanodisc diameters. In theory, MSPs can incorporate any lipid mixture and membrane protein into the nanodiscs system, but in practice reconstitution

yields have been shown to be lipid and protein dependent.[124] Nanodiscs have shown great promise for structural and functional assays of membrane proteins within these systems, and are compatible with a range of biophysical assays, such as small angle X-ray scattering (SAXS),[125] NMR,[126] and fluorimetry.[127]

1.4 Polymer-based nanoparticles

1.4.1 Amphipols

Amphipols are a class of surfactant polymers, consisting of alternating hydrophilic and hydrophilic units. Amphipols can not solubilise membrane proteins independantly, but instead are designed to stabilise integral membrane proteins once extracted by detergent to form a solubilised version of an integral membrane protein (Figure 1.6 A).[128] Use of amphipols can therefore reduce the detergent concentration required once solubilisation is achieved, this lower detergent concentration has been shown to increase membrane protein stability, compared to detergent alone.[129] Various amphipols have been developed,[130] and have been shown to be compatible with common biophysical techniques such as circular dichroism,[131] NMR,[132] and cryo-EM.[76] However, the replacement of detergent with amphipols still has limitations when compared to bilayer systems,[133] which has limited their widespread use.

1.4.2 Lipid-polymer nanoparticles

Historically, detergent based extractions have been the only general methodology of membrane protein solubilisation, with a few notable detergent-free methods for specialised proteins and membrane systems, such as bacteriorhodpsin.[134] This has led to a range of model membranes, which all currently require detergent based methods to extract, purify, and reconstitute the systems. As discussed previously (§1.2), the exposure of membrane proteins to detergent is known to cause destabilisation, affecting protein structure and activity.[135]

A detergent-free method of membrane protein solubilisation was initially patented in 2006, using a random co-polymer of styrene maleic acid (SMA, Figure 1.7 A).[136]

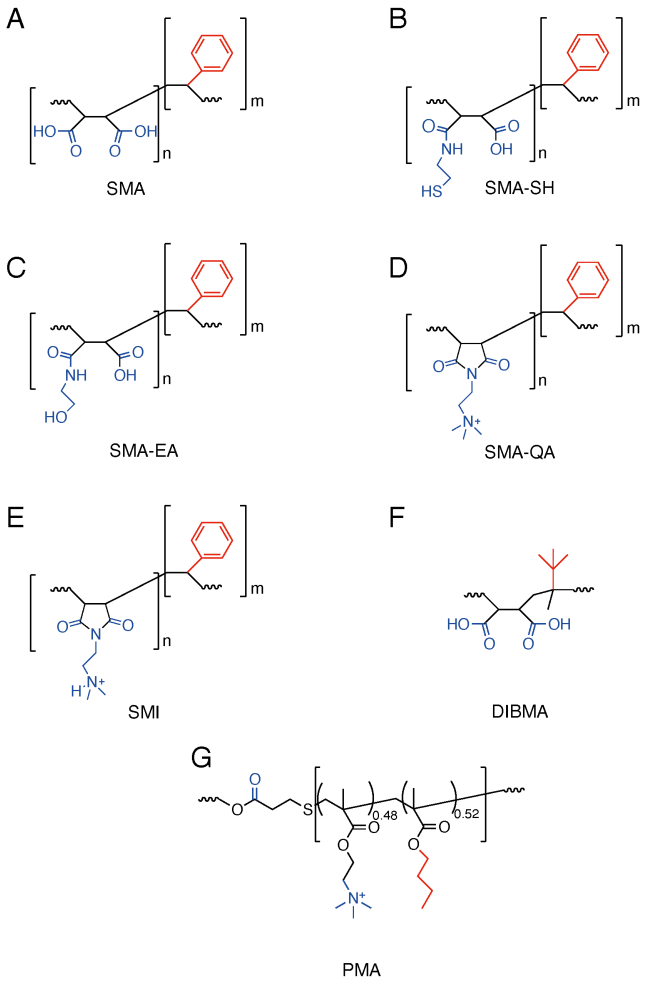


Figure 1.7: Chemical structures of currently available polymers used for forming polymer-lipid nanoparticles. (A) SMA: Styrene-maleic acid copolymer (unmodified). (B) SMA-SH, a styrene-maleic acid copolymer with partial thiol functionalisation on the maleic acid groups. (C) SMA-EA, a styrene-maleic acid modified by partial ethanolamine substitution on the maleic acid groups. (D) SMA-QA: a modified styrene maleic acid polymer, with a closure of the maleic acid groups to form a maleimide group, with a quaternary amine group acting as the major hydrophillic group. (E) SMI, a poly(styrene-co-maleimide). (F) DIBMA: Diisobutylene-maleic acid. (G) PMA: polymethacrylate polymer. Polymers C, D, and E were developed to increase the operable range of SMA (most notably in pH and divalent cation tolerance) through chemical modification of the original SMA (A). Polymers DIBMA and PMA (F and G respectively) are novel polymers not based upon the SMA framework. The hydrophilic groups are highlighted in blue, and hydrophobic groups highlighted in red.

This polymer showed a remarkable ability to solubilise biological membranes, without the use of detergent, and extract membrane proteins to form discoidal lipid-polymer nanoparticles averaging an approximate diameter of 10 nm (Figure 1.7 A).

The retention of the native lipid interactions was seen as a great advantage, and

it was has been shown that membrane protein stability is greater in lipid-polymer nanoparticles than in detergent micelles.[137] Since this initial patent, several polymer variants have been developed, both upon the SMA structure (Figure 1.7 B-E) and novel polymer types (Figure 1.7 F,G). The following section aims to review the polymers available, with particular interest for those used within this thesis.

1.4.3 Styrene-maleic acid copolymers (SMA)

SMA polymers were first patented in 2006, however there are two major classes of SMA now commercially available, SMALP and Lipodisq™ [98, 138] and are discussed in this thesis interchangeably. The difference is largely a trademark definition, with Lipodisq (LQ) referring to a specific SMA weight variant distributed by Malvern Cosmeceutics, with an average molecular weight of 9.5 kDa. SMALP is a more general term to refer to any lipid-polymer nanoparticle formed by any SMA variant, and are currently distributed by Polyscience. In addition to this legal definition in terms of average molecular weight, SMA polymers are produced with varied styrene:maleic acid ratios. As SMA is a random copolymer, this distribution refers to the *w/w* distribution of styrene:maleic acid, with ratios between 2:1 and 3:1 showing optimal solubilisation efficiency.[139]

Table 1.3 shows the variations of SMA polymers available, with the commonly used terms in this thesis. The SMA polymers used in this thesis are of the LQ variant,

Table 1.3: Versions of commercially available SMA polymer used by, or referenced by, this thesis. Information has been adapted from `http://www.smalp.net/polymers.html`. * denotes unknown commercial name, as product was a gift from Malvern Cosmecuetics

Version in thesis (SMALP *vs*) LQ	**Product name**	**S:MA ratio**	**M_r (g/mol)**	**Distributed by**
SMALP	SMALP 1100I	1.4:1	5000	PolyScience
SMALP	SMALP 25010P	3:1	10 000	PolyScience
SMALP	SMALP 30010P	2.3:1	6500	PolyScience
LQ	*	3:1	9500	Malvern Cosmeceutics
LQ	*	2:1	9500	Malvern Cosmeceutics

however the majority of the membrane protein solubilised by SMA in the literature are of the SMALP variant. It is important to note that no significant difference in both membrane solubilisation or nanoparticle characteristics between SMALP and LQ polymers of the same variation (i.e. SMA 3:1) has been identified yet. Due to the additional, non-SMA, polymers in this thesis LQ solubilised membrane are also referred to as polymer-lipid polymer nanoparticles, in particular for Chapters 2 and 3.

Low resolution ('coarse-grain') computer simulations have shown that SMA is able to solubilise membranes through an initial adsorption on the membrane through the insertion of the polymer's styrene groups into the lipid bilayer, in addition to charge-charge interactions with the polymer's maleic acid groups and the lipid head groups of the membrane.[140] After a short time (500 ns), SMA is absorbed into the bilayer, disrupting the bilayer structure -leading to perforation and the eventual formation of lipid-polymer nanoparticles.

Membrane solubilisation by SMA presents the first general protocol for membrane protein solubilisation without the use of detergents. This detergent free solubilisation not only removes the possibility of detrimental detergent-protein interactions, but allows for the retention of native lipid interactions once solubilised. Combined, polymer based solubilisation shows enhanced protein stability in these systems, and more native-like activity over detergent solubilised proteins, or reconstituted membrane protein systems (such as LUVs).[137]

However, SMA solubility in aqueous media is strongly dependent on both pH of the buffer.[141] This is primarily due to the high hydrophobicity of the styrene group, the high ratio of styrene:maleic acid in the commonly used 3:1 polymer variant, and the pKa of the maleic acid moieties of the polymer. The pKa range limits the operational pH of SMA to pH greater than 6, with values below 6 showing precipitation of the polymer.[142] Similarly, it has been shown that polymer solubility is highly sensitive to divalent cation presence in solution, precipitating above a 1 mM concentration of X^{2+}.[143] This is, again, due to the presence of the maleic acid moieties, which strongly coordinate with divalent cations.[144] Finally, it has

been shown that SMA stability in solution is ionic strength dependant.[145] All of these conditions must be accounted for when undertaking SMA-based solubilisation.

These limitations, due to the chemical structure of SMA, numerous modified SMA variants have been developed both for general and specific use. For example, the amine modified styrene:maleic acid variant, SMA-EA (Figure 1.7 C).[146] The addition of an amine to the maleic acid group generates a polymer with an expanded tolerance of pH, ionic strength, and divalent cation concentration, in addition to generating nanodiscs of a larger size (10-50 nm). SMA-EA has also shown an additional use in solid state NMR assays, due to the ability to align the nanoparticles with the addition of Yb^{3+}.[147] SMA-EA has been further adapted to allow the association of paramagnetic ions through the use of additional metal chelating groups.[148] Other functional modifications, such as the addition of a thiol group to a maleic acid moiety has also been developed (Figure 1.7 B).[149] This SMA-SH (SMASH) variant was developed for easy conjugation to functional compounds, such as fluorescent dyes for FRET-based assays.[150]

However, the major limitation of SMA-based polymers are aromatic groups, which can not be simply modified. Whilst the styrene hydrophobicity enhances solubilisation efficiency, the aromatic ring can interfere with spectroscopy methods, such as far-UV circular dichroism (CD).[137, 151] Novel polymers without a styrene group have since been developed to overcome this limitation of SMA, and to build upon the general and specific limitations of SMA solubilisation.

1.4.4 Diisobutylene-maleic acid (DIBMA)

Diisobutylene-maleic acid (DIBMA) is structurally similar polymer to SMA, initially developed in 2017, with an average molecular mass of 6.7 kDa.[143] It possess the non-aromatic diisobutylene in place of SMA's styrene moiety (Figure 1.7 F *vs* A), allowing the use of far-UV spectroscopy on formed nanoparticles. Additionally, DIBMA is an alternating polymer of diisobutylene:maleic acid in a 1:1 ratio, and therefore possess a higher charge density than the commonly used SMA 2:1 and 3:1. This increased charge density has been shown to increase the tolerance of

DIBMA solubilisation in terms of divalent cations presence.[152] However, due to the presence of maleic acid groups, DIBMA still shows sensitivity to divalent cation presence in solution. Additionally, the decreased hydrophobicity of the diisobutylene can lower the solubilisation efficiency, and purity of, extracted membrane proteins when compared to SMA extraction.[153]

1.4.5 Polymethacrylate copolymer (PMA)

Polymethacrylate is novel random co-polymer (Figure 1.7 G), with an optimal composition ratio of 0.48:0.52 cationic methacroylcholine:butyl methacrylate, and an average molecular mass of 4.7 kDa.[154] The novel composition, in particular the lack of acidic or basic groups, shows a great deal of promise in pH insensitive solubilisation. Similarly, due to the lack of chelating groups, it is predicted to be insensitive to the presence of divalent cations in solution. However, due to the relatively recent development of this polymer, it is as of yet under characterised.

1.5 Biophysical techniques for nanoparticle characterisation

1.5.1 Spectrophotometry

Every material absorbs, transmits, and reflects light over certain wavelengths due to their innate chemical structure and order.[155] Spectrophotometry is a commonly used technique that utilises this ubiquitous property to enable quantitative analysis of a substance in solution, either at a certain wavelength or across a range.[155] A spectrophotometer measures the absorption (or reflection) of light through the measurement of the initial intensity of light (I_0) compared to the intensity of light after the sample (I_t). The absorption (Equation 1.2), or in the case of non-absorbing compounds optical density (OD), is often reported as absorption (no units), or transmittance in % (Equation 1.1).

$$T = \frac{I_t}{I_0} \tag{1.1}$$

where T is transmittance (in %), I_0 is the initial light intensity (no units), and I_t is the transmitted light intensity (no units).

$$A = -log(T) = -log(\frac{I_t}{I_0}) \tag{1.2}$$

where A is absorbance (no units), T is transmittance (in %), I_0 is the initial light intensity (no units), and I_t is the transmitted light intensity (no units).

The work in this thesis used spectrophotometry for both optical density (OD) as a measure of particulate size (for polymer-based solubilisation assays), as well as the specific absorption of light at a certain wavelength by a compound (such as measurement of the oxidation of cytochrome c). Both of these techniques utilise the same principles of spectrophotometry (Figure 1.8), however the values attributed to these measurements are not interchangeable.

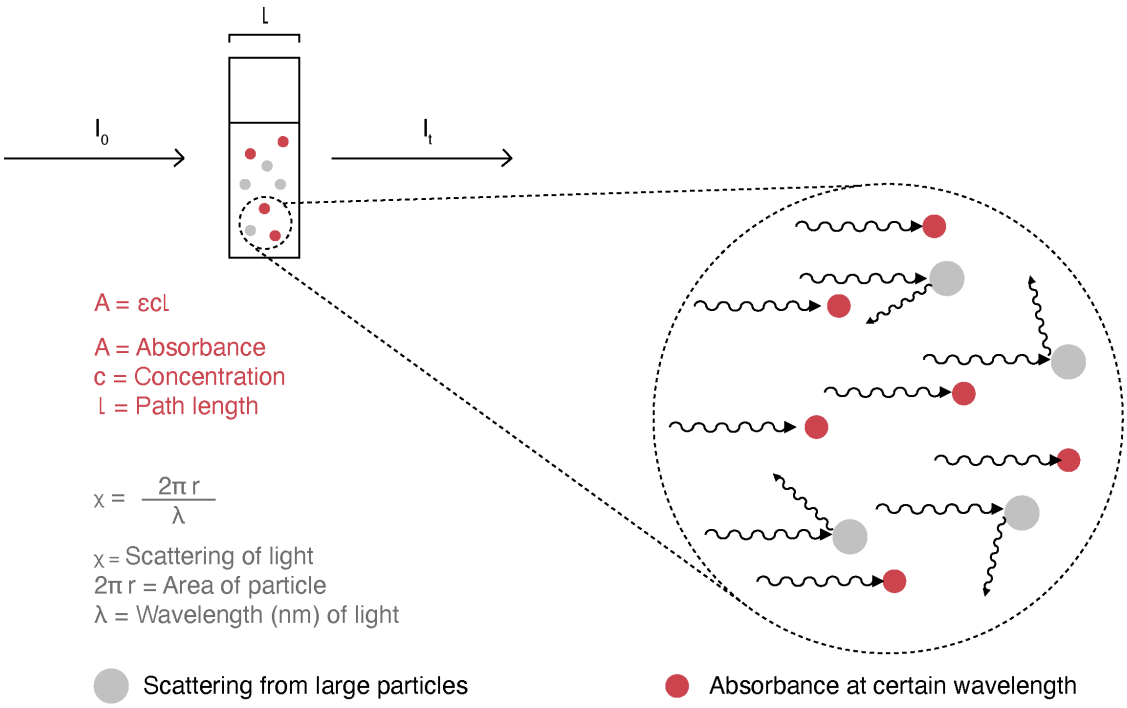


Figure 1.8: Diagram of spectrophotometry principles for both optical density (OD) and absorbance

Absorption

Absorption spectrophotometry utilises the Beer-Lambert law (Equation 1.3), which defines the linear relationship of absorbance (A), with the concentration of the sample

in solution (c). However, the measurement assumes that there is no other interaction of light with the solution, such as light scattering or solvent refraction.[155]

$$A = \epsilon c l \tag{1.3}$$

where A is the measure of absorbance, ϵ is the molar extinction coefficient, c is the concentration of the sample in solution, and l is the pathlength of measurement cuvette used.

Optical Density (OD)

Whilst absorbance as measured through the Beer-Lambert law negates non-absorption interactions, optical density (OD) is the quantitative measure of light absorption, scattering, and reflection of a solution of a known volume. These non-absorptive interactions causes the loss of light intensity whilst passing through the sample, and can be measured by an increase in measured absorbance of the sample by a spectrophotometer.

The scattering of light by particles was first mathematically described by Van Hulst in 1957, and has been shown to be proportional to particle concentration and size.[156] It has been shown that light scattering only occurs for wavelengths of light that are twice as large as the particle diameter. For example, a laser with a wavelength of 350 nm will only be scattered by particles that are larger than 175 nm in diameter (Equation 1.4).

OD is commonly used in biochemistry to measure the opaqueness of non-homogenous solutions at certain wavelengths, such as OD_{600} for bacterial growth measurement.[157] OD is also often used as a semi-quantitative measurement of membrane solubilisation by both detergent and polymer addition, measuring the decrease in optical density as membranes are solubilised into small micelles or nanoparticles.[145]

$$OD \propto x = \frac{2\pi r}{\lambda} \tag{1.4}$$

where OD is the optical density of the solution, x is the proportion of scattered light (no units), r is the radius of the particle (in nm) , λ is the wavelength of scattered light (in nm).

OD in this thesis is used to measure the solubilisation of liposome dispersions (multilamellar vesicles, MLVs) of model membranes ($D_H > 100$ nm) by a range of polymers to form lipid-polymer nanoparticles ($D_H < 20$ nm). Due to the low absorbance of the assay components at a wavelength of 350 nm, this wavelength was used in this thesis. The technique is therefore limited to the detection of particles greater than 175 nm in diameter, below which negligible scattering occurs. For more sensitive size measurements, dynamic light scattering was used in tandem to OD measurements.

1.5.2 Dynamic light scattering (DLS)

One commonly used method to measure small particle size is through the use of dynamic light scattering (DLS), which has been shown to have a spatial resolution to 1 nm, with some reports of sub-nanometer sizing in specialised experimental assays.[158] Assuming spherical particles and a homogenous sample, DLS is able to measure a particle size through the principles of brownian motion.[159] The rate of Brownian motion of a particle is dependant on the particle size, the viscosity of the solvent, and the temperature (Equation 1.5).

$$D_H = \frac{kT}{3\pi\eta D} \tag{1.5}$$

where D_H is the hydrodynamic diameter of the particle, k is the Boltzmann constant, T is the temperature, η is the dispersant viscosity, and D is the translational diffusion coefficient.

DLS measurement requires the recording of sample intensity over time, which is then correlated to the initial intensity through a correlation function (Equation 1.6). The correlation of the measured intensity will persist for longer when recording larger particles, due to the slower brownian motion. Smaller particles, with a

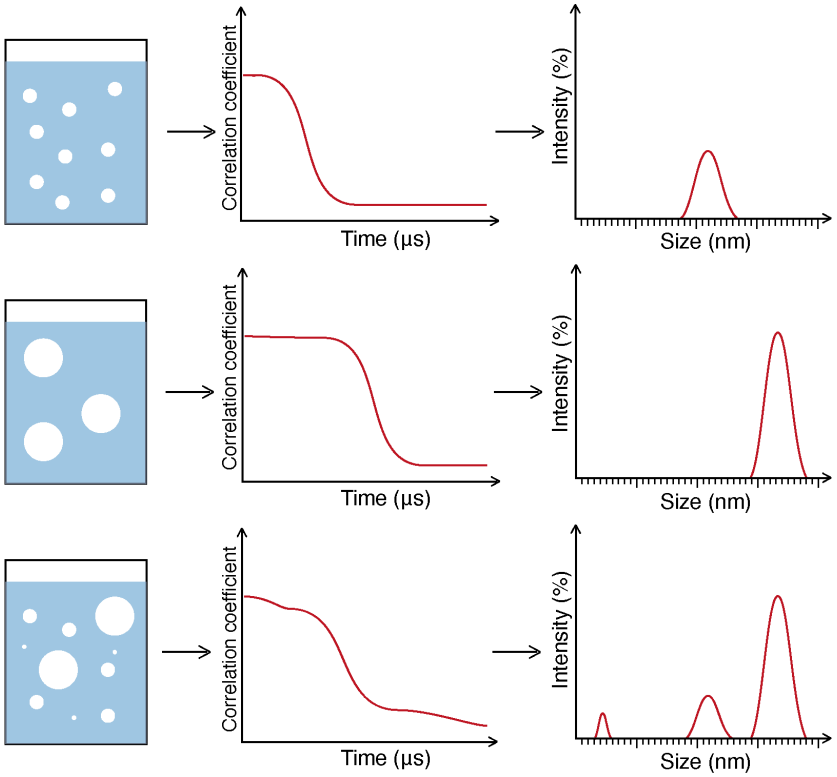


Figure 1.9: Principles of dynamic light scattering (DLS) measurement. (A) Small particles generate a rapid loss of intensity correlation with respect to initial intensity. (B) Larger particles show a delayed loss of correlation, due to the difference in diffusion speeds caused by brownian motion. (C) Polydisperse samples show a mixed correlation decay, dependant on the component sizes. Overall showing a shallow gradient of correlation decay than observed for homogenous samples.

higher brownian motion speed, will lose correlation to the initial intensity more rapidly (Figure 1.9 A,B).

$$G_\tau = A(1 + Be^{-2\Gamma_\tau}) \tag{1.6}$$

where G is the correlation of light intensity to the initial intensity (τ), A is the baseline autocorrelation function, B is the intercept of the correlation function, Γ_τ is related to the translational diffusion coefficient, defined by Equation 1.7.

$$\Gamma_\tau = Dq^2 \tag{1.7}$$

$$q = (\frac{4\pi n}{\lambda_0}) \cdot sin(\frac{\theta}{2}) \tag{1.8}$$

where n is the refractive index of the solvent, λ_0 is the incident wavelength of scattered light, and θ is the scattering angle. Therefore, by measuring the decay of correlated scattered light intensity, the hydrodynamic radius of the particles (D_{H}) can be calculated through Equation 1.5.

1.5.3 Förster resonance energy transfer (FRET)

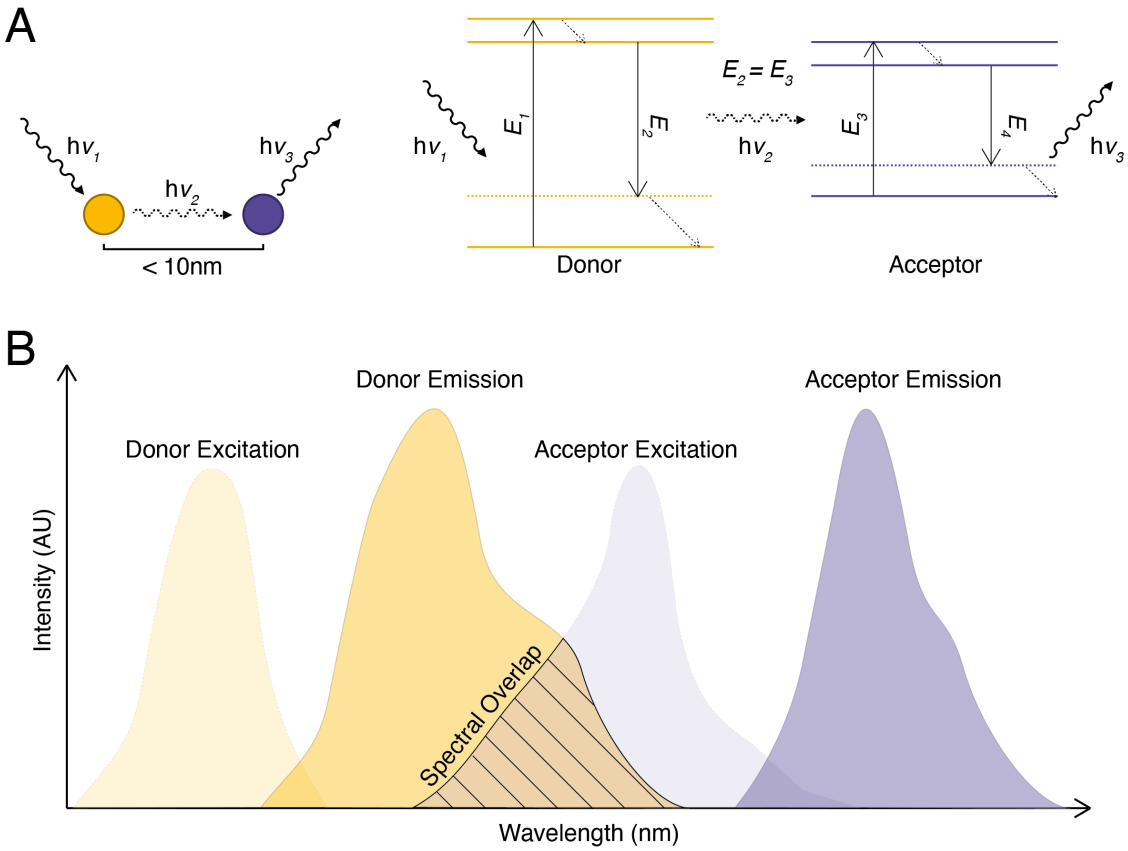


Figure 1.10: The principles of FRET (A) The donor (orange) and acceptor dyes (purple) must be within the Förster radius of < 10 nm, and have overlapping donor emission and acceptor excitation energy levels. The Förster radius can be determined with a spectral scan (B).

Förster resonance energy transfer (FRET) is a commonly used molecular ruler technique used in the biochemical field. FRET relies on the non-radiative energy transfer between two fluorophores, which have a spectral overlap between the 'donor' emission spectra, and the 'acceptor' excitation spectra (Figure 1.10 B). This energy transfer quenches the donor's excited state, and leads to the acceptor fluorophore being excited and fluorescing (Figure 1.10 A). A key feature of FRET

is the distance limitation of this energy transfer. FRET has a cutoff distance of approximately 10 nm,[160] due to FRET being dependant on dipole-dipole interactions. The efficiency of the energy transfer between the acceptor and the donor dyes is dependant on the distance between the two dyes, and their Förster radius (R_0). The Förster radius is a unique property of the individual dye molecules and is defined by the distance at which the energy transfer efficiency (E) is 50%, and is defined by Equation 1.9.

$$E = \frac{k_\tau}{k_\tau + 1/\tau_D} = \frac{R_0^6}{R_0^6 + r^6} \tag{1.9}$$

where E is the efficiency of transfer, k_τ is the rate of energy transfer (defined by Equation 1.10, τ_D lifetime of donor in excited state (in the absence of acceptor), R_0 is the Förster distance which can be defined by Equation 1.11, and r is the distance between the donor and acceptor dyes.

$$k_\tau = \frac{1}{\tau_D}\left(\frac{R_0^6}{r^6}\right) \tag{1.10}$$

$$R_0^6 = \frac{9(ln10)\kappa^2\Phi_D J}{128\pi^5 n^4 N_A} \tag{1.11}$$

where κ is the orientation factor, ϕ_D is the quantum yield of the donor fluorescence (in absence of acceptor), J is the integral of the spectral overlap (Figure 1.10 B) and calculated by Equation 1.12, n is the refractive index of the medium, and N_A is Avogadro's number. For general use, it is assumed that the dyes are isotropic, resulting in $\kappa^2 = \frac{2}{3}$.

$$J = \int f_D(\lambda)\epsilon_A(\lambda)\lambda^4 d\lambda \tag{1.12}$$

where f_D is the normalised donor emission spectrum, and ϵ_A is the acceptor molar extinction coefficient.

In practice, for simple experiments, one can simply measure the level of quenching of the donor by presence of the acceptor dye, or alternatively the increase in emission from the acceptor.[161] Due to the relatively short distance cut off (<10 nm) this is sufficient for a great deal of experimental designs.[110, 160] However, for

more specific experimental designs a more careful approach is required to avoid unnecessary excitation of the acceptor dye which can be caused by direct emission of the acceptor by the initial laser excitation (due to spectral overlap of the donor and acceptor excitation spectra).[160] Additionally, experimental designs must be careful to take into account other factors that could affect FRET observation, such as the level of 'crosstalk' across the membrane bilayer for lipid-labelled dyes, due to the membrane bilayer being approximately only 4 nm in thickness.[162]

For the work presented in this thesis, 1,2-dioleoyl-*sn*-glycero-3-phosphoethanolamine-N-(7-nitro-2-1,3-benzoxadiazol-4-yl) (NBD-PE) was selected as the donor dye, and 1,2-dipalmitoyl-*sn*-glycero-3-phosphoethanolamine-N-(lissamine rhodamine B sulfonyl) (Rho-PE) was selected as the acceptor dye. This FRET pairing has a known R_0 of 6.6 nm.[163]

1.5.4 Electron paramagnetic resonance (EPR)

Principles of cw-EPR

Electron paramagnetic resonance (EPR), otherwise known as electron spin resonance (ESR) is a spectroscopic technique that detects unpaired electrons through the use of an applied magnetic field (Figure 1.11 A,C). It is a technique that is similar to nuclear magnetic resonance (NMR), however it detects electronic transitions, rather than nuclear transitions. EPR as a general technique enables the exploration of the molecular structure, electronic environment, and molecular dynamics of a sample. These properties has made it a long-standing favourite for use in membrane studies.[110, 134, 164, 165]

There are two main EPR techniques; continuous wave EPR (cw-EPR) and pulsed EPR (pulsed-EPR). In cw-EPR, a continuous microwave frequency is applied to the sample to induce electronic transitions, whilst pulsed-EPR uses short (ns) pulses of microwave radiation *in lieu* of continuous irradiation. The assays performed in this thesis utilise the cw-EPR technique.

Electrons can be thought of as negatively charged particles, possessing an intrinsic property known as spin. This spin can be characterised by the spin angular

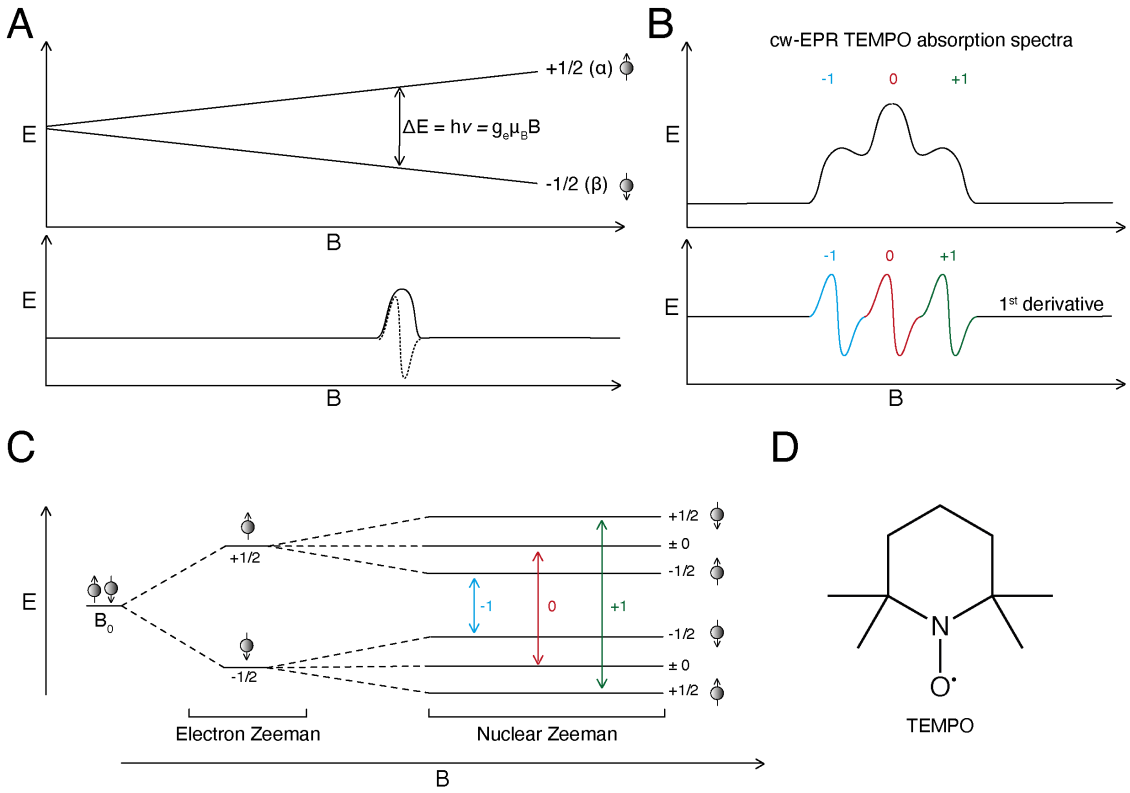


Figure 1.11: Diagram of EPR magnetisation principles in EPR spectra generation. (A) Simplistic diagram of electron Zeeman splitting of spin-states within an applied magnetic field, showing the interdependence of magnetic field strength and energy level splitting (top) and model absorption spectra observed by EPR measurement (bottom). (B) Model absorption spectra (top) and first derivative (EPR spectra) for nitroxide spin-label, showing three peaks labelled -1, 0, +1 due to the nitrogen spin quantum number (Table 1.4). (C) Diagram of both electron and nuclear Zeeman splitting in an applied magnetic field for nitroxide spin-labels, with annotated peaks and allowed spin states. (D) Example of nitroxide spin-label, in the form of 2,2,6,6-tetramethyl-1-piperidinyloxy (TEMPO).

momentum ($\mathbf{S}$), which is a vector with a magnitude quantized in units of $\hbar$, where $\hbar = \frac{h}{2\pi}$. On an arbritarily chosen axis there are $2S + 1$ projections allowed for electrons. Therefore, the allowed orientations of the spin angular momentum (also quantised by $\hbar$) are given by the m_S values of the electron's spin. Where m_S is the electron spin angular momentum quantum number with $2S + 1$ values in integral steps between $+S$ and $-S$ (Equation 1.13).

$$m_S = -S, -S + 1...S - 1, S \tag{1.13}$$

An electron with $S = \frac{1}{2}$ therefore has two allowed spin states: 'spin-up' ($m_S = +\frac{1}{2}$ denoted as $\uparrow$, or α) and 'spin-down' ($m_S = -\frac{1}{2}$, denoted as $\downarrow$, or β).

Additionally, electrons are not static within an orbital, but instead are constantly moving throughout space (with a spin angular moment of **S**). As they are charged, this movement generates magnetic dipole moment (μ_S) which has a gyromagnetic ratio (the ratio of its magnetic moment to its angular momentum) of γ. These can be related by Equation 1.14:

$$\mu_S = -\gamma \mathbf{S}\hbar = -g_e \frac{e\hbar}{2m_e}\mathbf{S} \tag{1.14}$$

where e is the electron charge, m_e is the electron mass, and g_e is the free-electron g-factor, with an approximate value of 2.0023. This can be simplified to form:

$$\mu_S = -g_e \mu_B S \tag{1.15}$$

where μ_B is the Bohr magneton of $9.274 \times 10^{-24}\text{JT}^{-1}$.

In the absence of an applied magnetic field, the two states of electron spin (the $\uparrow$ and $\downarrow$) are energetically the same, and an electron has equal probability in either the 'spin-up' or 'spin-down' state (known as degenerate). However, this is not true when a magnetic field is applied, where the interaction energy (E) of the electron magnetic moment (μ_S) and the magnetic field induction vector (**B**) can be described by Equation 1.16:

$$E = \mu_S \cdot \mathbf{B} \tag{1.16}$$

The z-component of the electron magnetic moment (μ_z) can be linked to the electron spin states (m_S) along the applied magnetic field (**B**) through Equation 1.17:

$$\mu_z = -g_e \mu_B m_S \tag{1.17}$$

From Equation 1.16 it can be understood that E is directly proportional to $|\mathbf{B}|$. The scalar value of μ_z (aligned electron magnetic moment along the z-axis) in a magnetic strength of B (the magnitude of the vector **B**) can be described by Equation 1.18:

$$E = -\mu_z B = E = g_e \mu_B m_S \times B \tag{1.18}$$

Therefore under an applied magnetic field the two possible states of electron spin ($\uparrow$ and $\downarrow$) can exist, however their states are no longer degenerate. The two states

of different energy levels are referred to as *Zeeman levels* (Figure 1.11 A,C). The lowest energy level, the β spin state, corresponds to the magnetic moment aligned with the magnetic field (parallel), whilst the higher energy level, the α spin state corresponds to the anti-parallel alignment.

In EPR spectroscopy, the the sample is irradiated with microwave radiation ($h\nu$) with an applied magnetic field (B). When the generated energy difference between the generated Zeeman levels (ΔE) matches the photon energy of the microwave radiation, the photon is absorbed. This absorption is observed (Figure 1.11 A), and can be defined by Equation 1.19:

$$\Delta E = h\nu = g_e \mu_B B \tag{1.19}$$

where ν is the frequency of microwave radiation absorbed. The magnetic field experienced by the electron in a molecule will differ from $\mathbf{B}$, and therefore the frequency of radiation absorbed (the 'resonance frequency') is characteristic of the molecule in question and the chemical environment. One major component in the electrons local environment is presence of the nuclei, with a magnetic spin (I). The electron-nuclear interaction leads to further splitting of Zeeman levels, known as the Nuclear Zeeman splitting (Figure 1.11 C). Additional splitting can occur (termed hyperfine interaction) and can be summarised with nuclear Zeeman splitting by Equation 1.20:

$$E = g\mu_B B m_S - g_N \mu N B m_I + a m_S m I \tag{1.20}$$

where g_N is the effective nuclear g-factor, μ_N is the nuclear magneton, m_I is the nuclear spin angular momentum, and a is the hyperfine splitting. The extent of this perturbation of the nucleus is primarily dependant on the spin quantum number of the nucleus. The nuclear spin quantum numbers of commonly occuring nuclides is listed in Table 1.4.

The most commonly used spin label in biochemistry, the nitroxide radical (such as TEMPO, Figure 1.11 D), has a spin quantum number of 1, and therefore three non-degenerate Zeeman levels ($2I+1$), this can be observed as the well-known three

peaks of the EPR spectra (-1, 0, +1 as observed in Figure 1.11 B). The hyperfine splitting of this spectra (observed by a change in line-width of the three peaks) can be used to study the spin label environment and anisotropy.[166] In this thesis, it is used to analyse the motional freedom of a spin-labelled lipid in a membrane bilayer.

Lipid order parameter measurement of membranes

A nitroxide spin label on the acyl chain of a phospholipid (such as the one used in this thesis) undergoes a fast long axis rotation and wobbling within a defined cone around the long axis (Figure 1.12 A). The spectra recorded by EPR spectropscopy therefore contains information of the lipid dynamics of the membrane. The anisotropic motion of the spin-labelled lipid can be elucidated through analysis of the EPR spectra, primarily through the use of line width measurements (Figure 1.12 B). Visually, a higher lipid order (more restricted motion) results in a broader spectrum, and *vice versa*. The anisotropic motion can be quantified through the use of Equation 1.21.

$$S = \frac{A_{\parallel} - A_{\perp}}{A_{zz} - (\frac{1}{2})(A_{xx} + A_{yy})} \cdot \frac{a'_0}{a_0} \tag{1.21}$$

where

$$a'_0 = (\frac{1}{3})(A_{xx} + A_{yy} + A_{zz}) \tag{1.22}$$

Table 1.4: Nuclear spin quantum numbers (I) of commonly occurring nuclides

I	Nuclide
0	^{12}C, ^{16}O
$\frac{1}{2}$	^{1}H, ^{13}C, ^{15}N, ^{19}F, ^{29}Si, ^{31}P
1	^{2}H, ^{14}N
$\frac{3}{2}$	^{11}B, ^{35,37}Cl, ^{63,65}Cu
$\frac{5}{2}$	^{17}O, ^{55}Mn
$\frac{7}{2}$	^{51}V

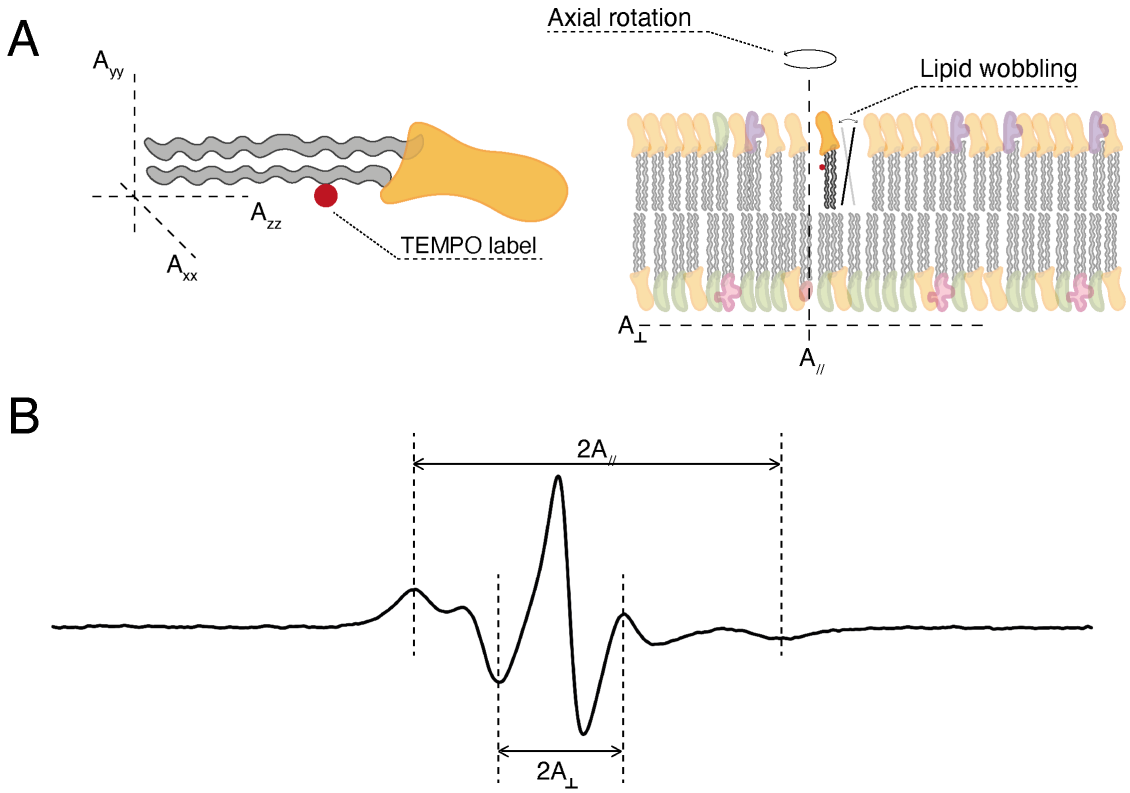


Figure 1.12: EPR spectra and measurement positions for the calculation of lipid order (S) used in this thesis.(A) Representative diagram of 5-PCSL spin-labelled lipid in a complex bilayer, showing relevant axial labels. (B) EPR spectrum of 1% 5-PCSL in DMPC LUV at 33°C, showing example measurement points of two hyperfine splittings, 2A‖ (upper) and 2A⊥ (lower) used in Equation 1.21.

and

$$a_0 = (\frac{1}{3})(A_{\|} + 2A_{\perp}) \tag{1.23}$$

Where S is the spin label order parameter, $A_{\|}$ is the hyperfine splitting arising from the spin label molecules parallel to the bilayer normal, $A_{\perp}$ is the hyperfine splitting arising from the spin label molecules perpendicular to the membrane normal. A_{xx}, A_{yy}, and A_{zz} are the principal hyperfine splittings corresponding to the molecular axis of the spin label, respectively.[167] S is calculated through the measurement of the anisotropy ($A_{\|}$-$A_{\perp}$) normalised relative to the maximum possible anisotropy for a static, crystalline, probe. As hyperfine splittings are dependant upon the polarity of the label environment, the polarity normalisation term is used ($\frac{a'_0}{a_0}$), which can be found in Equation 1.22 and 1.23. The values of A_{xx}, A_{yy} and A_{zz}

Table 1.5: Principle hyperfine values for DOXYL nitroxide spin label, used in this thesis, obtained from [166]

A_{axis}	**Hyperfine value (Gauss)**
A_{xx}	5.9
A_{yy}	5.4
A_{zz}	32.9

are dependant on the spin label used. For the nitroxide label used in this thesis, these values can be found in Table 1.5.

Various spin-labelled lipids are used throughout this thesis to elucidate the lipid mobility and order within lipid-polymer nanoparticles. Figure 1.13 is designed to aid visualisation for the notation used in this work when referring to the various probes, primarily to the numerous spectra in Chapter 3. This figure does not however include the TEMPO spin-label, whose structure can be observed in Figure 1.11 D. As can be seen in Figure 1.13, the label position - especially those in Figure 1.13 A - is varied. Generally speaking, there is an increase in amplitude of chain motion along the length of the acyl chain towards to the terminal methyl at the centre of the bilayer,[166] leading a requirement of label positions along the acyl chain length to fully characterise the lipid order parameter within bilayers. This is further explored in Chapter 3.

TEMPO titration experiments for the determination of lipid phase

The simultaneous partitioning of spin-label 2, 2, 6, 6-tetramethyl-piperidine-1-oxyl (TEMPO) between aqueous buffer and a lipid bilayer in the liquid-crystalline phase is well characterised.[168] TEMPO is water soluble, but can readily partition into the head group region of lipid bilayers that are in disordered lipid phases, such as the liquid-crystalline phase (L_O). However, in more ordered lipid phases, such as the gel phase, TEMPO is unable to partition into the bilayer. The partitioning of TEMPO into the bilayer can be detected through small changes in the isotropic hyperfine splitting and g factors. The differential partitioning of TEMPO allows for

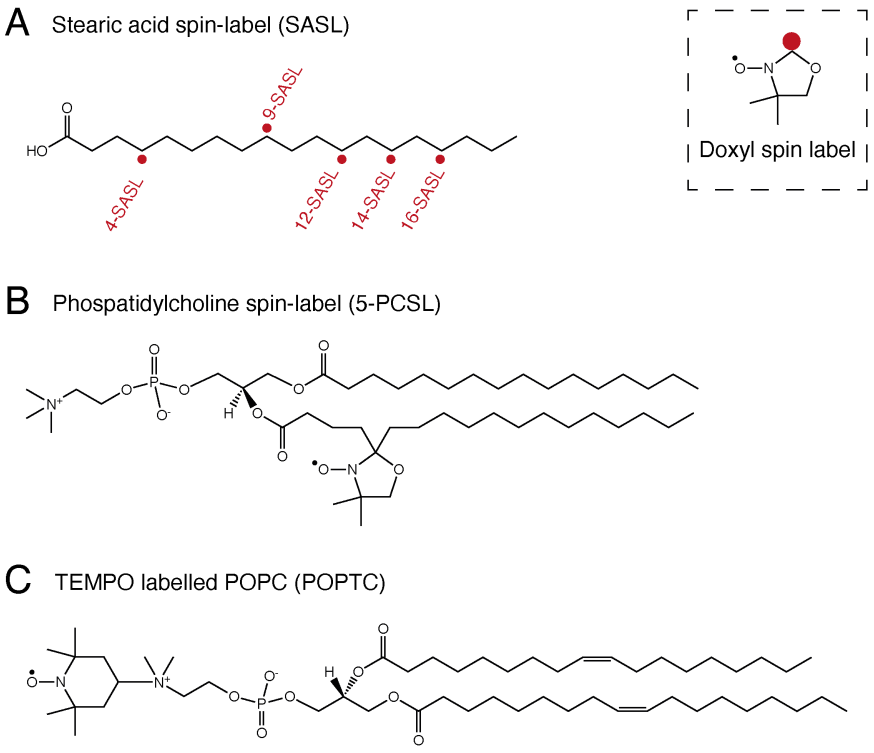


Figure 1.13: Spin-labelled lipid probes used within this thesis. (A) Stearic acid spin-label (SASL), with red dot markers for individual positions labelled with the doxyl spin label. Nomenclature used in this thesis is shown in red over these markers. (B) The lipid-probe 1-palmitoyl-2-stearoyl-(5-doxyl)-sn-glycero-3-phosphocholine (5-PCSL). (C) The lipid probe 1,2-dioleoyl-sn-glycero-3-phospho(tempo)choline (POPTC).

the detection of phase changes of a lipid bilayer from ordered to disordered phases, such as the gel-liquid crystalline transition. One can measure two amplitudes, H and P, which are the two high field lines caused by TEMPO in the polar (P) or hydrophobic (H) environment (Figure 1.14). H is approximately proportional to the amount of TEMPO within the membrane environment, and P is proporitonal to the concentration of TEMPO within the aqueous environment. The ratio of the partitioning can be defined by the partitioning factor, f:

$$f = \frac{H}{H + P} \tag{1.24}$$

where plotting f *vs* temperature can be used to elucidate phase transition temperatures.[166, 168]

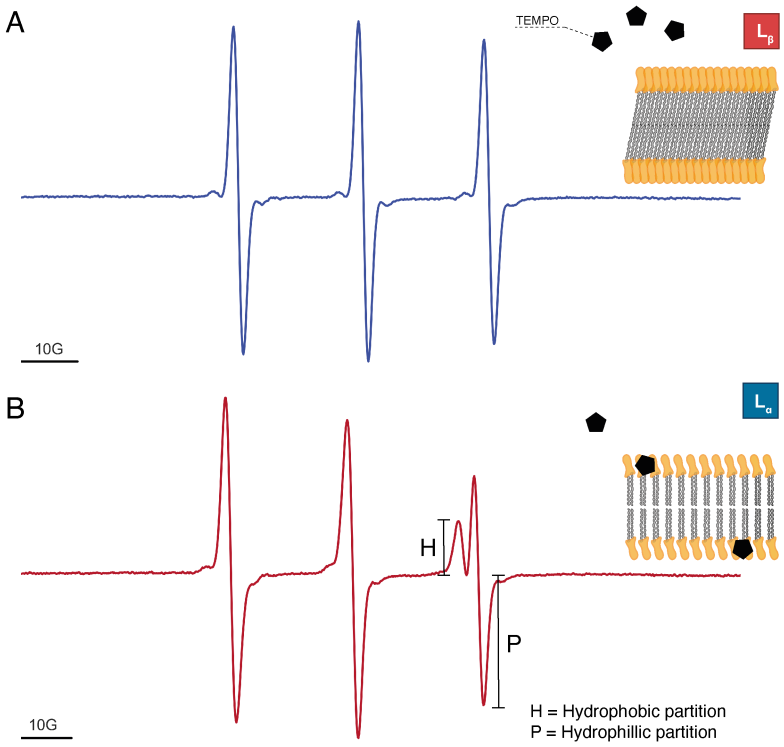


Figure 1.14: Principles of TEMPO partitioning. (A) TEMPO EPR spectra in a DMPC dispersion below the DMPC main transition temperature (L_β), with diagram of TEMPO solely in the aqueous buffer. (B) TEMPO EPR spectra in a DMPC dispersion above the DMPC main transition temperature (L_α), with a diagram of TEMPO partitioning into the lipid bilayer from the aqueous buffer. Measurement points for the *H* and *P* peaks are also annotated.

1.5.5 Principles of solid phase peptide synthesis (SPPS)

The generation of polypeptides of a defined sequence is performed ubiquitously in the biological realm, however this has proven extremely difficult to mimic synthetically. Solid phase peptide synthesis (SPPS), first developed by Merrifield in 1963, improved upon the initial solution-based methods through the use of a functionalised polystyrene resin bead.[169] Whilst selective protection of undesirable reactive groups was not novel for peptide synthesis, the attachment of the C-terminus to a insoluble resin bead allowed for the removal of the reagents and soluble intermediates through filtration alone, simplifying and speeding up the process.[169]

Optimisation of the synthesis and associated protecting groups was developed over the following years, leading to increased yield and faster production.[170]

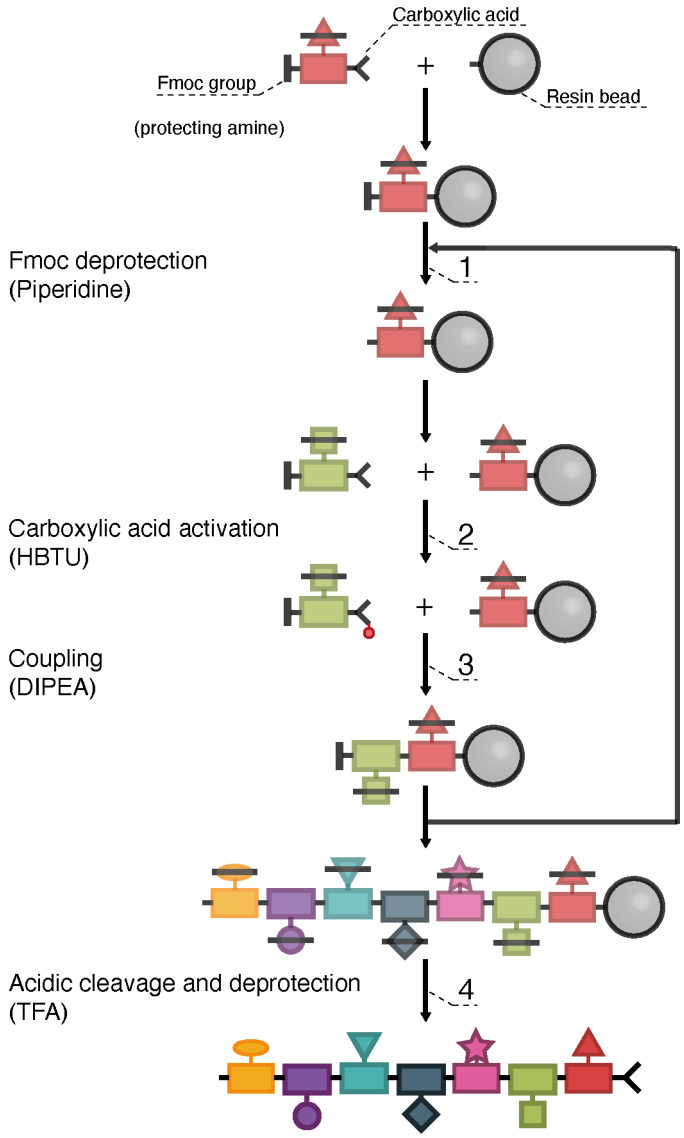


Figure 1.15: Stages of solid phase peptide synthesis (SPPS) showing the addition of Fmoc-protected amino acid residues to insoluble polystyrene bead in a step-wise manner. Numbered reactions indicate important reaction steps (1) Fmoc deprotection of N-terminus in basic conditions. (2) Carboxylic acid activation through HBTU reaction, which is activated upon addition of DIPEA. (3) (DIPEA) addition and coupling of amino acid to N-terminus of polypeptide chain. (4) Acidic cleavage of polypeptide from resin bead, and deprotection of side groups (removal of t-Bu protecting group). this can form both acidic peptide (free carboxylic acid) or amide peptide (with an attached amide group)

However, whilst these optimisations were extremely useful for peptide chemists, the reagents required for the reactions and subseqeunt deprotection steps slowed the adoption of SPSS beyond organic chemistry labs. This was primarily due to the need for a strong acid (commonly hydrogen fluoride, HF) to cleave the assembled

peptide from the resin at the end of the synthesis. However, the introduction of base-labile Fmoc protecting groups in 1970,[171] together with acid-labile resin linkers that can be cleaved using weaker acids (e.g. TFA) led to the establishment of the Fmoc/t-Bu protection protocols. The removal of iterative acid additions not only lowered the potential for side-chain deprotection every reaction step, [172] but also allowed for the automation of peptide synthesis, following the stages outlined in Figure 1.15. The use of orthogonal protecting groups allows for simultaneous deprotection and cleavage of synthesised peptides.

These adaptations have permitted the rapid adoption of peptide synthesis in the biochemical and material fields. The synthesis of small peptide sequences of up to 50 amino acids in length is a routine task these days.[172] In addition to this, peptide synthesis allows for much more flexibility in sequence design and modification, without the need for strenuous cloning and primer design for each desired sequence. This allows for a greater exploration of sequence space.

1.6 Aims of the thesis

The aims of this thesis are to characterise the formation and intrinsic properties of self-assembling nanoparticles in a systematic manner over a range of conditions, with a particular focus on lipid-polymer nanoparticles. Initial characterisations were previously performed had been previously performed by past students for SMA 3:1 (Lipodisqs) in the lab. In addition the characterisation of SMA 3:1 nanoparticles, the assays were also extended to include additional polymers DIBMA and PMA, as well as the SMA 2:1 (Lipodisq) variant.

Chapter 2 focusses on the characterisation of lipid-polymer nanoparticle formation through membrane solubilisation. Optimisation of these assays is discussed to cover a wide range of conditions, such as pH, ionic strength and divalent cation presence, and to fully characterise the four polymers in a standardised manner. This chapter hopes to discover the optimal solubilisation conditions for the four polymers in two model membrane systems, the neutral DMPC, and the commonly used bacterial membrane mimetic POPC:POPG (3:1). This is the first comprehensive characterisation of multiple polymers solubilisation ability, and offers a basis for future solubilisation assays with novel polymers and membranes in future solubilisation attempts.

Chapter 3 aims to utilise the 'ideal' solubilisation conditions discovered in Chapter 2, to characterise DMPC-polymer nanoparticles formed in conditions of pH 7.4, and 100 mM NaCl. This chapter hopes to show the comparative differences of the formed nanoparticles in terms of overall structure, with EM imaging, as well as their thermotropic characteristics through a range of biophysical techniques, namely differential scanning calorimetry (DSC), and electron paramagnetic resonance spectroscopy (EPR).

Chapter 4 goes on to explore the recently reported novel property of lipid-polymer nanoparticles: collisional lipid mixing. It hopes to elucidate whether this is an intrinsic property of lipid-polymer nanoparticles, and the rate of mixing for each lipid-polymer nanoparticle characterised in Chapter 3. Chapter 4 applies this novel property of lipid-mixing for the specific titration of lipids into

protein containing nanoparticles, using the well characterised cytochrome oxidase c dependence on cardiolipin.

Chapter 5 explores a different form of self-assembling nanoparticle during a placement at the National Physical Laboratory. This chapter aims to optimise the purification of a synthetically produced peptide, ST1-QAA, using high pressure liquid chromatography (HPLC). This chapter then looks to characterise the self-assembly of this peptide to form viral like particles through the use of EM imaging, circular dichroism (CD) spectroscopy and Fourier transform infra-red (FTIR) spectroscopy.

Season food with the proper amount of salt at the proper moment;
choose the optimal medium of fat to convey the flavor of your ingredients;
balance and animate those ingredients with acid;
apply the right type and quantity of heat for the proper amount of time—do all this and you will turn out vibrant and beautiful food, with or without a recipe.

Samin Nosrat, Salt, Fat, Acid, Heat:
Mastering the Elements of Good Cooking

2 Characterising the formation of lipid-polymer nanoparticles

Contents

2.1 Introduction 45
2.1.1 Aims 49
2.2 Materials & methods 49
2.2.1 Preparation of polymer 49
2.2.2 Preparation of lipid dispersion (MLVs) 50
2.2.3 Initial solubilisation assay by spectrophotometry 50
2.2.4 High-throughput spectrophotometry (96-well plate) . . 51
2.2.5 Dynamic light scattering (DLS) 52
2.3 Results & discussion 52
2.3.1 Development of solubilisation assay by optical density (OD) 53
2.3.2 Formation of lipid-polymer nanoparticles across pH range 58
2.3.3 Formation of lipid-polymer nanoparticles across NaCl concentration 60
2.3.4 Formation of lipid-polymer nanoparticles across divalent cation (Mg^{2+}, Ca^{2+}) concentration 63
2.4 Summary and Conclusions 66

2.1 Introduction

There are currently multiple techniques used to aid membrane protein solubilisation,[48] the most common being through the use of detergents.[102] However,

detergent solubilisation can lead to protein denaturation,[173, 174] and loss of native protein-lipid interactions through delipidation.[32, 70, 175] This can also have the effect of disassembling membrane complexes.[176] A detergent-free method of membrane protein purification introduced in the form of styrene maleic-acid (SMA) lipid-polymer nanoparticles in 2009.[138] The result is a coin-shaped nanoparticle containing a membrane protein, with a lipid annulus surrounded by a polymer 'belt' (Figure 2.1 A) that shields the hydrophobic acyl core from unfavourable interactions with water molecules. Since then, membrane-interacting polymers have been seen as a revolution in membrane protein purification in a detergent-free manner.[177, 178]

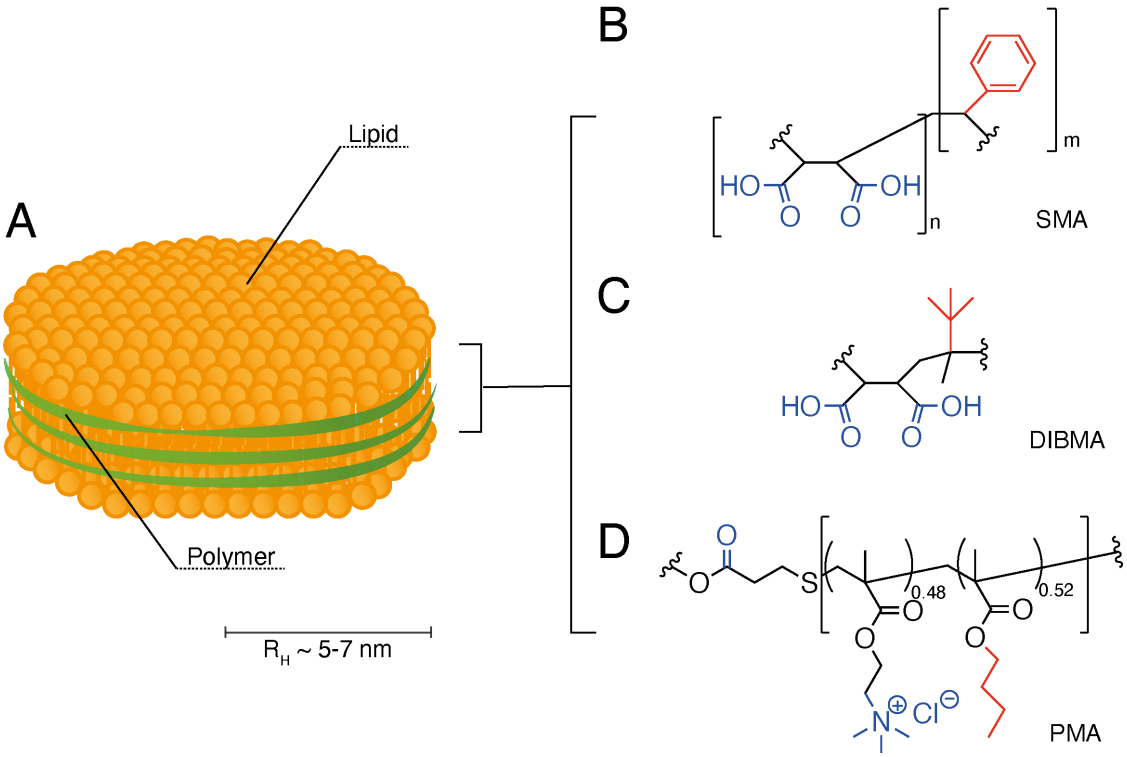


Figure 2.1: Diagram of polymer structure used for forming polymer-lipid nanoparticles. (A) Cartoon representation of polymer-lipid nanoparticles resulting from interaction with polymers (B-D), comprised of lipids (shown in yellow) surrounded with a polymer 'belt' (shown in green). Multiple polymers have been shown to be capable of forming nanoparticles, such as: (B) SMA, (C) DIBMA, and (D) PMA. The hydrophilic groups are highlighted in blue, and hydrophobic groups highlighted in red.

Amphipathic polymers (shown in Figure 2.1 B-D) contain similar functional groups to detergents.[179] These contain both hydrophobic groups that interact with the acyl core of the lipid and hydrophilic groups that primarily interact with

the lipid head groups and the solvent. Importantly, whilst detergents generally work *via* replacing lipid association with detergent association (known as delipidation) with some (often random and variable) indigenous lipids being retained,[180] these polymers instead are thought to retain a lipid annulus surrounding the protein.[139, 181]

The retention of a native lipid environment during extraction[182, 183] has been demonstrated to enhance stability and a more native-like behaviour over detergent-based extraction methods.[134, 184] This behaviour has been attributed to both the lateral pressure supplied by the native membrane,[185] as well as the presence of native protein-lipid interactions.[186] In addition to the protein stability enhancements in these nanoparticles, a detergent-free extraction mechanism has allowed for exploration of the lipid-protein interactions through lipidomics, most notably through the use of mass spectrometry.[187–189]

The first polymer designed to generate lipid-polymer nanoparticles of this form was styrene-maleic acid (SMA) in 2009,[98, 138] however some examples of membrane-interacting polymers has been known for longer.[190] SMA is a co-polymer, containing a random mix of both styrene and maleic acids, with weight ratios of 3:1 or 2:1 showing the highest membrane solubilisation efficiency.[139, 191] However, this co-polymer has shown two notable limitations; Firstly, the aromatic nature of the styrene moieties absorb in the UV range with a peak maxima at 245 nm.[192] This has limited SMA nanoparticles for use in the characterisation of membrane proteins, due to overlapping absorbance spectra between the polymer's styrene groups, and the intrinsic absorbance of proteins' in the near UV region.[193–195] Secondly, the maleic acid groups lead to a high sensitivity to divalent cations such as magnesium and calcium, in addition to limiting SMA's use in low pH vales (< 6).[196] Divalent cations are often vital co-factors involved in membrane protein activity such as ATPases,[197] or calcium dependant ion channels.[40] Various modifications to the SMA chemistry have been developed to reduce these limitations, such styrene maliec acid - quaternary amine (SMA-QA).[198] SMA-QA has shown to possess an insensitivity to divalent cations through the conversion

of the maleic acids moieties to a maleimide and a quaternary amine (or choline group). This modification has also been shown to expand the operable pH from 6-10 to between 2.5-10.[198, 199]

Despite SMA's limitations, the use of polymer-based solubilisation has been a revolution in membrane protein extraction over detergent-based methods. Further polymers have been developed to improve on the success of SMA. Di-isobutylene-maleic acid (DIBMA) was developed by Keller *et al.*,[143] with the replacement of the aromatic styrene with an isobutylene group. In addition to this replacement, DIBMA is an *alt* polymer, of a 1:1 hydrophobic:hydrophilic ratio, whilst SMA is a random co-polymer of varying ratios. It has been reported that DIBMA is more tolerant of divalent cations than SMA.[143] It has even been shown that doping the solubilisation buffer with ~10 mM of magnesium ions can increase the solubilisation efficiency.[152] Despite these improvements, DIBMA is still structurally similar to SMA, conserving the maleic acid moiety which leads to both divalent cation and pH sensitivity to some degree. The limiting maleic acid moieties present in both SMA and DIBMA were later removed by Ramamoorthy *et al.*,[154] by developing a polymethacrylate (PMA) framework. Polymethacrylate possesses no aromatic moieties, so does not absorb in the UV, or visible, range.[192] Additionally, Ramamoorthy *et al.* showed that the lack of maleic acid, or any protonatable groups was shown to increase the range of pH tolerance to a similar range to that of the SMA-QA variant (3-10).[200]

While there is a great deal of literature for the comparison of SMA variants[142, 196, 201] and their membrane solubilisation ability through various biophysical methods,[177, 202, 203] there is a distinct lack of in-depth comparison between the newly generated polymers, such as DIBMA and PMA. This makes direct comparison of solubilisation efficiency between literature values difficult, and standardisation of results almost impossible. With polymer choice for membrane studies now expanding beyond SMA, it is important to fully characterise and compare the currently available polymers, and for a standardised framework of assays to be developed for future additions.

Various techniques have been developed in recent years to understand the process of membrane solubilisation through the use of polymers, most notably for SMA polymer variants.[110, 142, 204, 205] However, as new polymers and biophysical techniques become available, there is need for standardised, high throughput assays to allow direct comparisons between existing polymers, and polymers that are yet to be developed.

2.1.1 Aims

The work presented in this chapter focusses on comparing the formation of lipid-polymer nanoparticles formed by solubilisation of lipid dispersions. Studies were performed on synthetic models of both neutral (DMPC) and charged (POPC:POPG 3:1) membranes by four commercially available nanoparticles forming polymers available: SMA 3:1, SMA 2:1, DIBMA, and PMA. The formation of these lipid-polymer nanoparticles was measured by a combination of optical density (OD_{350}) and dynamic light scattering (DLS) measurements. To determine the 'ideal' solubilisation conditions for each polymer, a range of buffer conditions were studied varying pH, ionic strength and divalent cations. This was used to probe how each factor affects the interactions between the membrane and polymer, through solubilisation and subsequent stability in solution.[206]

This chapter also shows the optimisation of a high throughput and low-waste method to examine these conditions, and additionally explains how the processing of experimental data was optimised through the use of python scripts. The automation of analysis allowed for the generation of a high-throughput assay, in addition to the development of a novel parameter, solubilisation efficiency. This toolkit can be found in full *via* GitHub.[207]

2.2 Materials & methods

2.2.1 Preparation of polymer

SMA 3:1 and SMA 2:1, with an average molecular weight of 9.5 kDa, were obtained from Malvern Cosmeceutics. They were hydrolysed from the anhydrous form as

previously described by Gulati *et al.*[208] DIBMA was a kind gift from Sandro Keller whilst PMA was purchased from Avanti (Alabaster, AL). All polymers, unless otherwise, stated were stored and used at room temperature (RT) in 20mM HEPES buffer containing 100 mM NaCl at pH 7.4 at a polymer concentration of 100 mg/mL (10% *w/w*). Solubilisation was achieved using 1.5× (*w/w*) excess of polymer to lipid equating to 1.5% (*w/v*), with an incubation of 1 hr at RT, unless otherwise stated.

2.2.2 Preparation of lipid dispersion (MLVs)

All lipids in this thesis were purchased from Avanti (Alabaster, AL) and used without further modification. Two lipid types were used in this chapter, DMPC and a POPC:POPG (3:1 molar) mixture. DMPC was stored at -20^{o}C at a concentration of 25 mg/mL in chloroform. POPC:POPG (3:1) was prepared as powder, prior to solubilisation in a 3:1 chloroform:methanol (*v/v*) solution to a concentration of 25 mg/mL. This was similarly stored at -20^{o}C until required.

The required amount of lipid was dried under nitrogen and then under a high vacuum for at least 4 hours. This lipid film was then resuspended in distilled water (dH_2O) to a concentration of 5 mg/mL and incubated at 30^{o}C for 30 minutes, with gentle agitation to generate a dispersion of multi-lamellar vesicles (MLVs). This dispersion was then used as described in the following sections.

2.2.3 Initial solubilisation assay by spectrophotometry

The initial protocol for measurement of membrane solubilisation by OD_{350} was developed in collaboration with a previous student, Tongran Zhang,[209] a MBiochem student in the lab, and was slightly modified to reduce material waste for the generation of Figure 2.2.

For each sample, 100 μL of the lipid dispersion (generated as described by §2.2.2) was aliquoted, and diluted with 400 μL of the required buffer to a final lipid concentration of 1 mg/mL (for a full buffer list, see Table A.1). The sample was briefly agitated at 30^{o}C before the OD_{350} was recorded in triplicate at 30^{o}C, using a Jasco V-630 UV Spectrophotometer, to obtain an initial OD of the lipid dispersion.

The desired polymer (generated as described by §2.2.1) was added from a 10% (*w/v*) stock solution in 20 mM HEPES, 100 mM NaCl, at pH 7.4 to a final concentration equal to 1.5× (*w/w*) the DMPC weight. The solution was subsequently incubated for at least 30 minutes at 30°C with gentle agitation prior to a second recording (again in triplicate). All titration points were measured with three repeats, prior to averaging and estimation of standard deviation. Data were processed using the statistics library in Python 3. Plotting of absorbance *vs* conditions (Figure 2.2) utilised the Matplotlib library, and supporting Seaborn library.[210] Example python scripts for both the analysis and plotting can be viewed on Github.[207]

2.2.4 High-throughput spectrophotometry (96-well plate)

Optical density measurements were recorded within a 96-well plate, using a CLARIOstar plate reader at 350 nm, with a final lipid concentration per well of 1 mg/mL. For preparation, 20μL of lipid dispersion per well (generated as described by §2.2.2) were then diluted with 80 μL of buffer condition (at 1.2× final concentration) and samples were gently agitated at 30^{o}C for 20 minutes prior to an initial OD measurement at 30^{o}C. The polymer (generated as described by §2.2.1) was then added at a 1.5× (*w/w*) excess and incubated at 30°C with gentle agitation followed by secondary OD measurement.

These measurements are then processed through the use of python, utilising the NumPy (https://numpy.org), pandas (https://pandas.pydata.org/), and statistic packages. The metric of solubilisation efficiency was calculated through Equation 2.1:

$$Solubilisation efficiency = \frac{OD_{2c} - OD_{1c}}{OD_{min} - OD_{1c}} \times 100 \tag{2.1}$$

where OD_{2c} is the secondary OD measurement for condition c, OD_{1c} is the initial OD measurement for condition c, and OD_{min} is the ideal solubilisation OD (0.58 AU), obtained from a concentration control measurement (Figure A.1). For visual clarity, any condition with a secondary OD value greater than the initial OD measurement value was fixed to 0% This greater OD is indicative of polymer aggregation in non-optimal buffer conditions.

Plotting of both the unprocessed data (§A.3) and solubilisation efficiency for all conditions was achieved using Python, utilising the Matplotlib and Seaborn packages. Example Python scripts for both the analysis and plotting can be viewed on Github.[207]

2.2.5 Dynamic light scattering (DLS)

DLS samples were directly recorded after measurement of solubilisation by spectrophotometry. Per buffer condition, 100 μL of spectrophotometry sample was extracted and filtered using Durapore PDVF 0.22 μm filters to remove non-solubilised membrane, or polymer aggregates. 20 μL of filtrate was then measured using Malvern Zetasizer Nano S. Between 10-20 scans at 20^{o}C were recorded per sample. Hydrodynamic radii was then calculated using the OmniSize 3.0 software using the 'mass' mode, and histograms generated from this software were exported for plotting by Python, using the Matplotlib and Seaborn packages. The unprocessed histograms can be found in the appendix (§A.4). Example python scripts for both the analysis and plotting can be viewed on Github.[207]

2.3 Results & discussion

Since the discovery of polymer solubilisation[138, 190, 211] there have been several attempts to understand how polymer, buffer, and lipid composition affect membrane and bilayer solubilisation by polymers, primarily SMA.[203, 212–215] These comparative studies have shown that there is no difference in solubilisation between the 9.5 kDa (Lipodisq, LQ)[211] and the 7.5-10 kDa (SMALP)[138] SMA variants. Both variants showed that a styrene:maleic acid ratio of 3:1 and 2:1 is preferred for solubilisation, with a correct balance of hydrophobic and hydrophilic groups to form the lipid-polymer nanoparticles. Additionally, it was found that SMA is highly susceptible to changes in pH, with an increased solubilisation efficiency in alkaline conditions.

However, the vast majority of biophysical characterisation has, to date, been performed on SMA and its variants alone. The lack of comparative literature for

emerging polymers such as DIBMA and PMA is most likely due to their relative novelty, both being first characterised in 2017.[151, 154] While all currently available polymers have been well characterised individually,[138, 151, 154, 211] and are often compared to the 'original' polymer of SMA, there has been a distinct lack of directly comparable studies of all currently available polymers. This is in addition to a lack of characterisation of polymers in a broad range of conditions, with the current literature understandably only reporting within historically favoured conditions. This has led to a glut of comparative studies for SMA and SMA-variants at a pH of 7-9, but a distinct lack of publications in which a comparison of the available polymers have been made directly. The work in this chapter aims to show a direct comparison of membrane solubilisation efficiency of the currently available polymers (SMA 3:1, SMA 2:1, DIBMA and PMA) across a broad range of possible conditions to fully explore the optimal conditions that could be used for lipid-polymer nanoparticles. These characterisations will add to the knowledge base for bilayer solubilisation and lead to routes that may enhance conditions required for higher solubilisation efficiency of membrane proteins using these polymers.

2.3.1 Development of solubilisation assay by optical density (OD)

A commonly used method to analyse membrane solubilisation by SMA has been to measure the change in amount of light scattered by a sample (optical density, OD) upon addition of the polymer. The change in OD has previously been monitored at 350 nm,[141] due to the lack of absorption at this wavelength by SMA, or common buffer ingredients. Whilst OD is a largely outdated term, it is used in this thesis to avoid any confusion between the light scattering by the lipid dispersions used in this chapter, and absorbance (as defined by the Beer-Lambert law) in later work §4.2.4.

A pilot study by a previous student has shown that this wavelength is also minimally absorbed by the polymers and buffer materials used in this thesis, and that OD_{350} is a suitable wavelength for measuring solubilisation of model membranes for all polymers over a range of conditions.[216] This initial work showed that it was

possible to examine DMPC membrane solubilisation by different polymer types in a relatively quick and simple manner, where a low OD (< 2) indicated fully solubilised membrane (and nanoparticle formation), and a higher OD (> 2) was indicative of low solubilisation, or even polymer aggregation in unfavourable buffer conditions.

However, the assay design needed further development for several reasons: Firstly, the assay design did not control for ionic strength within pH and divalent cation titrations, potentially affecting the observed trends. Secondly, there was a high degree of wasted material of both lipid and polymer per measurement point.

As the assay was ultimately intended for high throughput analysis of membrane solubilisation over many samples, and the polymers are prohibitively expensive to commercial users. Therefore, modifications were proposed (discussed in §2.2.3) to reduce material consumption and ensured that total ionic strength was maintained as the divalent cation concentration was varied across the range of titration points. The OD_{350} was able to successfully quantify the solubilisation of DMPC in the presence of the four commercially available polymers, SMA 3:1, SMA 2:1, DIBMA, and PMA. Initial studies showed this method had the scope to characterise this solubilisation over a range of pH, salt, and divalent cation concentrations (Figure 2.2).

Whilst the findings in Figure 2.2 showed an improvement in precision relative to previous results,[209] the general trends observed by a previous student are still observed. For pH (Figure 2.2 A) , SMA 3:1 and 2:1 were only able to solubilise membrane above a pH of 6, shown by the rapid decrease in OD at pH > 6. Meanwhile, DIBMA was able to solubilise above a pH of 5. The SMA and DIBMA polymers contain maleic acid groups, and this switching point of solubilisation was most likely linked to the pKa of these acidic groups, leading to two populations of maleic acid being protonated across two different pH ranges. The protonation state of these maleic acid groups has previously been linked to polymer solvation, in addition to membrane solubilisation.[141, 199] SMA has been shown to possess two pKas, with a pKa_1 of ~5.5 and a pKa_2 of ~8.6 for the SMALP variant of SMA.[141] Whilst the exact pKa may differ for the LQ polymer variant, this range does align with the trends observed for SMA in Figure 2.2 A. DIBMA's pKa value has yet to be reported,

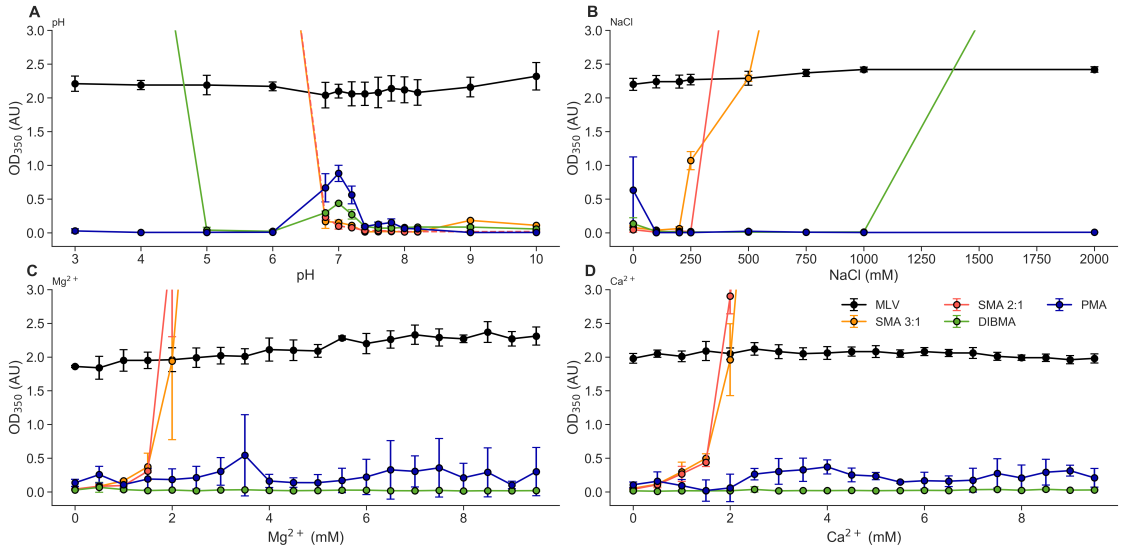


Figure 2.2: OD_{350} measurements of DMPC dispersions solubilised by SMA 3:1 (orange), SMA 2:1 (red), DIBMA (green), and PMA (blue) across pH range (A), ionic strength (B) and divalent cation titrations of magnesium (C) and calcium (D). Average initial membrane OD_{350} is shown in black (MLV). Axis are limited to usable detection range (0-2 AU), for full data points, including aggregated samples, please see Figure A.2

however it can be estimated to be between 4 and 5 due to the change in OD_{350} in Figure 2.2 A. PMA, possessing no proton-labile groups and therefore no affected by pH in the same manner as the maleic acid containing polymers, was able to solubilise the DMPC membranes across the entire range tested with a high efficiency.

For ionic strength (Figure 2.2 B), SMA variants again show the least tolerance of the four polymers, showing reduced solubilisation above 200 mM. The lack of membrane solubilisation was combined with visual polymer precipitation above a salinity of 400 mM. SMA 3:1 and 2:1 posses a low charge density due to the high degree of hydrophobic groups relative to hydrophilic groups. In addition to this, the styrene groups are particularly hydrophobic due to their aromatic nature. These factors together mean that the SMA polymers are able to form relatively few favourable interactions with the water in the aqueous buffer. These favourable interactions are easily disrupted by the increased presence of salt ions within the solution as salt concentrations increase. This leads to the hydrophobic collapse and precipitation of the polymer at a lower salinity than would be expected of a more highly charged polymer.

DIBMA again showed a higher tolerance of ionic strength than SMA, solubilising DMPC membranes effectively up to > 1 M. This was most likely due to a combination of higher charge density (DIBMA is an alternating polymer of di-isobutylene and maleic acid in a 1:1 molar ratio) and an overall less hydrophobic group of the di-isobutylene.

PMA was insensitive to the conditions tested in neutral DMPC membranes, most likely due to the high number of hydropholic groups present along the polymer length (Figure 1.7 D). Indeed, the solubilisation observed even at 4 M NaCl (not shown) indicate that it is insensitive to ionic strength to any significant degree.

Two divalent cations, Mg^{2+} and Ca^{2+}, (Figure 2.2 C and D respectively) were tested regular intervals between 0-10 mM. These ions are known to impact the solubilisation of membrane by maleic acid containing polymers.[198] The data showed reduced solubilisation efficiency of SMA and DIBMA, as expected, when titrated into to the solubilisation buffers. However whilst SMA variants were highly insensitive to divalent cation presence (visually precipitating > 2 mM for both magnesium and calcium titrations), DIBMA showed a relatively high tolerance and only precipitated above 10 mM (not shown). As with ionic strength, the higher relative maleic acid population in DIBMA polymers, as well as a smaller, less bulky hydrophobic group, are most likely the major contributors to this difference. PMA, a polymer with no carboxylic acid groups, was insensitive to divalent cations across the range examined.

Whilst the results observed in Figure 2.2 are very broad in range, the resolution of the individual measurements are restricted by the machine used to a range of 0-2 AU, with a maximum value of 6 being reported for any solution above this range. The use of individual plastic cuvettes per measurement point was also seen was highly wasteful, not only in respect to preparation time, but also material waste. To this end a more high throughput, and sensitive, assay was designed with the of 96-well plates.

The assay was redesigned to accommodate an entire 96-well plate for the complete titration range of two polymers, in addition to buffer and membrane controls. A general set up can be observed in Table 2.1 which shows the standardised layout for

Table 2.1: Basic layout of 96-well plate formation for high-throughput OD_{350} assay. C1-12 represent the 12 conditions used across the 12 columns available. P1 and P2 represent polymer 1 and 2 positions respectively, with a-c showing repeats used for averaging and standard error calculation. MLV (lipid suspension) control was used to ensure that membrane OD did not alter throughout the incubation of the assay. Blank represents the buffer blank used for each condition.

C1	C2	C3	C4	C5	C6	C7	C8	C9	C10	C11	C12
P1a	P1a	P1a	P1a	P1a	P1a	P1a	P1a	P1a	P1a	P1a	P1a
P1b	P1b	P1b	P1b	P1b	P1b	P1b	P1b	P1b	P1b	P1b	P1b
P1c	P1c	P1c	P1c	P1c	P1c	P1c	P1c	P1c	P1c	P1c	P1c
MLV	MLV	MLV	MLV	MLV	MLV	MLV	MLV	MLV	MLV	MLV	MLV
Blank	Blank	Blank	Blank	Blank	Blank	Blank	Blank	Blank	Blank	Blank	Blank
P2a	P2a	P2a	P2a	P2a	P2a	P2a	P2a	P2a	P2a	P2a	P2a
P2b	P2b	P2b	P2b	P2b	P2b	P2b	P2b	P2b	P2b	P2b	P2b
P2c	P2c	P2c	P2c	P2c	P2c	P2c	P2c	P2c	P2c	P2c	P2c

each experiment. As described in §2.2.4, this new method allowed for 192 individual measurements within 1.5 hours, due to the capacity for the incubation of two plates.

The data produced from the 96-well plate was also compatible for fast analysis and processing, through the use of Python.[207] This was not the case for the previous cuvette method, and increased the relative rate of data generation even further. By ensuring the use of a standardised plate format it was possible to utilise automatic analysis scripts to import multiple 96-well plate experiments and automatically process and plot the data. The new, high-throughput method allowed for an expansion of conditions to include: an increased divalent cation range to examine DIBMA tolerance, increased resolution of the commonly used pH range (6.8-8.2), and allowed for the inclusion of a charged membrane model, POPC:POPG (3:1).

A primary aim of this solubilisation assay was to establish a widely adopted standard framework, which enables the direct comparison of any conditions, membrane type, and polymer as required. To aid the adoption of this assay, it was decided to convert the previously used OD_{350} into a more applied term: 'Solubilisation efficiency'.[141] The term solubilisation efficiency is not novel to the field, having previously been reported by Swainsbury *et al.* using absorbance of extracted protein, RC-LH1.[139] However, solubilisation efficiency in this thesis is calculated from the

normalised OD_{350} of membrane dispersions pre- and post- polymer incubation (Equation 2.1).

2.3.2 Formation of lipid-polymer nanoparticles across pH range

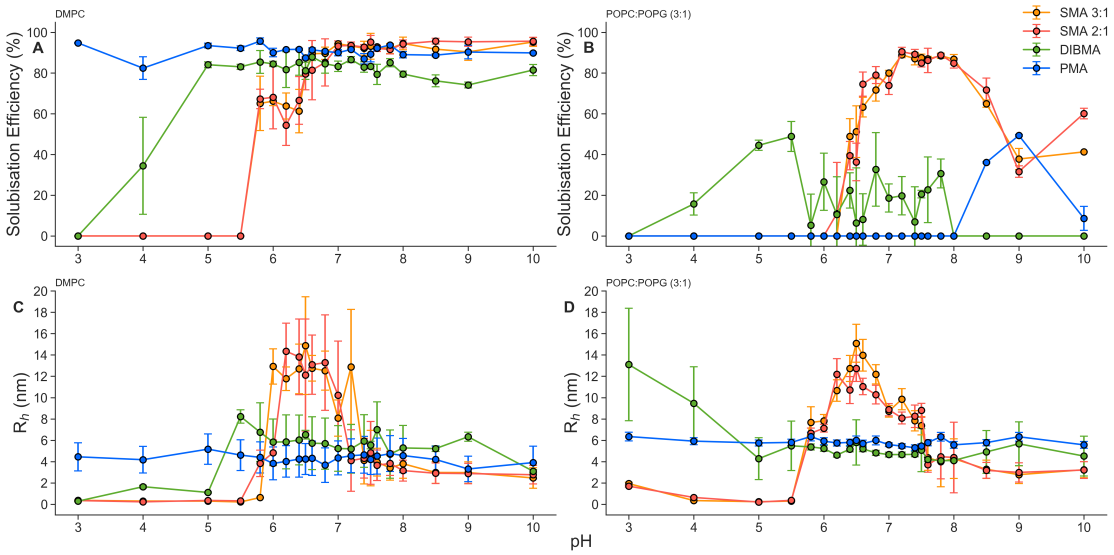


Figure 2.3: Formation of nanoparticles across pH range using SMA 3:1, SMA 2:1, DIBMA and PMA in two membrane models. (A) Solubilisation efficiency of DMPC membranes measured by normalised OD_{350}. (B) Solubilisation efficiency of POPC:POPG (3:1) membranes measured by normalised OD_{350}. (C) Hydrodynamic radius (R_H) of DMPC-polymer particles as measured by DLS. (D) Hydrodynamic radius (R_H) of POPC:POPG (3:1)-polymer nanoparticles as measured by DLS.

The resulting data (which can be seen in its unedited form in §A.3) was normalised against a buffer control (representing 100% solubilisation) and initial membrane measurement (representing 0% solubilisation), and allowed the data to be used to estimate solubilisation efficiency of synthetic membranes as shown in Figure 2.3 A and B. To ensure a decrease in absorbance (and therefore an increase in solubilisation efficiency) was an accurate measure of nanoparticle formation, samples for DLS measurements were immediately taken and recorded per condition, per polymer. The DLS measurements, as shown in Figure 2.3 C and D, also gave insights to the size of the nanoparticles formed across the conditions and membranes tested.

All polymers solubilised the neutral DMPC membrane model above pH 5.5 (Figure 2.3 A). However, the size of these nanoparticles was shown to vary across

the pH range (Figure 2.3 C). This was most noticeable for the SMA based particles, where two distinct forms were characterised. The first form can be observed between pH 5.5 and 7, with an average solubilisation of ~70%. SMA-DMPC particles were seen to be well above the expected size, with a hydrodynamic radius (R_H) of ~12.5 nm compared to an expected R_H of ~6 nm in more favourable conditions.[98] The second form can be observed at a higher pH (> 7), where the solubilisation efficiency dramatically increased to > 90%, with a decrease in overall size of particles to previously reported R_H values.[98]

Similar pH dependant results were observed for DIBMA; however, solubilisation efficiency was overall slightly lower (~80%), and with more consistent particle size across both this range and literature precedent.[143] Interestingly, PMA was observed to be pH insensitive to the range tested, with an average solubilisation efficiency of 80-90% in neutral (DMPC) membranes. It also maintained a consistent R_H of 4-5 nm over the pH range, consistent with the literature.[154]

A charged membrane model was also subject to the same characterisation, using POPC:POPG 3:1 (Figure 2.3 B,D). As was expected, all four nanoparticles showed a reduced solubilisation efficiency compared to neutral membrane models, and all nanoparticle sizes were larger. Additionally, DIBMA was observed to possess the two-phase solubilisation properties as noted previously for SMA in neutral membranes. This was accompanied with an increased solubilisation efficiency (~50%) and an increased particle radius (> 10 nm) between pH values of 3-5 (Figure 2.3 B,D). PMA underwent relatively efficient solubilisation (> 30%) between pH 8-9 for charged membrane samples, however it was shown to still form nanoparticles for the entire range tested by DLS, with a consistent size similar to that reported previously (R_H 6-7 nm).[154] The discrepancy between a high OD_{350} and a consistent R_H across the entire pH range can be said to show that PMA is able to solubilise membranes across the entire pH range examined, however efficiency of this solubilisation is dramatically improved between a pH of 8-9 for POPC:POPG (3:1) membranes. As this window of solubilisation is not observed in DMPC membranes (Figure 2.3 A

vs B), it is likely that this is due to a change in the charge of POPG lipids over this pH range, rather than an intrinsic PMA property.

Particle formation is highly dependent on polymer charge, and therefore dependent on the pH of the buffer during solubilisation.[141] For SMA it is known that the maleic acid groups must be at least partially deprotonated for the polymer to exist in solution.[142] The pKa of acid groups are dependent on many factors, such as the local environment hydrophobicity, ionic strength, and other neighbouring interactions.[217]

Scheidelaar *et al.* have shown that for the SMALP version of SMA tested in this paper the pK_1 and pK_2 of the maleic acid groups are approximately 5.7 and 8.6, respectively.[213] The results presented in this chapter showed solubilisation of neutral membranes can still be observed above a pH of 5.5, however with a lower solubilisation efficiency and larger particle formation between 5.5 and 7.2, this first form of solubilisation can therefore be explained by a partial protonation of the maleic acid groups between this pH range.

DIBMA is also composed of maleic acid groups and so is susceptible to similar pH dependant solubilisation. To date, there is no literature data regarding the pKa values of the maleic acid groups of DIBMA. However, the data shown in Figure 2.3 indicated that the maleic groups of DIBMA had a common pKa of ~5, shown as the solubilisation point in the neutral membranes in Figure 2.3 A. The estimated pKa was supported by DIBMAs lack of a pseudo-solubilisation period observed in SMA, near neutral pH values (Figure 2.3 A). This indicated that DIBMAs alternating, rather than SMAs random co-polymer nature, gave the maleic acid groups a common pKa value, rather than the pK_1 and pK_2 as observed in SMA.

2.3.3 Formation of lipid-polymer nanoparticles across NaCl concentration

Ionic strength is an important decision in experimental design, and has been shown previously to be a major factor in membrane solubilisation by membrane-interacting polymers.[203] To understand the effect of ionic strength on solubilisation efficiency

and particle stability a range of concentrations, up to 1 M, were tested against all polymers, in both charged and neutral membrane models. This range was selected after initial studies (not shown) found all polymers were capable of forming lipid-polymer nanoparticles in up to 1 M NaCl at pH 7.4, with only PMA forming particles at concentrations of >1 M NaCl.

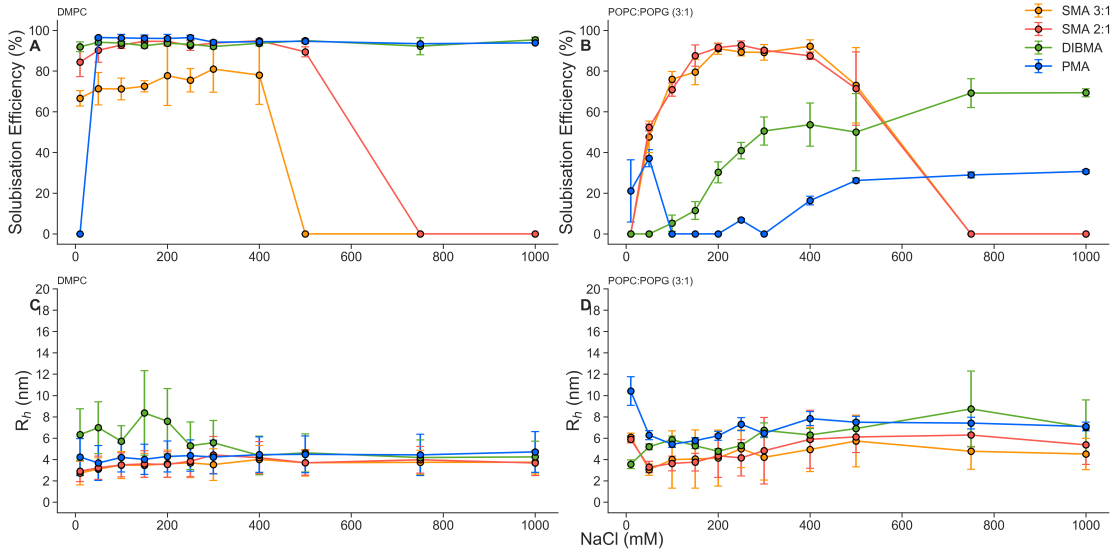


Figure 2.4: Formation of nanoparticles across an ionic strength gradient of NaCl using SMA 3:1, SMA 2:1, DIBMA and PMA in two membrane models. (A) Solubilisation efficiency of DMPC membranes measured by normalised OD_{350}. (B) Solubilisation efficiency of POPC:POPG (3:1) membranes measured by normalised OD_{350}. (C) R_H of DMPC-polymer particles as measured by DLS. (D) R_H of POPC:POPG (3:1)-polymer nanoparticles as measured by DLS.

Despite this tolerance, solubilisation efficiency is severely affected by ionic strength. Sufficient ionic charge in the buffer enables the solvation of a polymer, by increasing favourable hydrophilic group interactions with the water through an effect known as 'salting in'. For charged membranes this additional ionic strength also aids charge screening between the charged membrane and the solvated polymer. This enables adsorption of the polymer onto the membrane surface prior to insertion of the polymer hydrophobic groups into the acyl core. Neutral membranes, such as DMPC, do not require significant charge screening and therefore the trends observed in Figure 2.4 A were most dependant on the polymer solvation across ionic strength conditions. This assumes that if the polymer was sufficiently solvated, solubilisation

would occur. At lower ionic strengths both the polymer hydrophilic groups and salt ions compete evenly for solvation by water. As the ionic strength of the buffer increased the excess ions out compete the polymer for solvation - leading to the hydrophobic collapse of the polymer and subsequent precipitation. This is an effect known as 'salting out', initially described mathematically by McDevit *et al.*[218]

Studies in neutral DMPC membranes (Figure 2.4 A) showed that SMA 3:1 had a solubilisation efficiency threshold of 400 mM, whereas SMA 2:1 efficiency was more tolerant of ionic strength, with an increased threshold of 500 mM. Above this concentration there was visual precipitation of the polymer in solution, as well as a reduced solubilisation efficiency as seen in Figure 2.4 A. The decrease in efficiency was most likely the result of hydrophobic collapse of the polymer and a change of form, from the membrane-interacting supercoiled state to a globular form.[142, 190] However, after filtration of the SMA samples used for DLS isolated the soluble components, it was possible to show the soluble nanoparticles possessed a consistent R_H across ionic strengths (Figure 2.4 C). Meanwhile, studies in neutral membranes showed that DIBMA and PMA, possessing both weaker hydrophobic groups and a higher overall polymer charge distribution then SMA, did not experience this hydrophobic collapse until much later ($>$ 1 M NaCl for DIBMA, $>$ 4 M for PMA).

All polymers showed a consistent size as measured by DLS for both neutral and charged membrane across the range tested, indicating that ionic strength only affects membrane solubilisation and nanoparticle formation, and does not affect the properties of formed nanoparticles in terms of size. Charged membrane particles showed consistently higher R_H values than the neutral membrane particles, with an overall increased size distribution between polymers (Figure 2.4 B and D respectively).

For charged membranes models, the driving force for membrane solubilisation is the interaction between the charged membrane head groups and the polymer during polymer adsorption.[140, 219, 220] At low ionic conditions there is little charge screening of the negative POPG head groups and this had various impacts on the four polymers. In SMA and DIBMA this negative charge repels the negative

maleic acid groups of the polymers and screening reduces this negative interaction. For SMA, the strong hydrophobicity of the styrene groups and the higher density of these groups compared to DIBMA, forced the styrene to interact with the charged membrane even in relatively low salt conditions (~50 mM). Whereas DIBMA did not efficiently solubilise the charged membranes until sufficient charge screening occurred at > 200 mM. After this the efficiency linearly increased until > 1 M where the polymer begun to precipitate out of the solution. Although PMA has an overall positive charge, it was not able to solubilise negatively charged membranes until sufficient ionic strength (above 200 mM), indicating that the weak hydrophobicity of the polymethacrylate group required additional salt to allow for solubilisation in addition to a favourable charge attraction. A preliminary experiment containing positively charged POPC:POPE (3:1) membranes (Figure A.5) showed that PMA does not efficiently solubilise positively charged membranes at any ionic strength tested, indicating that the weaker hydrophobicity is the root cause of this issue. DIBMA was also tested with POPC:POPE (3:1) membranes, and showed a similar threshold of 200 mM before efficient solubilisation was observed (Figure A.5 B).

2.3.4 Formation of lipid-polymer nanoparticles across divalent cation (Mg^{2+}, Ca^{2+}) concentration

The same solubility and size analysis assays were used to study the nanoparticles in the presence of the Mg^{2+} and Ca^{2+} buffers. SMA polymer-based nanoparticles were shown to be most sensitive of the polymers studied to divalent cations, in line with literature precedent.[201, 208] The data (Figure 2.5 and 2.6) showed that both SMA variants are only able to solubilise membranes tested in the presence of < 1 mM concentrations of divalent cations, in both membrane models tested. DIBMA was shown to be more tolerant to divalent cation presence than SMA, with an observed increase in solubilisation efficiency for magnesium between 5-8 mM in a neutral membrane. A decrease in efficiency was then observed for > 8 mM Mg^{2+} and > 3 mM Ca^{2+}, however DLS data (Figure 2.5 C and 2.6 C) showed that DIBMA is able to form nanoparticles up to 20 mM X^{2+}, albeit with some

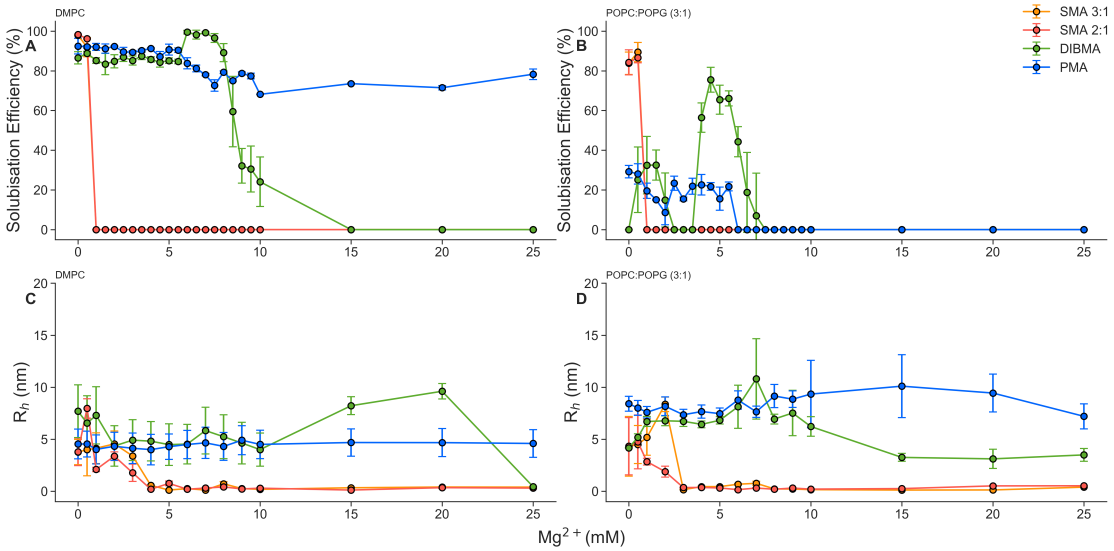


Figure 2.5: Formation of nanoparticles across a Mg^{2+} concentration gradient using SMA 3:1, SMA 2:1, DIBMA and PMA in two membrane models. (A) Solubilisation efficiency of DMPC membranes measured by normalised OD_{350}. (B) Solubilisation efficiency of POPC:POPG (3:1) membranes measured by normalised OD_{350}. (C) Hydrodynamic radius (R_H) of DMPC-polymer particles as measured by DLS. (D) Hydrodynamic radius (R_H) of POPC:POPG (3:1)-polymer nanoparticles as measured by DLS.

size variation. Similarly, DIBMA showed a more gradual change in the size of the particles formed in presence of magnesium, but the polymer still visibly precipitated at $>$ 5 mM for both cations.

DIBMA experienced an increase in solubilisation efficiency in both neutral and charged membranes, however this was most notable in magnesium solutions of POPC:POPG (3:1) membranes (Figure 2.5 B). The increased efficiency was most likely due to magnesium aiding polymer adsorption onto the membrane through charge screening of the negative lipid charge from the negative polymer charge. The increased efficiency was also observed in calcium solutions (Figure 2.6 B), but at a lower concentration (1-2 mM Ca^{2+}) and to a lower extent. The observed difference my be due to the solvation of ions, magnesium is known to possess a tight octagonal first co-ordination shell, leading to a rigid coordination geometry. However, calcium often less tightly, usually in the second coordination shell.[221] Calcium being more 'flexible' in coordination geometry may explain why it appeared to have a more

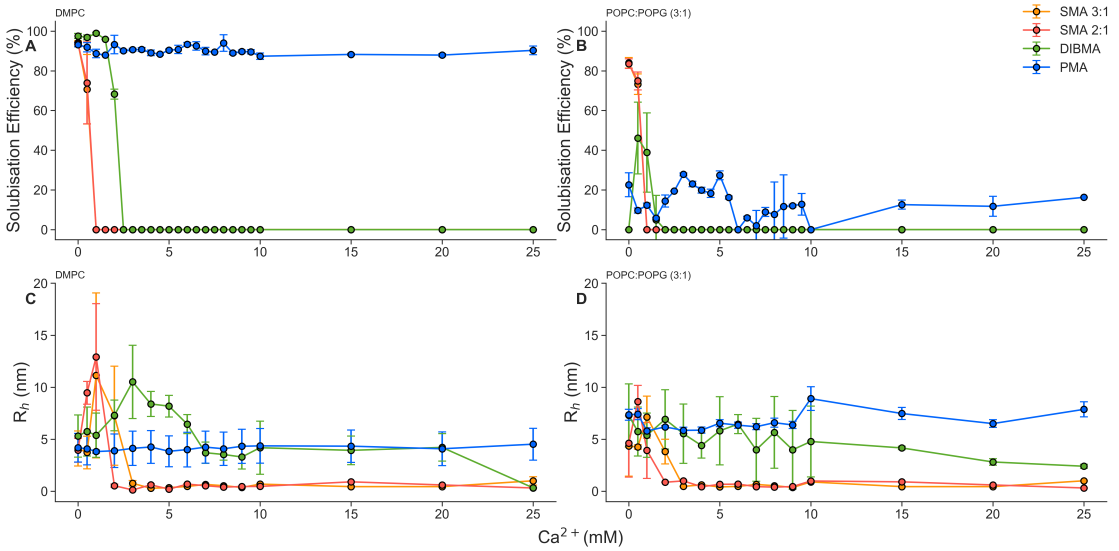


Figure 2.6: Formation of nanoparticles across a Ca^{2+} concentration gradient using SMA 3:1, SMA 2:1, DIBMA and PMA in two membrane models. (A) Solubilisation efficiency of DMPC membranes measured by normalised OD_{350}. (B) Solubilisation efficiency of POPC:POPG (3:1) membranes measured by normalised OD_{350}. (C) Hydrodynamic radius (R_H) of DMPC-polymer particles as measured by DLS. (D) Hydrodynamic radius (R_H) of POPC:POPG (3:1)-polymer nanoparticles as measured by DLS.

pronounced effect on DIBMA solubilisation, as it may be able to chelate more maleic acid groups due to this increased flexibility.

Maleic acid groups are able to co-ordinate with divalent cations.[144] This strong interaction to the metal ion led to the precipitation of the polymer as the polymer preferentially interacted with the metal ions over the bulk water. SMA is a random co-polymer in either a 2:1 or 3:1 ratio of styrene:maleic acid, whereas DIBMA is an alt- polymer of 1:1 isobutylene:maleic acid. Both the overall higher charge ratio and the even dispersion of maleic acids along the length of the DIBMA polymer, rather than random dispersion in SMA may explain SMA's increased sensitivity to divalent cations. There are less maleic acid groups in SMA overall which are able to chelate divalent cations before part of, or the whole polymer precipitates.

PMA solubilisation efficiency was not affected by divalent cation presence in neutral membrane models, but it was affected in charged membranes models, with a sharp decline in efficiency observed for both magnesium and calcium above 5.5 mM. however, for all conditions tested, PMA was able to form nanoparticles

of the expected size for both DMPC and POPC:POPG (3:1) membranes. PMA's particle size showed an average R_H of 4-5 nm for neutral membranes, and 6-7 nm for charged membrane models (Figure 2.5 D and 2.6 D for Mg^{2+} and Ca^{2+}, respectively) throughout the range tested. PMA is not expected to co-ordinate divalent cations, as it does not possess carboxylic acid groups and is also already cationic. Therefore the increasing divalent cation presence throughout the titration would only be observable as a general increase in ionic strength of the solution. However, the divalent cation titration the overall ionic strength was maintained at 100 mM and no differences were observed in both solubilisation efficiency and R_H. However, in charged membranes there was a decrease in solubilisation observed for PMA (Figure 2.5 B). This is most likely due to cation coordination with POPG head groups, causing a net positive charge on the membrane surface, therefore reducing the charge attraction and polymer adsorption onto the membrane surface. This net surface charge, combined with PMA's relatively weak hydrophobicity can explain the low solubilisation efficiency shown by absorbance measurements, yet the consistent particle formation as measured by DLS.

2.4 Summary and Conclusions

Initial, preliminary, studies in collaboration with a previous student showed that OD_{350} was a useful tool to simply measure solubilisation efficiency of polymers across a range of buffer conditions. However issues with ionic strength discontinuity and a limited resolution of OD_{350} led to a desire to improve and expand upon the assay. The assay was therefore optimised for a more high-throughput means of examining the inter-dependance of buffer conditions and membrane complexity for four commercially available polymers. This required the use of 96-well plates and a plate reader to obtain more data points simultaneously, as well as an expansion of testing capacity. These findings are paired with DLS measurement of the formed nanoparticles for all four polymers across these conditions in Chapter 3, and give a clear overview of solubilisation efficiency of the four polymers across a range of possible conditions.

This chapter characterised four nanoparticle-forming polymers over conditions consistent with those previously in the literature for individual solubilisation attempts of membrane proteins (§A.5). Whilst the work present in this thesis does not involve the solubilisation of native membranes or integral membrane proteins, the use of synthetic membrane models allowed for an in-depth understanding of membrane solubilisation by polymers, and can be applied to more complex membrane systems. When combined, these models can provide researchers with recommendations of ideal starting conditions for novel membrane systems containing these commercially available polymers. The techniques used also provide a robust framework for future polymer characterisation.

A pH of 8 has been shown to be an effective condition, allowing for the maximal solubilisation efficiency for all polymers (Figure 2.3 A,C). However, there is a sharp solubilisation penalty for acidic pH solubilisation for both SMA variants and DIBMA. This is reflected in the lack of publications showing solubilisation with these polymers below a pH of 6.5.[222] However, extraction of ZipA has been shown at a pH of 5 with a modified version of SMA, SMI.[191] Currently, PMA has no published record of integral membrane protein purification. However, the data within this chapter show it may be possible to extract membrane proteins in highly acidic conditions for specialised membrane proteins.

Charge screening is an important consideration for membrane solubilisation using polymers. Neutral model membranes, such as DMPC, require approximately 100-200 mM NaCl for efficient solubilisation (Figure 2.4 A). However, as membrane charge and complexity increases, higher salt concentrations are recommended to ensure sufficient solubilisation (Figure 2.4 C). This has been observed in native membrane solubilisation, such as in *E.coli*, where a pH of 8, with an ionic strength of approximately 200-300 mM appears to be most common ionic strength reported (Table **??**).[223, 224] However, it has been shown that solubilisation is possible with no additional salt other than buffering salts,[222, 225–229] but the data in this chapter indicates that this could severely impair solubilisation efficiency.

This work has shown that SMA polymers are tolerant up to an ionic strength of 500-600 mM. This is in line with a literature precedent of protein extraction with SMA at an ionic strength of 500 mM for *E.coli* membranes,[184, 230–232] and even one publication at 600 mM.[187] In this chapter DIBMA has been shown to tolerate up to 1 M NaCl (Figure 2.4), with PMA showing tolerance up to 4 M NaCl (not shown). This is in-line with a previous report of DIBMA requiring 500 mM for the extraction of an *E.coli* protein from native membrane,[184] and it is likely that PMA would require similarly high salt concentrations to achieve efficient solubilisation in similarly complex membrane preparations.

PMA has been shown, in this work, to be tolerant of divalent cations to the maximum tested concentration (25 mM). This is in-line with the similarly quaternary amine containing SMA-QA, which has been shown to be tolerant up to 200 mM.[198] Conversely, maleic acid containing polymers should not be subjected to divalent cation containing buffers where possible, as SMA was shown to be highly intolerant of the presence of these ions in solution (Figure 2.5 and 2.6). DIBMA however is able to tolerate low concentrations and even see an increase in membrane solubilisation efficiency within a narrow range of concentration of magnesium, as seen in Figure 2.5. This has also been reported by Keller *et al.* in relation to *E.coli* membrane solubilisation.[154] Further work is required to ascertain whether this ideal range of divalent cation concentration affects the lipid-polymer particle characteristics, and membrane protein stability within these systems. Additionally, the tolerance by the polymer to divalent cations does not necessarily mean divalent ion presence in solution. There is a possibility that divalent cations are chelated from the buffer by the polymer, which may affect biochemical assays dependent on divalent cation availability in solution.

As can been seen in previous works (§A.5) the temperature of solubilisation is the most diverse variable in membrane protein extraction. Solubilisation has been successfully shown with polymer incubation at 4°C for 20 minutes,[228] as well as functional protein has been observed after solubilisation at 37°C for 3 hours.[184] Initial protocols for solubilisation with polymer follow often adapted protocols

proven for protein solubilisation with detergents. However, it has been reported that bulk properties of the membrane, rather than individual lipid composition, are the key factors in membrane solubilisation kinetics.[219] This, combined with an increased thermal stability of proteins in nanoparticles over detergents,[138, 208, 233] implies that a fast, warm, extraction may be beneficial with polymer solubilisation. For maximal fluidity, without potential damage to the system of interest, extraction at the growth temperature of the cells might be suggested as an ideal initial temperature. It is worth highlighting a recent paper by Dörr *et al.*[203] examining the solubilisation efficacy of SMA variants for the solubilisation of *E.coli* membrane proteins, using KcsA as a model protein. This work examined similar factors of pH and ionic strength on solubilisation efficiency with the additional factors of SMA concentration and solubilisation kinetics and is a good foundation for future works of this chapter.

This chapter has shown the role that buffer conditions and polymer structure play in the efficiency of solubilisation of lipid membranes, with a distinct trade-off between strongly solubilising polymers with reduced buffer stability (such as SMA), and weaker solubilising polymers with a broad buffer stability (such as PMA). This exact relationship will likely become clear with the inevitable development of additional polymers, and further work into the effect of solubilisation temperature on nanoparticle formation -although it is unlikely to produce a single polymer for all desired conditions. In addition, and not explored in this chapter, is relationship between the polymer and the protein of interest during solubilisation. There is increasing evidence to indicate that polymer-protein charge repulsion can impede solubilisation efficiency,[234, 235] although further work is needed to explore the synergistic effects of both membrane, polymer, and protein characteristics in solubilisation.

This work has also shown that initial users of polymer based solubilisation should take care to not simply convert previously solubilisation protocols using detergent, as the conditions for favourable detergent extraction do not always equate to favourable polymer-based solubilisation conditions, but are in fact much more dependant on

the type of polymer used. It is hoped that the assays used in this chapter form a foundation of future, additional, assays to further examine the optimal conditions for solubilisation, including the role of temperature on the solubilisation of additional model membranes, or even protein containing membranes.

Nothing in life is to be feared, it is only to be understood. Now is the time to understand more, so that we may fear less.

— Marie Curie

3

Biophysical characterisation of DMPC-polymer nanoparticles

Contents

3.1 Introduction 71
3.1.1 Aims 72
3.2 Materials & methods 73
3.2.1 Polymer preparation 73
3.2.2 Transmission electron microscopy (TEM) 73
3.2.3 Differential scanning calorimetry (DSC) 74
3.2.4 Laurdan fluorescence 75
3.2.5 Continuous wave electron paramagnetic resonance (cw-EPR) 76
3.3 Results & Discussion 80
3.3.1 Negative stain transmission electron microscopy (TEM) 80
3.3.2 EM particle analysis 83
3.3.3 Thermotropic characterisation 85
3.3.4 Differential scanning calorimetry (DSC) 86
3.3.5 cw-EPR 92
3.4 Summary and conclusions 97

3.1 Introduction

The work previously shown in this thesis (Chapter 2) has described the development of techniques for characterising the formation of lipid-polymer nanoparticles across a

range of buffer conditions for both POPC:POPG (3:1) and DMPC lipid dispersions. Similarly to the characterisation of membrane solubilisation by polymers, there is a lack of literature available for the biophysical characterisation of lipid-polymer nanoparticles, with the exception of SMA 3:1 and SMA 2:1.[177, 183, 236–239] The lack of comparative studies on the biophysical properties of these nanoparticles could potentially affect the biophysical characterisation of membrane proteins and lipids that have been extracted in these systems.

3.1.1 Aims

The following chapter aims to show an in depth and comparative characterisation of lipid-polymer nanoparticles formed, utilising the same four polymers as previously used in Chapter 2. This characterisation focusses on DMPC-polymer nanoparticles generated in 'ideal' conditions of pH 7.4, 100 mM NaCl. The comparative size and shape of the four DMPC-polymer nanoparticle types is explored through the use of negative stain transmission electron microscopy (TEM). The analysis of these TEM images was also compared to previously shown DLS measurements from Chapter 2.

Further to the characterisation of the nanoparticle structure by EM imaging and DLS, this chapter aims to perform an in-depth characterisation of the thermotropic properties of the formed nanoparticles. Initially this was attempted with fluorescence spectroscopy with the fluorescent probe Laurdan to determine how the gel to liquid crystalline phase transition and the lipid packing within these phases is affected within the nanoparticles, through the analysis of DMPC-polymer nanoparticles.

Later optimisation steps lead to the use of differential scanning calorimetry (DSC) to elucidate the thermotropic properties of these nanoparticles, with particular focus on the gel to liquid crystalline phase transition of DMPC-polymer nanoparticles. These DSC measurements were performed in combination with electron paramagnetic resonance techniques, such as TEMPO partitioning and the use of spin labelled stearic acid (SASL) and spin labelled phosphatidylcholine phospholipids (PCSL) probes, to analyse the effect of the lipid phase transition on the lipid packing and order within these systems.

3.2 Materials & methods

3.2.1 Polymer preparation

SMA 3:1 and SMA 2:1, with an average molecular weight of 9.5 kDa, were obtained from Malvern Cosmeceutics. They were hydrolysed from the anhydrous form as previously described by Gulati *et al.*[208] DIBMA was a kind gift from Sandro Keller whilst PMA was purchased from Avanti (Alabaster, AL). All polymers, unless otherwise, stated were stored and used at room temperature (RT) in 20mM HEPES buffer containing 100 mM NaCl at pH 7.4 at a polymer concentration of 100 mg/mL (10% *w/w*). Solubilisation was achieved using 1.5× (*w/w*) excess of polymer to lipid equating to 1.5% (*w/v*), with an incubation of 1 hr at RT, unless otherwise stated. All lipids in this thesis were purchased from Avanti (Alabaster, AL) and used without further modification.

3.2.2 Transmission electron microscopy (TEM)

TEM images were recorded from DMPC-polymer nanoparticles formed in 'ideal' solubilisation conditions of 20 mM HEPES, 100 mM NaCl at pH 7.4. Due to the small amount required for TEM preparation of nanoparticles for TEM and DSC was combined. TEM samples were removed after size exclusion and spin concentration steps were performed in combination with preparation of DSC samples (§3.2.3). 20 μL aliquots (at a lipid concentration of 6.5 mM) was removed for TEM imaging. The aliquots were then diluted prior to staining and imaging to a final lipid concentration of 0.01 mg/mL.

Staining and imaging were kindly performed by Dr Sabine Heit (Department of New Biochemistry, Oxford for SMA 3:1, SMA 2:1, PMA samples) and Dr Juliette Devos (Institut Max von Laue - Paul Langevin (ILL) for the DIBMA sample). Samples were briefly incubated for 30 seconds on 400 mesh carbon-copper grids before being subjected to 4 × 3 μL H_2O washes without incubation. Staining of the grids was achieved with 2 × 3 μL incubations of 2 % uranyl acetate, each for 15 seconds. Images were recorded using a Tecnai Fei operated at 120 kV. Diameters

of major and minor axis were measured manually using GMS3 software, with 100 particles measured per sample (§B.1).

3.2.3 Differential scanning calorimetry (DSC)

DSC measurments were recorded from DMPC-polymer nanoparticles formed in 'ideal' solubilisation conditions of 20 mM HEPES, 100 mM NaCl at pH 7.4. Briefly, 13 μmol (8.8 mg) of DMPC was removed from a 25 mg/mL chloroform stock and dried under nitrogen. The resulting lipid film was then stored under high vacuum for at least 4 hours, prior to resolubilisation in 20 mM HEPES, 100 mM NaCl at pH 7.4 to a total volume of 4 mL. 1 mL fractions were then taken and polymer was added at 1.5 $\times$ (w/v) excess and incubated at 30°C with gentle agitation.

Samples then underwent SEC, using a Superdex S200 increase column, to remove excess polymer. For calibration, a 400 nm DMPC LUV sample was also prepared, through the same lipid film hydration technique. The resulting MLVs were subjected to 5 $\times$ freeze-thaw cycles and then extruded through 400 nm polycarbonate filters to form LUVs.

The purified samples were concentrated to final lipid concentration of 6.5 mM, with a final volume of 500 μL. All samples were kindly measured by Professor Gerhard Gröbner (Umeå University, Sweden) between 7-35°C at a heating rate of 60°C/hr. Calibration of samples to a 400 nm LUV standard prepared earlier was also performed by Dr Gröbner. Data was received in text format and processed by home-made python script. Enthalpy data was obtained through integration of the processed curve between 10-35°C using the python library scipy's integrate function using the Simpson rule for integration. Calibration of the enthalpy values were performed relative to DMPC LUV literature value of 5.26 kcal/mol.[98] Plotting of DSC graphs was performed with python library matplotlib. Example python scripts for both the analysis and plotting can be viewed on Github.[207]

3.2.4 Laurdan fluorescence

To measure the phase properties of nanoparticles through fluorimetry a commonly used probe, Laurdan (2-dimethylamino-6-lauroylnaphthalene), was added to the lipid-polymer nanoparticles at a molar ratio of 200:1 (lipid:probe).[98, 204] Laurdan is a commonly used fluorescent probe, due to the a well characterised red shift of Laurdan's emission peak during a lipid bilayer's phase transition. The red shift (from 440 nm to 490 nm) is caused by a change in polarity experienced by the napthalene moiety that resides in the lipid head group region of the bilayer. During the gel-liquid crystalline phase transition the bilayer head groups become less tightly packed, allowing for increased interactions with water molecules. This increase in polarity can be monitored by a red-shifting of Laurdan's emission spectra, and has been used to characterise the phase transition of lipid bilayers in various model membrane systems.[240–244]

The Laurdan protocol in this chapter was adapted from previous work in the lab,[240] and designed so that 3 mg of DMPC (4.5 μmol of lipid) was used for each sample. This was removed from a 25 mg/mL lipid stock (in chloroform) was combined with 22.5 nmol of laurdan probe, from a 1 mg/mL stock (in methanol). The solution was then briefly agitated, dried under nitrogen, and stored under vacuum for at least 4 hours in the absence of light.

The dried lipid film was resuspended in a buffer containing 20 mM HEPES, 100 mM NaCl, pH 7.4 to a final lipid concentration of 4.5 mM. The solution was incubated at 30°C for 30 minutes with gentle agitation, in the absence of light. To generate large unilamellar vesicles (LUVs), the resulting MLVs were subjected to 5× freeze-thaw cycles and then extruded at least 11× through 400 nm polycarbonate filters to form LUVs. For the polymer containing samples, 1.5× polymer (*w/w*) was added to the LUV solution from a 10% (*w/v*) stock in a buffer of 20 mM HEPES, 100 mM NaCl, pH 7.4 and incubated at 30°C for 30 minutes with gentle agitation. The solution was then centrifuged (30 minutes; 30,000 g;4°C) to remove any undispersed membrane.

Fluorimetry measurements were recorded on a Perkin Elmer LS 55 Luminescence Spectrometer, with temperature control provided by a Haake K10 water bath, controlled by a Haake DC10 thermocouple. Prior to recording, all samples were incubated at the desired temperature for 5 minutes. Temperature measurements were recorded at 1° intervals between 1 - 30°C. Samples were excited at 340 nm with an excitation/emission ratio of 5/2.5 and recorded between 400-600 nm with a scan speed of 40 nm/min.

Data analysis was performed in Python. The data for each sample and temperature point was plotted (using the Matplotlib package), using a colour scale to show visually the change with temperature. Python was also used to develop a tool to determine membrane phase change, which used automatic location of the intensity at 440 nm and 490 nm, before calculation and plotting of the generalised polarisation (GP, as described by Equation 3.1, [243]) of Laurdan, to obtain a measure of membrane phase change. Example python scripts for both the analysis and plotting can be viewed on Github.[207]

$$GP = \frac{I_{440} - I_{490}}{I_{440} + I_{490}} \tag{3.1}$$

where I_{440} is Intensity at 440 nm, and I_{490} is Intensity at 490 nm.

3.2.5 Continuous wave electron paramagnetic resonance (cw-EPR)

TEMPO

The spin probe 2,2,6,6-tetramethylpiperidine-1-oxyl (TEMPO, Figure 1.14) is a cyclic nitroxide radical able to partition into hydrophobic environments, such as lipid membranes from aqueous buffers.[98] As a lipid membrane undergoes the gel- to liquid-crystalline-phase transition, the lipid packing becomes less dense. This spacing allows more TEMPO molecules to diffuse into the lipid head-group region of the membrane from the aqueous buffer. The partitioning, as measured by a hyper-fine splitting at the high field peak (Figure 1.14 B) is very well characterised indicator of membrane phase behaviour and lipid packing,[166, 245] and has been used previously

by Orwick *et al.*[204] to compare DMPC LUV and SMA 3:1 nanoparticles to measure phase change above and below the DMPC melting point (T_m).

TEMPO experiments were performed on two lipids membranes, DLPC and DMPC, in four membrane models: LUVs, and SMA 3:1-, SMA 2:1- and DIBMA-lipid nanoparticles. For the LUV samples, the lipid film was resuspended to 100 μL, and subjected to 5× freeze-thaw cycles and then extruded through 400 nm polycarbonate filters to form LUVs. The dilute LUVs were then centrifuged at 30,000 g for 30 minutes at 4°C. The pelleted LUVs were then resuspended to a final volume of 30 μL and inserted into a capillary tube.

For polymer samples, the lipid film was resuspended in 20 mM HEPES, 100 mM NaCl, pH 7.4 to 20 μL, with the desired polymer being added at a 1.5× excess lipid mass (*w/w*) from a 10% (*w/v*) stock in 20 mM HEPES, 100 mM NaCl, pH 7.4 and incubated at 30°C for 30 minutes with gentle agitation. All samples were then diluted to a final volume of 30 μL, prior to centrifugation at 30,000 g for 30 minutes at 4°C. The supernatant was then taken for insertion into capillary tubes.

cw-EPR measurements were recorded on an EMXmicro X-band CW, with an Oxford instruments liquid nitrogen thermocouple. Prior to measurement, samples were incubated at the desired temperature for 3 minutes, then recorded for 32 scans at a sweep width of 150 Gauss (G) per measurement point. For data analysis, spectra of TEMPO samples were aligned to the central peak automatically through the use of numpy's *peak_finder* function. The same tools allowed automatic detection of H and P values, which determined the location of H and P maxima/minima. These values were then used to generate the partition coefficient, *f*. Plotting of *f* (Figure 3.6 B) was then performed using the matplotlib and seaborn libraries. The python used for this analysis can be found on Github.[207]

SASL and POPTC

Stearic acid spin labels (SASL) are well characterised spin label probes used to elucidate the lipid packing within a lipid bilayer.[35, 91, 98, 246]. They are formed of a stearic fatty acid, and possess a doxyl spin label at various points (Figure

1.13 A). In this chapter 5 SASL probes are used; 4-, 9-, 12-, 14-, 16-SASL. In addition to this the head-group labelled lipid, POPTC, was used in conjunction with the SASL probes. POPTC is formed from POPC, with a TEMPO-labelled head group (Figure 1.13 C).

For the SASL experiments ten samples were generated, namely, four polymer variants (SMA 3:1, SMA 2:1, DIBMA, and PMA) containing a POPTC probe in a DMPC membrane, and 5 samples of SMA 3:1-DMPC nanoparticles with SASL probes along the lipid structure (4-SASL, 9-SASL, 12-SASL, 14-SASL, and 16-SASL). For each sample, 3 nmol of probe was added from a 1 mg/mL stock in methanol to a 300 nmol aliquot of DMPC from 25 mg/mL chloroform stock solution. The sample solution was then briefly agitated, prior to being dried under nitrogen, and stored under vacuum for at least 4 hours.

Once dried, the lipid film was then resuspended in 20 mM HEPES, 100 mM NaCl, pH 7.4 to 20 μL, with the desired polymer being added at a 1.5× excess lipid mass (w/w) from a 10% (w/v) stock in 20 mM HEPES, 100 mM NaCl, pH 7.4 and incubated at 30°C for 30 minutes with gentle agitation. All samples were then diluted to a final volume of 30 μL, prior to centrifugation at 30,000 g for 30 minutes at 4°C. The supernatant was then taken for insertion into capillary tubes.

cw-EPR measurements were recorded on an EMXmicro X-band CW, with an Oxford Instruments liquid nitrogen thermocouple. Prior to measurement, samples were incubated at 30°C for 3 minutes, then recorded for 32 scans at a sweep width of 150 Gauss (G) per measurement point. For data analysis, automatic detection of $A_\perp$ and $A_\parallel$ measurement points (Figure 1.12 B) was performed through an automated peak maxima and trough minima finding function within a defined range. The order parameter for the probe in lipid bilayers was then calculated using these values, using Equation 1.21, as described by Watts *et al.*[166] Plotting was performed using the libraries described previously. The code and examples have been made available online *via* GitHub.[207]

5-PCSL

Spin-labelled phospholipids, such as 1-palmitoyl-2-stearoyl-(5-doxyl)-sn-glycero-3-phosphocholine (5-PCSL) are well characterised spin-labelled lipid probes for the measurement of lipid dynamics within membrane bilayers, in a similar manner to SASL probes.[71, 242] In this thesis, only the 5-PCSL probe was used for the measurement of the lipid order parameter, as this position historically shows the tightest lipid packing within a bilayer.[110, 166, 204, 247]

For 5-PCSL experiments lipid films were prepared with a molar ratio of 100:1 (lipid:probe) and a final probe concentration of 100 μM. For each sample, 3 nmol of probe was added from a 1 mg/mL stock in methanol to a 300 nmol (0.2 mg) aliquot of DMPC from chloroform stock. This organic solution was then briefly agitated, prior to being dried under nitrogen, and stored under high vacuum for at least 4 hours.

For polymer samples, the lipid film was then resuspended in 20 mM HEPES, 100 mM NaCl, pH 7.4 to 20 μL, with the desired polymer being added at a 1.5× excess lipid mass (w/w) from a 10% (w/v) stock in 20 mM HEPES, 100 mM NaCl, pH 7.4 and incubated at 30°C for 30 minutes with gentle agitation. All samples were then diluted to a final volume of 30 μL, prior to centrifugation at 30,000 g for 30 minutes at 4°C. The supernatant was then taken for insertion into capillary tubes.

For the LUV sample, the lipid film was resuspended to 100 μL, and subjected to 5× freeze-thaw cycles and then extruded through 400 nm polycarbonate filters to form LUVs. The dilute LUVs were then centrifuged at 30,000 g for 30 minutes at 4°C. The pelleted LUVs were then resuspended to a final volume of 30 μL and inserted into a capillary tube.

Measurements were recorded on an EMXmicro X-band CW, with an Oxford instruments liquid nitrogen thermocouple. Prior to measurement samples were incubated at the desired temperature for 3 minutes, then recorded for 32 scans at a sweep width of 150 Gauss (G) per measurement point. For data analysis, automatic detection of $A_{\perp}$ and $A_{\parallel}$ measurement points (Figure 1.12 B) was performed through an automated peak maxima and trough minima finding function within a defined range. The order parameter for the probe in lipid bilayers was then calculated

using these values, using Equation 1.21, as described by Watts *et al.*[166] Plotting was performed using the libraries described previously. The code and examples have been made available online *via* GitHub.[207]

3.3 Results & Discussion

This chapter aims to show a systematic approach to comparatively characterise the biophysical properties of DMPC-polymer nanoparticles formed under 'ideal' conditions (20 mM HEPES, pH 7.4, 100 mM NaCl) as discovered in Chapter 2. Visualisation of the nanoparticles from this 'ideal' condition was performed by negative stain transmission electron microscopy (TEM) to observe population heterogeneity of each polymer nanoparticle, and compare between the polymers tested.

In addition to visualisation, thermotropic properties of the nanoparticles was measured by a combination of differential scanning calorimetry (DSC) and continuous wave electroparamagnetic resonance (cw-EPR) to elucidate the lipid packing behaviour of these nanoparticles across a commonly used temperature range. Together, these results allow for a comparison of the commercially available polymers in an applied manner from initial solubilisation conditions through to nanoparticle size, shape, and lipid packing. These characteristics, once described in such a manner, allow for the comparison of the best use of these available polymers for new users, and a standardised framework for the comparison of novel polymers when developed.

3.3.1 Negative stain transmission electron microscopy (TEM)

An important feature of lipid-polymer nanoparticles is the co-solubilisation of membrane proteins with an annulus of native lipid membrane. This retention of native lipids leads to enhance stability of membrane proteins within these systems, over detergent based methods.[226, 248] All lipid-polymer nanoparticles possess the same overall structure of a lipid annulus and a polymer 'belt' surrounding it, leading to the now iconic coin-shaped disc. It is now common to image these nanoparticles through the use of transmission electron microscopy (TEM) to show complete solubilisation of the membrane (and the associated protein of interest).[98,

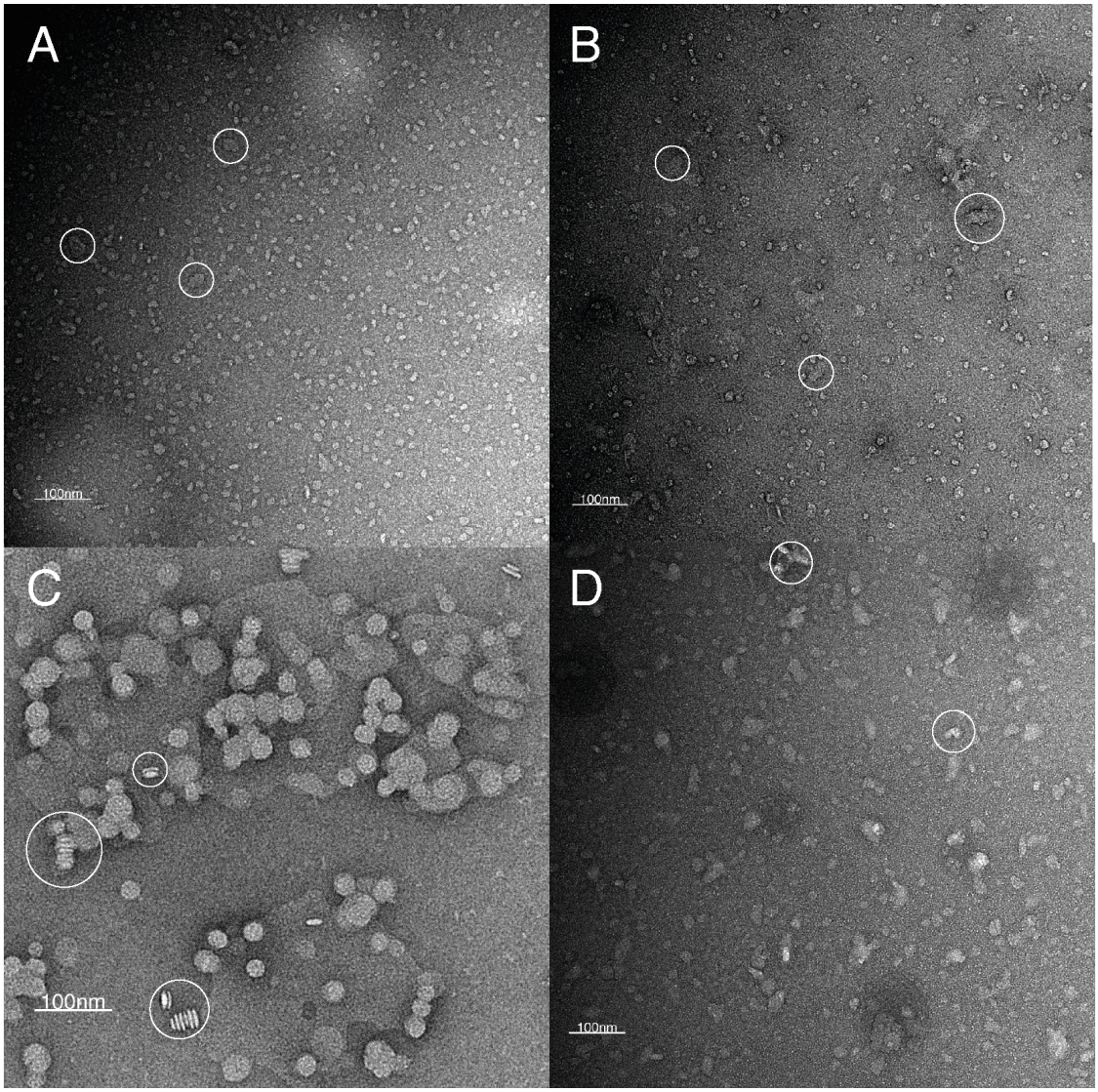


Figure 3.1: Negative stain TEM images showing nanoparticle macromolecular structure. SMA 3:1 (A), SMA 2:1 (B), DIBMA (C) and PMA (D) DMPC-nanoparticles prepared in 20 mM HEPES, 100 mM NaCl at pH 7.4 before staining with a 2% uranyl acetate solution. Samples were mounted and dried on 400 mesh carbon-copper grids. White circle highlights have been used to show unusual particle formations for each polymer type.

[154, 249] Direct imaging of the formed nanoparticles is not only visually pleasing, but can be used to quantify the level of homogeneity between particle shape and size. EM imaging is often used in tandem with particle averaging methods, such as dynamic light scattering (DLS) to obtain a more accurate view of particle size.

To visualise the nanoparticles generated by the polymers used in this thesis, transmission electron microscopy (TEM) was performed to directly compare the relative size and shape of particles formed by the solubilisation of DMPC membranes

by each polymer variant used in this thesis under 'ideal' conditions of 20 mM HEPES, 100 mM NaCl at pH 7.4 (Figure 3.1 A-D).

Particles formed from 'ideal' conditions were shown to possess the disc-like shape indicative of lipid-polymer nanoparticles, with approximately the same diameter across all polymers tested (shown in Figure 3.1). However, some heterogeneity in particle size can be observed within each polymer population. This is most notable in the SMA variant images where particles of a much larger than expected size can be observed (Figure 3.1 A and B annotated by white circles). These anomalous particles are unlikely to be unsolubilised membrane as this would have been removed during the size exclusion step, which aimed to remove both unsolubilised membrane and excess polymer. It was hypothesised that these larger particles could be two (or more) nanoparticles in a temporary 'fused' state. This could either be caused by dehydration of the nanoparticles during sample preparation leading to an abnormal fusion of neighbouring particles, or the capturing of a transient event known to occur in solution during the staining and dehydration process.[250] Chapter 4 goes into exploring this phenomenon in more detail.

DIBMA nanoparticles (Figure 3.1 C) show a good homogeneity of particles shape, however show a large variance in particle size. In addition to this, the nanoparticles form stack-like aggregates (or 'rouleaux') which have been observed previously for SMA nanoparticles.[142, 239] These can observed in Figure 3.1 C, highlighted by a white circle. This stacking phenomenon has also been observed in membrane scaffold protein (MSP) nanodiscs.[251] This is often attributed to the staining protocol causing an association between the -PC lipid head-groups in different nanoparticles, causing a stacking artefact on EM grids.[251] These stacks were also observed to a lesser degree in the SMA 3:1 and 2:1 images, but were not selected for use in this thesis.

PMA nanoparticles did not show the formation of rouleaux stacks, however small aggregates could be observed in some images, such as those highlighted in Figure 3.1 D. PMA nanoparticles also showed a high degree of heterogeneity in particle shape, with particles being observed as distinctly more 'blobby' than particles

formed by SMA or DIBMA. This could indicate a looser association of the polymer to the lipid, which could have led to a less tight packing of the acyl core.

3.3.2 EM particle analysis

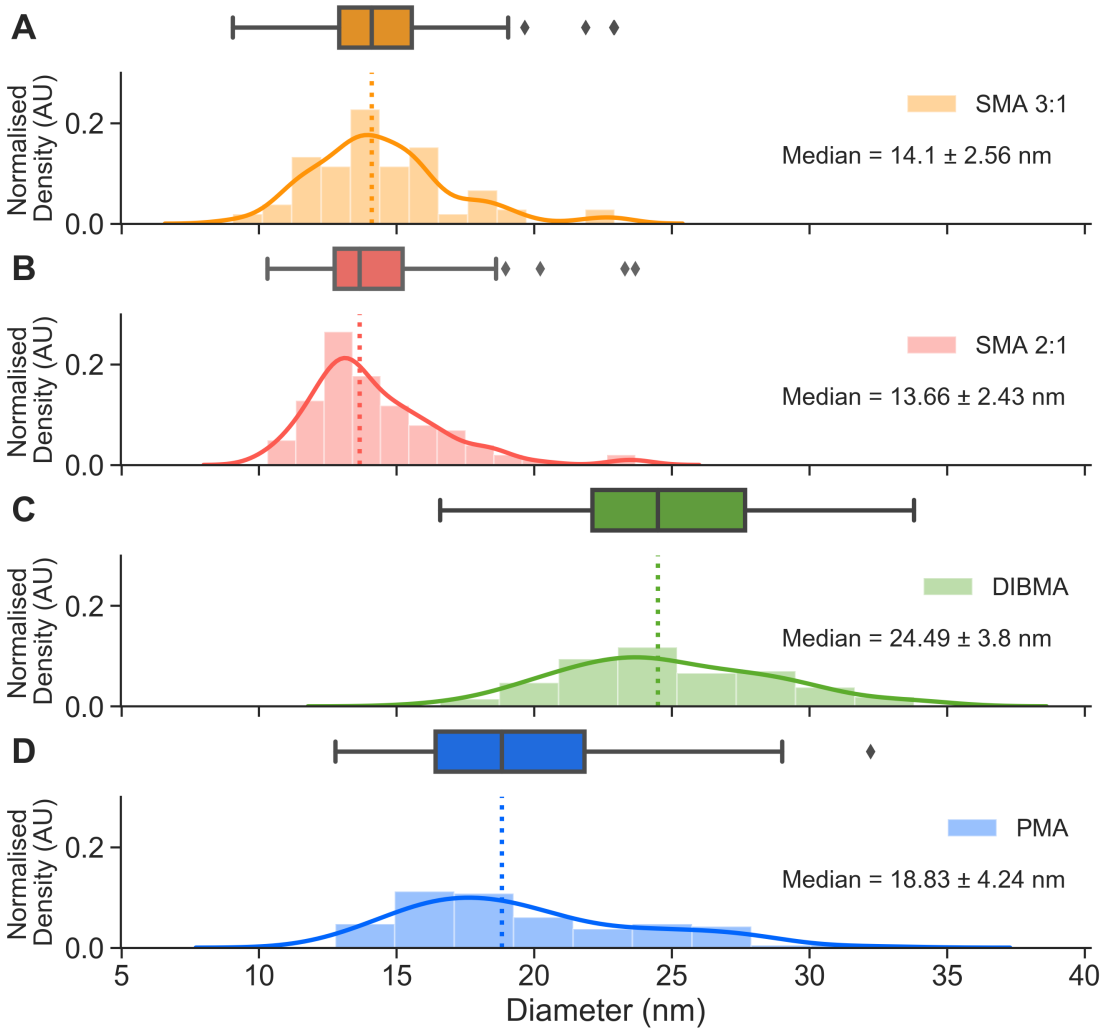


Figure 3.2: Dimensional analysis of 100 particles selected manually per polymer type. Box plots indicate the size and distribution of major axis per particle, whilst histogram show population distribution of the major axis length as described in §B.1.

Analysis of particle diameters were in good agreement to the literature precedent, and could be qualitatively confirmed from the inspection of the data in Figure 3.1, [98, 143, 154]. The SMA variants were very similar in size and population distribution. Quantification (as described in §B.1) showed there was an average homogenous median diameter of 14.10 nm (±2.56 nm) and 13.66 nm (±2.43 nm) for SMA 3:1

and 2:1, respectively. Figure 3.1 A,B showed a second macromolecular structure as a distinct population around 20-25 nm in diameter (Figure 3.2 A,B), however when quantitatively measured this population is less abundant than expected by visual observation of particles Figure 3.1.

DIBMA showed a larger average diameter than the other polymer variants (24.49 nm) along with a greater distribution of size compared to the SMA variants (±3.80 nm). The broad distribution could could have been due to DIBMA possessing a less hydrophobic group than SMA (isobutylene compared to styrene). This reduced hydrophobic surface are could have caused weaker association of DIBMA with the acyl core of the DMPC lipids. A looser association could allow for more flexibility in packing size during particle formation, and is examined more closely through the use of DSC (Figure 3.3) and cw-EPR (Figure 3.8).

Finally, PMA showed a similarly large distribution of diameters, but with a lower median diameter of 18.83 nm (±4.24 nm). This could again be due to a looser association of hydrophobic groups with the lipid acyl core, relative to the SMA variants.

Table 3.1: Comparison of TEM median particle diameter from particle analysis and hydrodynamic diameter (D_H) from dynamic light scattering (DLS) measurements. Both samples were initially generated in 20 mM HEPES at pH 7.4, 100 mM NaCl with no divalent cations. TEM samples were then subjected to SEC prior to staining and dehydration, whilst DLS samples were filtered with 0.22 μm filter prior to measurement.

Polymer	EM Diameter (nm)	EM Error (nm)	DLS D_H (nm)	DLS Error (nm)
SMA 3:1	14.10	±2.56	8.24	±4.44
SMA 2:1	13.66	±2.43	8.64	±3.72
DIBMA	24.49	±3.80	11.86	±4.94
PMA	18.83	±4.24	9.28	±3.44

TEM was used as an orthogonal technique to measure particle diameter, in conjunction with the dynamic light scattering (DLS) measurement technique used to understand optimal solubilisation conditions for the polymers (§2.2.4). Comparison of the average diameter by TEM and dynamic light scattering (DLS)

shows an average trend for measurement by DLS to underestimate particle size for nanoparticles formed (Table 3.1). This discrepancy was likely due to the modelling underlying DLS measurements assuming a solid, spherical particle,[158] whilst in actuality the particles were coin-shaped. The difference in modelled *vs* empirical shape could explain the smaller average hydrodynamic radius calculated by the software due averaging of the anisotropic particle.

The discrepancy between TEM and DLS measurements was larger when comparing both DIBMA and PMA values gained by EM to their DLS counterparts. The factor of two difference in diameter was hard to explain and was hypothesised to be due to differences in sample preparation for DLS measurements *vs* TEM imaging. Comparison of the protocols shows the main difference, aside from EM requiring dehydrated samples, is that DLS samples did not undergo SEC prior to measurement, but were instead filtered. Whilst this difference would have removed any large aggregates that would affect accurate DLS measurement, it would have not removed the excess polymer required for efficient solubilisation. Preliminary work (not shown) has observed the effect of excess polymer on PMA-particle size, with the excessive polymer causing a shrinking effect measured by DLS, with similar effects observed for SMA and DIBMA nanoparticles to a lesser extent (not shown).

3.3.3 Thermotropic characterisation

As lipid-polymer nanoparticles are increasingly being used for membrane mimetics, due to their native-like composition, it is important to understand the nature of the lipid membrane within these systems. It is known that lipid within SMA-bound nanoparticles experience an increased lateral pressure compared to the commonly used LUV systems,[98] in addition to experiencing a change in membrane phase behaviour.[239] For a single lipid species bilayer, the phase transition is expected to be highly cooperative, leading to a well characterised shift from gel- to liquid-crystalline-phase across the transition temperature of the lipid. For physiological temperatures, the majority of membranes exist in the liquid-crystalline state, which is characterised by relatively loose lipid order, and a high degree of

lipid movement compared to the liquid-crystalline phase. The organisation and fluidity of a membrane can drastically affect protein behaviour,[32] and therefore it is imperative that the lipid packing and thermotropic properties within these lipid-polymer nanoparticles are fully characterised. If the lipid in these nanoparticles are not similar to native membranes in their lipid organisation and dynamics, this could potentially affect the proteins activity in these systems.[137, 185]

Until recently, only SMA polymers have been fully characterised in terms of the lipid packing and how this affects lipid phase behaviour. [98, 239] The addition of the characterisation of DIBMA nanoparticles by Colbasevici *et al.*[252] has allowed for the comparison of lipid fluidity of maleic acid containing polymers. This has shown there are significant differences between SMA and DIBMA polymers, most likely due to the difference in hydrophobic groups inserted into the acyl core.

3.3.4 Differential scanning calorimetry (DSC)

Differential scanning calorimetry (DSC) was used to show how DMPC phase transition properties are modified within DMPC-polymer nanoparticles, to help elucidate how 'native-like' the lipid behaviour is within these nanoparticles. A known benefit of lipid-polymer nanoparticles over detergent based solubilisation methods is the retention of 'native-like' lipids and membrane organisation. However, it has been shown previously that the normally sharp transition in LUVs from gel- to liquid-crystalline-phase is significantly broadened in lipid-polymer nanoparticles, such as SMA 3:1 and DIBMA,[98, 143] The level of broadening is affected by polymer structure,[239] with a larger hydrophobic bulk increasing the broadening affect. Alteration of this phase behaviour in lipid-polymer nanoparticles is therefore indicative of an altered lipid packing, which may alter membrane protein behaviour within these systems.[253]

DSC allows for the measurement of enthalpic change of a sample over a given temperature range. As DMPC has a well characterised phase change at 23.6°C in LUVs, and it is known from the literature that DMPC-SMA 3:1 nanoparticles

experience a downshift of this phase transition,[98] it was decided to measure the enthalpy of the DMPC-polymer samples between 5-35°C.

In addition to this, a DMPC LUV sample was used for comparison in this thesis, as well as for calibration of the samples during measurement. As can be observed in Figure 3.3, the DMPC LUV sample (black) showed a two sharp peaks indicating phase transitions. The first peak around 15°C is indicative of the 'pre-phase' transition, whilst the larger peak at 23.6°C is the main phase-transition peak.[254] As the DMPC membrane undergoes this transition lipid packing is remodelled from the rigid gel-phase below the transition temperature (T_m), to the more mobile liquid-crystalline-phase above the T_m. This re-ordering is cooperative in nature, with the rate of phase change being proportional the number of lipids per 'cooperative unit', or particle.[243, 255] A sharp peak indicates a large number of lipids per cooperative unit, whilst a shallow peak is indicative of few lipids.

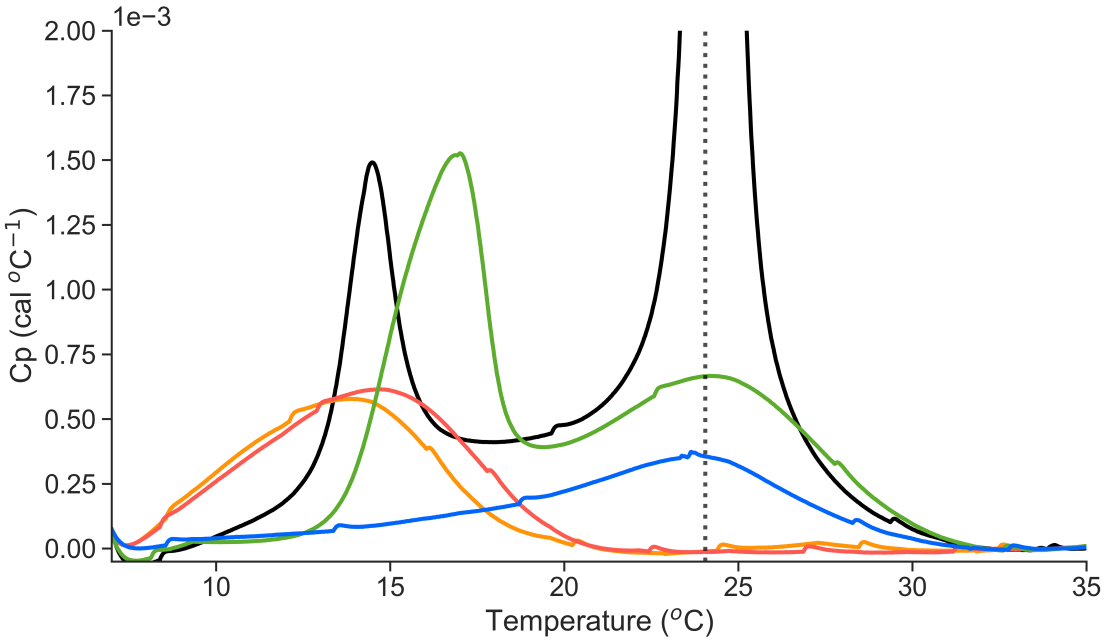


Figure 3.3: Differential scanning calorimetry (DSC) data of DMPC-polymer nanoparticles of DMPC LUVs (black), SMA 3:1 particles (orange), SMA 2:1 particles (red), DIBMA particles (green) and PMA particles (blue). Scale has been fixed to highlight polymer range, with DMPC main transition peak at ~24°C shown as vertical line (black, dotted).

All DMPC-polymer particles showed a broadening of the peak observed for DMPC LUVs, indicating there is a smaller cooperative unit undergoing phase

transition within each particle (Figure 3.3). This was to be expected due to the large decrease in lipid per nanoparticle (~200),[98] compared to the many thousands present in 400 nm LUVs. Additionally to the smaller cooperative unit, there was a downward shift of the transition temperature away from the expected 24°C - indicating some alteration of lipid behaviour through polymer interaction. In particular, the presence of SMA appeared to lower the melting temperature of DMPC in the particles from 23.6°C to around 15°C. This may have been due to the effect of the styrene groups on ordering the acyl chain packing of the lipid. Similarly, DIBMA appeared to shift the main transition temperature from 23.6°C to around 15°C. However it did retain a secondary, smaller, transition at around 24°C. PMA, with the smallest of hydrophobic bulk of the polymers tested appeared to disturb the melting temperature the least. This is observed as a single small broad peak correlating to the smaller cooperative unit, but a retention of the original melting temperature of the DMPC bilayers, albeit without the expected pre-transition at 15°C.

Table 3.2: Enthalpy values of DMPC-polymer nanoparticles calculated by integration of base-line corrected DSC data.

Polymer	**Enthalpy (kcal/mol)**	**Error (kcal/mol)**
LUV	5.26	±0.26
SMA 3:1	0.79	±0.16
SMA 2:1	0.89	±0.18
DIBMA	2.06	±0.41
PMA	0.69	±0.14

Integration of the DSC curves allowed for the quantification of the enthalpy of the phase transition as shown in Table 3.2. The quantification highlighted the change of the lipid-polymer nanoparticles from the LUV control. Importantly, it also shows that all polymers underwent a reduced enthalpic change across the temperature range than the LUV sample. Both SMA variants and PMA showed a similar magnitude of enthalpic change which, combined with the similar shapes of the DSC curve, highlighted that SMA- and PMA-lipid particles have broadly the same thermal stability and properties, albeit at differing transition temperatures.

DIBMA, however, appeared to be the most native like for shape of the curve, being reminiscent of the LUV phase transition. Quantification of the enthalpy changes showed a ~2 fold reduction in the enthalpy compared to the LUV sample. Overall, this indicates that DIBMA-DMPC nanoparticles were the most native like in terms of bulk lipid behaviour, whilst SMA and PMA particles were unable to undergo a transition within this temperature range in a similar manner.

Laurdan fluorescence

Initially (in 2017), measurements of lipid packing was hoped to be performed through a readily available probe-based assay using Laurdan fluorescence, as previously developed by Dominguez Pardo *et al.*[239] the initial design was to explore the difference in thermotropic properties of asymmetric SMA-lipid nanoparticles, In particular the Lipodisq variant (LQs), which were currently being explored at that time. The Laurdan fluorophore is sensitive to the hydrophilicity of its environment, shifting from an emission maxima at 440 nm in hydrophobic environments to 490 nm in hydrophillic environments.[241] The structure of the Laurdan fluorphore causes it to reside between the glycerol backbone of membrane phospholipids.[242] This allows for the detection of the transition between gel- and liquid- phase in lipid membranes, as this phase change alters the relative hydrophobicity of the environment due to lipid re-ordering. The relationship between 440/490 nm, often referred as general polarisation (GP, as described by Equation 3.1) has been widely used to analyse lipid phase changes in biophysical studies.[256, 257] It has also been used previously to successfully study lipid-SMA nanoparticles.[239]

The original aim of the Laurdan characterisation was to use the probe as a tool to differentiate between LQs of mixed DMPC:DLPC membranes *vs* asymmetric LQs (aLQs) of DLPC / DMPC (where the '/' denotes leaflet change, mentioned in more detail in Chapter 4 and §C.2). This combination of lipid was chosen for the large transition temperature difference (-2°C *vs* 24°C) which would be clearly observable in aLQs if generated. However as explained later (Chapter 4) aLQs were not generated.

The Laurdan assay and the TEMPO assay later in this chapter therefore show both DLPC and DMPC samples but DLPC is not observed in the remainder of this thesis.

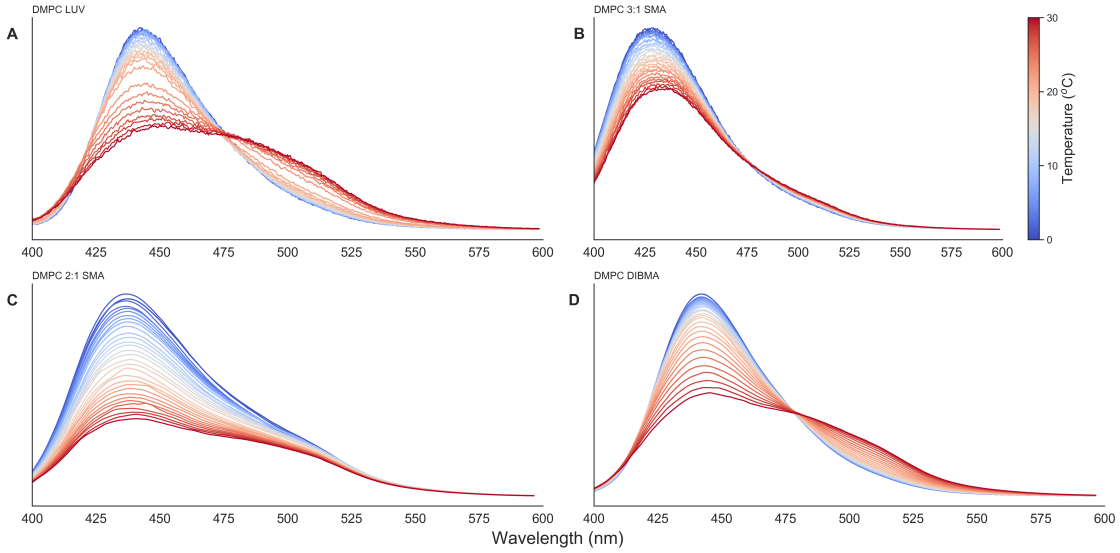


Figure 3.4: Measurement of thermotropic behaviour of DMPC membranes in (A) LUVs, (B) SMA 3:1 nanoparticles, (C) SMA 2:1 nanoparticles and (D) DIBMA nanoparticles as shown by red-shifting of Laurdan fluorophore during phase transition from ~440 nm to ~490 nm. Blue to red colouration indicates temperature range (as seen by legend in (B).

Figure 3.4 demonstrates a pronounced shift in the emission of laurdan in the DMPC LUV sample (A) as temperature increases (blue to red lines), indicating a re-ordering of lipid head groups due to a lipid phase change. DMPC LUVs are known to undergo a gel to liquid crystalline phase change (T_m) at 23.6°C.[255] This shift is severely dampened in both SMA variants (B and C). However, the shift was partially observable in the DIBMA sample (Figure 3.4 D). At the time of measurement PMA was not available, so was not included in these preliminary studies.

Plotting the general polarisation (GP) of Laurdan in relation to temperature allowed for a detailed view of the phase behaviour of the lipid membrane. Figure 3.5 A shows the LUV sample undergoes a change in GP around the transition temperature reported for DMPC LUVs (~24°C, dotted line).[255] Similarly, there is a distinct change in the GP for DIBMA-DMPC nanoparticles, also around this temperature. However there is less definition of this transition in DIBMA samples compared to LUVs.

It was originally sought to understand the phase behaviour of asymmetric LUVs (aLUVs) and asymmetric nanoparticles using this Laurdan method, based upon preliminary experimental evidence for the potential existence of asymmetry in LQs. For this, both DMPC and DLPC membranes were selected due to a high separation of the T_m of 24°C and -2°C respectively.[254, 255] It was hoped that asymmetric LQs would show a two separate transition points as the individual leaflets underwent the lipid-specific phase transition. The data showed that the phase transition of DMPC was observable (Figure 3.5 A), however it was much broader than expected. The pre-phase transition expected at ~12°C was also not observed. For the DLPC membrane, the T_m of -2°C was not observed due to the water bath limiting the lower range to +1°C. Instead, the GP plot showed a linear progression across the temperature range tested. For these reasons, Laurdan was deemed too insensitive for the desired characterisation of lipid-packing in these nanoparticles..

Laurdan is often used for visualisation of a membranes phase transition and the characterisation of lipid packing of complex membranes.[256] However, the large fluorescent dye structure, with the naphthalene ring moiety, within the glycerol backbone region make it a rather blunt measuring tool for sensitive experiments in simple model membranes. The large naphthalene ring moiety, in the tight packing region of the glycerol backbone, has limited the use of this probe due to the label potentially affecting the phase transition, or misreporting due to spontaneous

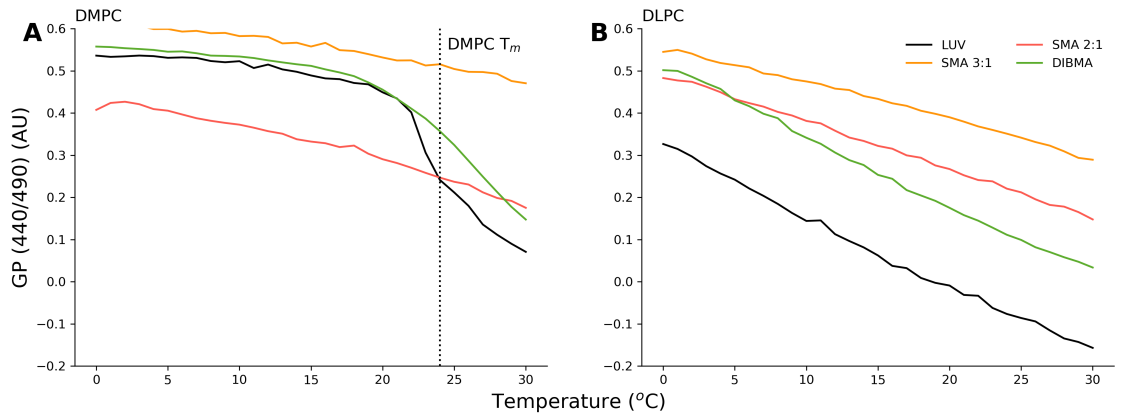


Figure 3.5: General polarisation of laurdan fluorophore within (A) DMPC, (B) DLPC membranes in LUV (black), SMA 3:1 (orange), SMA 2:1 (pink), and DIBMA (green).

conformational changes within the glycerol region of the membrane.[258, 259] More specialised techniques, such as TEMPO partitioning[245, 260] or stearic acid spin labels (SASL)[91] are also available and can provide more sensitive results than Laurdan in terms of lipid packing within a bilayer. Due to prior experience within the lab, TEMPO partitioning was trialed in the hopes of a more sensitive detection of the phase transition. The use of a liquid nitrogen thermocouple also allowed for the examination of a broader temperature range, from -10 to +40°C.

3.3.5 cw-EPR

TEMPO partitioning

The measurement of TEMPO partitioning into the bilayer can be used to determine the gel- liquid crystalline phase transition temperature of a lipid bilayer (Figure 1.14). As a lipid membrane undergoes this transition, the bilayer is less densely packed which allows for the association of free TEMPO in the aqueous medium into the headgroup region of the bilayer. The TEMPO in this region experience a different environment, and show reduced anisotropy, leading to the hyperfine splitting of the EPR spectra at the +1 peak (Figure 1.14 B). By plotting this hyperfine splitting, as measured by the H and P peaks, against temperature TEMPO partitioning can be used to determine the phase transition temperature of a bilayer.

Plotting the partitioning of TEMPO into the bilayer against temperature (Figure 3.6) showed a sharp transition of DMPC LUVs at 24°C. However, the pre-phase transition temperature for DMPC at 12°C could not be observed. Similarly, the DLPC phase change at -2°C was not as sharp as expected for a phosphatidylcholine headgroup lipid,[255] indicating that a more sensitive method would be required for the desired purpose. An alternative approach, using stearic acid spin labelled lipids, which would allow for different positional labels across the acyl core of the nanoparticles was then considered. This additional information in conjunction with a thermal scan per label position would reveal far more information than TEMPO labelling alone.

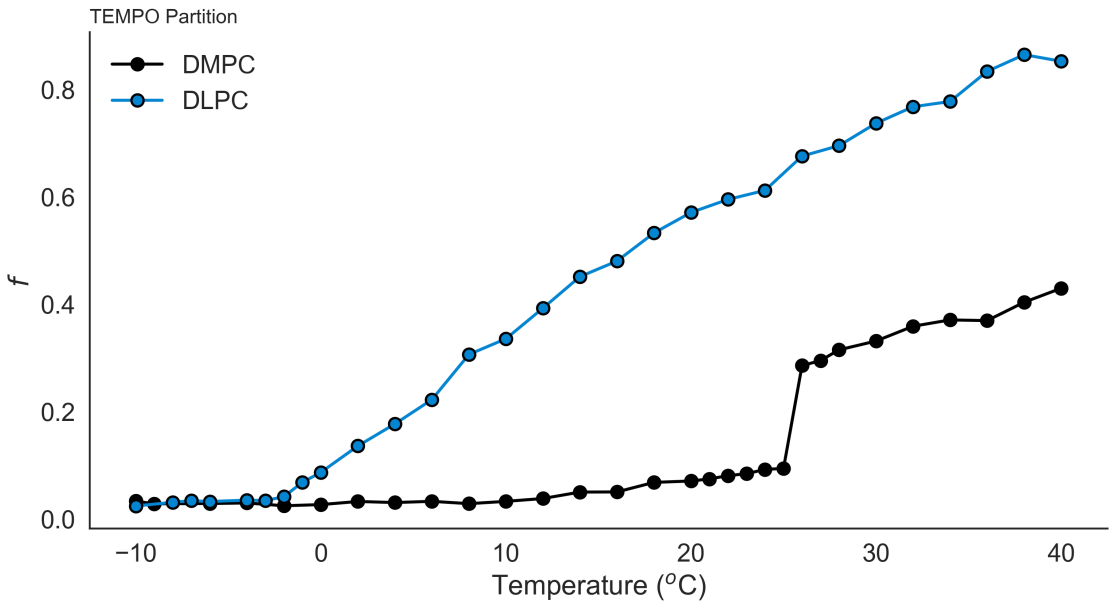


Figure 3.6: Plot of TEMPO partition coefficient (f) over temperature, showing sharp DMPC LUVs (black) with a transition at 24°C and broad DLPC LUVs (blue) with a transition at -2°C.

Stearic acid spin labels (SASL)

Stearic acid spin labels (SASL) have been used previously for analysis of acyl chain packing within membrane systems previously in the lab,[91, 110, 204] and so were available for preliminary assays to determine whether lipid packing differs between nanoparticles formed of different polymers. To examine the packing of lipids and how this is altered during phase changes of the membrane two sets of experiments were designed with the relatively limited label stock available (Figure 3.7).

Firstly, 18:1 TEMPO PC (POPTC), a head group labelled lipid, was used to ascertain whether the labelled lipids can be solubilised by the polymer range. Figure 3.7 A-E shows that all polymers were able to solubilise a 1% (molar) POPTC mixture within a DMPC membrane, as evidenced by the spectra being present for all polymers. In addition, all POPTC spectra have a generally similar spectral width (peak to peak distance, Figure 3.7 A-D), indicating that they probe experienced similar lipid packing at the head group region. Not only does this show that the polymers could solubilise the labelled lipids sufficiently, but also that the polymers tested did not significantly interact within the head groups of

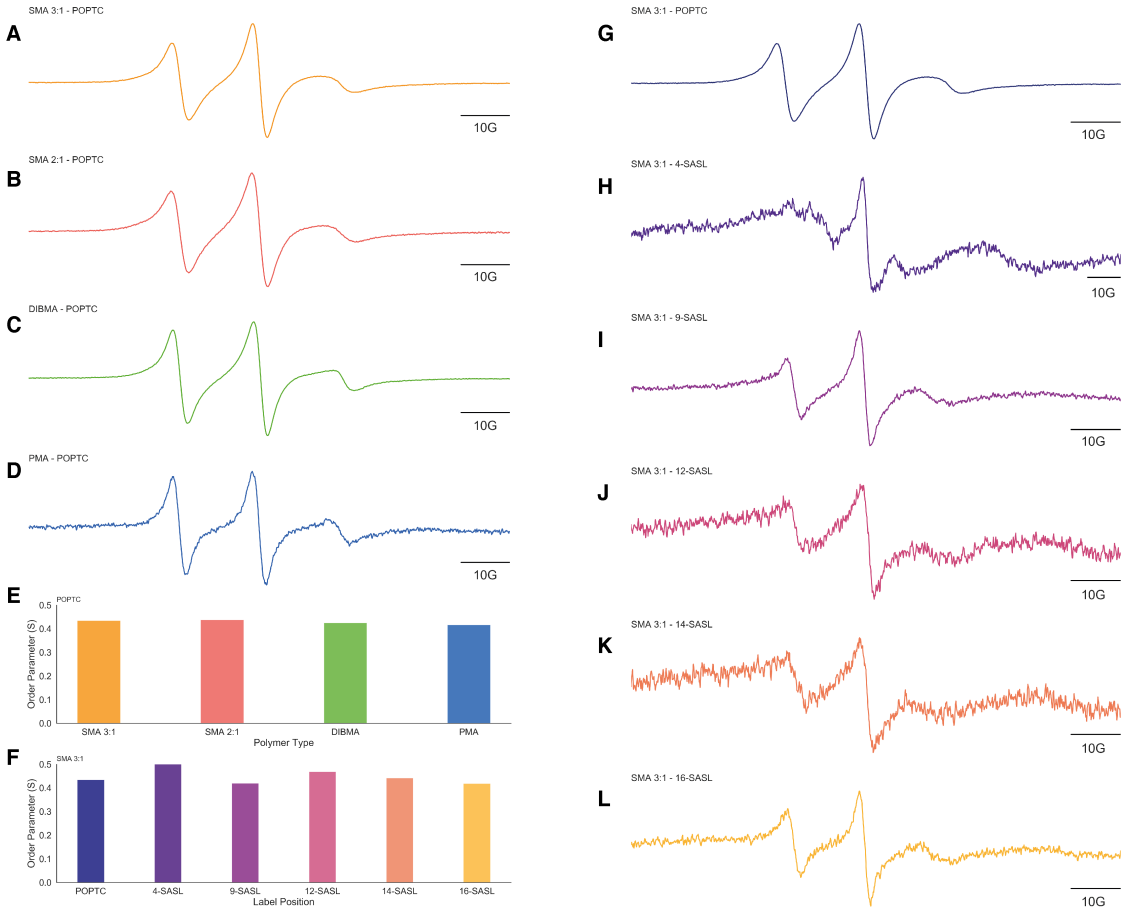


Figure 3.7: EPR spectra of TEMPO-labelled POPC (POPTC) and stearic acid spin label (SASL) probes in a 1% (molar) mixture within DMPC recorded at 25^{o}C. (A) SMA 3:1-DMPC nanoparticle POPTC spectra, (B) SMA 2:1-DMPC nanoparticle POPTC spectra, (C) DIBMA-DMPC nanoparticle POPTC spectra, (D) PMA-DMPC nanoparticle POPTC spectra, (E) Comparison of calculated order parameter of spectra A-D. (F) Comparison of SASL spectra of SMA 3:1-DMPC nanoparticle (shown in G-L). (G) POPTC spectra of SMA 3:1-DMPC nanoparticle, as shown in (A). (H) 4-SASL spectra of SMA 3:1-DMPC nanoparticle, (I) 9-SASL spectra of SMA 3:1-DMPC nanoparticle, (J) 12-SASL spectra of SMA 3:1-DMPC nanoparticle, (K) 14-SASL spectra of SMA 3:1-DMPC nanoparticle, (L) 16-SASL spectra of SMA 3:1-DMPC nanoparticle.

the lipid. However, by plotting order parameter, S, (as described previously in Figure 1.12), as seen in Figure 3.7 E, it can be seen that there are slight differences between the head group motional freedom across the polymers. This may be due to excess polymer interacting with head groups of the lipid, rather than being confined to the acyl core region in the 'belt'.

Use of a secondary set of probes to analyse the lipid packing along the acyl environment of the DMPC membrane was also devised. Utilising spin labels located

along the acyl chain at the 4-, 9-, 12-, 14-, and 16-positions (Figure 3.7 H-L, respectively) it was possible to examine the lipid packing of the lipid membrane for each polymer, as steric bulk from the polymer's hydrophobic groups affect motional freedom of the lipid probes. Due to a limited supply of SASL probes available, SMA 3:1 was chosen for a better comparison to literature values as a similar walk had been previously performed by Orwick *et al.*[204] SMA 3:1 was also predicted to have the most rigid acyl core of all polymers available due to the large styrene groups in the polymer structure. The 4-SASL probe showed the most restricted motion within the acyl environment (Figure 3.7 F), whilst the POPTC and 16-SASL label broadly showed the most motional freedom. The ideal reporter of lipid packing is historically the 5^{th} carbon position, as it is in the tightest region of lipid packing and therefore most sensitive to a change. Meanwhile the head group and the end of the carbon tail (i.e. the 16^{th} position in the probes used in this thesis) are not often used for this purpose due to their loose, disordered, packing in general membrane structures.[204, 261] Overall, the results shown in Figure 3.7 indicate that EPR probes are a highly sensitive and cost-effective assay for the characterisation of thermotropic properties of lipid-polmyer nanoparticles, with the added benefit of requiring very low amounts of material relative to fluorimetry (Figure 3.5).

Sadly, the quantity and quality of the labels used in this preliminary experiment were too low for further assays with other polymers - and the probes have since been discontinued. However, due to the sensitivity of the EPR methodology, it was decided to obtain a modern alternative to the SASL probes at a single location of the membrane to best compare acyl chain order within each polymer nanoparticle. For this reason this work was continued in Chapter 3, utilising a phosphocholine spin label at the 5-n position (5-PCSL).

As has been stated previously, DMPC large unilamellar vesicles (LUVs) undergo a well characterised phase change around 23.6°C (Figure 3.8 A, black), with a sudden decrease in lipid packing at this temperature as the lipid under goes a phase change from the gel- to liquid-crystalline-phase.[166] However, 5-PCSL labelled lipids within polymer-lipid nanoparticles experienced reduced motional freedom

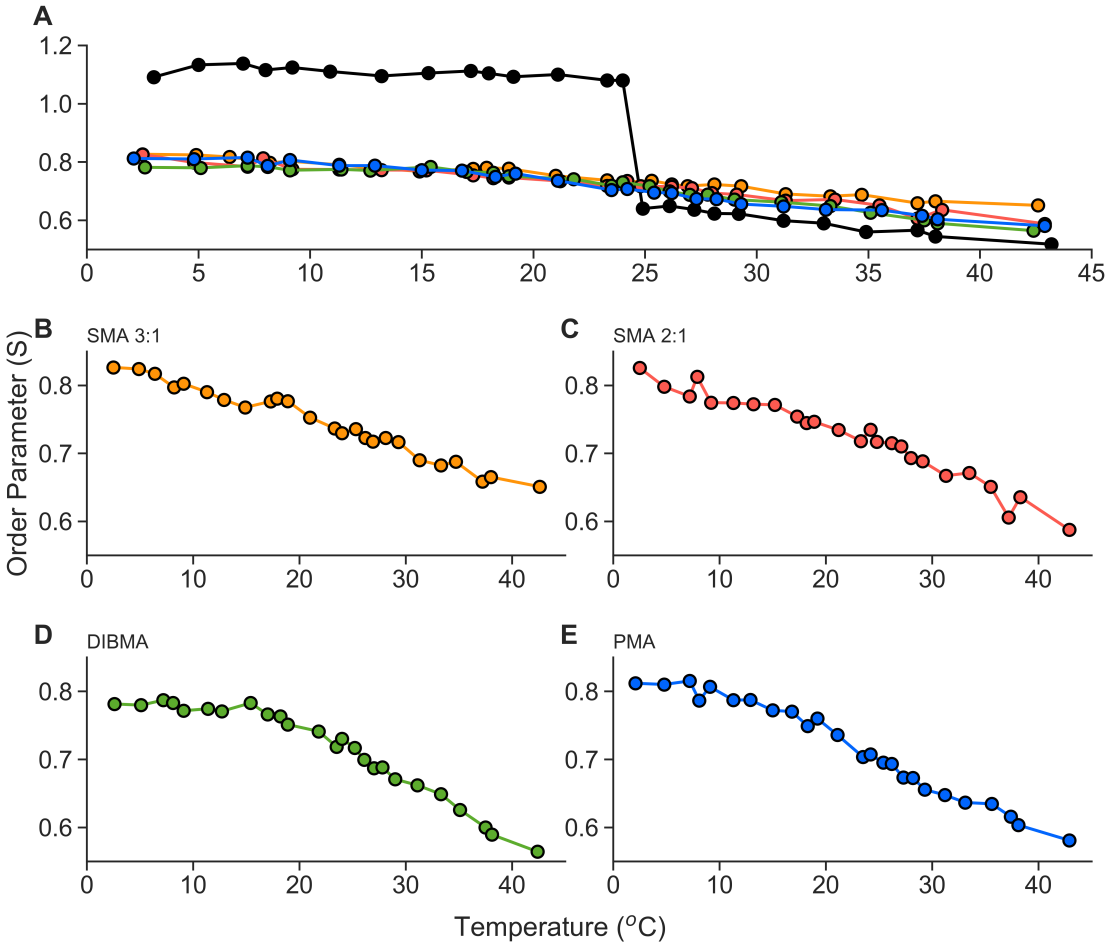


Figure 3.8: Order parameter (S) of lipid membrane generated from cw-EPR measurement of 1% (molar) 5-PCSL in DMPC-polymer nanoparticles.(A) Order parameter of 400 nm DMPC LUVs (black), SMA 3:1 (orange), SMA 2:1(red), DIBMA (green), and PMA (blue). Isolated order parameters of SMA 3:1 (B), SMA 2:1 (C), DIBMA (D), and PMA (E) nanoparticles.

when compared to liquid-crystalline-phase LUVs (Figure 3.8 B-E), but more freedom than their gel-phase LUV counterparts. All nanoparticles experienced a similar level of lipid packing to one another. However there was a slight trend towards tighter packing in SMA containing particles, with DIBMA and PMA experiencing similar levels of packing to each other. Additionally, all nanoparticles did not experience a detectable gel to liquid-crystalline phase transition across the temperature range tested, this is in line with the broad transitions observed in the DSC data. One exception may be noted, which is the transition of DIBMA nanoparticles (Figure 3.8 D), where there was a slight transition from a plateau to a linear decrease at

around 15°C. This was in line with the major peak observed through DSC (Figure 3.3, green) and could signal a slight phase change around this temperature.

3.4 Summary and conclusions

This chapter has systematically characterised the biophysical properties of DMPC-polymer nanoparticles of four polymers, SMA 3:1, SMA 2:1, DIBMA and PMA. Through the use of negative stain EM imaging it has been shown that DMPC-SMA nanoparticles, both SMA 3:1 and 2:1 variants, possess a more homogenous size distribution, and a median diameter of around 14 nm (±2.5 nm). Similarly, it has been shown that DMPC-DIBMA and PMA nanoparticles show a higher degree of size distribution than SMA, with median diameters of 24.49 (±3.80 nm) and 18.83 (±4.24 nm) respectively.

Additionally, through the use of both DSC and EPR techniques a comparison of the polymer variants to more native LUV membrane models was performed. The DSC showed that lipid-polymer nanoparticles do not experience the sharp gel to liquid-crystalline phase change observed in DMPC LUVs, but instead experience a broadening of the phase transition enthalpy, due to a small cooperative unit. However, DMPC-DIBMA nanoparticles showed the most similarity to DMPC LUVs in both melting temperature and enthalpy as measured by DSC, with an enthalpy at 39% of the DMPC LUV sample. In contrast, both SMA polymer variants and PMA showed approximately 15% of this value.

Whilst DSC can inform of the enthalpy and phase properties of DMPC-polymer nanoparticles, it does not give precise information on the packing of the lipids within these systems. To understand how the lateral pressure applied by the polymer association affects lipid packing, electron paramagnetic resonance (EPR) was performed with an nitroxide spin-label at the 5^{th} carbon of the acyl chain of a POPC lipid (5-PCSL). For a single known temperature point this would only allow for a measurement of the lipid motional freedom within these systems. This is given by a change in order parameter (S) through measurement of the hyper-fine splitting as observed in §B.3. By measuring the 5-PCSL motional freedom

across a temperature range, one can can examine the change in lipid-packing over the observed phase changes in the DSC data. By comparing DSC and EPR measurements it is possible to determine whether the enthalpic transition measured by DSC for the nanoparticles result in an increased motional freedom of lipids in the membrane as measured by EPR.

Measurement of the lipid order and packing through EPR techniques showed more consistent lipid-packing behaviour than would be expected from DSC alone. 5-PCSL measurements showed that these nanoparticles possess a higher degree of lipid-packing at temperatures that would normally indicate a liquid-crystalline phase in DMPC LUVs ($> 24^{o}$C), but at cooler temperatures ($< 24^{o}$C) the lipid packing of the nanoparticles is much looser than the gel phase equivalent of LUVs.

Together, these findings show that the polymers tested do not just vary in solubilisation efficiency as shown in Chapter 2, but have an affect on the biophysical properties of the extracted membrane. This data, in addition to data in the literature related to lipid mobility in these systems,[98, 151, 154, 165, 252] raises questions as to the accuracy of the term 'native-like' when applied to these nanodiscs (and indeed to the similarly sized MSP nanodiscs) in terms of membrane fluidty. There is now consistent evidence showing that peptide-based or lipid-polymer nanodiscs do not experience native-like phase properties, but instead experience a pseudo-fluid phase as observed in Figure 3.8. This may have previously unexplored effects on proteins within these 'native-like' systems, and further work is required to fully understand the implications on more complex membrane models than used in this thesis.

It is better to be roughly right than precisely wrong.

— John Maynard Keynes

4

Investigations into lipid mixing of lipid-polymer nanoparticles

Contents

4.1 Introduction 99
4.1.1 Aims 100
4.1.2 Asymmetric model membranes 101
4.2 Materials & methods 102
4.2.1 aLUV generation 102
4.2.2 FRET & TR-FRET measurements 104
4.2.3 NMR 106
4.2.4 Cytochrome oxidase c (CcO) and cardiolipin titration . 106
4.3 Results & discussion 110
4.3.1 Measurement of LUV and LQ asymmetry by FRET . . 110
4.3.2 Kinetics of lipid mixing by TR-FRET 115
4.3.3 Unlabelled lipid mixing as measured by NMR 121
4.3.4 Titration of cardiolipin into CcO-Lipodisqs 126
4.4 Summary and conclusions 131

4.1 Introduction

This chapter investigates the collisional mixing of lipids within lipid-polymer nanoparticles. The phenomenon was first identified by Keller *et al.* within SMA nanoparticles, containing SMA 3:1 (with an average molecular weight of 6.7 kDa

-SMALPs) in 2017.[262] However, preliminary results produced by D.Yin (2016) indicated that SMA nanoparticles containing SMA 3:1 (with an average molecular weight of 9.5 kDa -LQs) were able to retain the leaflet asymmetry present in asymmetric LUVs.[110] However, the work shown in this chapter shows that the mixing described initially for SMALPs by Keller *et al.* was not only observed in LQ systems, but also appeared to be a conserved property of all lipid-polymer nanoparticles. Furthermore, this chapter showed that this property is present from first formation of nanoparticles *via* aLUV FRET experiments. The chapter goes on to discuss the kinetics of lipid mixing through TR-FRET using fluorescent labelled lipids, NBD-PE and Rho-PE. Unlabelled lipid studies were performed using ^{31}P solution NMR to show that the lipid-mixing is due to nanoparticle collision and not through the diffusion of labelled lipid monomers between nanoparticles. Finally, this lipid exchange phenomenon is then used for a preliminary experiment to show that this unique property of lipid-polymer nanoparticles can be utilised to specifically titrate cardiolipin (CL) to cytochrome oxidase c (CcO) containing LQs. This is the first known case of lipid-protein titration within nanoparticles, without the use of detergent or organic solvents. This newly explored methodology has the potential to explore more delicate lipid-protein interactions than currently used in the literature.

4.1.1 Aims

The following chapter aims to show an in depth exploration into the previously reported collisional lipid mixing[250]. Initially this is explored through the generation of asymmetric LUV membrane model (aLUV) from which FRET- and EPR-based assays are used to measure the loss of asymmetry during lipid-polymer nanoparticle formation for the four previously characterised polymer variants (§Chapter 3). Using the same FRET based assay, preliminary experiments are performed to ascertain where asymmetry is lost; during nanoparticle formation, or through collisional lipid mixing.

Further assays, utilising TR-FRET, were used to fully calculate, and compare, the mixing rate within the lipid-polymer nanoparticles across a range of temperatures

(4, 20, 30, and 45°C). Controls including calculation of mixing rates of purified nanoparticles, with excess polymer required for fully formation of the particles removed through size exclusion chromatography (SEC), and the measure of mixing in non-labelled ^{31}P NMR experiments were also performed.

Finally, this chapter goes on to explore a biological use for this collisional lipid mixing; the specific titration of a lipid into a protein containing nanoparticle. This is performed with the well characterised cytochrome oxidase c (CcO) activity dependence on cardiolipin (CL), and in this chapter includes the removal of native CL by phospholipase A2 digestion, followed by recovery of native-like activity by the re-addition of CL through collisional lipid mixing in Lipodisqs.

4.1.2 Asymmetric model membranes

Leaflet asymmetry, whilst ubiquitous and well defined in natural membranes, has been challenging to replicate in model membrane systems. Many methods of asymmetry generation have been used to try and mimic natural membranes, but these have compromised between native-like properties and asymmetry, and often have short half life of asymmetry compared to natural membrane systems.[263–265]

A new procedure, developed by London *et al.* in 2012 (Figure 4.1 A),[266] and later refined by Pabst *et al.* in 2014 (Figure 4.1 B)[119] have allowed for the relatively easy, bulk, preparation of asymmetric LUVs (aLUVs). Unlike previous methods this directly prepares asymmetric versions of commonly used LUV models, without the use of oil, which has been shown to affect membrane structure.[267] The principle relies on the exchange of lipids between a donor and acceptor liposome through the use of cyclodextrin (MβCD) to 'shuttle' individual lipids from the donor outer leaflet to the acceptor outer leaflet (Figure 4.1). This leaflet specificity allows for the generation of asymmetric LUVs, with purification of asymmetric acceptor LUVs utilising centriugation to selectively pellet either the acceptor (London) or donor (Pabst) liposomes using a sucrose core. Preliminary experiments by D.Yin (2016) showed that the asymmetry generated for LUVs can be retained in LQ systems.[110] and was initially thought proof that SMA generated LQs from membrane bilayers in

a 'cookie-cutter' like fashion (i.e. with minimal lipid mixing during solubilisation), and therefore might retain asymmetric leaflet distribution during this process.

As LQ systems were known to have a higher lateral pressure over LUV systems,[98] it was thought beneficial to explore asymmetric LQs ('aLQs') as this increased lateral pressure could increase the half-life of asymmetry over aLUV systems. Particularly the short life-span of the sucrose entrapped aLUVs initially developed by London *et al.*

4.2 Materials & methods

4.2.1 aLUV generation

Asymmetric large unilamellar vesicles (aLUVs) were generated as described by London *et al.*[266] (Figure 4.1, A). Briefly, donor MLVs of the outer leaflet lipid mixture ***O*** (Table 4.1) were prepared by resuspension of dried lipid film (3 mg) in 0.5 mL 20 mM HEPES, 100 mM NaCl, pH 7.4 at 30°C for 30 minutes with gentle agitation. Donor MLVs were then incubated with an 8:1 (molar) ratio of MβCD:DMPC from a 0.69 M MβCD stock for 2 hours at 50°C with vigorous agitation.

Acceptor LUVs of lipid mixture ***I*** (Table 4.1) were resuspended in 0.5 mL of 27% sucrose, 20 mM HEPES, 100 mM NaCl, pH 7.4 at 30°C for 30 minutes with gentle agitation. The the lipid mixture was then subjected to 5× freeze-thaw cycles, and extruded through a 400 nm filter at least 11× to form LUVs.

For lipid exchange, acceptor LUVs were added to pre-mixed donor MLV-MβCD solution and incubated for 30 minutes at 50°C with vigorous agitation (500 rpm). Once finished, the solution was diluted with 9 mL of 4.5% sucrose prior to ultracentrifugation at 190,000 g at 10°C for 2 hours. The supernatant, containing donor MLV and free MβCD-lipid complexes was discarded. The pellet, containing the acceptor LUVs (now asymmetric, or aLUVs) was resuspended in 0.5 mL of chilled (4°C) 20 mM HEPES, 100 mM NaCl, pH 7.4 and used immediately. Samples were not heated above 4°C after centrifugation unless otherwise stated.

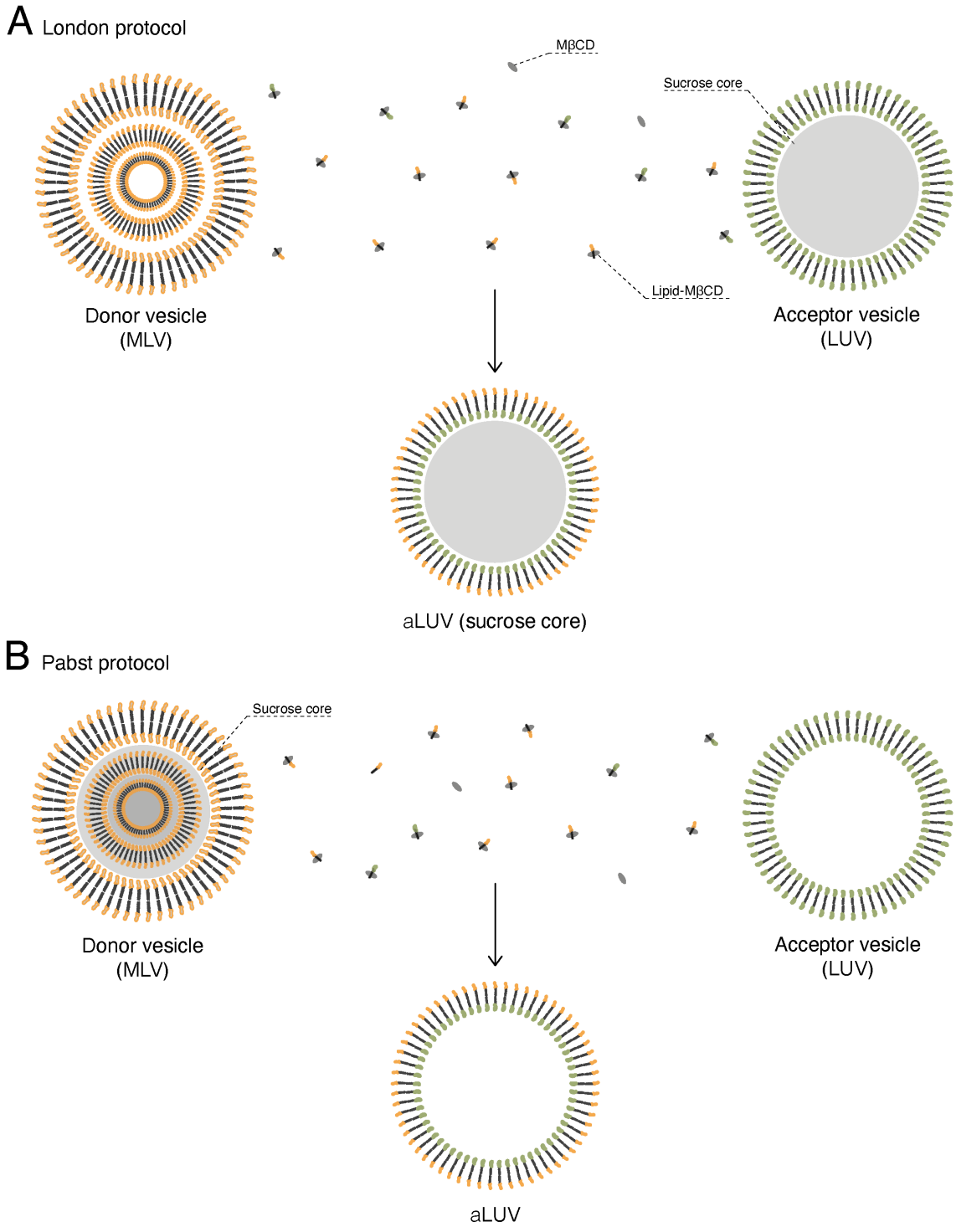


Figure 4.1: Method of asymmetric LUV generation through MβCD lipid exchange, showing (A) the initial protocol developed by London *et al.*[266] utilising a sucrose core within the acceptor LUV. This generates an aLUV with a sucrose core. (B) The modified protocol developed by Pabst *et al.*[119] which reversed the purification method, to require a sucrose core within the donor MLVs. This generates an aLUV with no sucrose core, and therefore has enhanced stability.

Table 4.1: Composition of outer (***O***) and inner (***I***) leaflet lipids used for aLUV measurements by FRET.

Sample Number	**Sample Name**	**Outer Leaflet** *O*	**Inner Leaflet** *I*
1	NBD-PE / DMPC	1% (molar) NBD-PE in DMPC membrane	DMPC membrane
2	Rho-PE / DMPC	1% (molar) Rho-PE in DMPC membrane	DMPC membrane
3	NBD-PE / Rho-PE	1% (molar) NBD-PE in DMPC membrane	1% (molar) Rho-PE in DMPC membrane
4	NBD-PE + Rho-PE / DMPC	1% (molar) NBD-PE + 1% (molar) Rho-PE in DMPC membrane	DMPC membrane

4.2.2 FRET & TR-FRET measurements

All FRET measurements were measured on a Perkin Elmer LS 55 luminescence spectrometer, with temperature control provided by a Haake K10 water bath, controlled by a Haake DC10 thermocouple. All measurements were recorded at 4°C, unless otherwise stated. aLUV FRET samples are shown in Table 4.1, with same buffer conditions as described previously. Samples were excited at 460 nm (NBD-PE excitation maxima) with an excitation/emission ratio of 5/2.5 and recorded between 470-650 nm with a scan speed of 40 nm/min.

For initial FRET with SMA 3:1 (as seen in Figure 4.2) solubilisation of aLUVs was performed with the addition of 1.5× (*w/v*) polymer from a 10% (*w/v*) polymer stock in 20 mM HEPES, 100 mM NaCl at pH 7.4 and incubated for 10 minutes at 4°C. Samples were then centrifuged at 30,000 g for 10 minutes (4°C). The supernatant, containing the LQ sample, was collected and immediately recorded.

Solubilisation was initially attempted at 4°C for the samples shown in Figure 4.3. However, sufficient solubilisation did not occur for DIBMA and PMA polymers

at this chilled temperature. Meanwhile, initial aLUV FRET experiments for SMA 3:1 showed loss of asymmetry with a 4°C solubilisation temperature - indicating that maintaining a 4°C temperature was not sufficient in halting lipid-mixing during solubilisation. Solubilisation of aLUVs was therefore performed with the addition of 1.5× (*w/v*) polymer from a 10% (*w/v*) polymer stock (in 20 mM HEPES, 100 mM NaCl at pH 7.4), followed by incubation for 5 minutes at 30°C. Samples were quickly cooled to 4°C, then centrifuged at 30,000 g for 10 minutes. The supernatant was collected and immediately recorded as 'initial nanoparticle formation' samples. NBD-PE/Rho-PE emission maxima ratios was calculated using Python,[207] through automatic peak maxima detection of the data through SciPy's *peak_finder* function within a specific range identified *via* visual inspection of emission spectra.

For the preparation of TR-FRET samples two nanoparticle were prepared per mixing experiment independently prior to mixing: Sample A ('high-FRET') consisted of a 1% (molar) NBD-PE and 1% (molar) Rho-PE lipid mixture, within 4.5 μmol of DMPC. Sample B consisted of just 4.5 μmol of DMPC. Between 0-5 minutes only sample A nanoparticles were recorded for baseline measurement, after which sample B nanoparticles were injected and recorded for a further 30 minutes. Each temperature point was recorded in triplicate.

TR-FRET measurements were recorded using 750 μL of 4.5 μmol lipid at 4, 20, 30 and 45°C. Samples were excited at 460 nm with emission recorded at 510 nm every 0.1 s. All samples were centrifuged at 30,000 g for 30 minutes to remove any unsolubilised membrane prior to measurement. Samples were incubated at the desired temperature for 5 minutes prior to measurement start, with the cuvette contents also being mixed during recording to ensure thorough mixing of solution upon injection.

Analysis of TR-FRET spectra was also performed using Python. Briefly, triplicate repeats were baseline corrected, converted to NBD-PE concentration using a NBD-PE concentration standard curve (performed separately, not shown). Repeats were then averaged before plotting, where the standard deviation was used for errors. For the rate of lipid mixing calculation, fluorescence minima (indicating injection

point) was identified by the function *trim* and the initial gradient of free NBD-PE generation was calculated using the *gradient_finder* function, using a specified range. Python scripts used for processing and plotting can be found on Github.[207]

4.2.3 NMR

All measurements were recorded on a Bruker 400 Hz machine, using the protocol developed within the Department of Chemistry for ^{1}H decoupled ^{31}P 1D NMR (pulse sequence zgpg30). 256 scans per measurement were taken, with a sweep width of 200 ppm. Measurements were calibrated to reference values using using Mestrenova (version 12.0.3) prior to plotting in Python.[207] All samples, unless otherwise stated, were prepared in 10% D_2O with a final buffer of 50 mM HEPES, 100 mM NaCl, pH 7.4 with a final lipid concentration of 14.77 μmol (10 mg of lipid). Mixed samples were incubated 30 minutes prior to measurement at 4°C, whilst measurements were recorded at 20°C due to constraints with cooling the NMR machine prior to use. Peak calibration was performed using a 50 μL, 100 mM Tetraphenylphosphonium chloride reference at 23.5 ppm.[268] Reference sample was recorded using a glass insert to prevent lipid binding, and suspended in 20 mM HEPES, 100 mM NaCl, pH 7.4.

4.2.4 Cytochrome oxidase c (CcO) and cardiolipin titration

Purification of CcO from yeast mitochondrial membranes

Purified yeast (*S.cerevisiae*) mitochondrial membranes within 50 mM Tris, 120 mM KCl, 2 mM EDTA at pH 7.0 was kindly supplied by Juan Escobar (Oxford Biochemistry teaching labs). 20 mL of purified mitochondrial membranes (20 mg/mL) in 50 mM Tris, 120 mM KCl, 2 mM EDTA at pH 7.0 was thawed, and 4 mL of 20% sodium cholate solution was added. The mixture was incubated at 4°C for 30 minutes with continuous stirring, after which 4 g of dehydrated ammonium sulfate was added incrementally, whilst ensuring the pH remained between 6.5 and 8.5. Once fully dissolved and within a stable pH range, the solution was incubated

overnight with continuous stirring, at 4°C. The solution was decanted after 12 hours and centrifuged at 12,000 g for 20 minutes (4°C). The supernatant was retained and 10% (*w/v*) dehydrated ammonium sulfate was added, again ensuring stable pH. This was stirred at 4°C for 45 minutes, prior to another round of centrifugation at 12,000 g for 20 minutes (4°C). The pellet was resuspended in 5 mL 250 mM sucrose, 50 mM Tris, 0.5% sodium cholate (*w/v*) at pH 7.0. Protein concentration (BCA assay) and specific activity was then determined.

Removal of endogenous cardiolipin

To remove the endogenous cardiolipin, to ensure reduced initial activity, CcO-cholate micelles required exchange into CcO-DDM micelles to allow for PLA2 digestion (as described by Robinson *et al.*[269]). CcO-cholate micelles were therefore slowly diluted to a final concentration of 1 mg/mL (CcO concentration) in 0.1% DDM, 100 mM KPO_4, pH 7.5. The solution was then stirred gently for at least 4 hours at 4°C. Free cholate micelles were then removed by two rounds of dialysis using a 50 kDa molecular weight cut off (MWCO) to a final dilution factor of at least a 1000×.

Once exchanged, digestion of endogenous lipids by PLA2 followed the protocol of Robinson *et al.*[269] CcO-DDM micelles were concentrated to a final concentration of 5 μM CcO as measured by Abs_{422} ($\epsilon_{422} = 1.54 \times 105\ M{-}1\ cm^{-1}$). PLA2 was then diluted to a final concentration of 10 μM and activated by the addition of Ca^{2+} (in the form of $CaCl_2$) to a final concentration of 10 mM. Endogenous lipid digestion was performed at room temperature for 2 hours with gentle agitation. 50 mM EDTA was then added to remove calcium ions and halt digestion. Dialysis using a 50 kDa MWCO with 2× 1 L 0.1% DDM, 100 mM KPO_4, pH 7.5 at 4°C was then performed, to a final dilution factor of 100×. Delipidated CcO was then spin-concentrated using a 50 kDa MWCO filter to approximately 1 mL, prior to a BCA and activity assay seen in Figure 4.9.

CcO insertion into membrane models

Once delipidation was confirmed by electron transport activity decrease (Figure 4.9), The CcO DDM (-lipid) sample was then inserted into proteoliposomes with a 200:1

POPC:CcO (molar) ratio. A cardiolipin-doped (+CL) lipid film was also generated with the same concentration of POPC and doped with 2% (molar) cardiolipin. To generate this, lipids (suspended in chloroform) were mixed and dried under nitrogen stream then held under high vacuum for at least 4 hours. For cardiolipin containing lipid mixtures, lipid films were either used immediately after drying, or were stored at -20°C, in the absence of light, in an inert nitrogen atmosphere. The POPC lipid film for CcO insertion was then resuspended in 1 mL 50 mM KPi, 50 μM EDTA, pH 7 at 30°C for at least 30 minutes with gentle agitation. The resulting lipid suspension was then subjected to 5× freeze-thaw cycles, and then extruded at least 11× through 400 nm polycarbonate filters to form POPC LUVs.

The POPC LUVs were then incubated with a 0.025% (*w/v*) DDM for 3 hours at 4°C. For CcO insertion, 0.5 mL CcO solution (of a concentration determined previously by BCA assay) was added and co-incubated for 1 hour at 4°C. Bio-Beads (Bio-Rad™) were added at a concentration of 0.3 g/mL (wet weight), and gently agitated overnight at 4°C. Bio-Beads were previously activated with methanol, followed a wash with dH_2O, and buffer equilibration with 50 mM KPi, 50 μM EDTA, pH 7. After overnight incubation, Bio-Beads were removed and proteoliposomes were pelleted through ultracentrifugation at 100,000 g for 3 hours at 4°C. Pelleted proteoliposomes were then resuspended in 0.2 mL 50 mM KPi, 50 μM EDTA at pH 7.

Preparation of CcO-LQs and Cadiolipin-doped LQs

To form CcO-Lipodisqs (CcO LQs (-CL)), 1.5×(*w/v*) SMA 3:1 was added to pelleted CcO-liposomes from 10% (*w/v*) stock solution (20 mM HEPES, 100 mM NaCl, pH 7.4) and incubated for 1 hour at 30°C, then 4°C for 2 hours.

To form cardiolipin doped Lipodisqs (LQs (+CL)) the lipid film of 100:2 POPC:CL was resuspended in 0.2 mL 50 mM KPi, 50 μM EDTA at pH 7 and incubated at 30°C for 30 minutes. The resulting MLVs were then similarly solubilised with 1.5×(*w/v*) SMA 3:1 from 10% (*w/v*) stock solution (20 mM HEPES, 100 mM NaCl, pH 7.4) and incubated for 1 hour at 30°C, then 4°C for 2 hours.

Both LQ samples (CcO LQs (-CL) and LQs (+CL)) were then centrifuged (30,000 g, 4°C for 30 minutes) and supernatant collected. LQs then underwent size exclusion chromatography (SEC), using a Superdex S200 increase column, to remove excess polymer. Fractions containing LQs (as determined by Abs_{280}) were pooled and spin-concentrated using a 50 kDa MWCO filter to a final volume of 0.6 mL.

Titration of CL into CcO-LQs

For the titration, a 0.1 mL aliquot of CcO LQs (-CL)(contained in only POPC lipid) was removed for concentration and activity assay use later. 0.5 mL of LQS (+CL) were then added to the remaining 0.5 mL CcO LQs (-CL) sample and co-incubated at 30°C for 2 hours. The mixed sample (now called 'CcO LQs (+CL)') was then cooled to RT prior to a concentration and activity assay. To maintain a visually similar activity rate, the 0.1 mL CcO LQs (-CL) aliquot was diluted with 0.1 mL 50 mM KPi, 50 μM EDTA at pH 7 and a concentration and activity assay was performed with the same approximate dilution as the mixed CcO-LQ sample.

BCA assay for protein concentration determination

A Pierce™ BCA protein assay kit (Thermofisher, catalogue number #23225) was used to determine CcO concentration for each activity assay attempt to obtain a comparable rate between samples. The assay was performed using the 'Enhanced Test Tube Protocol' values as stated in the kit. Each measurement required 45 μL of sample to 360 μL of 'working reagent' (WR), as used previously by C. Davies.[240] Samples were measured in triplicate and averaged for accuracy as recommended by kit instructions.

Activity assay of CcO by cyt.c absorbance shift

Activity assay followed a general procedure as described by C.Davies 2015.[240] Briefly, 250 μL of buffer (50 mM KPi, 50 μM EDTA, pH 7) was taken, to which 2 μL of cytochrome c ($cyt.c_{red}$), at 1 mM was added and a blank was taken of this mixture. Within a maximum of ten minutes of $cyt.c_{red}$ addition, 20 μL of sample (of an appropriate dilution to obtain a straight line) was performed. Measurement

of 500 nm was recorded for 600s, in 2s intervals. Decrease in absorbance at 550 nm was plotted by Python script, with plots starting at 1 AU for visual comparison. Rates were calculated using the initial gradient (after initial noise of sample mixing), between 20-200s, according to the Equation 4.1 first described by Miró *et al.*[269]

$$SA = \frac{(\Delta A^{550}/\Delta t) \times V \times 10^6}{P_{\text{total}} \times l \times \epsilon} \tag{4.1}$$

Where SA is the specific activity of CcO (nmol min^{-1}mg protein^{-1}) as defined by the change in absorbance of reporter protein cytochrome c at 550 nm (ΔA, AU) with an absorbance coefficient of 19.1×10^{-3} (ϵ, $\text{mol}^{-1}\text{cm}^{-1}$)[270] Δt is the time (in minutes) as it is oxidised by CcO (P_{total}, mg) in volume of solution (V, μL). An example of the analysis scripts used for rate calculation and plotting is available on Github.[207]

4.3 Results & discussion

4.3.1 Measurement of LUV and LQ asymmetry by FRET

Measurement of leaflet asymmetry in LUVs is now well established since the cyclodextrin-mediated generation protocol was first developed in 2012.[119, 266, 271] These measurement techniques generally rely on the different aqueous environment experienced by either leaflet, or by measurement of the zeta potential (ζ) of the outer leaflet.[271] Due to the entrapped volume within a liposome, it is relatively trivial to ascertain the level of asymmetry upon generation. The rates of mixing as lipid flip-flop occurs can also be measured through the use of fluoresence quenching, NMR spectroscopy, or small angle scattering (SAXS or SANS). [110, 119, 272]

However, for lipid-polymer nanoparticles both leaflets of the bilayer are accessible to the same aqueous environment. This presented a challenge for measuring overall nanoparticle asymmetry and the subsequent lipid mixing. As fluorescent labelled lipids were used previously by D. Yin 2016,[110] it was decided to continue this protocol, with modifications to measure asymmetry by FRET, rather than fluoresence quenching. FRET is able to act as a molecular 'ruler' as resonance transfer only occurs when two dyes are close together (within the Förster radius)

within approximately 10 nm.[273] As the thickness of a DMPC bilayer is known to be 4.45 nm (±0.03 nm),[162] it is therefore likely that some FRET may occur due to lateral diffusion of lipids within their respective leaflets, but this was hypothesised to be negligible and unlikely to be measurable. A second technique that utilised the same molecular measurement techniques, but instead using spin-spin exchange measured by continual-wave electron paramagnetic resonance (cw-EPR) was also trialed. This led to unsuccessful distinction between LUV or LQ sample, which may have been due to lack of sensitivity of the assay or the assay design itself (§C.2).

Initially two dye-lipid conjugates, Cy3-PE and Cy5-PE, were selected for the FRET labelled experiments. These dyes are a commonly used for FRET pairing, due to a high quantum yield (due to a high degree of spectral overlap) and were readily available to the lab.[274–276] However, as seen in Figure C.1, the Cy5 dye failed to perform within the LQ systems. Hence alternatives were found in the form of NBD-PE and Rho-PE (Figure 4.2).

Four leaflet orientations were examined in total (Table 4.1): NBD-PE / DMPC (***1***) and Rho-PE / DMPC (***2***) were designed as a single dye controls to obtain a baseline fluorescence (where '/' marks leaflet division). A sample of asymmetric NBD-PE / Rho-PE (***3***) was prepared, as well as a positive control of NBD-PE + Rho-PE / DMPC (***4***). If asymmetry is present in aLUVs, there should be a noticeable drop in FRET efficiency between the spectra of (***3***) and (***4***). Similarly, if asymmetry is present in the LQ sample, a similar difference should be obtained. If asymmetry is not present in LQ systems then both (***3***) and (***4***) should have similar spectra for LQ samples, but not for the aLUV samples.

Figure 4.2 shows the four samples as described in Table 4.1 for both LUV (solid line) and LQ (dashed line) systems. No major differences in the emission spectra of (***1***) and (***2***) could be observed in both (A) and (B), indicating that NBD-PE and Rho-PE were functional in both systems. The asymmetric sample (***3***, Figure 4.2 C) was initially interpreted to show that asymmetry in the aLUV system was retained in LQs as the distinctive two peaks for NBD-PE fluoresence and Rho-PE fluorescence for the LQ sample were observed (as observed in the aLUV sample).

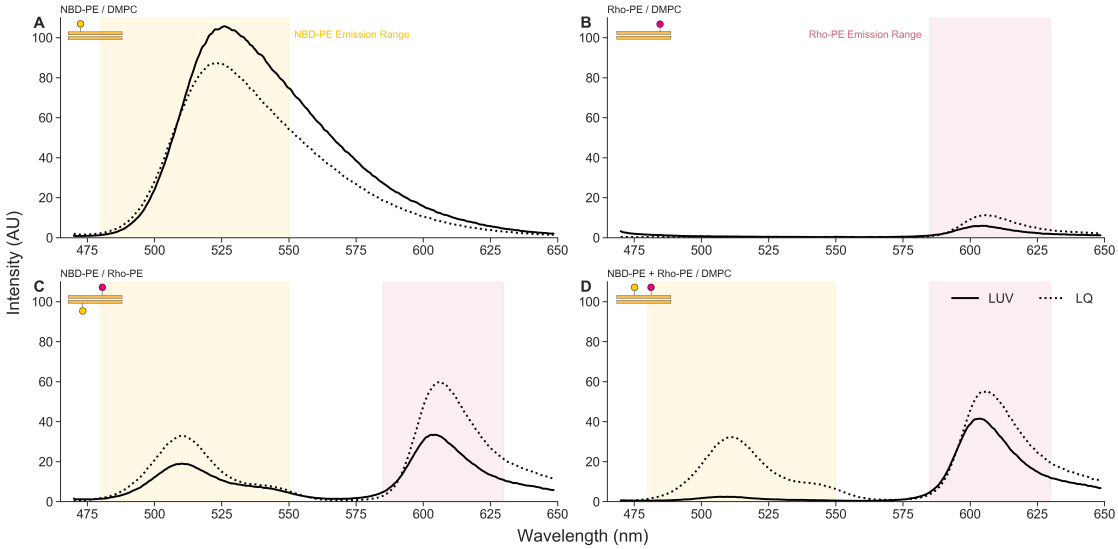


Figure 4.2: Fluorescence spectra for NBD-DLPE and Rhodamine-DLPE labelled lipids in aLUV and LQ systems. (A) NBD-PE / DMPC (***1***). (B) Rho-PE / DMPC (***2***). (C) NBD-PE / Rho-PE (***3***). (D) NBD-PE + Rho-PE / DMPC (***4***). Where / denotes change in leaflet. All samples were prepared to 1% (molar) dye-lipid to DMPC. NBD-PE excitation (A,C,D) = 460 nm, Rho-PE excitation (B) = 560 nm

The double peak indicates the excited NBD-PE dye was unable to transfer sufficient excess energy to the Rho-PE dye (i.e. FRET), indicating that the dye pair were too distant (>10 nm). This could be interpreted as LQ sample ***3*** being asymmetric.

However, the positive control for FRET, ***4***, (Figure 4.2 D) indicated that the observed asymmetry in Figure 4.2 C was actually due to the difference in LQ nanoparticle size, and the number of lipids per particle affecting FRET efficiency. Single LQ particles possess a relatively small collection of lipids (~200), [98] compared to the large collection of lipids in LUVs (>10,000). It is therefore possible that there were distinct populations of single dye particles, mixed particles and possible asymmetric particles during measurement. Whilst some of these mixtures would have been able to undergo FRET, there would inevitably be a population of NBD-PE only particles that would be unable to transfer the excitation to Rho-PE only particles. This could have skewed the resulting spectra to show the falsely-asymmetric LQ system observed in Figure 4.2 C. It is unclear therefore whether the similarity of Figure 4.2 C and D was due to loss of asymmetry, or the difference in particle size.

Around the same time as the experiment was performed, a publication by Keller

et al. showed that SMA 3:1 bound nanoparticles (SMALPs) undergo rapid lipid mixing through nanoparticle collision.[262] The results of D. Yin (2016) indicated this may not occur in LQ systems, indicating there may be a difference in stability between SMALPs and LQs. It was then hypothesised that the leaflet mixing would occur at a slower rate (if at all) for LQ systems due to a difference in polymer length and length distribution.

A variant of the previous FRET assay was developed, utilising aLUV solubilisation, to estimate the rate of lipid mixing during nanoparticle formation and in solution. If the mixing observed in Figure 4.2 occurs in other nanoparticle systems it would suggest either a loss of asymmetry by all polymer based nanoparticles, or the possibility that nanoparticle size was a major factor in the change of FRET efficiency of the assay. Alternatively, if the similarity of Figure 4.2 C and D is not observed in other polymer systems, it suggests that asymmetry is lost during solubilisation of aLUVs by the LQ form of SMA 3:1, as shown by Keller *et al.* for SMA 3:1 SMALPs.[262]

From measuring the emission maxima of NBD-PE and Rho-PE for asymmetric samples and the mixed control, and by plotting the FRET efficiency ($\frac{NBD-PE_{\mathrm{Em}}}{Rho-PE_{\mathrm{Em}}}$) it was possible to estimate the asymmetry of the sample. From this it is possible to elucidate when asymmetry is lost; either during nanoparticle formation or whilst in solution.

Two samples, ***3*** and ***4***, were again generated and measured across four timepoints were analysed to understand whether asymmetry might be lost in nanoparticle formation, or during storage. Firstly, an initial measurement of the individual aLUV samples to be solubilised were recorded at 4°C, a secondary measurement was recorded after solubilisation of the aLUV samples by their respective polymer as described in §4.2.2. The samples were then incubated at 4°C overnight before a third recording. Prior to the fourth recording, both the 'asymmetric' sample and mixed control were sonicated at 60°C for 30 minutes to ensure full asymmetry loss if retained. These timepoints therefore capture the full 'life-cycle' of a nanoparticle from first formation, through to long term storage at 4°C and then a positive

mixed control. In addition, by using FRET efficiency over the full spectral plot, it is possible to show these time points for the four polymers types in a concise manner, with negligible loss of detail.

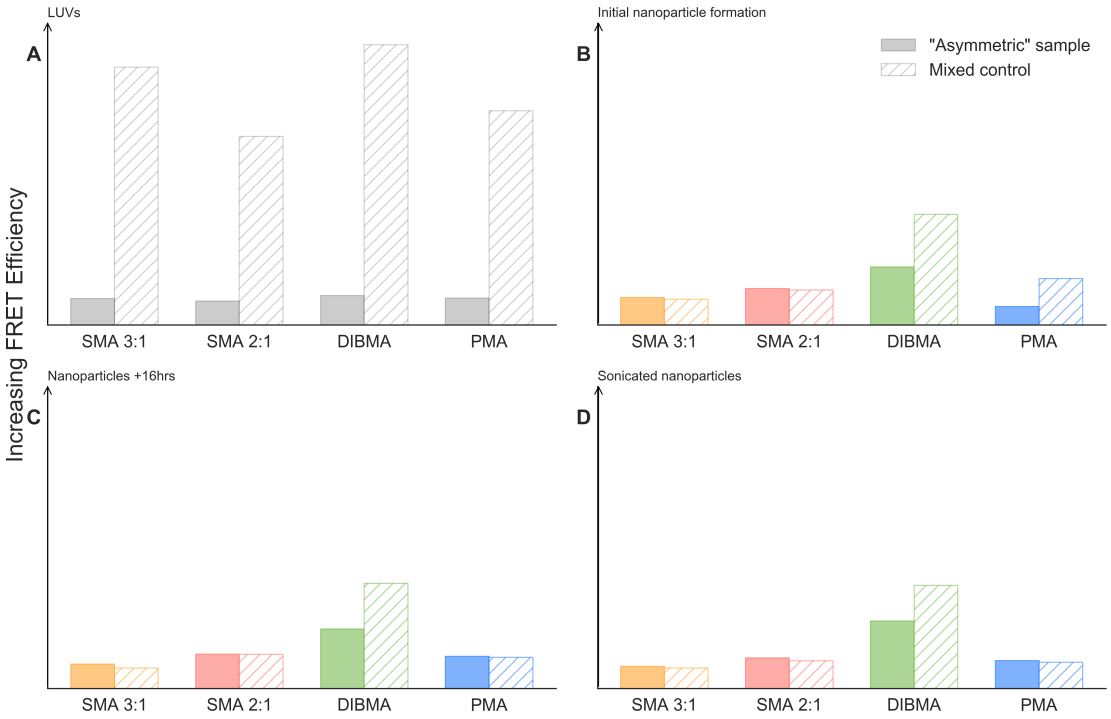


Figure 4.3: FRET efficiency of NBD-PE and Rho-PE labelled lipids in aLUV and polymer nanoparticles. Showing 'asymmetric' sample (solid colour) of NBD-PE/Rho-PE and mixed control (hatched colour) of NBD-PE + Rho-PE / DMPC. (A) aLUVs generated through the London *et al.* protocol (B) Initial nanoparticles generated from aLUV samples after 5 minutes solubilisation at 30°C. (C) Nanoparticles generated from aLUVs stored overnight at 4°C post solubilisation. (D) Nanoparticles generated from aLUVs that were sonicated for 15 minutes in water bath at 60°C.

Figure 4.3 shows the stark difference observed between the FRET efficiency of samples for aLUVs (Figure 4.3 A) and for nanoparticles (Figure 4.3 B-D). The large difference in efficiency observed between the asymmetric samples and the mixed control in aLUVs is lost when solubilised by any polymer. This implies that asymmetry is lost upon nanoparticle formation. There was a slight difference, however, between the polymer samples. SMA variants showed no difference between the 'asymmetric' sample and the mixed control, while there was a significant difference in FRET efficiency observed for the DIBMA and PMA polymers. This suggested that the rate of lipid mixing varied between polymer type.

However, whilst the difference between the asymmetric sample and the mixed control implies DIBMA did not undergo this lipid mixing (Figure 4.3 B,C), the height difference between the two samples was consistent for all nanoparticle time points, including after sonication. This indicates that the DIBMA sample is fully mixed at the time of initial formation, and the difference observed is an artefact from solubilisation. In addition, the mixed control sample used for DIBMA (Figure 4.3 A, 3rd from left) showed a particularly high FRET efficiency compared to the other samples, which may have been exacerbated by DIBMA solubilisation.

The difference observed for PMA's initial solubilisation for the mixed control sample varies over time, with the difference in FRET efficiency being removed completely after overnight storage (Figure 4.3 B vs C). Whilst this change is observed in only the mixed control, the change over time does indicate that some form of dynamic process was occurring in PMA nanoparticles, even at cooler temperatures.

These data imply that any lipid spatial order, such as asymmetry or even lateral order within leaflets, is therefore lost during lipid-polymer nanoparticle formation; or soon after formation in solution. It was clear through comparing SMA variants to PMA that the rate of mixing is vastly different between polymer types. And further publications from Keller *et al.* also showed that the rate of mixing is dependant on factors such as buffer and nanoparticle charge.[277] It was therefore decided to again use the FRET between NBD-PE and Rho-PE to measure the mixing of lipids within the lipid-polymer nanoparticles. In particular, it was decided to quantify the rate of lipid mixing for SMA 3:1, SMA 2:1, DIBMA and PMA nanoparticles. The kinetic experiments were performed at 4, 20, 30 and 45°C to understand if temperature was a factor in collisional lipid mixing.

4.3.2 Kinetics of lipid mixing by TR-FRET

The lipid mixing rate was estimated to be extremely fast both due to preliminary experiments (such as those in Figure 4.3), and inferred from results from Keller *et al.* for SMALPS.[262] The NBD-PE/Rho-PE FRET pair was still used for measurement, but instead only the NBD-PE emission maxima at 510 nm was recorded. For the

new assay two samples were generated: A 'high-FRET' sample of NBD-PE+Rho-PE nanoparticles (***3***) and a sample of just DMPC-polymer nanoparticle. Firstly, the 'high-FRET' sample was incubated at the desired temperature, and the NBD-PE emission was recorded. After 5 minutes, a second sample was then added, containing pure DMPC nanoparticles (of equivalent molarity). By having two nanoparticle samples mix as described in §4.2.2 it is possible to measure the rate of lipid mixing through dilution of FRET dye pairs. Using the donor excitation as measure of FRET (as when FRET occurs, donor emission decreases as energy is transferred to the acceptor), one can estimate the rate of mixing through the increase in donor emission. As dye-lipids are diluted through the mixing of 'high-FRET' and DMPC-polymer nanoparticles, the average distance between FRET pairs increases, reducing FRET efficiency, and generating [D] and [A] from [DA] (Equation 4.2). The rate of [D] increase, as measured by NBD-PE emission, can therefore be used to estimate the rate of lipid mixing (Equation 4.3).

$$[\mathrm{DA}] \underset{k_2}{\overset{k_1}{\rightleftharpoons}} [\mathrm{D}] + [\mathrm{A}] \tag{4.2}$$

where:

$$k_1[DA] = \frac{\Delta[D]t}{\Delta t} \tag{4.3}$$

For the these experiments an initial recording for 5 minutes of sample A (the 'high-FRET' sample) was taken, after which an equimolar amount of sample B (DMPC-SMA 3:1 nanoparticles) were added. If lipid mixing occurs one would expect the concentration of unpaired NBD-PE to increase with time, as the average distance of NBD-PE and Rho-PE FRET pairs increases beyond the Förster radius. The rate of this increase would be directly proportional to the rate of lipid mixing (Equation 4.3).

Figure 4.4 showed that SMA 3:1 nanoparticles underwent lipid mixing for all temperatures tested, even at a chilled temperature of 4°C. This was to be expected

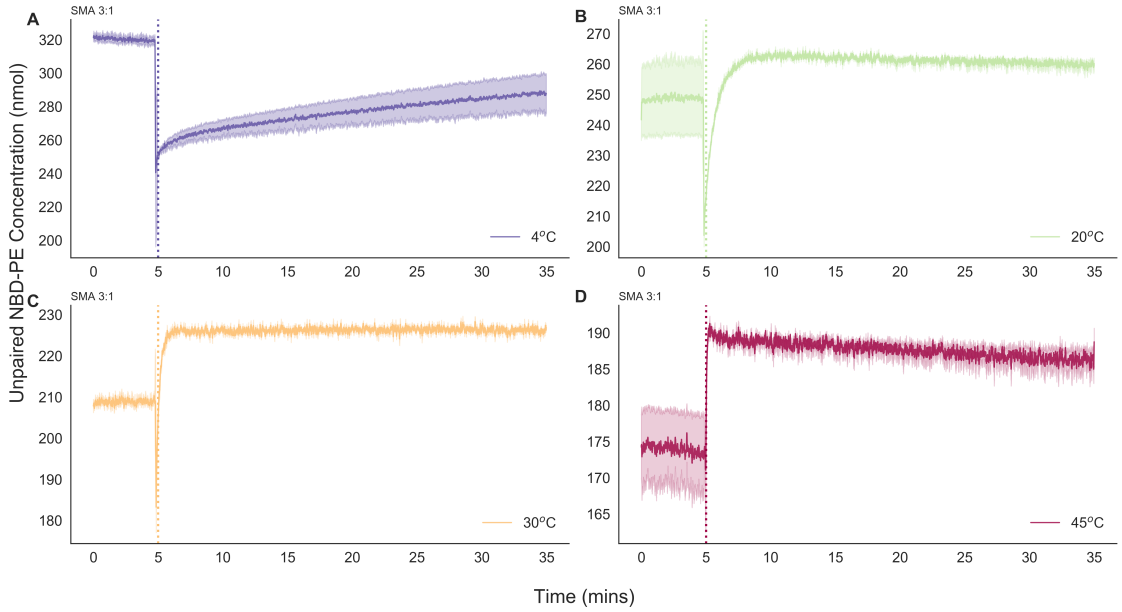


Figure 4.4: Rate of lipid mixing shown through NBD-PE emission at 510 nm for SMA 3:1 nanoparticles across a temperature range of 4°C (A), 20°C (B), 30°C (C) and 45°C (D). Shaded area indicates standard error (n=3)

from the results from Figure 4.3 and Figure 4.2, as all LQ samples for SMA 3:1 showed a loss of asymmetry 5 minutes after solubilisation - even when nanoparticle formation was undertaken at 4°C. The relationship between temperature and the rate of lipid mixing was also strongly correlated, as 4°C shows a slower rate of NBD-PE unpairing than 20°C and likewise for the higher temperatures. The rate of lipid mixing, calculated by the initial rate of NBD-PE generation after injection of sample B are shown in Table ?? and show a linear progression of lipid mixing rate with temperature, with the exception of 4°C which appears to be only slightly lower than the rate measured at 20°C. This change in rate may be caused by either the fluidity of the DMPC lipid changing between 4°C and 20°C, or due to a significantly lower collisional speed at cooler temperatures affecting lipid mixing upon collision.

At this point, it was hypothesised that the excess polymer often introduced to aid complete solubilisation would affect the rate of lipid mixing. It is known from Keller *et al.* comparing SMA 2:1 and SMA 3:1 nanoparticle mixing rates, that the relative charge of a nanoparticle affects the rate of lipid mixing, with a higher net charge resulting in faster mixing rates.[277] It follows that if there is

Table 4.2: Comparison of free NBD-PE generation through lipid dilution caused by particle collision in solution across different temperatures for DMPC-SMA 3:1 nanoparticles.

Temperature	Free NBD-PE Generation Rate nmol/min	Std. Dev nmol/min
4°C	0.592	±0.10
20°C	0.805	±0.02
30°C	1.509	±0.03
45°C	2.840	±0.30

excess polymer adhering to particles in solution and adding to a particles overall charge, the rate of mixing would be higher than of particles without this excess polymer. To test this, size exclusion chromotography (SEC) was performed on a set of sample A and B particles for SMA 3:1 nanoparticles to remove the excess polymer required for solubilisation. The measurements were then performed in the same manner described in §4.2.2 and resulted in Figure 4.5. For simplicity it was decided to initially measure only at 4°C.

Removal of excess polymer by SEC did appear to reduce the rate of lipid mixing (Figure 4.5). However, SEC only reduced the rate by around half of what is seen in non-SEC nanoparticles, and does not halt the mixing entirely.

Additionally, due to the rate of mixing for SMA 3:1 being so high even at 4°C it is likely that any LQ sample undergoing SEC would fully mix before sample injection, let alone during the later purification and concentration steps. The mixing rate of the SEC sample may also be lower in purified samples due to a difference in concentration due to some nanoparticle loss during the extended sample preparation required. It was initially assumed that no nanoparticles were lost during SEC, and this was confirmed by visual inspection of fractions for dyed nanoparticles in sample A. However when measured by fluorimetry, the initial starting concentration of nanoparticles after SEC was ~270 nmol, whilst without SEC the average concentration was ~320 nmol. The percentage variation

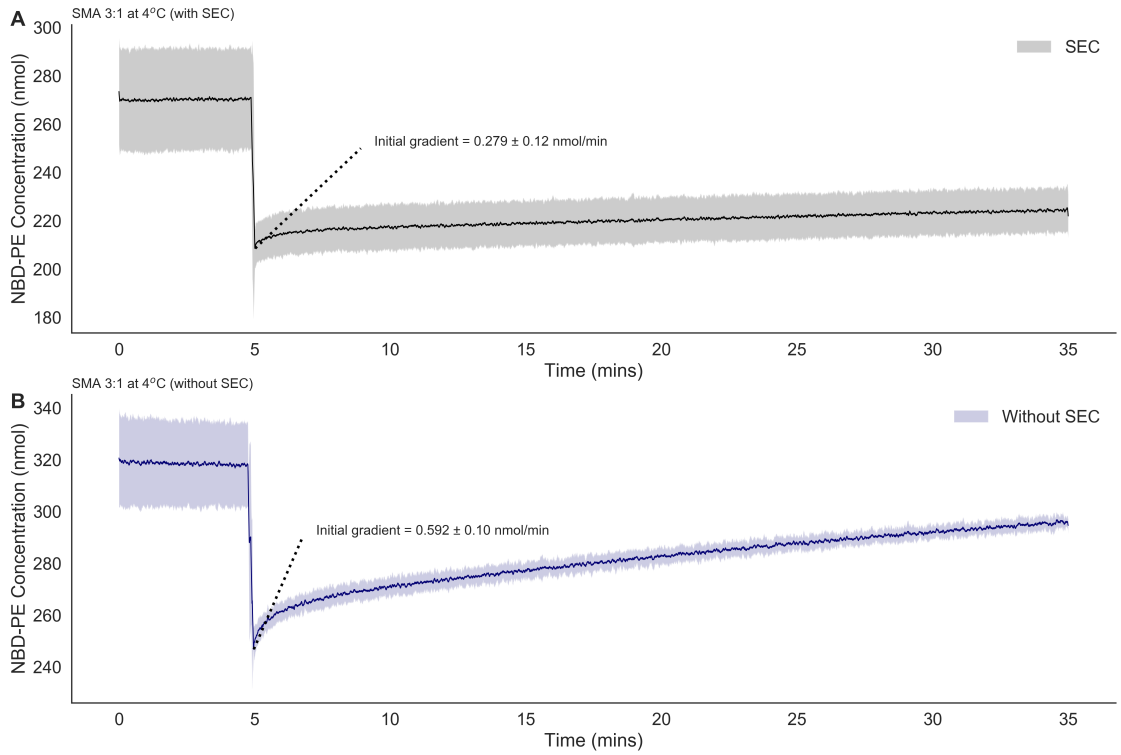


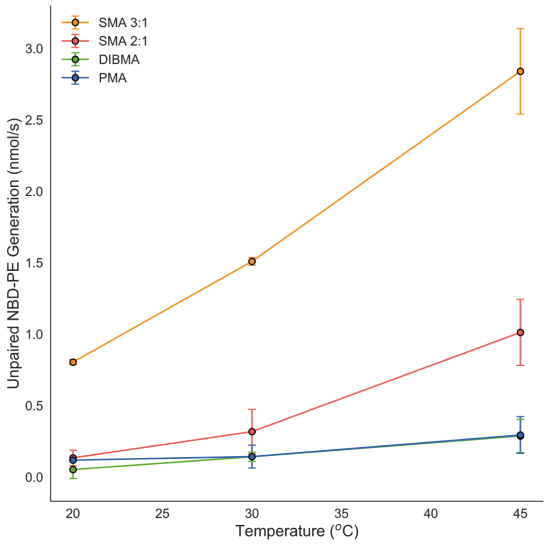
Figure 4.5: Rate of lipid mixing as measured by TR-FRET for SMA 3:1 nanoparticles with excess polymer removed by SEC (A), and without (B). Mixing rate measured at 4°C. Shaded area indicates standard error (n=3)

in concentration was relatively small, but would naturally factor into the difference in rates observed in Figure 4.5.

Further experiments to assay the lipid mixing of SMA 2:1 (Figure C.6), DIBMA (Figure C.7) and PMA (Figure C.8) were generated. These were performed in the same manner as seen in Figure 4.4 and therefore are supplied in the appendix (§C.4), a summary of which can be seen in Figure 4.6.

The data shown in Figure 4.6 summarises the data collected for SMA 3:1 (Figure 4.4), SMA 2:1 (Figure C.6), DIBMA (Figure C.7) and PMA (Figure C.8). Rates were calculated from all temperatures above 4°C as all polymers (aside from SMA 3:1) showed insignificant mixing. The lack of mixing observed at 4°C was most likely due to an issue with assay sensitivity at these temperatures, as aLUV solubilisation assays showed mixing at this temperature over a longer time period (Figure 4.3).

The most startling difference between polymers was that SMA nanoparticles mix at a faster rate than both DIBMA or PMA. SMA 3:1 was the fastest mixing



Polymer	Temperature (°C)	Generation Rate (nmol/s)	Error (nmol/s)
SMA 3:1	20	0.805	0.018
	30	1.509	0.027
	45	2.84	0.299
SMA 2:1	20	0.134	0.054
	30	0.318	0.156
	45	1.012	0.231
DIBMA	20	0.052	0.064
	30	0.142	0.032
	45	0.288	0.115
PMA	20	0.118	0.003
	30	0.143	0.080
	45	0.294	0.129

Figure 4.6: Rate of lipid mixing as measured by TR-FRET of lipid-polymer nanoparticles for SMA 3:1 (orange), SMA 2:1 (red), DIBMA (green), and PMA (blue) for three temperatures: 20°C, 30°C, and 45°C.

polymer nanoparticle, generating twice as much unpaired NBD-PE than SMA 2:1 at the same temperature (2.840 nmol/s for SMA 3:1 *vs* 1.012 nmol/s for SMA 2:1 at 45°C). This was significantly lower than the fourty-fold higher mixing rate by SMA 3:1 than SMA 2:1 observed by Keller *et al.*[277] However, this may be due to differences in polymer composition (SMALPs vs LQs), as well as limitations in the assay design in this thesis leading to insufficient mixing during injection. Overall, all polymers showed measurable mixing of lipids at and above 20°C and these rates broadly increased linearly with temperature.

With all available polymers showing lipid mixing as observed in SMA 3:1 nanoparticles, collisional lipid transfer can therefore be said to be a consistent property of all lipid-polymer nanoparticles. All polymers destroy asymmetry in aLUVs during solubilisation, or shortly after even when stored at 4°C and this rate can be measured by TR-FRET. It appeared that the rate of this mixing is variable by temperature changes. SMA 3:1 nanoparticles (LQs) showed that removal of excess polymer, and therefore additional charge per nanoparticle, appears to reduce this mixing but not completely halt this process. This implies that any extracted membrane protein within these systems would not be in a native, asymmetric environment in these polymer nanoparticles. This could have an affect on protein

stability or native-like function, as membrane asymmetry is destroyed, and co-localised lipids are transferred between nanoparticles over time.

However, collisional lipid transfer is not the only method of lipid transfer between particles, another (minor) component of mixing is inter-particle diffusion through the aqueous phase by lipid monomers. This spontaneous effect, first described by Nichols *et al.* for NBD-DLPC, states that the rate of lipid monomer diffusion is dependant on the critical bilayer concentration (cbc) of the lipid in question, as well as the packing of lipids within the bilayer.[278, 279] The cbc is in turn affected primarily by the hydrophobicity of the lipid, with fluorescent dyes being significantly more likely to undergo this spontaneous diffusion due to the addition of a large hydrophillic fluorescent group. Overall, the tighter packing of lipids within lipid-polymer nanoparticles would decrease this rate somewhat, but fluorescent reporter molecules -such as NBD-DLPE, used in the fluorimetry assays in this thesis- would be subjected to a potentially significant amount of mixing from this monomer diffusion. To confirm whether the mixing reported is solely due to the diffusion of reporter molecules in solution, a non-labelled assay was devised using solution state NMR.

4.3.3 Unlabelled lipid mixing as measured by NMR

To ensure lipid mixing reported through FRET was not a product of dye-lipid monomer diffusion, a label-free measurement technique was performed. Due to naturally occurring phosphorus (^{31}P) possessing a non-zero spin in a magnetic field, it is possible to measure non-labelled lipids through NMR spectroscopy alone. Two nanoparticles were prepared with different lipids: DMPC and DMPG. PG head groups, due to the negatively charged -OH groups of the glycerol, are more shielded than the uncharged DMPC. This difference in electron density between PC and PG lipids gives two different chemical environments for PC and PG, which can be observed as a difference in chemical shift in NMR spectra. Similarly, the chemical shift of these lipids can be affected by changes in the local chemical environment, such as the presence of a different lipid.[280] This chemical shift allows for the measurement of lipid mixing during a titration of PC-only nanoparticles

to PG-only nanoparticles. Through the measurement of the δ shift ($\Delta\delta$) across this titration it is possible to plot a standard curve of PC:PG ratio. Through the use of known mixtures of PC:PG and the formation of this standard curve, it is possible to accurately measure the relative quantity of -PG lipids in -PC nanodiscs and *vice versa* by the peak shifts of the mixing nanoparticles. As DMPG lipids are more acidic than DMPC lipids, pH measurements of all titration and samples used were also measured, with pH measurements being taken pre- and post- mixing. These showed no significant pH change between DMPG and DMPC (Table C.2), indicating that the ppm shifts observed in Figure 4.7 are due solely to local chemical environment changes.

Figure 4.7 shows the chemical shift between 100% DMPC (0.060 ppm) and 100% DMPG (1.230 ppm) Lipodisqs had an average $\Delta\delta$ of 1.170 ppm. This relatively large difference allows for an accurate titration of different PC/PG nanoparticles to obtain a standard titration curve. A titration of 0, 25, 50, 75 and 100% PC:PG was generated, and can be seen in Figure 4.7 B-F. As can be observed, both the PC and PG peaks appeared to move towards each other as the relative concentrations increase. For PC lipids this was seen as a steady increase in ppm from 0.060 ($\pm$0.006) ppm at 100% PC, to 0.154 ppm ($\pm$0.004) at 25% PC. This 0.094 ppm difference showed a significant local environment change that can only be explained by the effect of the electron shielding from the presence of a more negative lipid in the leaflet, i.e DMPG. Likewise, a decrease in ppm of DMPG lipids from 1.230 ppm ($\pm$0.000) at 100% to 1.153 ppm ($\pm$0.000) at 25%, was observed.

Through plotting the pre-mixed standards of a known PC:PG concentration it is possible to determine the amount of lipid mixing that occurred between the DMPC-LQ and DMPG-LQ samples (shown as 'Sample' in Figure 4.7 A). It is then possible to plot the average ppm of the sample onto the titration curve to estimate the concentration of DMPC:DMPG in the sample. The results of this can be seen in Figure 4.8.

There was a good agreement between the pre-mixed standards, showing a linear change of ppm as concentration was changed. There was a slight bowing of PC

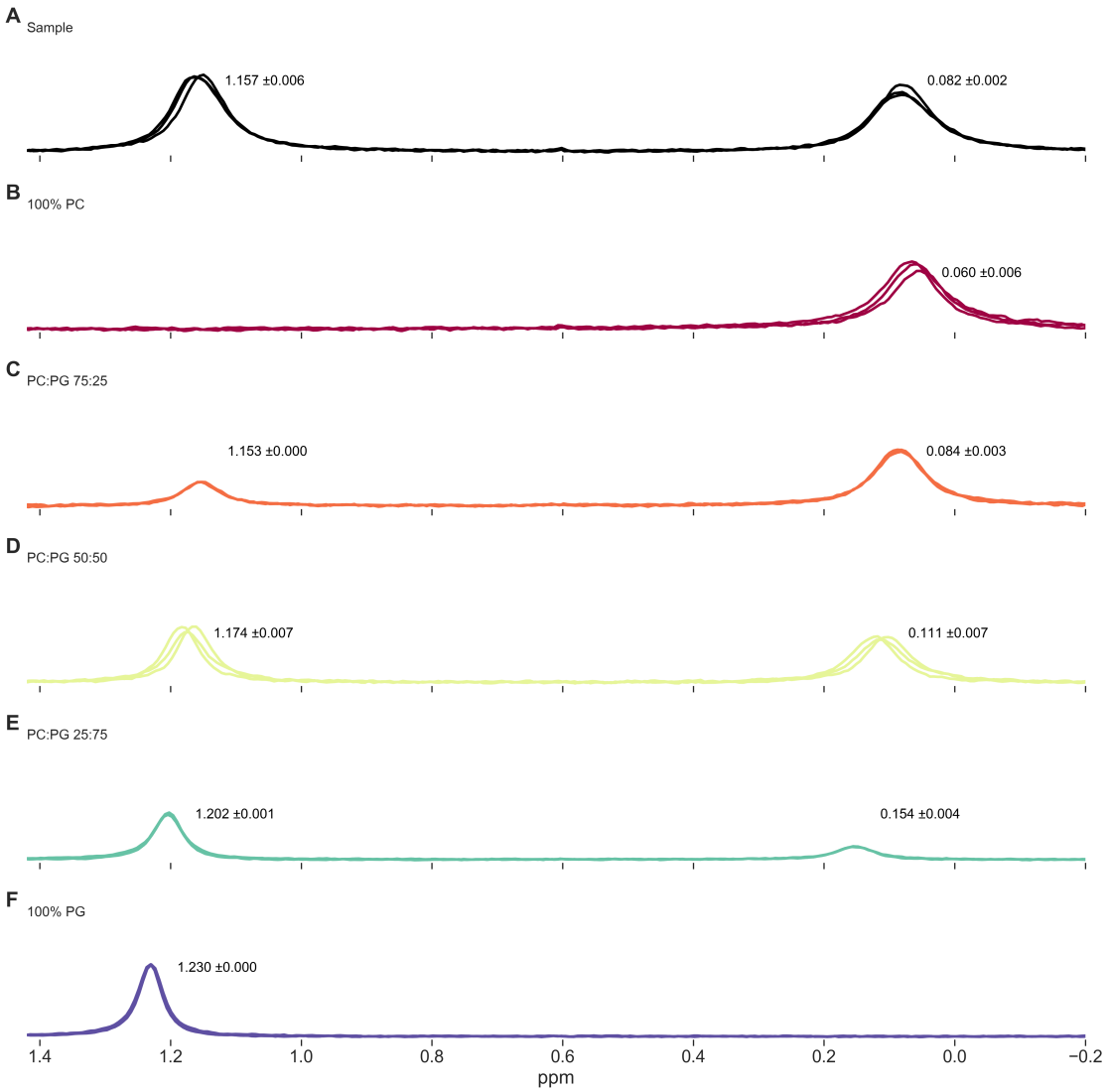


Figure 4.7: ^{31}P solution NMR spectra of SMA 3:1-DMPC and SMA 3:1-DMPG nanoparticles showing (A) Sample of DMPC-LQ and DMPG-LQ, and pre-mixed DMPC:DMPG titrations of (B) 100% DMPC LQs, (C) 75:25 DMPC:DMPG LQs, (D) 50:50 DMPC:DMPG LQs, (E) 25:75 DMPC:DMPG LQs, and (F) 100% DMPG LQs. Values given are average (n=3) peak maxima δ in ppm, with error given from standard deviation.

peaks below the expected linear decrease during this titration, which could be due to the PC peaks undergoing peak broadening as PG lipids are introduced (Figure 4.7). The sample peaks (Figure 4.8 A,B, shown in grey), showed an approximate 70:30 PC:PG mixing ratio of DMPC and DMPG nanoparticles. Similarly, comparing the integrated peak area (Table C.2), to give an estimate of molar ratio, showed that there is on average a 1:1 ratio of PC:PG within the solution, indicating that

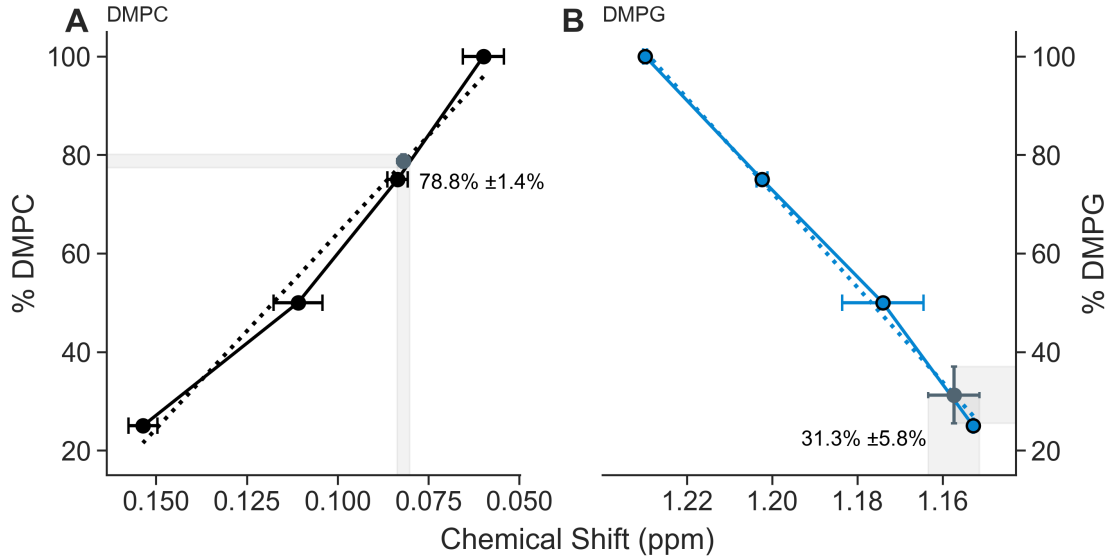


Figure 4.8: Lipid mixing of SMA 3:1-DMPC and SMA 3:1-DMPG nanoparticles as measured by ^{31}P NMR, showing DMPC (A) and DMPG (B) titration curves of pre-mixed standards. Average sample peak measurements (n=3) are shown in grey, with standard deviation shown in ppm. Error of % DMPC or DMPG are calculated by converting known ppm into % via the gradient of the line.

there was no significant difference in DMPC or DMPG molarity in the sample. This implies that the mixing rate of 70:30 PC:PG was an accurate representation of the mixing ratio within the solution. This is quite a significant difference from what would be expected of a fully mixed sample, which should be around 50:50. This indicated that incubation for 30 minutes at 4°C was not sufficient for full lipid mixing of LQs. 30 minutes of incubation was chosen as it was the same length of time for TR-FRET measurement, allowing for a comparison between the short term rate calculation as seen in Figure 4.5, and a measure of the level of mixing at the 'end-point'. A mixing level of 70:30 is in line with the data shown in the TR-FRET equivalent of this NMR data (Figure 4.5 B). At 30 minutes the NBD-PE used to measure the rate of mixing had not stabilised, indicating that mixing was still occurring at time of NMR measurement. However, the large difference in lipid concentration of both the TR-FRET (6 mg/mL) and the NMR (20 mg/mL) experiment may affect the mixing rate, making direct comparison difficult.

Lipid mixing through nanoparticle collision is therefore the major form of lipid mixing measured in this chapter. Furthermore, collisional lipid mixing seems to be

Table 4.3: Summary of DMPC and DMPG ^{31}P NMR spectra for both standards and SMA 3:1 sample.

Spectra Composition	**PC δ_P (ppm)**	**PC error (ppm)**	**PG δ_P (ppm)**	**PG error (ppm)**
Sample	0.082	±0.002	1.157	±0.006
100% PC	0.060	±0.006	-	-
PC:PG 75:25	0.840	±0.003	1.153	±0.000
PC:PG 50:50	0.111	±0.007	1.174	±0.007
PC:PG 25:75	0.154	±0.004	1.202	±0.001
100% PG	-	-	1.230	±0.000

a specific property of lipid-polymer nanoparticles, with varied rates depending on the exact polymer structure and charge. Whilst the rate can be slowed through lowering the sample incubation temperature (Figure 4.6), as well as buffer ionic strength,[277] it is unlikely that it can be halted indefinitely. Whilst this may raise issues on the stability of nanoparticles, and the subsequent resolution of lipidomics due to this mixing in solution, the dynamic nature of these nanoparticles may lead to more possibilities of interchange between polymer based and other membrane model systems.[281, 282]

The lipid mixing property of lipid-polymer nanoparticles has, so far, only been portrayed as a negative property of these systems. Whilst it is true this mixing destroys a previously positive view of the stability of these particles, and their ability to extract membrane proteins within their native environment, the ability to have dynamic lipid exchange without the need for the use of detergents is a powerful tool.

Whilst extraction and examination of membrane lipids have proven useful for the exploration of lipidomics using these nanoparticles in recent years,[183, 186, 189, 283] the new dynamic nature of the nanoparticles could, in theory, allow for a more active approach to understanding the protein-lipid interactions. The ability to introduce exogenous lipids, or remove endogenous ones, could allow for a simpler experimental

design to understand how specific protein-lipid interactions affect protein function, without any introduction of denaturing detergents or organic solvents. It was hypothesised that the well characterised dependance of cytochrome oxidase c (CcO) on cardiolipin (CL) for electron transport activity would be a suitable test-case. In the following section, it is demonstrated that the lipid exchange within lipid-polymer nanoparticles can have a relevant use for researching the interdependence of proteins and lipids in membrane biology.

4.3.4 Titration of cardiolipin into CcO-Lipodisqs

One of the most well characterised example of protein function being affect by lipid presence is the dependence of cytochrome oxidase c (CcO) on cardiolipin (CL). It is known that CcO possess at least two distinct binding sites for CL, without which the electron transport activity of CcO is roughly halved.[92, 97] However, complete removal of cardiolipin does not ablate electron transfer.[284] To ascertain whether the dynamic property of lipid-polymer nanoparticles can be used to titrate in specific lipids, a simple model of lipid-protein interaction is necessary. The properties of CcO make it an ideal candidate to determine whether a specific lipid can be titrated into nanoparticles. Through the removal of endogenous CL, and then reintroduction of CL through LQ exchange there should be a clear difference between CL-deficient (-CL) and CL-loaded (+CL) CcO electron transfer activity. Ideally showing a recovery of the original activity rate to endogenous CL levels as measured by the rate of electron transfer by CcO in native mitochondrial membranes.

Examination of CcO electron transfer activity is easily measured by the use of a reporter protein, cytochrome c. This protein is normally found within mitochondria and is oxidised by CcO as part of the electron transport chain during mitochondrial respiration.[285, 286] A simple assay can be performed to measure the oxidation of reduced cytochrome c ($cyt \cdot c_{red} \longrightarrow cyt \cdot c_{ox}$) by a decrease in absorbance at 550 nm as the heme iron converts from the ferric to ferrous form ($Fe^{3+} \longrightarrow Fe^{2+}$).[284, 287] If the concentration of cytochrome c_{red} is known, as is the concentration of

CcO, then a rate of specific protein activity can be obtained by the change in absorbance over time, shown in Equation 4.1.

Delipidation of endogenous cardiolipin was initially attempted by washing of CL by a 1000× molar excess of DMPC as previously performed by Watts *et al.*[284] However, due to the amount of CcO required for the multi-step protocol, the resulting DMPC concentration required affected purification attempts *via* ammonium sulfate precipitation. Endogenous lipids were instead digested with phospholipase A2 (PLA2), using a previously published protocol by Robinson *et al.*[269] However it was important to ensure digestion by PLA2 of all endogenous lipids. This required CcO in DDM micelles, as cholate micelles was found to negatively affect lipid digestion by PLA2.[269] A full protocol for CcO extraction, delipidation and LQ insertion can be found in §4.2.4.

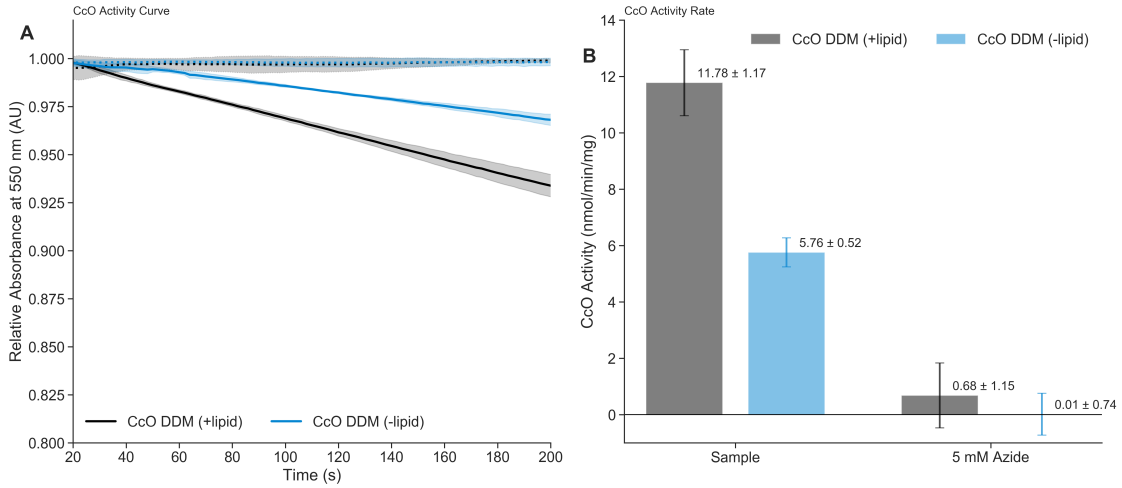


Figure 4.9: Activity of cytochrome oxidase c (CcO) as measured by the reduction of cytochrome c (Abs_{550}). (A) Relative absorbance change over time of CcO DDM (+lipid) (grey) and delipidated CcO by PLA2 digestion, CcO DDM (-lipid) (blue). Negative control using 5 mM Sodium Azide (a known CcO specific inhibitor) is seen as a dotted line version of respective sample colours. (B) Specific activity of CcO DDM (+lipid) (grey) and PLA2 digested CcO DDM (-lipid) (blue), with sodium azide inhibitor control shown in respective colours. Standard deviation is shown by shaded in respective colours in (A), whilst standard error is shown by error bars in (B) (n=3)

Figure 4.9 A shows the relative decrease in absorbance at 550 nm over time due to the oxidation of cyt.c by CcO. The activity of CcO in DDM micelles prior to delipidation was visually quite different to the decrease that was observed

for the delipidated sample. Similarly, the use of specific inhibitor sodium azide showed that only active component within the sample is CcO, as the oxidation activity was reduced to zero upon addition. However, whilst the comparison of activity before and after delipidation observed in Figure 4.9 A showed a visual difference in the gradient, the rate of electron transfer is dependent on the exact concentration of CcO per sample. For an accurate rate to be calculated the precise concentration of CcO was required. The activity rate shown in Figure 4.9 B is concentration independent, showing that the complete removal of endogenous CL by phospholipase digestion decreases CcO oxidative rate by 49%, this is in line with literature values for CL deficient CcO.[97, 284]

The delipidated CcO in DDM micelles was then subjected to detergent removal to form proteoliposomes and then solubilised by SMA 3:1 (as described in §4.2.4) CcO-LQs were then subjected to SEC to remove excess polymer, as this was previously found to interfere with the activity assay.[240] CcO-LQs were then split into two fractions: One being assayed as CL deficient (-CL) without the addition of CL doped LQs, and the other being assayed as CL sufficient (+CL), which was co-incubated with CL containing LQs as described in §4.2.4. The activity assay and specific activity for these CcO-LQs can be seen in Figure 4.10.

There is a clear qualitative difference in gradient between the CcO LQs (+CL) which was co-incubated with CL containing LQs (CL+) and the original, POPC only, CcO LQs (-CL) in Figure 4.10 A. The concentration of CcO of the two samples are similar, so the visual differences seen in Figure 4.10 A are indicative of an increased rate of activity by CcO LQs (+CL) sample. Controlling for differences in CcO concentration (Figure 4.10 B), the rate of activity by CcO LQs (-CL) sample was within error of the delipidated CcO sample in DDM (4.73 $\pm$0.52 *vs* 5.76 $\pm$0.52 respectively, Table 4.4). Similarly, the rates of the CcO LQs (+CL) are within error of the CcO sample in DDM prior to delipidation (12.28 $\pm$0.78 *vs* 11.78 $\pm$1.17 respectively, Table 4.4). The near perfect recovery of this activity could only be due to the presence of CL within previously cardiolipin deficient nanoparticles, which in turn can only have occurred through lipid mixing by collision of nanoparticles in

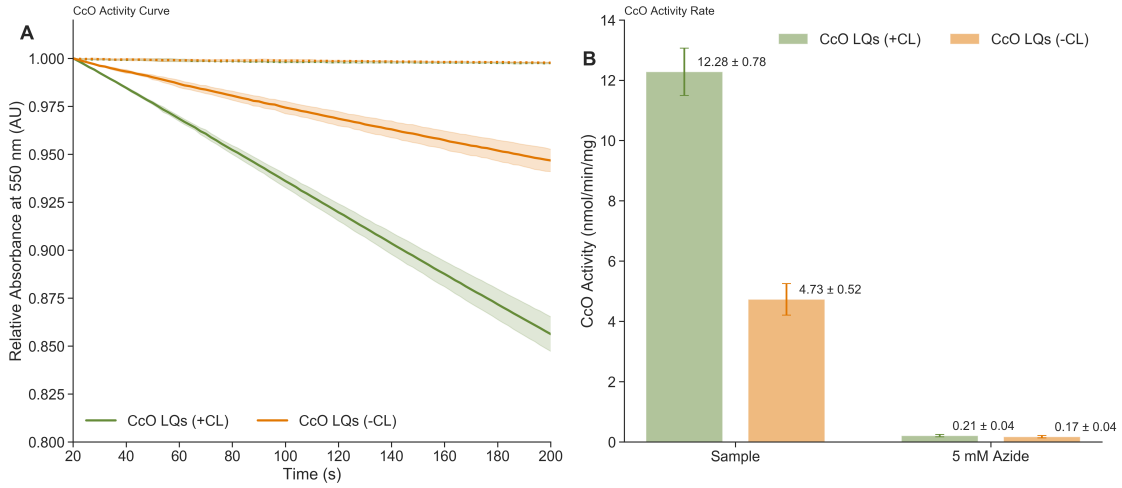


Figure 4.10: Activity of Cytochrome oxidase c (CcO) as measured by the reduction of cytochrome c (Abs_{550}). (A) Relative absorbance change over time of CcO LQs (+CL) (green) and CcO LQs (-CL) (orange). The negative control using 5 mM Sodium Azide (a known CcO specific inhibitor) is seen as a dotted line version of respective sample colours. (B) Specific activity of CcO LQs (+CL) (green) and CcO LQs (-CL) (orange), with sodium azide inhibitor control shown in respective colours.

solution. Whilst monomer diffusion is also a possibility, the bulky structure of the cardiolipin acyl chains makes this an unlikely contributor. This titration of a specific lipid by polymer nanoparticle collision is therefore the first example of a lipid being titrated into deficient protein complexes without the use of detergent or organic solvent of any kind. This relatively simple protocol therefore lays the groundwork for more complex experimentation to be performed to delineate specific protein-lipid interactions, without the use of destabilising detergents from the point of extraction.

Table 4.4: Comparison of activity rates for cytochrome oxidase c (CcO) as measured by reduction of bovine cytochrome c as measured by spectrophotometry normalised for protein concentration (in mg) by BCA assay.

Name	**Description**	**Activity Rate (nmol/min/mg)**	**Activity Std.Dev (nmol/min/mg)**
CcO DDM (+lipid)	Purified CcO in DDM micelles	11.78	±1.17
CcO DDM (+lipid) +Azide	Purified CcO in DDM micelles with activity inhibitor	0.68	±1.15
CcO DDM (-lipid)	CcO delipidated by PLA2 digestion	5.76	±0.52
CcO DDM (-lipid) +Azide	CcO delipidated by PLA2 digestion with activity inhibitor	0.01	±0.74
CcO LQs (+CL)	CcO-LQs with 2% CL (molar) LQs present	12.28	±0.78
CcO LQs (+CL) +Azide	CcO-LQs with 2% CL (molar) LQs present + activity inhibitor	0.21	±0.04
CcO LQs (-CL)	CcO-LQs	4.73	±0.52
CcO LQs (-CL) +Azide	CcO-LQs + activity inhibitor	0.17	±0.04

4.4 Summary and conclusions

The work presented here strongly suggests that lipid polymer nanoparticles formed from SMA 3:1, SMA 2:1, DIBMA, and PMA polymers undergo collisional lipid mixing in solution. This indicates that it is a native property of these nanoparticles and could be expected to be present in newly developed polymer types also. It goes on to show that this mixing occurs during or immediately after solubilisation through the destruction of asymmetric membrane order in aLUVs (Figure 4.3), and measurements with TR-FRET have shown that individual polymers possess vastly different mixing rates, which are highly temperature dependant (Figure 4.6). Whilst these properties have been known for SMA polymers,[262, 277] and even DIBMA nanoparticles,[288] the exploration of mixing in PMA based nanoparticles is unique within this thesis, as are the direct comparisons of the rate of mixing between polymers.

A novel unlabelled lipid study was also performed to ascertain whether the mixing phenomenon was due to the use labelled lipids, or was an inherent property of the lipid-polymer nanoparticles. Through the use of ^{31}P NMR to measure the local environment surrounding lipids it was shown that nanoparticles of solely DMPC and DMPG do undergo lipid mixing (Figure 4.8). However, incubation for 30 minutes at 4°C is insufficient for full mixing between nanoparticles, with an estimated ratio of 70:30 DMPC:DMPG. A similarly prepared sample measured by TR-FRET (Figure 4.5 B) also showed incomplete mixing at an incubation time of 30 minutes at 4°C, indicating that complete mixing would occur if incubated for longer. This confirms that nanoparticles do undergo spontaneous lipid mixing by nanoparticle collision, and not by monomer lipid diffusion of fluorescent or spin-label tagged lipids. This is in-line with a similar unlabelled experiment was performed by Keller *et al.* utilising TR-SANS in place of ^{31}P NMR, and using SMALPs rather than LQs.[262]

This property may impact the stability of the 'native-like' environment reputation of thee nanoparticles. The current 'cookie-cutter' model of membrane solubilisation suggest membrane proteins are captured with their native membranes and associated lipids are trapped in place. This model is no longer an accurate representation.

However, the dynamic property gained by this collisional lipid mixing has allowed for the development of a novel protocol for the extraction of membrane proteins in a detergent free manner. In addition, it can be used for the exchange of these proteins into other model membrane systems for downstream applications.[281, 282] In addition to the exchange of membrane proteins within lipid-polymer nanoparticles, the work present in this chapter has shown that it is possible to expand the use of these lipid-polymer nanoparticles from a broad extraction and characterisation lipidomics, into a more singular lipid-protein association role.[183, 186, 189, 283] By utilising the 'hydrophobic continuum'[262] of these nanoparticles, preliminary work in this chapter has shown that it is possible to titrate in a specific lipid of interest into protein nanoparticles without the use of detergent (Figure 4.10), to elucidate the interaction for a singular lipid-protein combination. This could be further expanded to the removal of endogenous lipids through dilution with excess lipid nanoparticles, similar to the process by Watts *et al.*, without the use of detergent.[284]

By performing this step without the use of detergents or organic solvents, which may destabilise or otherwise affect the protein-lipid interaction, this initial protocol lays the groundwork to elucidate the relationship between specific lipid association and protein behaviour without the use of detergent at any step. This detergent-free titration could enable the estimation of lipid preference for a protein-lipid association through displacement assay (where native lipid displaces an exogenous lipid or *vice versa*). In addition, by carful calculation of the rate of mixing by nanoparticle collision, it may even be possible to calculate K_D values for specific lipid-protein interactions. These values have only ever been estimated for peripheral proteins experimentally,[289] or for integral membrane proteins through MD simulations, [290] and recently through free energy calculations.[291] This will not only have an impact on our understanding of lipid-protein interactions in a healthy membrane, but also shed light on previously undiscovered disease states for membrane proteins.[35]

Men will not be content to manufacture life:
They will want to improve on it.

J.D Bernal

5

Purification and biophysical characterisation of self-assembling viral-like capsules

Contents

5.1 Introduction 133
5.1.1 Aims 136
5.2 Materials & methods 136
5.2.1 Peptide synthesis 136
5.2.2 High Pressure Liquid Chromotography (HPLC) 137
5.2.3 Mass spectrometry 138
5.2.4 Transmission Electron Microscopy 138
5.2.5 Circular dichroism (CD) 139
5.2.6 Fourier transform infra-red spectroscopy (FTIR) 139
5.3 Results & discussion 140
5.3.1 Purification of synthesised ST1-QAA 140
5.3.2 ST1-QAA self-assembly 144
5.4 Conclusions and future works 152

5.1 Introduction

This chapter endeavours to describe the synthesis, purification and biophysical characterisation of a self-assembling peptide nanoparticle, called ST1-QAA. This peptide is of a newly developed family of viral-like nanoparticles, which have been

developed at the National Physical Laboratory (NPL). Designs of this type have shown great promise in the enhanced antimicrobial efficacy,[292] and potential for gene transfer than previous, non-self-assembled peptides.[293]. Peptide-based biological applications have received renewed interest in recent years, with the development of self-assembling peptide nano-materials.[294] These nano-materials possess a vast range of self-assembled forms, from hydrogels, [295, 296] delivery vectors,[293, 297, 298] and antimicrobial nanoparticles.[292, 299]

Whilst rational peptide design has been in use for many years, they have most commonly been associated with the design of peptide-based therapeutics.[300–303] Historically, peptide therapeutics and self-assembly have been generated from 'Frankenstein' peptides; with the material's activity inspired by native active sequences, and the enhanced stability being generated from an artificial scaffold sequence.[292, 304, 305] One such example, the CapZip virus-like particle,[299] amplifies the antimicrobial effect of lactoferrin through generating a self-assembled viral like particle. The hybrid design method allows for the generation of structures with increased bio-compatibility (such as hydrogels with in-built growth factors),[296] with simple modifications to pre-existing self-assembling sequences. In more recent years, there has been an increased development of peptides of a *de novo* or biologically inspired sequence, utilising self-assembly principles.[292, 293, 295, 297, 305–308] Design of these structures is possible due to an understanding of the underlying dependance of overall structure on the primary sequence.[**Fletcher2013Noble2016**, 294, 297, 309, 310]

The first *de novo* virus-like topology at the NPL was achieved with a peptide called TecVir,[293] which was designed to imitate the natural viral ability to enter cells and deliver genetic information. TecVir is a 30 amino acid peptide that self-assembles to form a *tecto*-dendrimeric virus like shell with a central cavity. The secondary structure is an α-helical coiled-coil motif, based upon *gabcdef* heptad repeats, (Figure 5.1 B). In addition to the electrostatic and hydrophobic associations aiding dimer formation, the presence of a N-terminal cysteine for di-sulfide bond formation between the two monomers stabilises this structure. The resulting

viral like shell is monodisperse, with an average hydrodynamic diameter (H_D) of 18.4 ±6.6 nm.[293] Most importantly, there is a central cavity, with TecVir being shown to encapsulate both siRNA and DNA, and transfect HeLa cells with the encapsulated nucleic acids.

However, peptide-based materials and therapies are still in their infancy, and are yet to overcome some significant challenges. Factors such as a high synthesis cost and low metabolic half-life *in vivo* have limited the scale of these smart materials to academic labs and use in niche requirements,[311] such as gene transfection *in vitro*.[297] Further development of greener and cheaper peptide synthesis has shown some promise to allow for easier up-scaling of synthesis techniques,[312, 313] however the short half-life of peptide therapeutics in the body is still a limiting factor in the medical field.

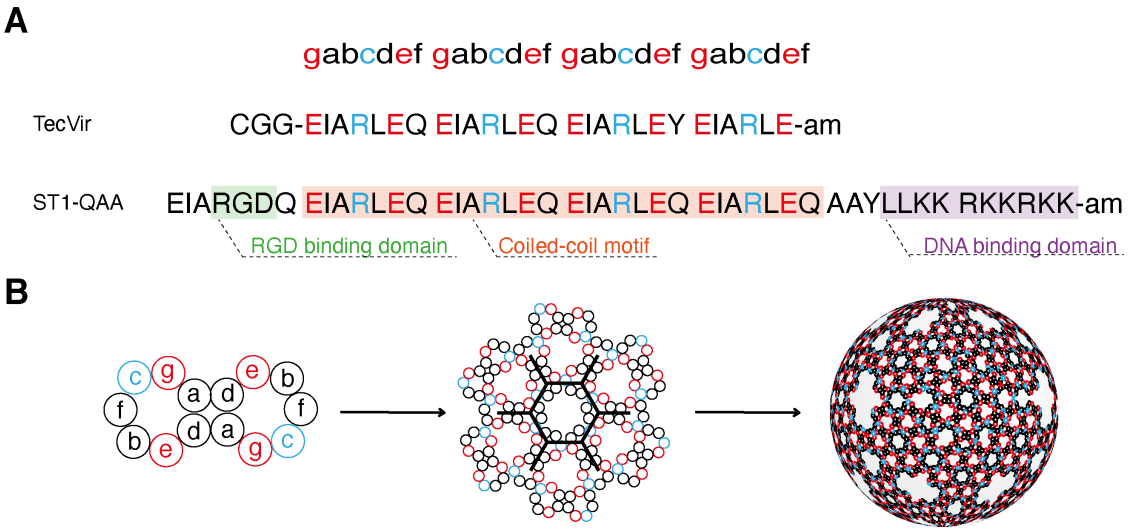


Figure 5.1: Sequence and rational design of ST1-QAA. (A) Sequence of TecVir and ST1-QAA aligned to heptad repeat pattern of gabcdef. ST1-QAA domains and modifications from TecVir are highlighted: RGD binding domain (green), coiled-coil motif (orange), DNA-binding domain (purple). (B) Coiled-coil heptad repeat pattern (gabcdef). Residues at a and d sites form the hydrophobic interface, and are isoleucine and leucine, respectively, favouring dimer formation. Residues at e and g are anionic glutamates (red) that interact with cationic arginines (blue) at c forming intra-helical (gc) interactions in the same dimer and inter-helical (ce) interactions between dimers. Stages of proposed self-assembly from coiled-coil monomer subunit, to *tecto*-dendrimer viral shell are also shown in (B).

The peptide studied in this chapter, ST1-QAA, is a successor to TecVir, with the same central heptad repeat structure of EIARLEQ for coiled-coil formation

(Figure 5.1 A). Three major modifications were made to generate ST1-QAA, which were made to expand upon TecVir's success: Firstly, the removal of the cysteine link between monomers to simplify the association and was anticipated to make the structure more flexible. Secondly, there was an addition of a lysine rich domain to the C-terminus. This was derived from the nucleotide binding domain of the hepatitis B core shell, and thought to aid in nucleic acid association during encapsulation *via* electrostatic interactions. Thirdly, the addition of the RGD integrin binding motif to aid in cellular uptake of the viral like particles.[314]

Whilst TecVir has been well characterised in terms of self-assembly and gene transfection potential,[293] ST1-QAA has to date only been preliminary examined in these aspects. These preliminary results showed good agreement to TecVir in terms of self-assembly and overall biophysics (not shown), however it is not yet known how the modifications have affected nucleic acid encapsulation and cellular uptake.

5.1.1 Aims

This chapter aims to develop and optimise a purification protocol of ST1-QAA, through the use of preparative HPLC. In addition to purification, this chapter aims to characterise the self assembly mechanism of ST1-QAA to form viral like particles, through the use of negative stain EM imaging, circular dichroism (CD) spectroscopy and Fourier transform infra-red (FTIR) spectroscopy.

5.2 Materials & methods

5.2.1 Peptide synthesis

ST1-QAA (sequence shown in Figure 5.1 A) was synthesised *via* solid-phase peptide synthesis methods (SSPS), using a Liberty blue microwave peptide synthesiser (CEM Inc. Matthews, NC, USA) on a 100 μmol synthesis scale. Rink amide MBHA resin was used with a 0.65 mmol/g substitution. Amino acids were purchased with Fmoc protection, and additional orthogonal protecting groups for amino acids with reactive side chains. Between synthesis steps, piperidine (20% (*v*/*v*) in DMF) was used for

the deprotection of the growing N-terminus. Amino acid coupling was achieved using HBTU (0.5 M) and DIPEA (1 M) as the activator and activator base, respectively.

Once the synthesis was completed, the peptide-resin beads were washed twice with DCM then diethyl ether. The resin was then dried under vacuum for 5 minutes prior to cleavage.

Cleavage of the polypeptide chain from the resin was achieved using a mix of 95:2.5:2.5 TFA:H_2O:TIS and incubation for 2-3 hours at room temperature, with gentle agitation. Once cleavage was complete, the crude (i.e. unpurified) peptide was precipitated using glacial ether. The precipitate was pelleted through centrifugation at 3,600 g at 4°C for 15 minutes. The pellet was resuspended in minimal dH_2O, with a few drops of ACN (as needed) to aid solubilisation. The resuspended peptide was freeze-dried overnight (lyophilised) to remove any excess volatiles.

5.2.2 High Pressure Liquid Chromotography (HPLC)

Lyophilised peptide powder was resuspended to a final concentration of 10 mg/mL in mobile phase (Buffer A, 95:5:0.1 H_2O:ACN:TFA) prior to sonication for ten minutes in a water bath to ensure complete solubilisation. Supernatent (solubilisd peptide) was purified using HPLC.

Preparative HPLC was performed using a Dionex Ultimate 3000, with a Vydac C18 semi-preparative column (Grace, Dearfield, IL, USA). Two buffers were used in the purification: Buffer A (hydrophilic, 95:5:0.1, dH_2O:ACN:TFA) and Buffer B (hydrophobic, 5:95:0.1, dH2O:ACN:TFA). Exact gradients for each purification attempt (step) can be found in their respective figures. 5 mL of sample was injected onto the column per HPLC run, equating to a maximum of 50 mg peptide injection onto the column at any time. All collected fractions were analysed with either Matrix-assisted laser desorption/ionization time of flight (MALDI-TOF) or electrospray ionisation mass spectrometry (ESI-MS), and pooled fractions were assessed for purity through analytical HPLC (A-HPLC).

Analytical HPLC was performed using a Dionex Ultimate 3000, with a Vydac C4 analytical column (Grace, Dearfield, IL, USA). Both Buffers A and B were

consistent with those used in preparative HPLC, however with a linear gradient of 10-70% Buffer B over 30 minutes for all samples.

5.2.3 Mass spectrometry

ESI-MS was used to determine pooled fraction purity of purification steps. ESI-MS was performed on a Thermo scientific exactive Q LC-MS machine, using manual injections per sample. Due to instrument sensitivity, pooled fractions were diluted to a 1:10 dilution in 95:5 dH_2O:ACN (LC-MS grade) and filtered using a coarse filter prior to injection. A total of 50 μL of sample at a rate of 5 μL/min was injected per pool. Between injections, equipment was washed with 3× with ultra-pure 200 μL dH_2O, followed by 3× 200 μL ACN (LC-MS grade).

For analysis, mass list and relative intensity spectra per injected pool was exported to ASCII format and analysed using Python. This plotted the intensity spectra, with automatic detection of desired mass per ion series (i.e ST1-QAA M_w = 4791 Da) using the mass list exported by the machine software, above a specified intensity threshold (>20% relative intensity). Example Python scripts can be found on Github.[207]

5.2.4 Transmission Electron Microscopy

Sample grids of 0, 3, and 24 hours incubation of ST1-QAA were prepared by incubation of 100 μM peptide in 10 mM 3-(N-morpholino)propanesulfonic acid (MOPS) buffer at pH 7.4 on 400 mesh carbon-copper grids for 3 minutes, followed by 2 staining rounds with 2× 10μL of 2% uranyl acetate (UA), the excess was blotted using filter paper between incubation and staining steps. A third, elongated, stain of 10μL UA was left for 15 seconds before blotting and left to air dry for 3 minutes. Images were kindly recorded by Dr Emiliana de Santis (NPL) using a JEOL JEM1400-Plus, at 120kV, and a One View camera (Gatan). Diameters of major and minor axis were measured manually using GMS3 software (version 3.4.1), with 100 particles measured per sample. The dimension components were

then analysed using python. Eccentricity was calculated as described previously (§B.1). Example python scripts can be found on Github.[207]

5.2.5 Circular dichroism (CD)

An aliquot of ST1-QAA peptide (from a stock of known concentration in dH_2O) was heated to room temperature, prior to dilution in 10 mM MOPS to a final concentration of 100 μM. Measurements were recorded using a JACSO J-810 spectropolarimeter, utilising a waterbath controlled by a JASCO PTC-23S thermocouple. Measurements (in ellipticity (mdeg)) were recorded between 260-180 nm, at a scan speed of 100 nm/min, a bandwidth of 1 nm, a response time of 1 second and a pitch of 0.5 nm using a 10 mm quartz cuvette. Four measurements were recorded per time point, with a 2 minute interval between each recording before averaging.

For time course measurements, measurement points were recorded as described every hour. For CD melt measurements, two data types were recorded: First, measurement at 222 nm were recorded every 1°C from 20-90°C, with 3 minutes delay per increment. A second, full spectral scan, measurement (260-205 nm) was recorded every 10°C increment from 20-90°C. This full spectral scan was recorded through averaging 4 spectra and a scan speed of 50 nm/min. After the completion of the CD-melt, the same sample was incubated at 20°C for 2 hours, prior to a manual post-melt measurement using the same parameters. Example python scripts can be found on Github.[207]

5.2.6 Fourier transform infra-red spectroscopy (FTIR)

All FTIR spectra were collected using a Tensor-37 series FTIR spectrophotometer with a BioATR II unit (Bruker Optics, UK) as the sampling platform with a photovoltaic mercury cadmium telluride (MCT) detector and a Bruker Optics workstation, which was equipped with OPUS software. 20 μL of the peptide sample (at 100 μM concentration, buffered to pH 7.4 by 10 mM MOPS) was placed in a circular sampling area of radius 2 mm with a pathlength of 6 μm. A temperature of 20°C was maintained using a circulating water bath. All FTIR spectra were

collected between 4000 and 850 cm^{-1} with parameters set at: resolution 4 cm^{-1}, scanner velocity 20 kHz, 256 scans, phase resolution 32 and zero filling factor 4.

Two timepoints were measured, T0 (0 hours after incubation) and T24 (+24 hours after incubation). For the T24 time point, the sample was stored for 24 hours at 20°C in a climate controlled room until required.

Initial data processing (atmospheric compensation and baseline subtraction) was performed using OPUS software. Data was then exported to ASCII format and plotted through python (using the matplotlib package). Subtraction spectra (T0-T24) was also generated using python,utilising tools in the numpy library. Example python scripts can be found on Github.[207]

5.3 Results & discussion

5.3.1 Purification of synthesised ST1-QAA

Synthesis and purification of ST1-QAA had been completed previously by a previous visiting researcher of the NPL, with preliminary studies performed to characterise the ST1-QAA particles in both biophysical and biological assays (not shown). The initial aim of this work was to complete the biophysical characterisation of formed ST1-QAA nanoparticles, as well as further explore the use of these nanoparticles in DNA/RNA transfection.

No crude or partially purified ST1-QAA was thought to be available at the time of arrival, so a synthesis was performed with the established protocol. One batch of ST1-QAA was synthesised. The purification attempts 1-4 (§D.1) are optimisation steps to the preparative HPLC protocol with this synthesised peptide. The initial purification can be observed in Figure 5.2, with the optimisation attempts in further detail in §D.1.

Initial purification of the ST1-QAA synthesised (Figure 5.2 A) used a linear gradient of 10-70% Buffer B for 20 minutes produced a single, broad peak of measured by UV chromatography. MALDI-TOF (not shown) was performed on individual fractions across the whole range (Figure 5.2 A) grey lines note fractionation points), with ST1-QAA containing fractions highlighted in red. These fractions were pooled,

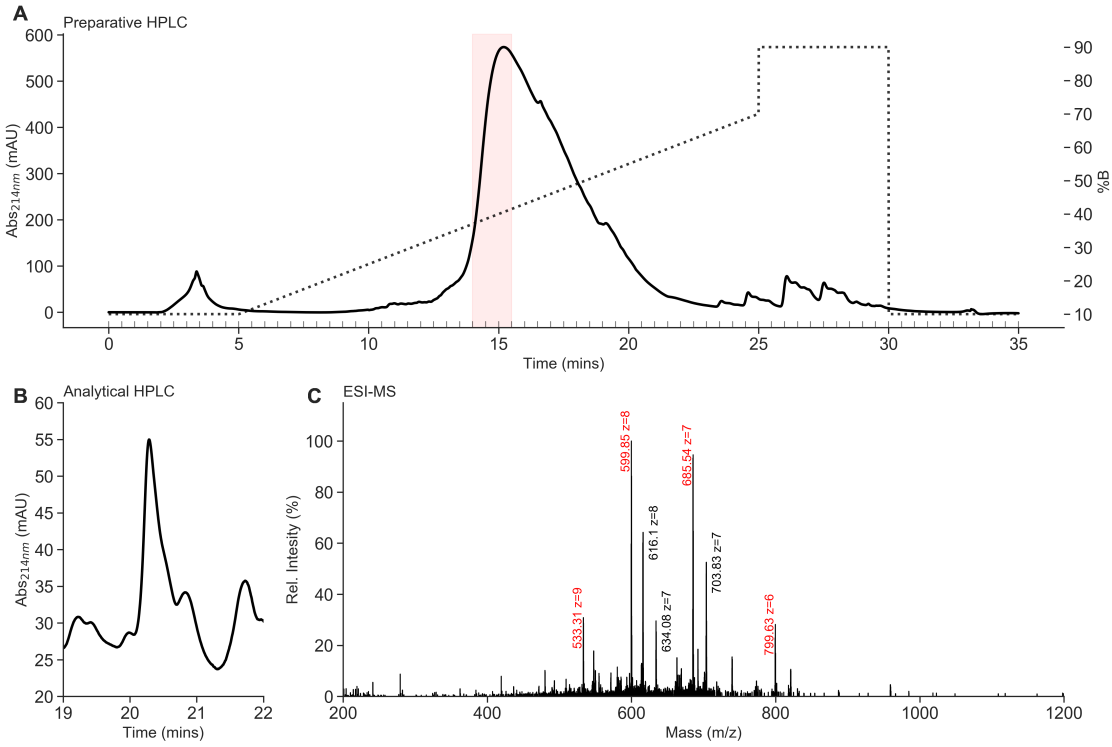


Figure 5.2: Initial purification attempt of ST1-QAA, showing preparative HPLC UV chromatogram (A), overlaid with linear gradient of Buffer B (dotted line) used for purification attempt. Red highlighted region indicates fractions pooled for shown analytical HPLC (B) to assess purity, and ESI-MS to assess contents of fraction (C). Red annotation indicates mass/charge ratio (m/z) of expected M_R for ST1-QAA (4791.52).

with purity determined by analytical HPLC (Figure 5.2 B), and pooled fraction content determined by ESI-MS (Figure 5.2 C).

HPLC shows the initial purification does not generate pure ST1-QAA, as analytical HPLC showed at least three contamination peaks, with an estimated purity through peak integration of ~60%. ESI-MS showed that there were two ion families present in the pooled fractions, in addition to ST1-QAA (highlighted with red text), with a relative masses of 4933.81 Da and 4445.56 Da.

The heavier mass contaminant can be attributed to incomplete cleavage of the Boc protecting group of a single lysine, along with an acetylation on the N-terminus. Combined, this incomplete cleavage would yield a mass of 4933.7 Da, which is within error of the ESI-MS ion mass. Similarly, the smaller contaminant is likely to be an incompletely reacted peptide, with calculations of expected mass predicting that the mass missing is equivalent to the N-terminal EIAR- sequence. This indicates

that the contaminant is due to a failed arginine coupling, as arginine coupling is notoriously difficult in solid-phase synthesis,[315] and often requires specialised conditions due to the steric hinderance by the Pbf-protecting group. Due to the high number of arginine residues in ST1-QAA, the original synthesis protocol included triple-coupling at 75°C for each arginine residue in the sequence. This clearly was not sufficient for the final arginine in the sequence, and it was noted that the next synthesis (when possible) should include an elongated coupling time at a lower temperature to improve yield at this position.

To improve purification by HPLC, optimisation steps (attempts 2-5) then focussed on the Buffer B concentrations and gradient (Appendix D). Which yielded 10.4 mg of peptide at approximately 70% purity by analytical HPLC (Figure D.4). Unfortunately, it was discovered through analysis of the preparative and analytical HPLC chromatograms that aggregation of the crude peptide solution occurs throughout the purification process. This aggregation appeared to cause two noticeable effects on purification attempts: Firstly, the contamination due to truncated peptide byproducts eluting in tandem with ST1-QAA and found in all the fractions containing ST1-QAA (not shown). Secondly, the number of peaks observed in preparative and analytical HPLC chromatograms did not equate to the number of contaminants observed through mass spectrometry.

The additional (and broader) peaks observed in HPLC chromatograms for attempts 1-4 (which are altered by different gradients of buffer A and B) therefore appeared to be due to aggregation of a combination of ST1-QAA and the truncated peptide contaminant in various ratios. To discourage this, later purification attempts (Figures D.4 and 5.3) were doped with 10% TFE (*v/v*) prior to preparative HPLC. TFE is well known to discourage aggregation,[316] and resulted in an improved preparative HPLC chromatograms (Figure D.3 A *vs* Figure D.4 A). However, some 'ghost' peaks were still observed even with the addition of TFE (Figure D.4 B), and no significant improvement in purity was measurable through ESI-MS. This continued the difficulties in ascertaining purity through analytical HPLC and it was therefore difficult to accurately measure purity of resulting ST1-QAA. An estimated

purity was calculated through a combination of analytical HPLC peak integration and ESI-MS relative intensity. The combined, final, purification of synthesised ST1-QAA (Figure D.4) was estimated to be approximately 75%, with a yield of 10.4 mg.

During the optimisation process, a previously synthesised batch of ST1-QAA crude was purified on the sixth attempt (Figure 5.3) using the optimised protocol described previously (Figure D.4).

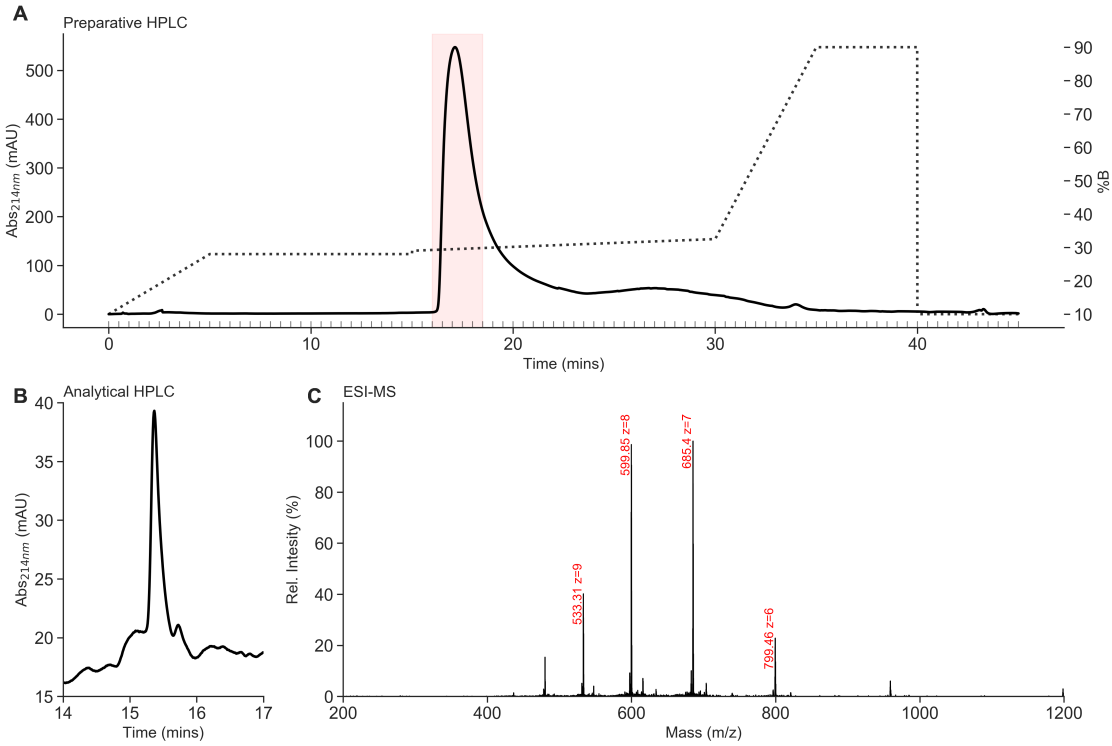


Figure 5.3: Sixth attempt of ST1-QAA purification, showing preparative HPLC UV chromatogram (A), overlaid with modified protocol of Buffer B gradient (dotted line) used for purification attempt. Red highlighted region indicates fractions pooled for shown analytical HPLC (B) to assess purity, and ESI-MS to assess contents of fraction (C). Red annotation indicates mass/charge ratio (m/z) of expected M_R for ST1-QAA (4791.52).

As can be seen in Figure 5.3 the contaminant of the EIAR- N terminal truncation was not observed in this crude ST1-QAA. After the synthesis in November, the peptide synthesis machine was discovered to have a major fault with nitrogen pressure regulation, affecting all stages of peptide synthesis requiring fluid distribution, and is likely to have affected the peptide yield in the November 2019 synthesis. However, ghost peaks observed in the analytical HPLC (Figure 5.3 B) indicated that the aggregation observed for previous purification attempts

are a conserved property of ST1-QAA, due to the self assembling design. Due to the lack of ionisable contaminants, purity was estimated to be above 90% by Analytical-HPLC (A-HPLC) and ESI-MS, with a 2.4 mg yield. This pure sample was used for the biophysical characterisation in this chapter.

5.3.2 ST1-QAA self-assembly

ST1-QAA undergoes spontaneous self-assembly to form viral like capsids, which can encapsulate DNA or RNA cargo for enhanced delivery into cells and lead to gene transfection. Previous work in the lab,[292, 293] has shown that viral like particles can be formed from rationally designed peptides, with these structures shown to enhance gene transfection into cells with no loss of cell survival. However, the exact mechanism of self assembly is not yet fully understood, and for this method of DNA transfection to be applied further, a rigorous understanding of self-assembly is required. To this end, a combination of DLS, TEM, CD, and FTIR were employed to monitor any changes in ST1-QAA structure over a 48 hour period.

Negative stain transmission electron microscopy of ST1-QAA assembly

The obvious first step in measurement of the formation of macromolecules was direct imaging. Directly imaging the size and shape of formed viral like particles for ST1-QAA's predecessor, TecVir, had already been achieved using negative stain transmission electron microscopy. This protocol was applied to ST1-QAA. Due to the manual nature of staining, samples for TEM were taken at three timepoints; 0, 3, and 24 hours. These were chosen as start (T0) and end points (T24), with T3 the typical incubation time before use in biophysical characterisation protocols at the time. In tandem to these manual measurement points, automatic DLS measurements of 1 hour increments from 0-24 hours was measured, however the DLS results proved unfruitful due to sample aggregation (Figure D.6).

This was similarly observed for the initial time-point of EM imaging, T0, which showed peptide aggregation (> 20 μm) of peptide (Figure D.5), and therefore particle analysis can not be performed (Figure D.5). These aggregates are likely

to be caused by buffer contaminants and excessive staining. The later timepoints of T3 and T24 showed discrete particles of the expected size (~20-50 nm), and were taken further for particle analysis.

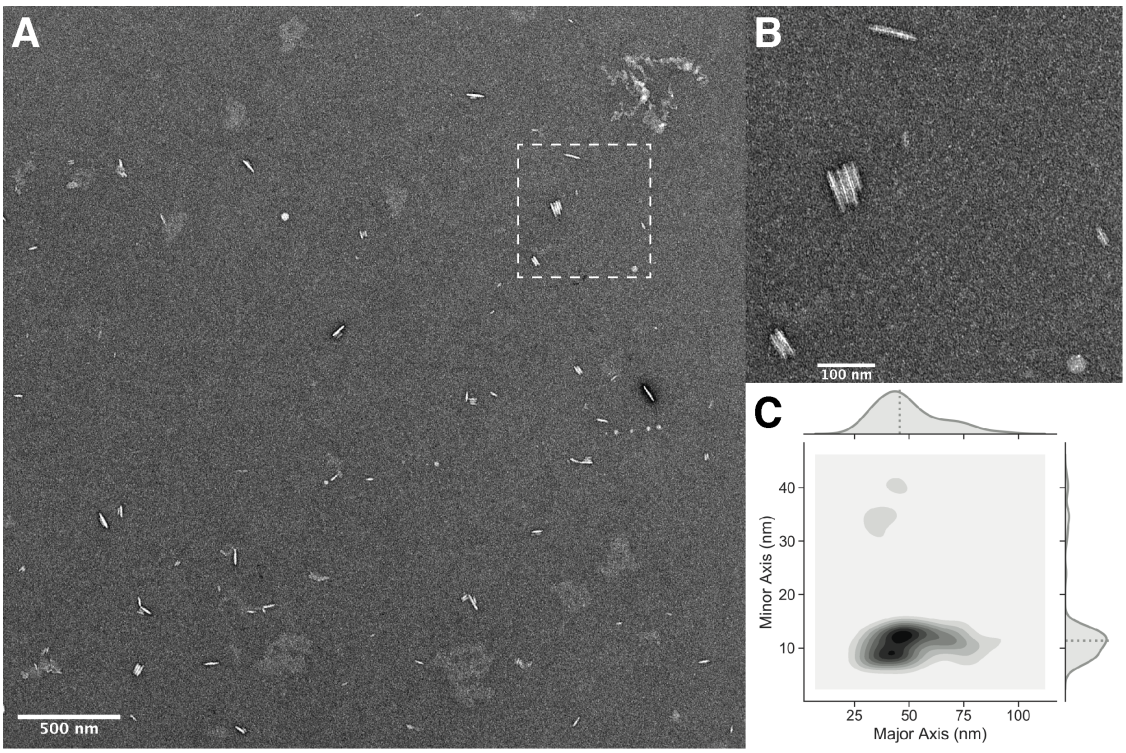


Figure 5.4: Negative stain TEM images showing nanoparticle macromolecular structure. ST1-QAA 3 hours after incubation in 10 mM MOPS at pH 7.4, before staining with a 2% uranyl acetate solution. Samples were mounted and dried on 400 mesh carbon-copper grids. (A) Original magnification of EM grid. (B) Zoomed in highlighted region of A showing increased resolution of selected particles. (C) Distribution of major and minor axis diameter measurements from 100 particles.

EM imaging 3 hours after incubation (T3, Figure 5.4 A and B) shows the large aggregates observed at T0 have dispersed, and the formation of discrete particles of the appropriate size (~20-50 nm) can be observed. Closer inspection showed two discrete populations of particles, appearing as rods and spheres, with the rod shaped particles far outnumbering the spherical particles. The spherical particles were expected, indicating ST1-QAA viral like particles were formed, and showed good agreement with TecVir's approximate size and shape in the literature.

There was a clear distinction between the rod form and the sphere form (Figure 5.4 C) when comparing the distribution of lengths along the major and minor axis,

with the rod form showing a high density with a major axis of ~50 nm and a minor axis of ~10 nm. Similarly, the less dense population was clearly observed as two discrete populations in the upper left corner of the density plot.

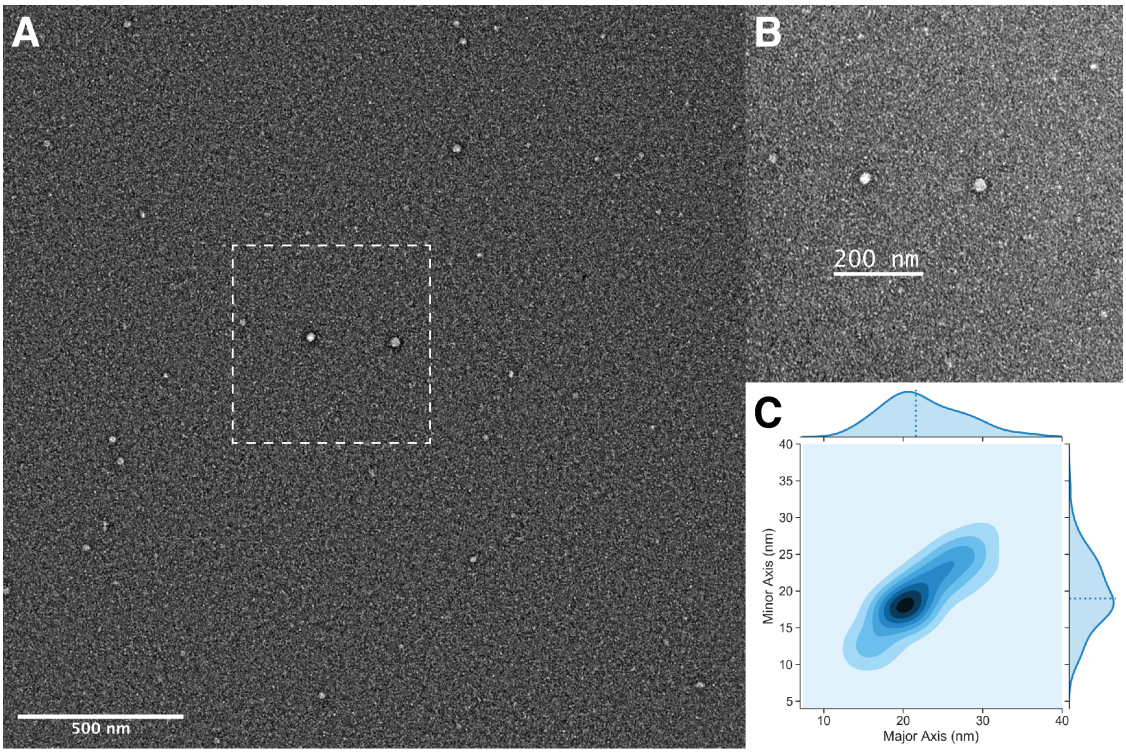


Figure 5.5: Negative stain TEM images showing nanoparticle macromolecular structure. ST1-QAA 24 hours after incubation in 10 mM MOPS at pH 7.4, before staining with a 2% uranyl acetate solution. Samples were mounted and dried on 400 mesh carbon-copper grids. (A) Original magnification of EM grid. (B) Zoomed in highlighted region of A showing increased resolution of selected particles. (C) Distribution of major and minor axis diameter measurements from 100 particles.

The EM image of T24 (Figure 5.5 A and B) show a disappearance of the rod-shaped particles previously observed in Figure 5.4. Instead, only the sphere shaped viral like particles remain. These spheres were very homogenous, and within expected values for ST1-QAA viral like particles. Additionally, the particles observed in the T24 images were of similar size to the previous spheres observed at T3. Comparison of the distribution of major/minor axis lengths (Figure 5.5 C) was diagonal, indicating that all particles measured are roughly spherical in shape and between 15-30 nm in diameter.

The relative abundance of rods over spheres in the T3 timepoint (Figure 5.4), so soon after incubation could imply that these rods were an intermediate form between peptide monomer and fully formed viral like particles. Additionally, the rod particles often appeared clustered together (reminiscent of the rouleaux stacking observed in DIBMA nanoparticles in Figure 3.1), which may be indicative of a mechanism of capsid formation *via* the rod form, or alternatively an artefact of staining and dehydration. Further assays are required to determine whether this is an artefact of this sample or an unidentified self-assembly intermediate. The disappearance of these particles by the T24 timepoint (Figure 5.5) does imply the former explanation however.

Additionally, there is also no detectable clustering of viral like particles, either at T3 or T24 incubation points. This is most likely a product of the homogenous charge design of ST1-QAA viral particles discouraging association in solution *via* electrostatic charge repulsion. This could indicate that the interacting surfaces of the rod particles observed in Figure 5.4 may be more heterogeneous than the sphere particles.

Quantification of particle dimensions (Figure 5.6) showed that T3 particles Figure 5.6 A) were varied largely across major axis length, with a median length of 45.80 ± 14.7 nm. There did not appear to be discrete populations of rod length or capsid diameter among this distribution, suggesting that the putative rod intermediate does not have an optimal length. At T24 Figure 5.6 B), the large distribution was lost and a narrower distribution of particles, with a median diameter of 21.60 ± 4.9 nm for the major axis developed. This slight variation indicates that there is some flexibility in viral particle size. However, this may be due to loose packing arrangements between ST1-QAA monomers, in addition to EM imaging artefacts.

As shown with lipid-polymer nanoparticles (Figure 3.2), eccentricity can be measured through the equation shown in §B.1 to give a value between 0 (not circular) to 1 (circular). This was applied to ST1-QAA images, shown in Figure 5.7 A. The eccentricity of the particles at 3 hours (Figure 5.4 A) showed two discrete nanoparticle shapes. The major particle form possessed an average eccentricity of

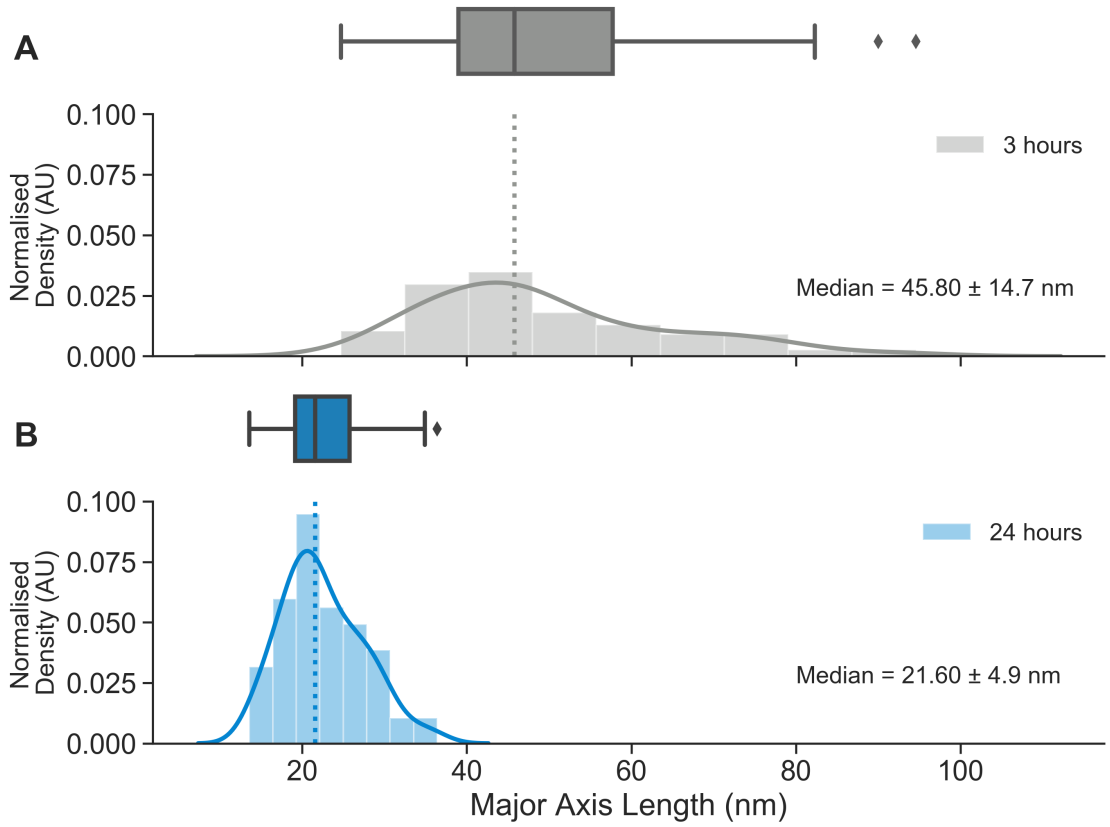


Figure 5.6: Dimensional analysis of 100 particles selected manually per time point; 3 hours (black) and 24 hours (blue) incubation in 10 mM MOPS at pH 7.4. Box plots indicate the size and distribution of major axis per particle, whilst histogram show population distribution of the major axis length as described in Chapter 3

~0.2, with the minor population showing an average eccentricity of ~0.7. It is worth nothing that the large number of outliers can skew the median average to 0.23 ± 0.2 for the whole population, emphasising that these particles are highly heterogeneous.

In contrast, the T24 particles (Figure 5.7 B) showed a high degree homogeneity, with a median eccentricity of 0.67 ± 0.0. There also appears to be a complete lack of the rod-shaped particles. However, the eccentricity of the formed viral particles was not truly spherical, showing an eccentricity of ~0.7 rather than 1. Similarly, the distribution of eccentricity was not symmetrical as one would expect for spherical particles. This may be due to the adsorption of the particles onto a solid scaffold for imaging, drying effects, or may imply that the viral like particles are more dynamic than initially expected.

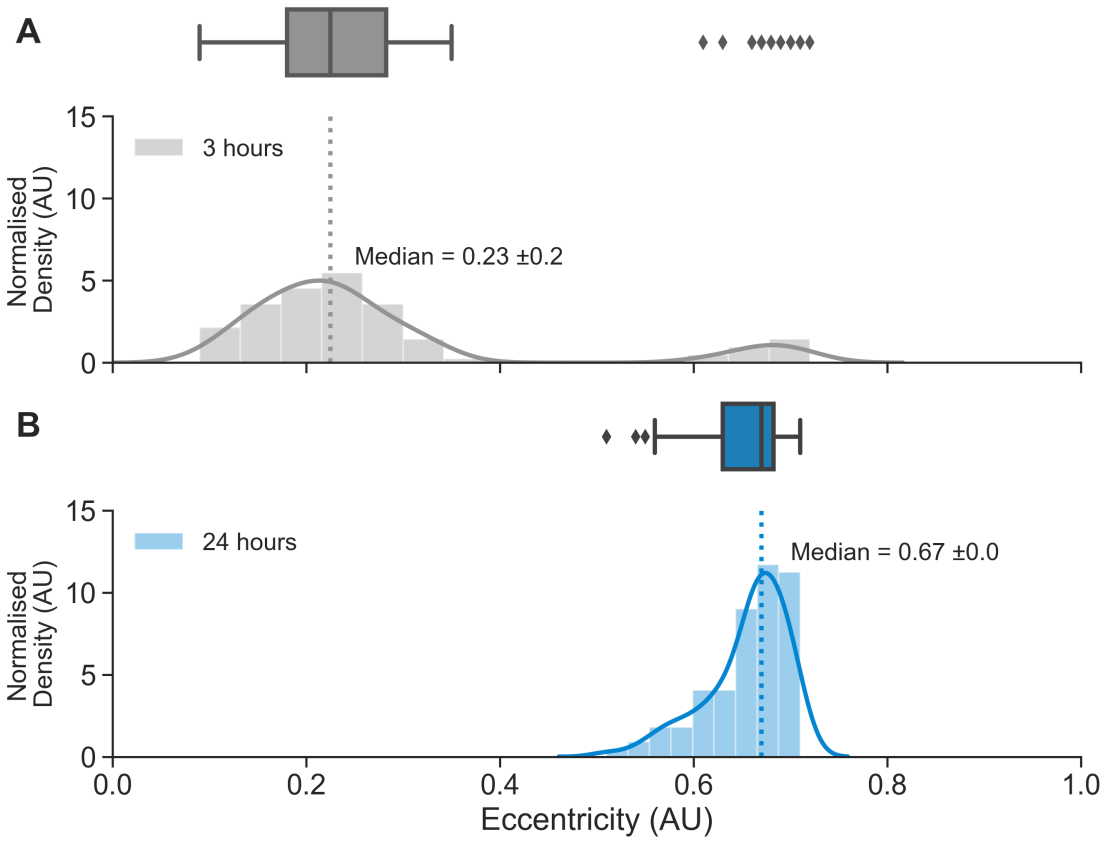


Figure 5.7: Eccentricity distribution of 100 particles selected manually per time point; 3 hours (black) and 24 hours (blue) incubation in 10 mM MOPS at pH 7.4. Box plots indicate the average value and distribution of eccentricity per particle (including outliers - dots), whilst histogram shows population distribution of the particle eccentricity.

Circular dichroism (CD)

The EM imaging showed significant change in the macromolecular structure over 24 hours, however EM imaging does not necessarily indicate any change in secondary structure. To ascertain whether peptide secondary structure was altered during capsid formation, circular dichroism (CD) was used to measure secondary structural characteristics over time.

Figure 5.8 shows ST1-QAA exhibited a strong α-helical spectral shape, with a characteristic positive band at 190 nm, followed by two negative bands at ~208 nm and ~222 nm. There was no significant change in the spectral characteristics throughout the 24 hour measurement period, with only minor fluctuations in the 190 nm peak amplitude being observed. This lack of spectral change indicates

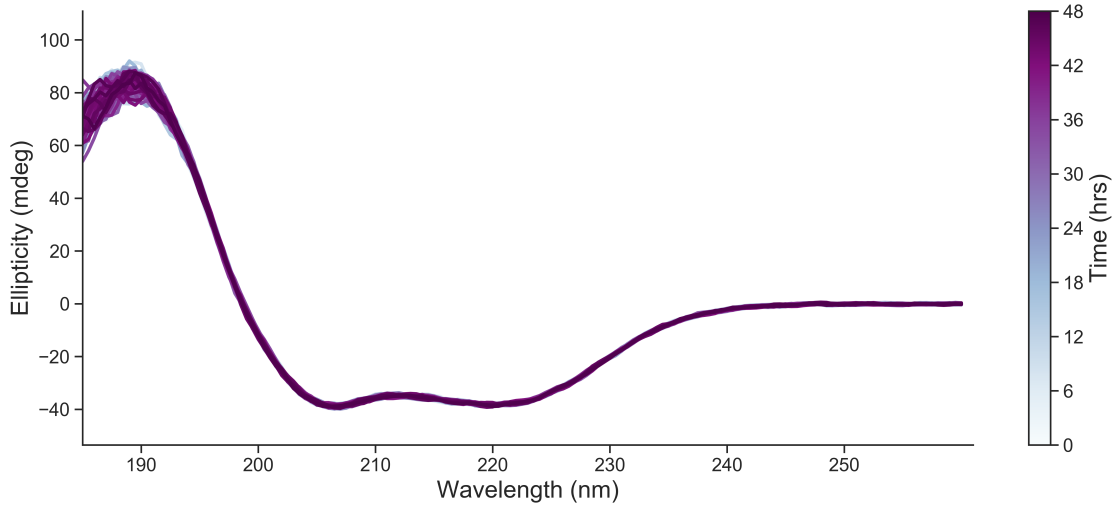


Figure 5.8: Circular dichroism spectra (CD) of ST1-QAA over time (0-48 hours, blue-purple) at 20°C. ST1-QAA sample prepared from stock to a final peptide concentration of 100 μM in 10 mM MOPS (pH 7.4).

no major restructuring of the peptide secondary structure occurs during capsid formation observed by EM imaging. This implies that the rod-shaped formations at T3 are either an artefact of EM imaging, or a simple rearrangement of monomers in the α-helical form. Additionally, the stable CD spectra indicates that the peptide fully folds within minutes of solubilisation in aqueous buffer, and that capsid formation is a gradual process of loose, specific residue coordination with minimal structural reordering of the peptide.

Fourier transform infra-red spectroscopy

Whilst CD spectroscopy was an ideal measurement tool for broad structural rearrangement of peptides, and for quantifying the α-helical, β-sheet, and disordered components of protein secondary structure. This technique is relatively insensitive to minor fluctuations in secondary structure.[206] A more sensitive method to detect bond strain and secondary structure rearrangements is Fourier transform infra-red spectroscopy (FTIR).[317] This technique uses the absorption of infra-red light at specific wavelengths relating to a molecules vibrational modes. In polymers, such as proteins and peptides, the strongest contributors to this absorption are the C=O stretch (Amide I band) and C-N stretching (Amide II band) vibrations of the

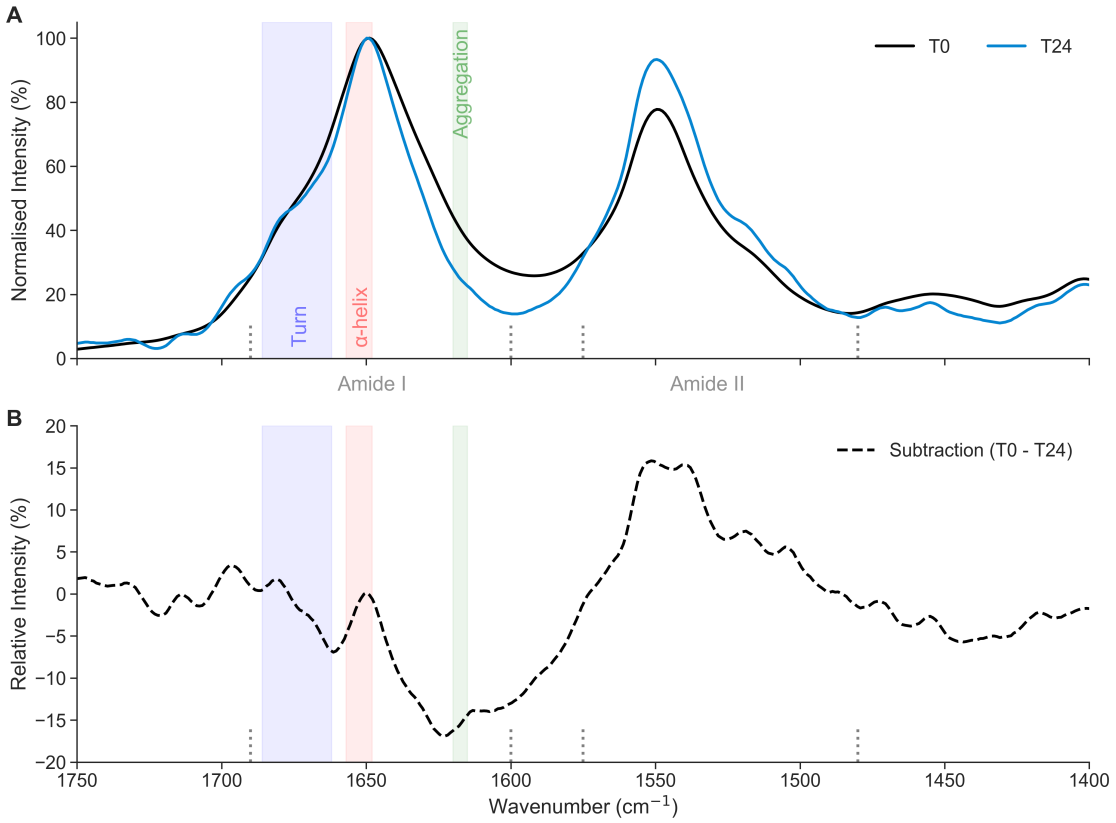


Figure 5.9: Fourier transform infra-red (FTIR) spectroscopy spectra of (A) ST1-QAA at T0 (black) and T24 hours (blue) incubation at 20°C. Amide I and II are shown using grey dotted lines to denote border of signature region. Highlighted regions (blue, red) show regions of FTIR spectra expected in ST1-QAA secondary structure (turns, α-helix respectively). Green highlight denotes signature region for β-sheet aggregation (not observed in FTIR spectra). (B) Subtraction spectra (T0-T24, black dotted line) used to highlight changes in spectra over time. ST1-QAA sample prepared from stock to a final peptide concentration of 100 μM in 10 mM MOPS (pH 7.4).

peptide backbone.[318] The frequencies of these vibrations correlate closely with secondary structure and overall conformational mobility of the peptide backbone. To ascertain whether slight secondary structure changes and backbone strain is induced by capsid formation, two time points were chosen, T0 and T24.

As can be observed in Figure 5.9 A, ST1-QAA possessed two peaks; one in the Amide I region (1690-1600 cm^{-1}, caused by C=O bond stretching) and one in the Amide II region (1575-1480 cm^{-1}, caused by N-H bond bending).[317] The Amide I region showed distinctive peaks for α-helix (red highlighted region) and turn structure (blue highlighted region). Additionally, the overall broad shape of the Amide I peak was indicative of the expected coiled-coil motif.[319] There

was a distinct lack of absorption around 1615-1620 cm^{-1} for both T0 (black) and T24 (blue) spectra, which are used to infer the formation of inter-molecular β-sheets, this is in agreement with the CD spectra. This indicated that the clusters observed at T0 by EM imaging are not permanent aggregates, but more temporary self-associating monomers.

The subtraction spectra of T0-T24 (Figure 5.9 B) did not show any significant structural re-ordering, but does emphasise the narrowing of Amide I and II bands that occurs between T0 and T24. Due to FTIR measuring on a short characteristic timescale ($\times 10^{-13}$ s), FTIR spectra are 'snap shots' of conformer populations, with individual conformations absorbing at individual frequencies per vibrational mode. Band narrowing, such as that observed for the spectra of T24 is indicative of a conformational rigidity in the later time point, which can be explained by a reduced conformational freedom through inter-molecular association in capsid formation.

5.4 Conclusions and future works

The work presented in this chapter describes an optimised purification protocol for ST1-QAA, and goes on to show preliminary work in understanding how rationally designed peptides self assemble into viral like nanoparticles through the use of EM imaging (Figure 5.5) and biophysical techniques (CD and FTIR). This showed viral particle self-assembly could be *via* rod-shaped intermediate structures (Figure 5.4). This work goes on to show that the secondary structure of the ST1-QAA peptide is consistent throughout this self-assembly process, through measurement with CD (Figure 5.8) and FTIR (Figure 5.9).

Due to a combination of machine failures and the Covid-19 pandemic, the work in this chapter is far away from what was hoped to be achieved upon arrival at the NPL. The sudden closure of the lab halted immediate work planned for ST1-QAA:DNA titration that week, to establish the optimal binding ratio for encapsulation. It also prevented the planned imaging of additional timepoints to fully analyse the formation of the viral like particles, including the in-depth imaging around the T3 point to understand the rod particle formations observed in Figure 5.4.

The exploration of the exact mechanism for peptide self-assembly into viral particles is a priority, as understanding this mechanism will allow for optimised protocols for DNA encapsulation and gene transfection. It is currently unknown what the minimal time of assembly is, and whether the addition of DNA or RNA affects the rate of self assembly. It is also unknown whether buffer conditions, such as pH or ionic strength affects self assembly. An ideal, automated method of measuring self assembly would be DLS, which has proven to be effective in measuring the size of formed TecVir particles,[293] but preliminary measuring attempts in this work failed to obtain similar reliable measurements (Figure D.6). Alternatively, EM images could be obtained for a range of buffer conditions at the T24 time point, which is known to form viral like particles at a pH of 7.4 in 10 mM MOPS.

Finally, ST1-QAA is a modified form of the original self-assembling viral like particle, TecVir, with two notable additions; a DNA-binding domain and the RGD-binding domain to the C- and N-termini, respectively. These additions aim to provide additional biological stability and increased uptake into cells for transfection. Preliminary studies showed that transfection with ST1-QAA was possible (not shown), however further work was required to validate this. Plans for cell survival assays were in place, in addition to transfection studies with HEK and HeLa cells. However, due to the high amount required per assay (1.5 mg peptide for each assay in triplicate), and the questionable purity of the peptide, it was decided to wait until pure peptide could be finally synthesised. This was then affected by the Covid-19 pandemic.

Viral-like particles, such as ST1-QAA and TecVir, are an example of the emerging technology in *de novo* design of peptides. This field has seen a rapid expansion since the new millennium - primarily in the form of small antimicrobial peptides and peptide based hydrogels.[295, 311, 320, 321] In addition, the generation of self-assembled peptide nanoparticles in the past decade have shown enhanced stability and versatility of function over non-self-assembled systems.[292, 293, 298, 322] These enhanced effects show great potential to take rationally designed peptides from the lab into commercial use, or even into a clinical setting.[294] However, more

work is needed to fully characterise the assembly and stability of these systems. The work in this chapter hopes to set the foundation for understanding how these nanoparticles form, which is vital knowledge for efficient future use of ST1-QAA for DNA or RNA into cells.

Started making it,
had a breakdown,
Bon appétit.

— James Acaster (The Great Celebrity Bake Off, Episode 2)

6 Summary

Since the development of SMA-based membrane solubilisation, and the formation of lipid-polymer nanoparticles, the rapid development of polymer based solubilisation of membrane proteins has revolutionised the field.[142] It has enabled for the extraction of membrane proteins, without the use of detergents, to retain the native lipid environment and therefore increasing protein stability and native-like behaviour.[137, 237, 323] However, the rapid expansion of SMA-based and novel polymers has led to a confusing landscape -with only SMA polymers being characterised in an in-depth and comparative manner.[141, 203, 324, 325] This makes it difficult to understand the optimal solubilisation conditions required for specific membrane and protein needs, and the effect of these conditions on solubilisation efficiency and the biophysical properties of membranes in these systems.

Chapter 2 presented the optimisation of a high-throughput, expandable, and standardised assay to assess polymer solubilisation of membrane models across several conditions. This is the first assay of its kind designed to assess lipid-polymer nanoparticle formation for numerous polymer types (SMA 3:1, SMA 2:1, DIBMA and PMA) in an adaptive framework. The work utilised a new metric, solubilisation efficiency (Figure 2.3 A,B) for an easier comparison of membrane solubilisation between polymers, to determine the optimal solubilisation conditions of SMA 3:1, SMA 2:1, DIBMA and PMA for two model membranes: DMPC and POPC:POPG

(3:1). This chapter corroborated literature findings that solubilisation by maleic acid containing polymers is preferred in alkaline conditions (pH > 7.2), with a sharp solubilisation efficiency penalty in acidic conditions (pH < 6.5 for SMA, < 5 for DIBMA) for both DMPC and POPC:POPG (3:1) membrane models.[141, 143] In addition to this, it showed a novel estimation of the pKa of DIBMA's maleic acid groups (pKa of ~5). PMA was shown to be pH insensitive in the formation of DMPC-PMA nanoparticles, however the solubilisation efficiency was affected when solubilising charged membrane models. Chapter 2 also shows that for neutral membrane models, minimal additional salt is required for solubilisation, with 50 mM NaCl being sufficient for optimal solubilisation by all polymers tested. However, in charged membrane models there are two distinct differences between SMA polymers and the DIBMA and PMA polymers: Firstly, the solubilisation efficiency is in general higher in SMA polymers for charged membrane models. Secondly, SMA polymers were observed to require low amounts of additional salt (150-300 mM) for optimal solubilisation (> 80%), whilst both DIBMA and PMA required > 500 mM for optimal solubilisation (> 50% and ~20%, respectively). This high-salt requirement for DIBMA and PMA in charged membranes was a novel finding of this chapter, and only possible due to the comparative nature of the assay.

Chapter 3 used the solubilisation conditions discovered explored in Chapter 2 to examine nanoparticles formed from DMPC lipid dispersions and the four polymers in 'ideal' conditions (pH 7.4, 100 mM NaCl). EM imaging showed the macromolecular structure of the DMPC-polymer nanoparticles, and indicated that the SMA-based nanoparticles are on average smaller and more homogenous than the DIBMA- and PMA-nanoparticles. Additionally, the chapter showed the development of assays using Laurdan fluorimetry, TEMPO partitioning, and the use of SASL probes to analyse the thermotropic properties of the DMPC-polymer nanoparticles. This eventually lead to an examination of these DMPC-polymer nanoparticles by a combination of DSC and 5-PCSL cw-EPR experiments and comparison to the well chracterised DMPC LUV model membranes. DSC and EPR methods showed that whilst all polymer types generated the same approximate degree of

lipid packing within these systems across the temperature range tested, the phase behaviour of the DMPC lipids was significantly more native-like in DMPC-DIBMA nanoparticles. However, DIBMA nanoparticles did still not under-go a similar phase transition as observed in DMPC LUVs.

Chapter 4 explored a unique feature of lipid-polymer nanoparticles, collisional lipid transfer. Whilst this was previously shown for the SMALP form of SMA 3:1 and 2:1 and DIBMA polymer, this chapter showed for the first time that this mixing method is also present in the LQ forms of SMA and the novel PMA polymer. This utilised the solubilisation of aLUVs, and showed that, for the first time, all native spatial order of the membrane is lost upon formation of the lipid-polymer nanoparticles. This will impact the current 'cookie-cutter' model of solubilisation currently held in the literature, as the degeneration of membrane order to become homogenous may affect the previously assumed native-like behaviour observed in protein-nanoparticle assays. Chapter 4 also showed that this dynamic process occurs at different rates, seemingly dependant on the polymer structure, with SMA showing the fastest mixing rates by an order of magnitude to DIBMA and PMA. This rate of mixing was also shown to linearly increase with temperature. The chapter goes on to show that this unique and ubiquitous property of lipid-polymer nanoparticles can be used to specifically titrate in lipids to polymer containing nanoparticles. This was shown through the use of the well characterised dependance of CcO activity on cardiolipin (CL). This novel finding has great potential to delineate specific lipid-protein interactions from generic membrane properties in membrane protein behaviour. However, to be more widely adapted the technique shown in this thesis requires further optimisation, in particular through a more optimised purification protocol, and to be better adapted to mass spectrometry methods. This property, in addition to the use of lipid-polymer nanoparticles in the extraction of native membrane lipids, highlights lipid-polymer nanoparticles as a favoured tool in lipidomics in the near future.

Chapter 5 explored the purification and biophysical characterisation of a novel self-assembling peptide, ST1-QAA. This peptide is a successor to the first *de novo*

self assembling peptide to form a viral like particle capable of transporting genetic material into mammalian cells, TecVir.[293] This chapter describes an optimised and robust protocol developed for the purification of ST1-QAA *via* HPLC. It goes on to characterise the self-assembly process of ST1-QAA through various biophysical techniques such as CD, FTIR, and EM imaging. In addition to general characterisation of the peptide, EM imaging at the 3 hour incubation time point has shown preliminary evidence of a putative intermediate stage of viral particle self assembly. However, due to the Covid-19 pandemic further exploration, such as capturing incubation times between 0-3 and 3-24 hours, was not possible. As ST1-QAA was designed based upon the basic template of TecVir,[293] the full characterisation of ST1-QAA formation and gene transfection is highly desirable to fully understand the impact of these modifications. Most importantly, the modification to improve cellular uptake (the RGD motif insertion), and the lysine-rich DNA binding region effectiveness must be fully understood to enable specialisation of these particles for even more specific targeting and improved DNA encapsulation.

The work in this thesis enables the future, wide-scale, characterisation of lipid-polymer nanoparticle formation. The assesment of this formation across a range of biophysical conditions should enable the optimised use of these polymers in terms of optimised membrane protein extraction condition using these polymers, replacing the currently used heuristic approach. Additionally, although this thesis shows that these lipid-polymer nanoparticles are more dynamic than previously assumed, the later work in this thesis (Chapter 4) has shown that this can be utilised as a novel tool in the exploration of lipid-protein interactions to compliment to the currently used lipidomic methods.

Appendices

I like boring things

— Andy Warhol

A

Appendix for Chapter 2

Contents

A.1 Buffers used for OD_{350} assay development 161
A.2 Concentration control for lipid concentration *vs* OD_{350} 163
A.3 Raw OD_{350} values for spectrophotometry 164
A.3.1 OD_{350} for pH range 164
A.3.2 OD_{350} for NaCl titration 166
A.3.3 OD_{350} for Mg^{2+} titration 168
A.3.4 OD_{350} for Ca^{2+} titration 171
A.4 Raw DLS histograms 173
A.5 Current solubilisation conditions in literature 182

A.1 Buffers used for OD_{350} assay development

All buffers were generated as a 100 mL stock, with a total concentration of 0.125 M. This large volume was to ensure lower measurement error during stock preparation, and consistent buffering environment throughout the assay lifetime. 0.125 M concentration of buffer components was chosen as when the aqueous lipid film (resuspended in dH_2O) was diluted in desired buffer the final ionic strength would be 0.1 M.

The different buffering salts used for pH titration are shown in Table A.1. For pH buffers all salts were dissolved initially in 80 mL of dH_2O prior to pH

Table A.1: Summary of all pH buffer stock mixtures used for OD_{350} solubilisation assays. Stocks were prepared at a 1.25× concentration, to account for the dilution required for lipid dispersion addition. Ionic strength is reported as final concentration, which is the concentration found within the plates during measurement of OD_{350}. * denotes the ionic strength for Tris calculated using online calculator tool (https://www.liverpool.ac.uk/pfg/Tools/BuffferCalc/Buffer.html)

pH Value	**Buffer components**	**Calculated ionic strength (M)**
3.0	0.33 g Sodium citrate dihydrate, 2.19 g Citric acid	0.9 M
4.0	1.24 g Sodium citrate dihydrate, 1.59 g Citric acid	0.9 M
5.0	2.12 g Sodium citrate dihydrate, 1.02 g Citric acid	0.9 M
6.0	0.28 g K_2HPO_4, 1.50 g KH_2PO_4	0.9
6.8	1.00 g K_2HPO_4, 0.92 g KH_2PO_4	0.9
7.0	1.17 g K_2HPO_4, 0.79 g KH_2PO_4	0.9
7.2	1.34 g K_2HPO_4, 0.65 g KH_2PO_4	0.9
7.4	1.52 g K_2HPO_4, 0.52 g KH_2PO_4	0.9
7.6	1.69 g K_2HPO_4, 0.38 g KH_2PO_4	0.9
7.8	1.86 g K_2HPO_4, 0.25 g KH_2PO_4	0.9
8.0	2.03 g K_2HPO_4, 0.11 g KH_2PO_4	0.9
8.5	1.514 g Tris-HCl	0.016*
9.0	1.514 g Tris-HCl	0.005*
10.0	0.49 g $NaHCO_3$, 0.71 g Na_2CO_3	0.4

being recorded and adjusted. Once the desired pH was reached, the buffer was diluted to a final volume of 100 mL.

NaCl, Mg^{2+}, Ca^{2+} stocks were buffered with 10 mM HEPES to a pH of 7.4 from a 0.5 M stock solution. The desired ionic concentration was then obtained with measured aliquots of 5 M NaCl stock solution. Divalent cation titration buffers were obtained from master stocks of magnesium chloride (1 M $MgCl_2$), and

calcium chloride (1 M $CaCl_2$) and had a consistent ionic strength of 0.125 M throughout the divalent cation titration range, with a final ionic strength of 100 mM during measurement.

A.2 Concentration control for lipid concentration *vs* OD_{350}

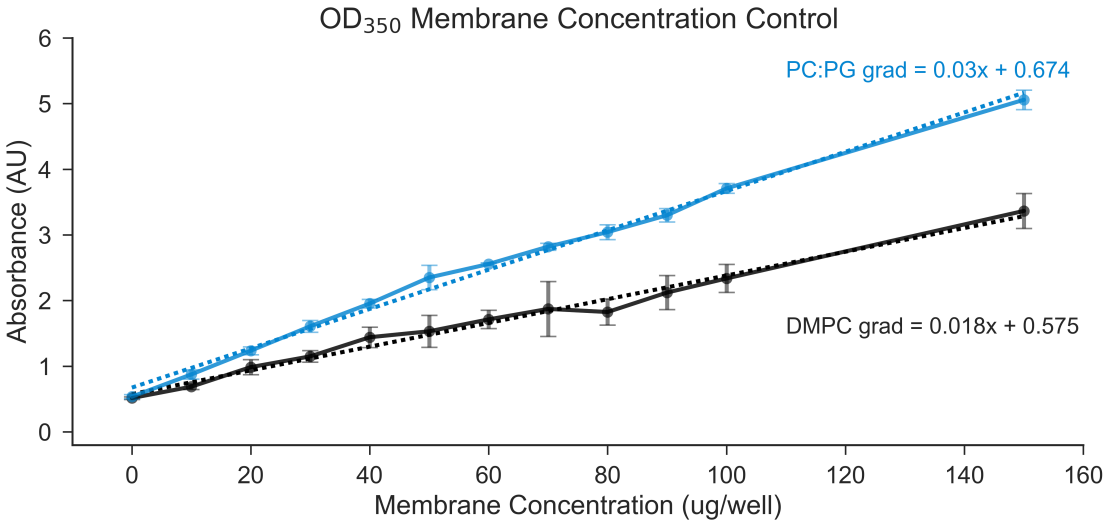


Figure A.1: OD_{350} measurements of DMPC and POPC:POPG (3:1) dispersions used in the high-throughput solubilisation assays in Chapter 2, showing linear increase in OD_{350} with lipid concentration in the range used in this assay. Control value of OD = 0.58 AU is used for the calculation of solubilisation efficiency, as described in §2.2.4

To ensure linearity of OD_{350} with respect to the concentration of lipid dispersion used throughout the assays described in §2.2.4, a concentration control was performed for both lipid types used within the chapter. The assay in question utilised a lipid concentration of 100 μg/mL, so the concentration control was designed from 0-150 μg/mL. As can be see in Figure A.1, both DMPC and POPC:POPG (3:1) lipid dispersions show a linear increase in OD_{350} for the concentration range tested. This indicates that it is possible to normalise the data, in the manner described in §2.2.4, to obtain a measure of solubilisation efficiency. Additionally, absorbance measurements were recorded for all polymers and buffer components used within this section (not shown) which showed that no assay component absorbed significantly at this wavelength.

A.3 Raw OD_{350} values for spectrophotometry

Original optical density and DLS data were gathered, under supervision by a previous lab member.[216] This preliminary work showed that OD_{350} can be used to efficiently analyse solubility of polymer/DMPC mixtures in different buffer conditions. However, the data were limited and lacked the required levels of sensitivity due to limitations in sample preparation volume and the machine used (As shown in Figure 2.2, and in full detail in Figure A.2). Further work, as discussed in §2 developed an assay utilising a plate reader. This allowed for a more high throughput, higher resolution, system with the addition of automatic analysis through python scripts, which is explained in detail in Chapter 2. The raw OD_{350} data can be seen in the following figures, with the processed data (normalised against membrane OD_{350} as a measure of efficient solubilisation) can be observed in Chapter 3.

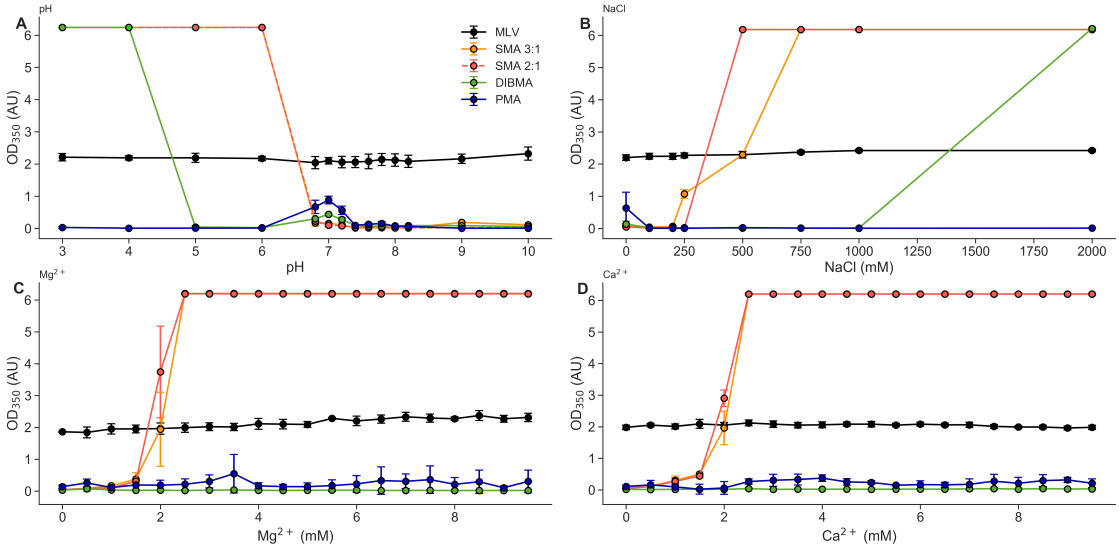


Figure A.2: OD_{350} measurements of DMPC dispersions solubilised by SMA 3:1 (orange), SMA 2:1 (red), DIBMA (green), and PMA (blue) across pH range (A), ionic strength (B) and divalent cation titrations of magnesium (C) and calcium (D). Average initial membrane OD_{350} is shown in black (MLV).

A.3.1 OD_{350} for pH range

Figure A.3 A (DMPC) shows the OD_{350} for all polymer samples decreased under preferable solubilisation conditions. This can be most obviously seen for SMA

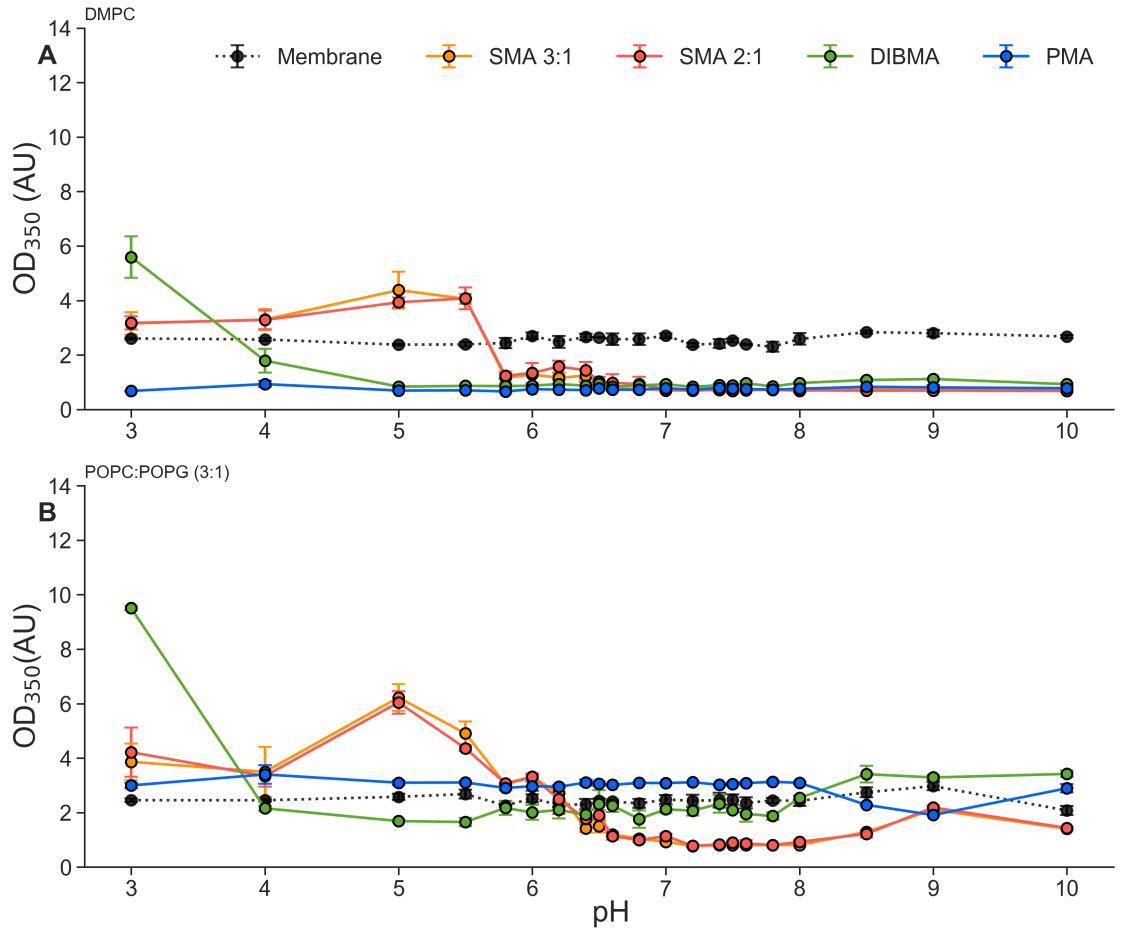


Figure A.3: OD_{350} measurements of (A) DMPC and (B) POPC:POPG 3:1 membrane solubilisation by SMA 3:1 (orange), SMA 2:1 (red), DIBMA (green), and PMA (blue) across pH conditions. Average initial membrane OD_{350} used for normalisation is shown in black.

variants greater than a pH of 5.5. For charged membrane systems (Figure A.3 B) the general trends as seen in DMPC membranes were conserved: For SMA polymers there is an 'ideal' solubilisation window above pH 5.5, whilst for DIBMA there was a slightly higher tolerance for a more acidic pH at around pH 4. However, PMA appeared to fail to solubilise any significant amount of membrane for all pH values tested, aside from pH 8.5-9. This was in contrast with DLS data showing PMA nanopaticles were formed under the range tested. It was therefore concluded that the best practice was to use the raw OD_{350} data to infer broad trends, especially for more complex systems. To ensure clarity, it was decided to normalise the OD_{350} data against the membrane average (shown in black) and a buffer control (not

shown) as seen in Figure 2.3 The equation can be observed in Equation 2.1.

A.3.2 OD_{350} for NaCl titration

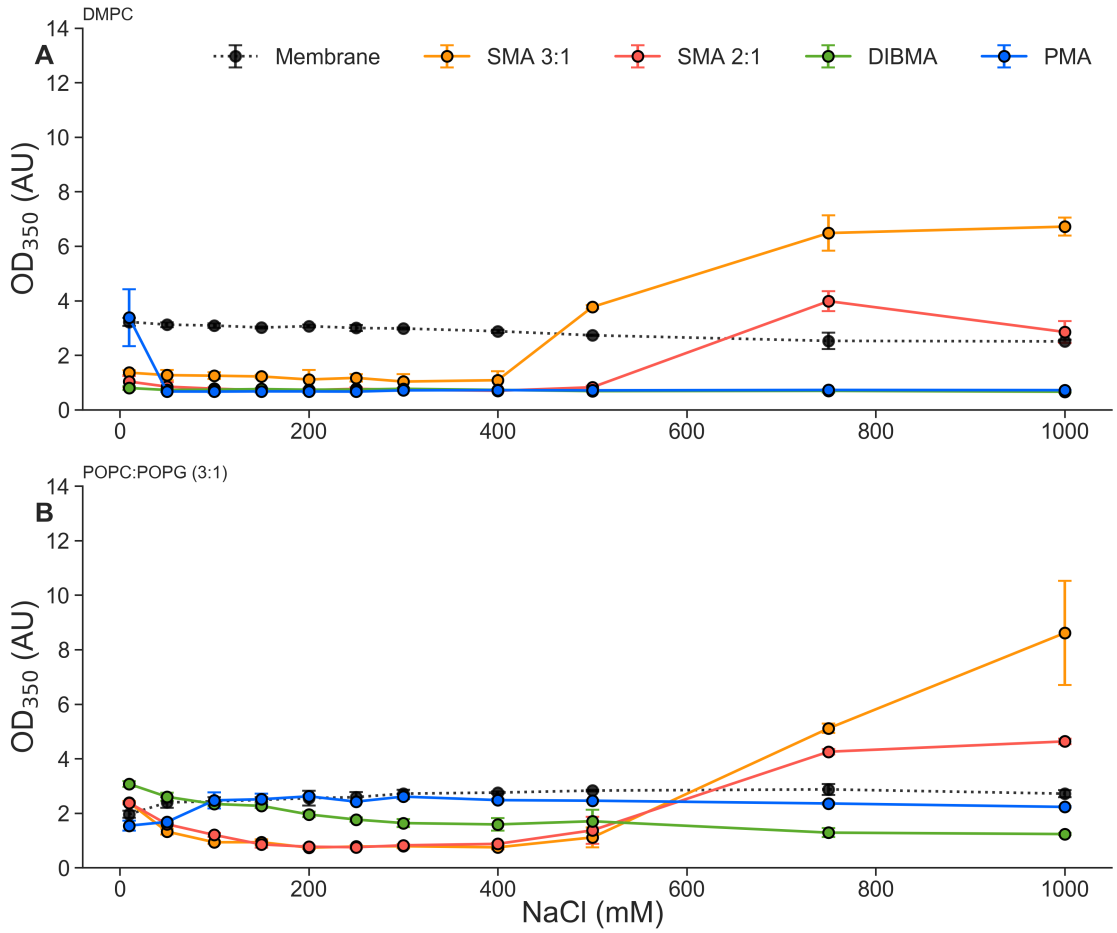


Figure A.4: OD_{350} measurements of (A) DMPC and (B) POPC:POPG 3:1 membrane solubilisation by SMA 3:1 (orange), SMA 2:1 (red), DIBMA (green), and PMA (blue) across NaCl concentration. Average initial membrane OD_{350} used for normalisation is shown in black.

Similarly to Figure A.3, the overall trends seen in Figure A.4 A were broadly repeated in the charged membrane system seen in Figure A.4 B. Solubilisation tends to be most efficient with some additional salt in the buffer, where the exact concentration was dependent on both the polymer composition and the membrane charge. For SMA systems this ideal range was observed to be between 100 mM-500 mM before polymer aggregation occured. For the less strongly hydrophobic polymers DIBMA and PMA solubilisation was preferred in strongly ionic conditions.

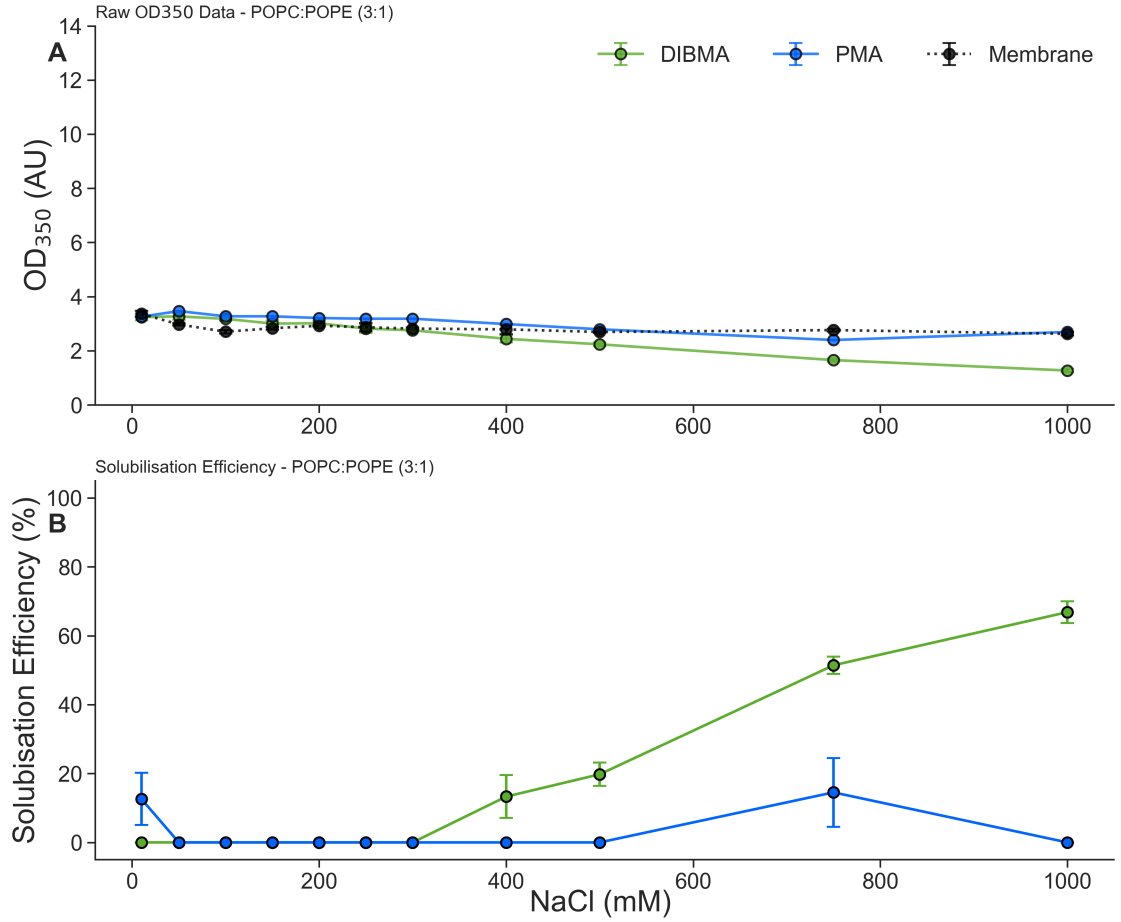


Figure A.5: Raw OD_{350} measurements for NaCl for POPC:POPE membranes (A), with membrane (black), DIBMA (green), and PMA (blue) average and errors shown. (B) shows solubilisation efficiency of DIBMA (green) and PMA (blue) of POPC:POPE (3:1) membranes.

Due to the low solubilisation efficiency of DIBMA and PMA of POPC:POPG (3:1) membranes, it was decided to do a preliminary test to compare between negatively charged membranes (POPC:POPG (3:1)) and positively charged membranes (POPC:POPE (3:1)). As it was known that both DIBMA and PMA can solubilise native membranes it was hypothesised that the low solubilisation efficiency of DIBMA and PMA in net negative charged membranes may be due to the simplistic membrane model used. Utilising a net positive charged membrane, the commonly used POPC:POPE (3:1), it was possible to show that DIBMA shows a similar necessity to ~200 mM NaCl before solubilisation occurs. However, PMA's positive charge appears to hamper the solubilisation of the positively charged membrane

more so than the negatively charged membrane shown in Figure A.4 B. This indicates that the weaker hydrophobicity of the DIBMA and PMA hydrophobic groups inhibits sufficient solubilisation (as detected by OD) of charged membranes, especially when presenting a net-positive charge. For simplicity and time limitations, only POPC:POPG (3:1) membrane models were examined in depth in addition to DMPC membranes.

A.3.3 OD_{350} for Mg^{2+} titration

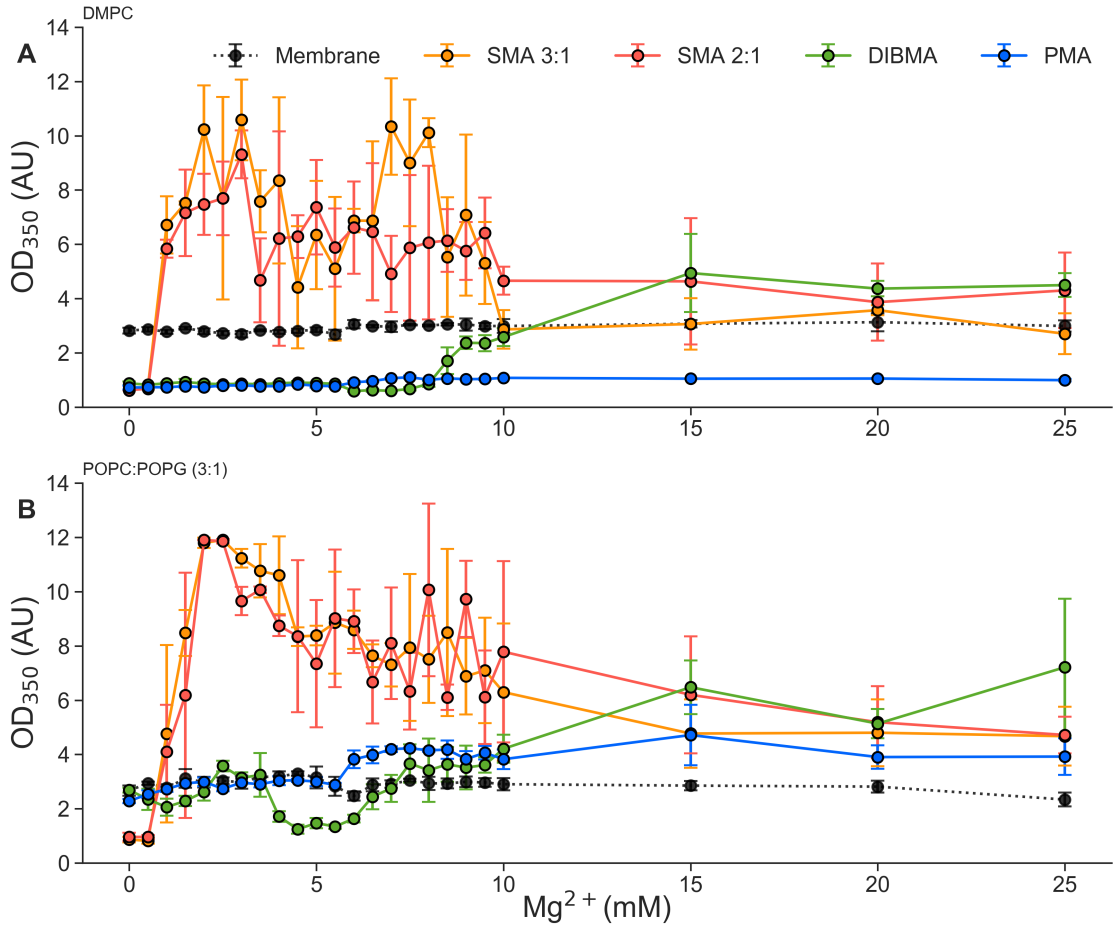


Figure A.6: OD_{350} measurements of (A) DMPC and (B) POPC:POPG 3:1 membrane solubilisation by SMA 3:1 (orange), SMA 2:1 (red), DIBMA (green), and PMA (blue) across Mg^{2+} concentration. Average initial membrane OD_{350} used for normalisation is shown in black.

The differences in polymer solubilisation efficiency was most prevalent when observing the effects of divalent cation concentration. The SMA variants were

intolerant to concentrations of even 1 mM of Mg^{2+}. Visual aggregates were observed immediately after addition of SMA above this concentration. These aggregates were also measured as an increase in OD_{350} (Figure A.6).

On the whole, DIBMA and PMA were more resistant to divalent cations than SMA. In neutral membranes, DIBMA was observed possessing a higher tolerance to divalent cation presence than SMA, showing precipitation of DIBMA above 8 mM Mg^{2+}, far above SMA's tolerance of 1 mM. For charged membranes however, a noticeable decrease in OD_{350} is observed for DIBMA between 3-6 mM. As has been noted by *Keller et al.*,[326] DIBMA has been observed previously to show an increased solubilisation efficiency of complex membranes with the addition of a small concentration of divalent cations. It is therefore likely that this the observed decrease in OD_{350} was due to this specific effect as described in the literature.

PMA was totally insensitive to divalent cation presence, showing no observable difference in neutral membrane models. For POPC:POPG (3:1) membranes, there is a slight increase in OD_{350} above 5 mM Mg^{2+}. This could be caused by an adsoprtion of magnesium ions onto the net-negative membrane surface, leading to a net-positive charge forming. As has been shown with POPC:POPE membranes (Figure A.5), PMA solubilisation efficiency decreases in buffers with low ionic concentration and positively charged membranes.

DLS measurements of the nanoparticles correlate well with the OD_{350} values, and confirm that optical density was a good indicator of solubilisation efficiency. For SMA it confirmed that in solutions of $>$ 1 mM Mg^{2+}, the polymer completely precipitates and therefore unable to form any nanoparticles of the expected size.[98]

DIBMA however, showed that particles were formed in solutions containing magnesium concentrations up to approximately 20 mM, although there was a shift in size distribution observed above 10 mM. This could be due to increased scattering of light by the polymer belt due to the presence of chelated magnesium ions, leading to a larger size being modelled by the software. However, it could be indicative of an increased particle size overall due to magnesium ion presence. As expected, both

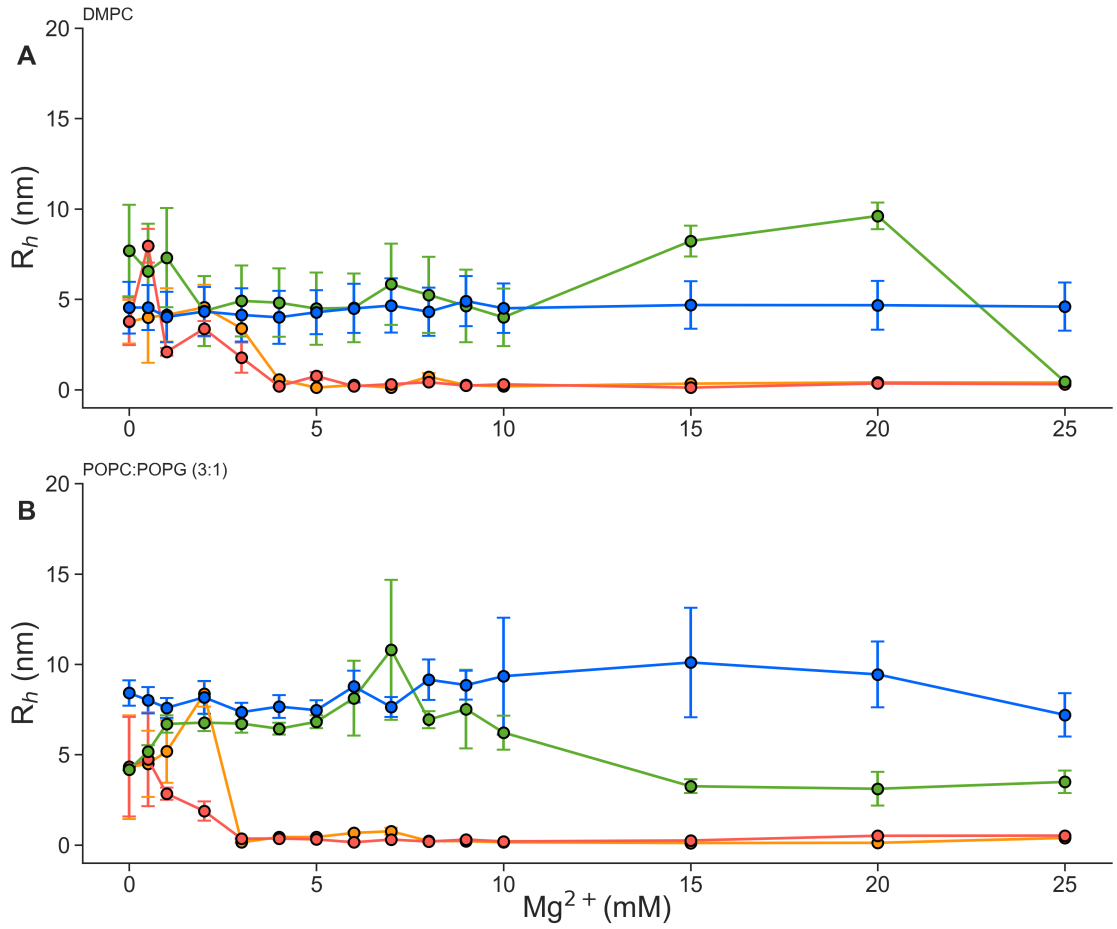


Figure A.7: DLS measurements of (A) DMPC and (B) POPC:POPG 3:1 membrane solubilisation by SMA 3:1 (orange), SMA 2:1 (red), DIBMA (green), and PMA (blue) across Mg^{2+} concentration.

the absorbance and DLS values showed that PMA was insensitive to the presence of divalent cations, at least in a neutral membrane systems.

For the charged model membranes, as seen in Figures A.6 and A.7, slight differences between the neutral DMPC membranes and the charged POPC:POPG (3:1) membranes can be observed. Whilst SMA continued to aggregate due to buffer conditions immediately, DIBMA showed an increase in solubilisation efficiency with small concentration of Mg^{2+} (4-6 mM, Figure A.6 B). This was correlated with a slight increase in average R_H value (Figure A.7). This peculiar behaviour could be linked to an enhanced charge screening effect between the negatively charged POPG and the negatively charged maleic acid groups through membrane associated divalent cations. The optimal concentration range would therefore

be dependant on the concentration of POPG within the system, as well as the concentration of DIBMA applied.

At a concentration > 5 mM the Mg^{2+} appeared to inhibit PMA solubilisation of POPC:POPG (3:1) membranes, most likely due to the charge repulsion of the positive PMA by the positive Mg^{2+} on the membrane surface. This inhibition appeared to also slightly affect particle size, where the R_H showed a slight increase in both size and error at higher concentrations of magnesium, within charged membranes (Figure A.7 B), but not for the DMPC membranes (Figure A.7 A).

A.3.4 OD_{350} for Ca^{2+} titration

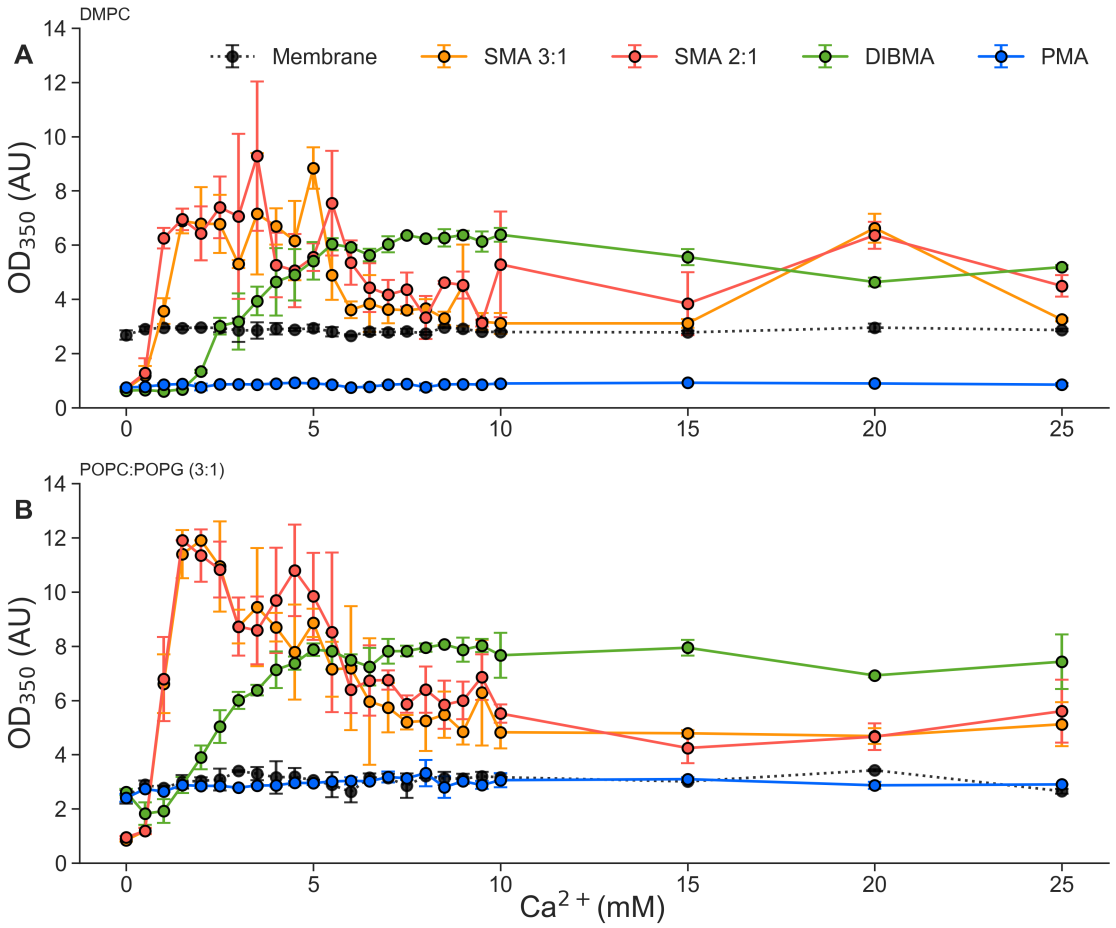


Figure A.8: OD_{350} measurements of (A) DMPC and (B) POPC:POPG 3:1 membrane solubilisation by SMA 3:1 (orange), SMA 2:1 (red), DIBMA (green), and PMA (blue) across Ca^{2+} concentration. Average initial membrane OD_{350} used for normalisation is shown in black.

Figure A.8 shows the sensitivity of the polymers tested to calcium concentration. As seen previously in Figure A.6 for magnesium. It was important to analyse both Mg^{2+} and Ca^{2+} presence, as these have been shown to have a differing effect on DIBMA solubilisation on membranes,[152] and both are common additions to buffers, especially for membrane protein activity, such as ATPases.[327]

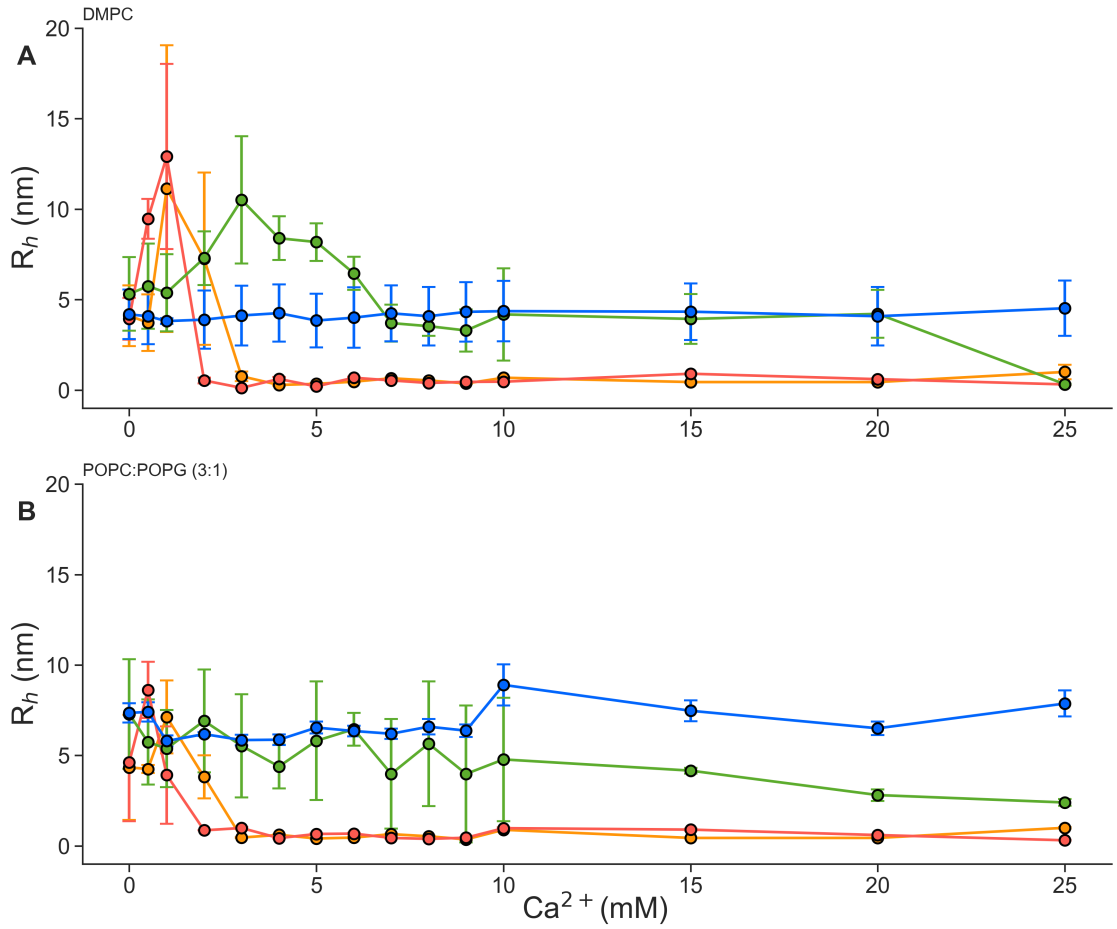


Figure A.9: DLS measurements of (A) DMPC and (B) POPC:POPG 3:1 membrane solubilisation by SMA 3:1 (orange), SMA 2:1 (red), DIBMA (green), and PMA (blue) across Ca^{2+} concentration.

SMA showed complete intolerance to Ca^{2+} (Figure A.8), this was in line with the trend observed for Figure A.6. Similarly, the R_H for the calcium titration for SMA-based nanoparticles were consistent with those observed for magnesium. Where the R_H showed a a brief increase in particle size above the expected R_H for SMA nanoparticles, this was in good agreement to the increase in OD_{350} between 1-3 mM for Ca^{2+}. As the divalent cation concentration increased the

solubilisation efficiency rapidly dropped off, which was quantified by an increase in OD_{350}, as the polymer precipitated, and a reduction of particle R_H to 0 nm as nanoparticles are no longer formed.

The effect of Ca^{2+} compared to Mg^{2+} on DIBMA was the most pronounced difference of the polymers. For neutral membranes, the tolerance for both cations appeared to be the same at approximately ~8 mM X^{2+}. However, DIBMA appeared to have an increased sensitivity to Ca^{2+} ions (~2 mM Ca^{2+}) over magnesium (8 mM Mg^{2+}), in charged membrane systems. Due to the increased sensitivity to Ca^{2+}, the enhanced solubilisation observed in the magnesium titration around 5 mM Mg^{2+} was not observed in the calcium titration at any concentration. However, the difference in ions did not affect the average size of DIBMA nanoparticles in the presence of either ion, nor the trends across concentration. This indicated that the effect is only present during solubilisation and does not affect nanoparticle stability.

A.4 Raw DLS histograms

The DLS measurements shown in Chapter 2 are reported as a single hydrodynamic radius per polymer per measurement point. In actuality the output of DLS is a histogram, which for clarity and size requirements were not included in the main body of the text in this thesis. The raw DLS histograms (in the 'mass' mode) for the pH, NaCl, and divalent cation titrations are shown below. A * symbol denotes the location of the R_H reported by the OmniSize 3.0 software, with the reported R_H and error values taken for plotting in Figures 2.3, 2.4, A.6, and A.8.

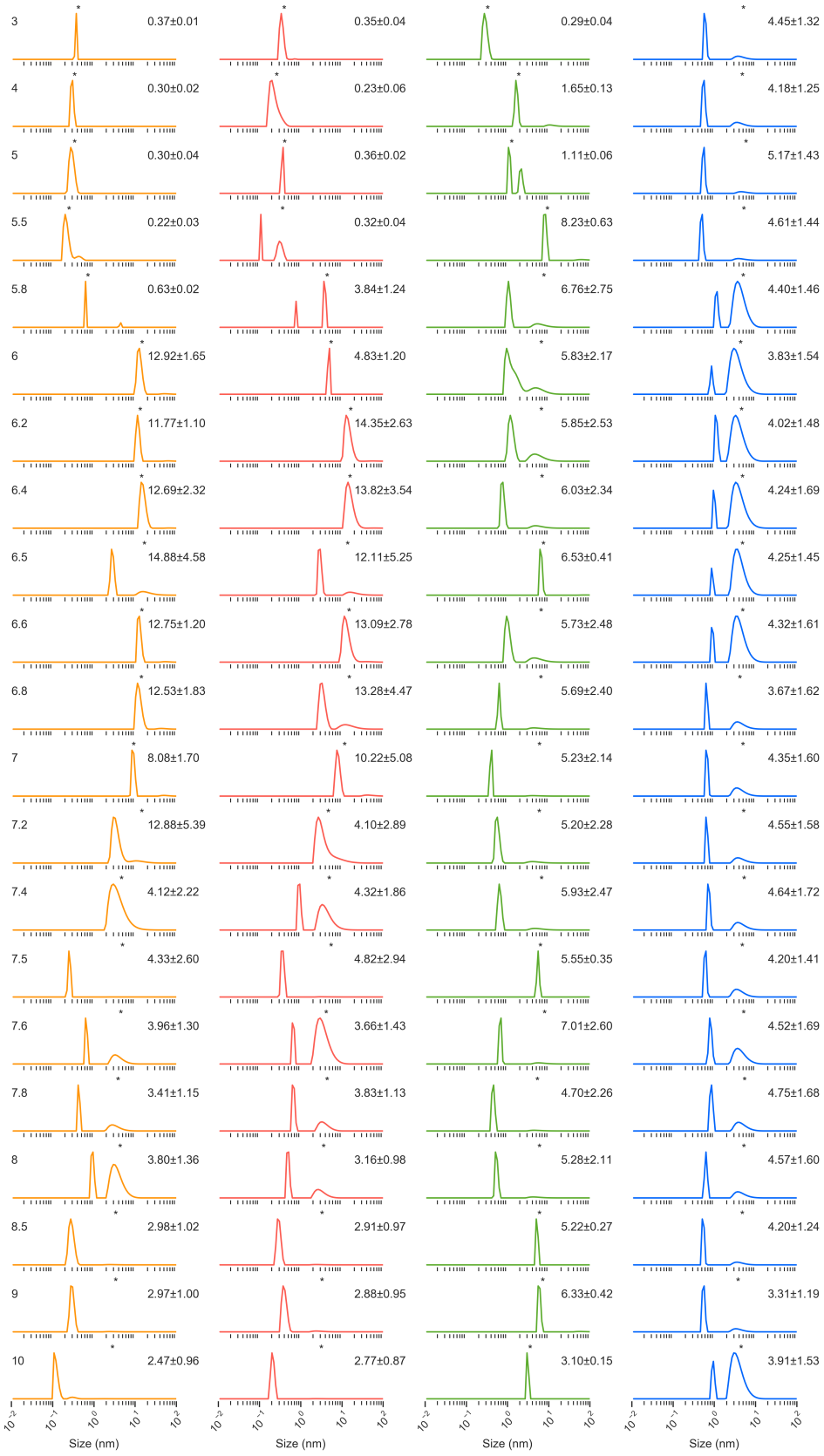


Figure A.10: DLS measurements of DMPC membrane solubilisation by SMA 3:1 (orange), SMA 2:1 (red), DIBMA (green), and PMA (blue) across pH range.

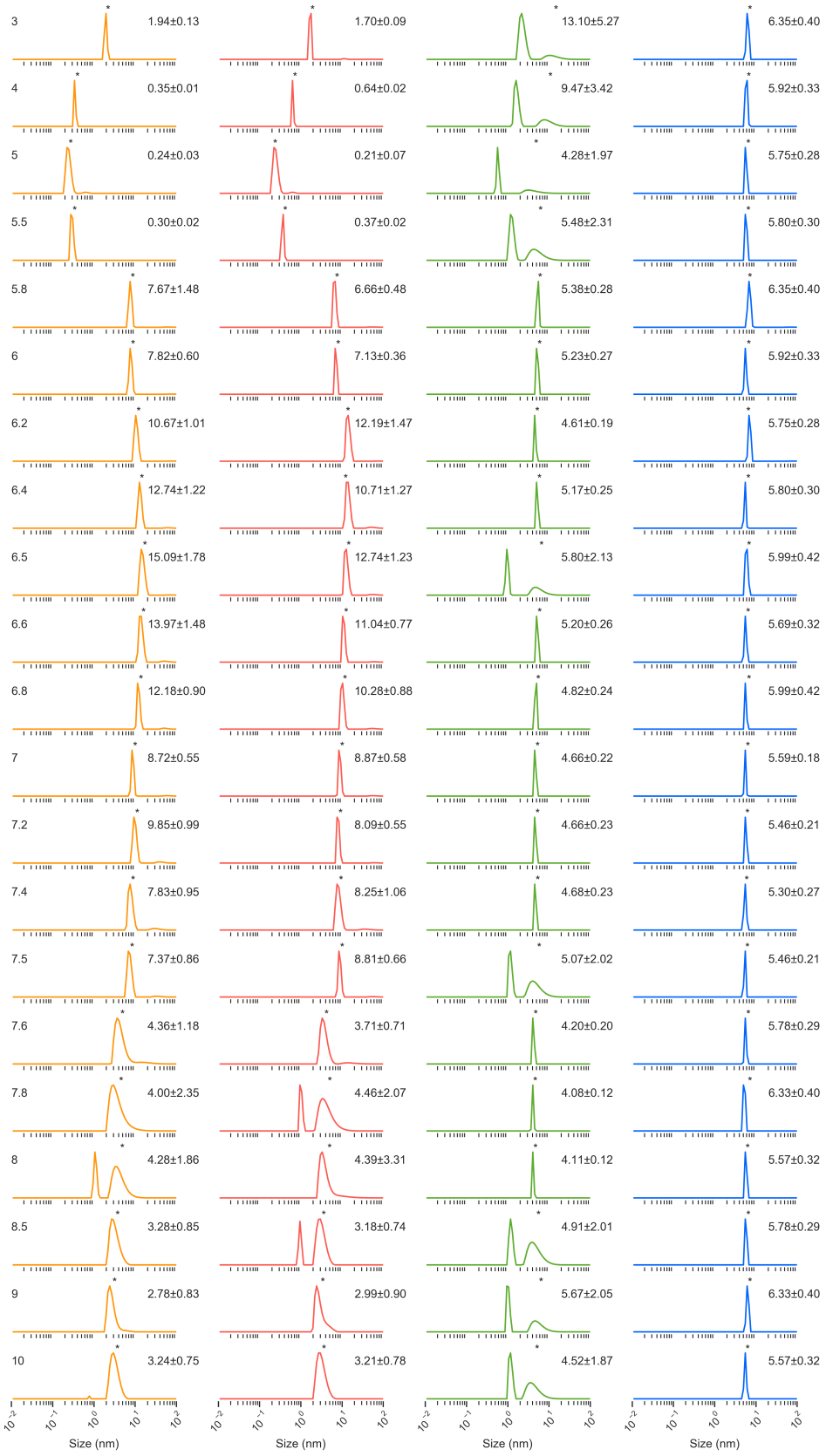


Figure A.11: DLS measurements of POPC:POPG (3:1) membrane solubilisation by SMA 3:1 (orange), SMA 2:1 (red), DIBMA (green), and PMA (blue) across pH range.

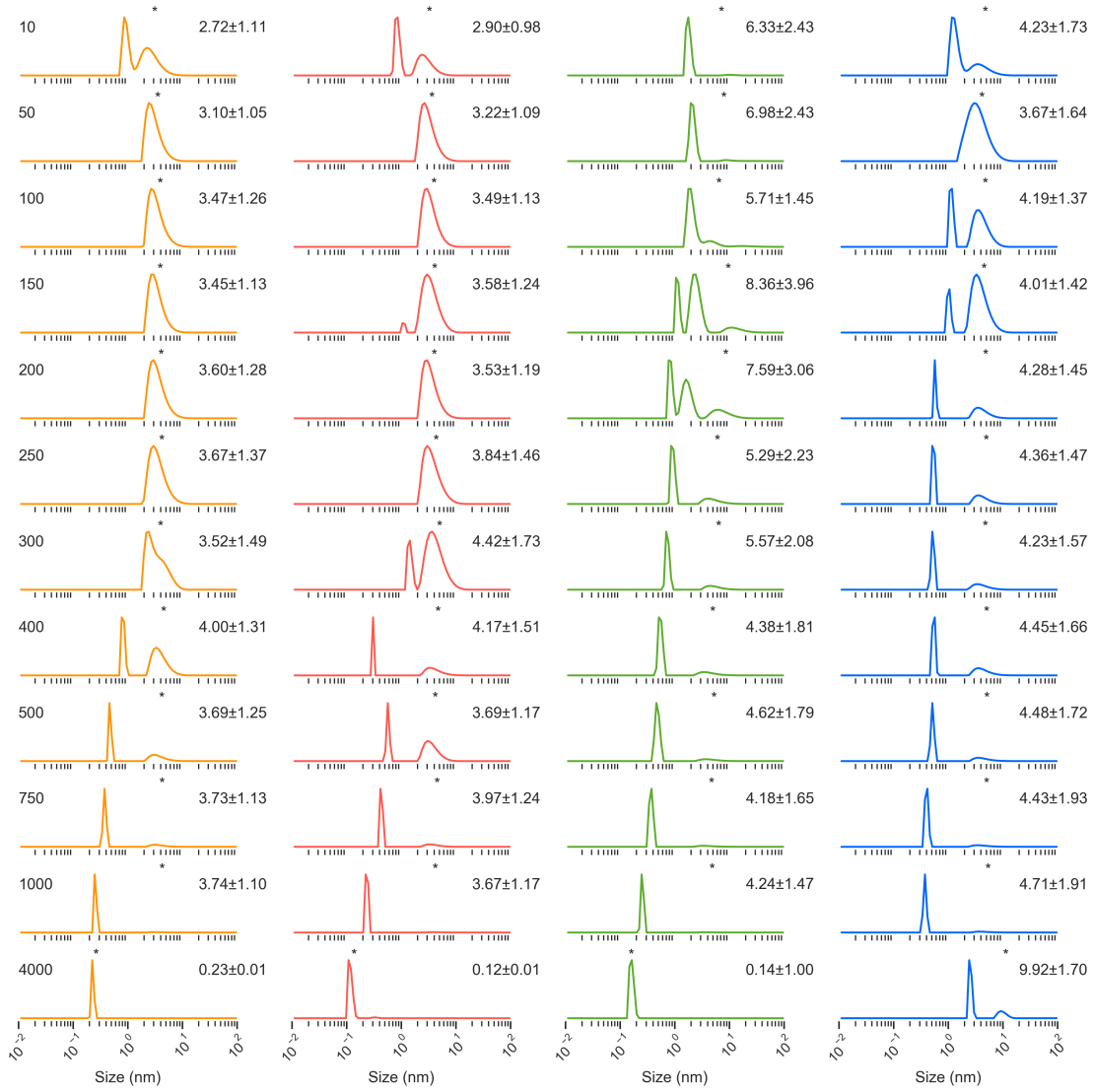


Figure A.12: DLS measurements of DMPC membrane solubilisation by SMA 3:1 (orange), SMA 2:1 (red), DIBMA (green), and PMA (blue) across NaCl concentration titration.

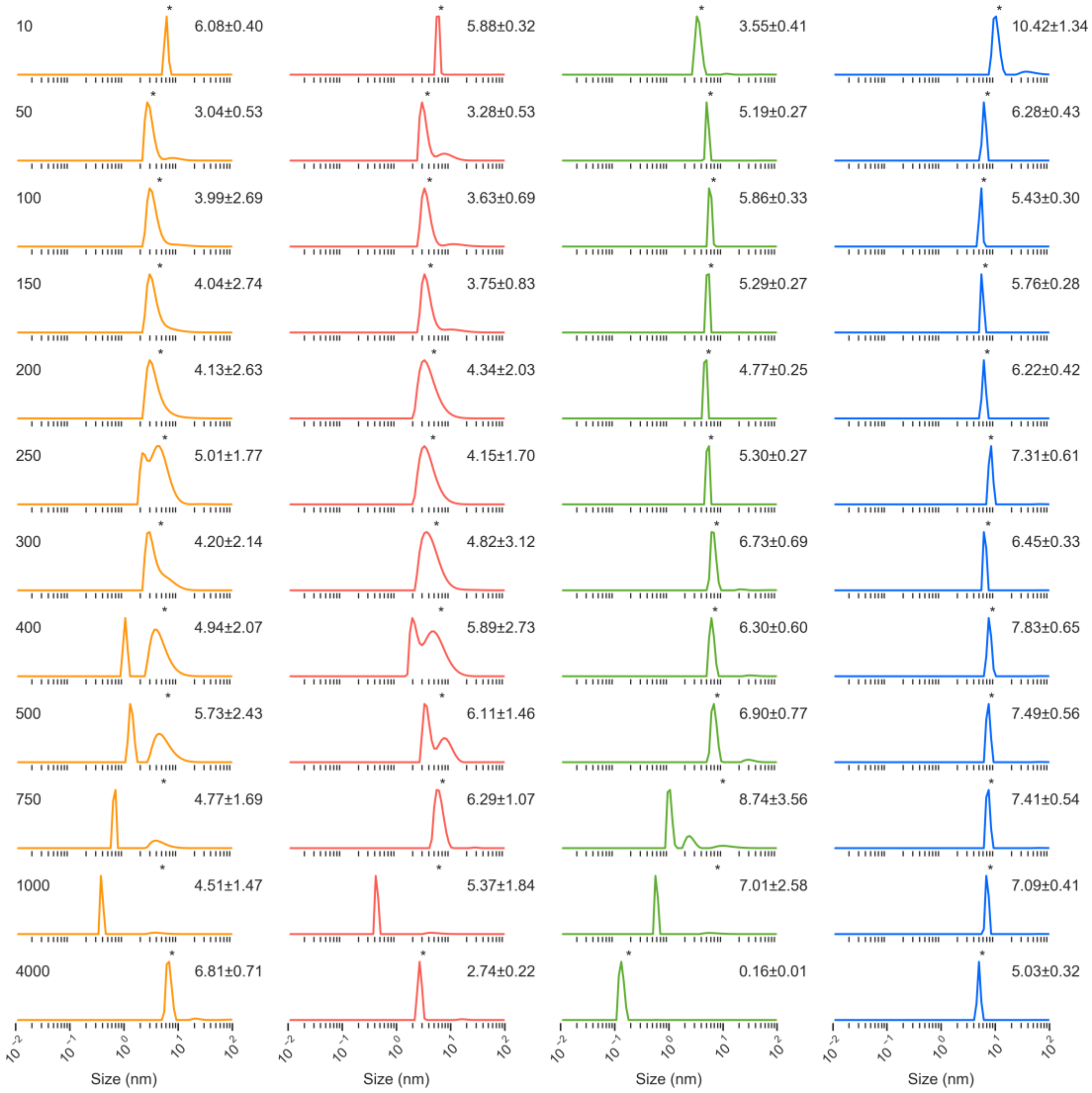


Figure A.13: DLS measurements of POPC:POPG (3:1) membrane solubilisation by SMA 3:1 (orange), SMA 2:1 (red), DIBMA (green), and PMA (blue) across NaCl concentration titration.

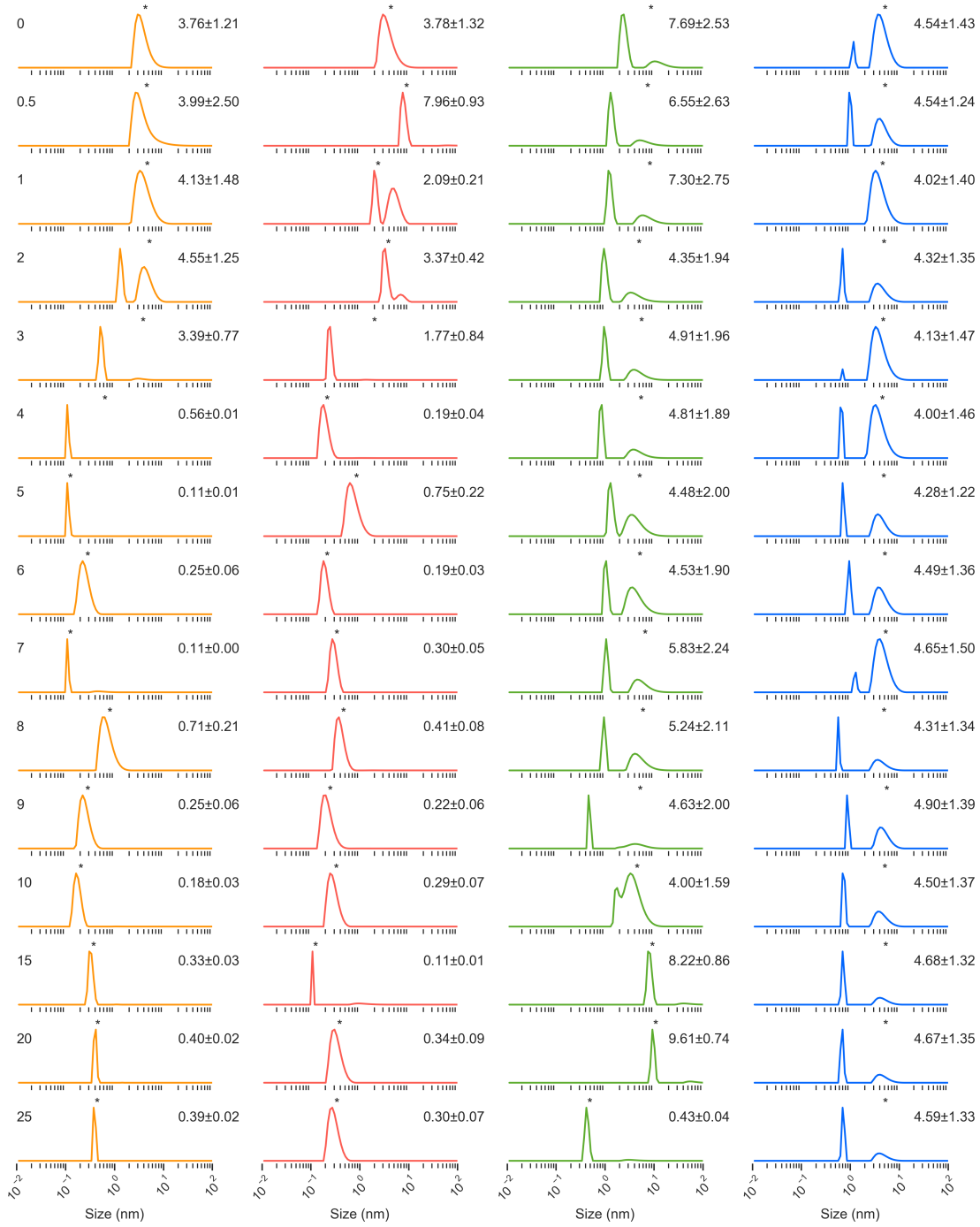


Figure A.14: DLS measurements of DMPC membrane solubilisation by SMA 3:1 (orange), SMA 2:1 (red), DIBMA (green), and PMA (blue) across Mg^{2+} concentration titration.

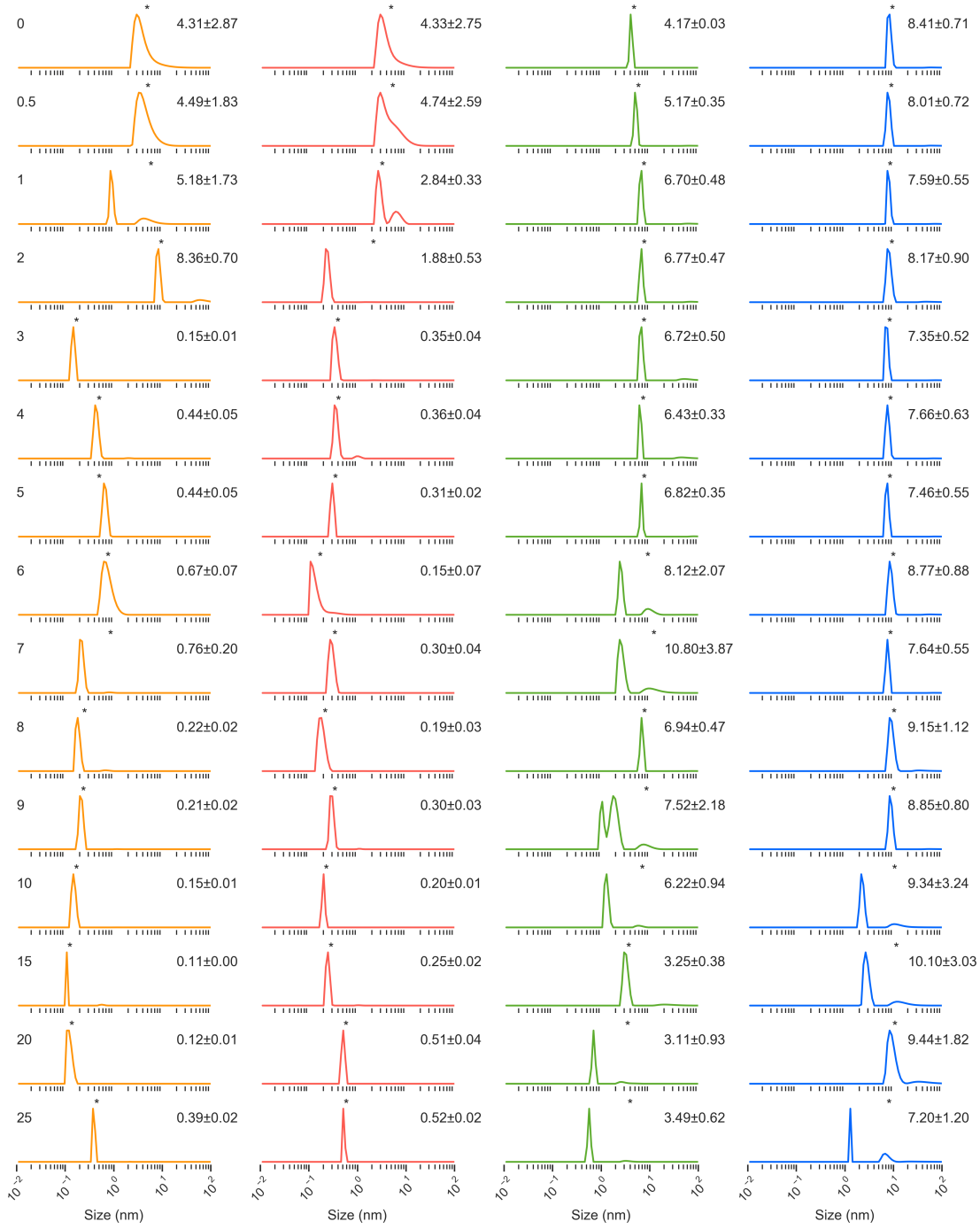


Figure A.15: DLS measurements of POPC:POPG (3:1) membrane solubilisation by SMA 3:1 (orange), SMA 2:1 (red), DIBMA (green), and PMA (blue) across Mg^{2+} concentration titration.

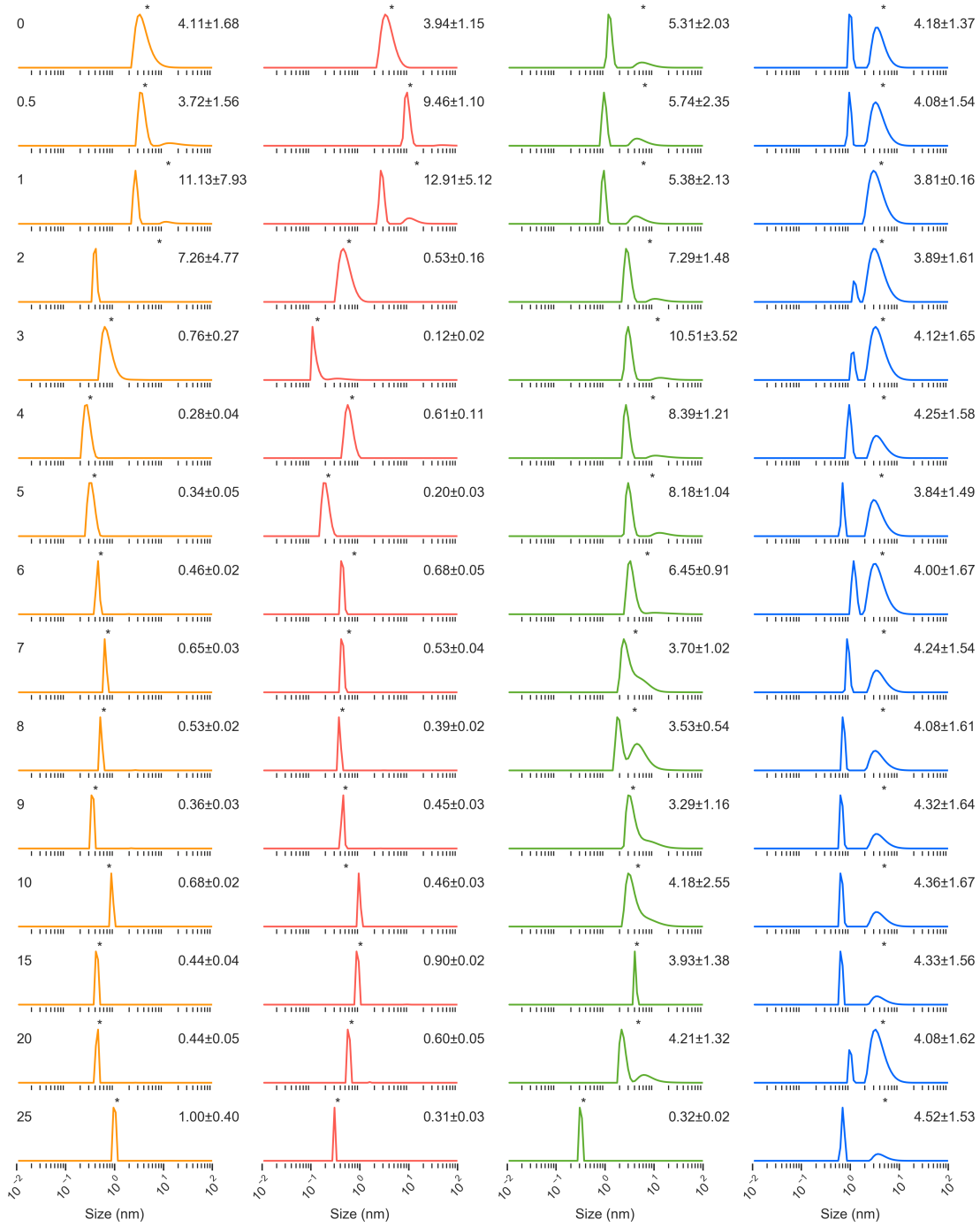


Figure A.16: DLS measurements of DMPC membrane solubilisation by SMA 3:1 (orange), SMA 2:1 (red), DIBMA (green), and PMA (blue) across Ca^{2+} concentration titration.

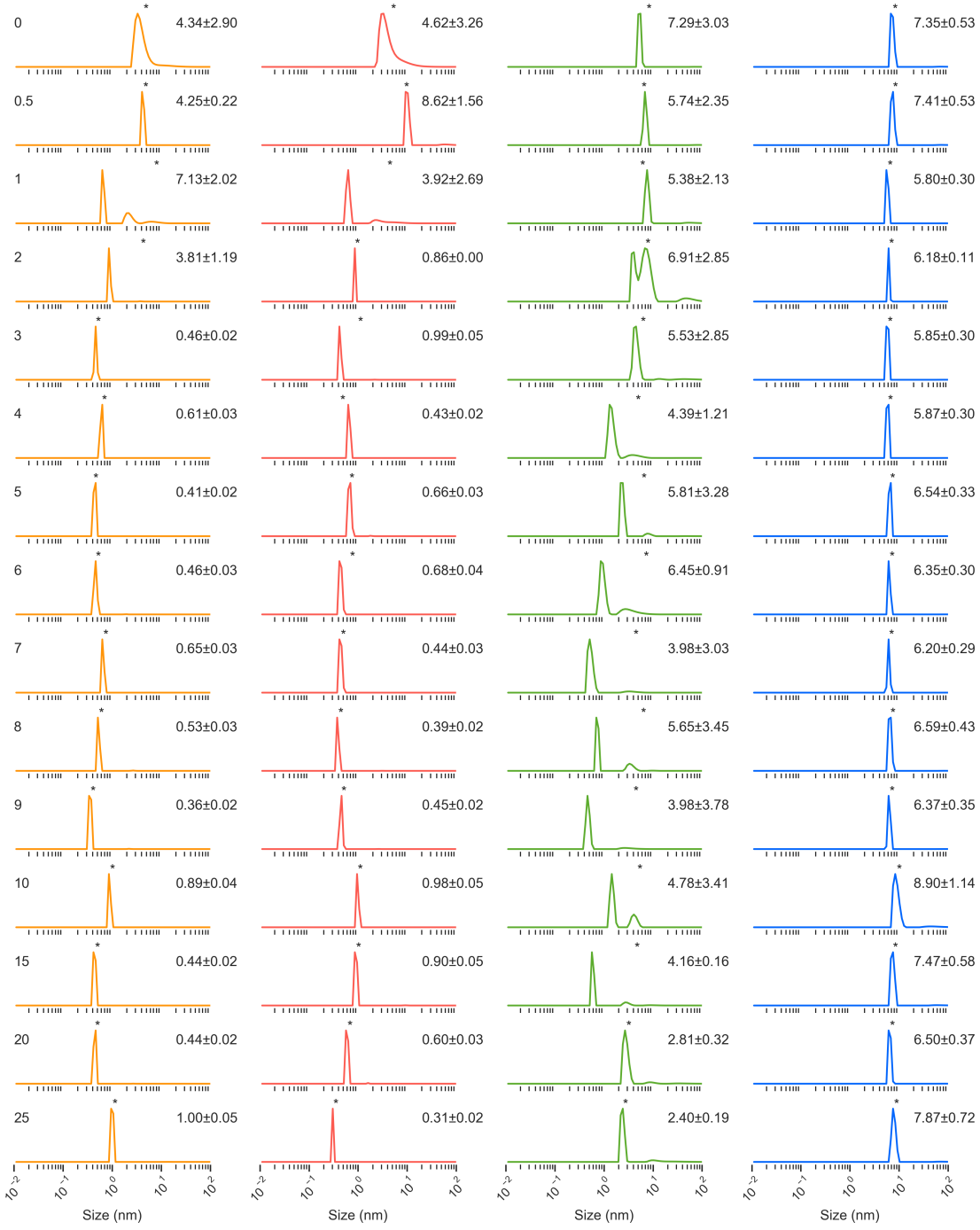


Figure A.17: DLS measurements of POPC:POPG (3:1) membrane solubilisation by SMA 3:1 (orange), SMA 2:1 (red), DIBMA (green), and PMA (blue) across Ca^{2+} concentration titration.

A.5 Current solubilisation conditions in literature

The table that follows is a compilation of all currently available conditions that have been used to successfully solubilise integral membrane proteins through the use of polymers.

Table A.2: Summary table of all successful conditions used to solubilise and extract membrane proteins with polymers to date, sorted chronologically from time of publication.

Date	Ref.	Protein	Organism	Polymer	Polymer Concentration	pH	NaCl	Incubation Time	Incubation Temp.	Additional Conditions
M. Orwick *et al.* (2012)	[137]	Bacteriorhodopsin (bR)	*H. salinarum*	SMA 3:1 (Lipodisq)	2.5% *(w/v)*	8	300 mM	1 hr	RT	Solubilised in presence of DMPC LUVs
Sahu *et al.* (2013)	[222]	KCNE1	*E.coli*	SMA 3:1 (Lipodisq)	1.25% *(w/v)*	6.5	-	Overnight	4°C	Solubilisation of 3:1 POPC:POPG proteoliposomes
Long *et al.* (2013)	[182]	Complex IV	*S.cerevisiae*	SMA 3:1 (Lipodisq)	2x excess *(w/w)*	8	200 mM	20 mins	26°C	Solubilised pre-purified mitochondria
Swainsbury *et al.* (2014)	[328]	Reaction Center (RCs)	*Rba.sphaeroides*	SMA 2:1 (Polyscience)	1.5% *(w/v)*	8	100 mM	1 hr	RT	-
Gulati *et al.* (2014)	[208]	ABCB1, ABCC1, ABCC4, ABCG2, ABCC7	*Trichoplusia ni*	SMA 2:1 (Polyscience)	2.5% *(w/v)*	8	150 mM	30-60 mins	RT	10% *(v/v)* glycerol)
Paulin *et al.* (2014)	[329]	PBP2/PBP2a	*S.aureus*	SMA 2:1 (synthesised in-house)	2.5% *(w/v)*	7.6	145 mM	1 hr	37°C	20% sucrose *(w/v)*, solubilised pre-purified membranes
Dörr *et al.* (2014)	[223]	KcsA	*E.coli*	SMA 2:1 (Polyscience)	3% *(w/v)*	8	300 mM	Overnight	RT	Solubilised pre-disrupted membranes
Jamshad *et al.* (2015)	[237]	hA2AR	*P.pastoris*	SMA 2:1 (Polyscience)	2.5% *(w/v)*	8	500 mM	20 hrs	25°C	10% glycerol
Jamshad *et al.* (2015)	[237]	hA2AR	HEK293T cells	SMA 2:1 (Polyscience)	2% *(w/v)*	7.4	-	1 hr	37°C	1 mM magnesium acetate, 1 mM EGTA
Bell *et al.* (2015)	[330]	LHC (II)	*S.oleracea*	SMA 3:1 (Polyscience)	3% *(w/v)*	7.6	-	20 mins	4°C	5 mM $MgCl_2$, 0.3 M sorbitol, solubilised pre-purified thylakoids
Postis *et al.* (2015)	[230]	AcrB	*E.coli*	SMA 2:1 (Polyscience)	2.5% *(w/v)*	8	500 mM	2 hrs	RT	10% glycerol
Logez *et al.* (2015)	[226]	MT1R	CHO-K1 cells	SMA 2:1 (Malvern)	2.5% *(w/v)*	8	-	*	4°C	Comparable results obtained with SMA 3:1 (LQ) also.

Date	Ref.	Protein	Organism	Polymer	Polymer Concentration	pH	NaCl	Incubation Time	Incubation Temp.	Additional Conditions
Logez *et al.* (2015)	[226]	GHS-R1a	CHO-K1 cells	SMA 2:1 (Malvern)	2.5% *(w/v)*	8	-	*	26°C	Comparable results obtained with SMA 3:1 (LQ) also.
Driessen *et al.* (2015)	[331]	SecYEG	*E.coli*	SMA 3:1 (Malvern)	3% *(w/v)*	8	200 mM	30 mins	25°C	-
Laursen *et al.* (2016)	[227]	P450 Oxidoreductase (POR)	*S.bicolor*	SMA 2:1 (Polyscience)	2.5% *(w/v)*	7.9	-	overnight	4°C	Solubilised microsomal membranes
Komar *et al.* (2016)	[332]	SecYEG supercomplex	*E.coli*	SMA 2:1 (Polyscience)	2.5% *(w/v)*	8	130 mM	2 hrs	21°C	10% glycerol
Bagrov *et al.* (2016)	[333]	NpSRII	*E.coli*	SMA 3:1 (Polyscience)	2.5% *(w/v)*	8	150 mM	1 hr then 16 hrs	4°C then RT	Solubilised pre-purified proteoliposomes
Broecker *et al.* (2017)	[334]	HwBR	*E.coli*	SMA 3:1 (Polyscience)	2.5% *(w/v)*	8	300 mM	Overnight	4°C	Additional DMPC during solubilisation (1.5% *(w/v)*)
Rehan *et al.* (2017)	[335]	hENT1	Sf9 cells	SMA 2:1 (Polyscience)	0.25% *(w/v)*	8	500 mM	20 hrs	4°C	0.2% cholesteryl hemisuccinate CHS *(w/v)* and 10% glycerol
Bersch *et al.* (2017)	[336]	CzcD	*E.coli*	SMA 2:1 (Polyscience)	0.5% *(w/v)*	8.5	250 mM	12 hrs	RT	In 100% D2O and 2 mM TCEP
Bersch *et al.* (2017)	[336]	CzcD	*E.coli*	SMA 3:1 (Polyscience)	0.3% *(w/v)*	8.5	250 mM	12 hrs	RT	In 100% D2O and 2 mM TCEP
Bos *et al.* (2017)	[228]	LHC PS(I)	*S.oleracea*	SMA 2:1 (Polyscience)	3% *(w/v)*	7.6	-	20 mins	4°C	5 mM $MgCl_2$, 0.3 M sorbitol, solubilised in absence of light, from pre-purified thylakoid membranes
Reading *et al.* (2017)	[232]	GlpG	*E.coli*	SMA 2:1 (Polyscience)	2.5% *(w/v)*	7.4	500 mM	2 hrs	RT	10% glycerol
Swainsbury *et al.* (2018)	[224]	Cytochrome bc1 complex (cytbc1)	*Rba.sphaeroides*	SMA 2:1 (Polyscience)	2.5% *(w/v)*	8	200 mM	1 hr	RT	-

Date	Ref.	Protein	Organism	Polymer	Polymer Concentration	pH	NaCl	Incubation Time	Incubation Temp.	Additional Conditions
Luna *et al.* (2018)	231	Human cannabinoid receptor 1 (CB1)	*E.coli*	SMA 2:1 (Polyscience)	2.5% *(w/v)*	8	500 mM	overnight	4°C	-
Damian *et al.* (2018)	337	GHSR:D2R heterodimer	E.coli / *P.pastoris*	SMA 2:1 (Malvern)	Lipid:Polymer ratio of 0.1	8	200 mM	*	25°C	Solubilised from proteoliposomes
Sun *et al.* (2018)	338	Alternative complex III (ACIII)	*F.johnsoniae*	SMA 3:1 (Polyscience)	1% *(w/v)*	8	300 mM	1 hr	RT	-
Hall *et al.* (2018)	200	ZipA	*E.coli*	SMI	5% *(w/v)*	5	200 mM	2 hrs	RT	Comparable results at pH 7 also
Liu *et al.* (2018)	339	MraY	*E.coli*	SMA 3:1 (Polyscience)	3% *(w/v)*	7.6	150 mM	1.5 hrs then Overnight	25°C then 4°C	Polymer added before cell disruption
Schmidt *et al.* (2018)	183	AqpZ	*E.coli*	SMA 3:1 (Polyscience)	3x excess *(w/w)*	8	150 mM	Overnight	4°C	-
Barniol-Xicota *et al.* (2018)	340	GlpG	*E.coli*	SMA 3:1 (Polyscience)	2.5% *(w/v)*	8	500 mM	3 hrs	37°C	-
Barniol-Xicota *et al.* (2018)	340	GlpG	*E.coli*	SMA 2:1 (Polyscience)	2.5% *(w/v)*	8	500 mM	3 hrs	37°C	-
Barniol-Xicota *et al.* (2018)	340	GlpG	*E.coli*	DIBMA (Polyscience)	2.5% *(w/v)*	8	500 mM	3 hrs	37°C	-
Hellwig *et al.* (2018)	187	KtrB	*E.coli*	SMA 3:1 (Polyscience)	2.5% *(w/v)*	8	600 mM	12 hrs	RT	600 mM salt as 420 mM NaCl and 180 mM KCl
Karlova *et al.* (2019)	341	hKCNQ1	CHO cells	SMA 3:1 (Polyscience)	2.5% *(w/v)*	8	150 mM	30 mins	4°C	Sonicated during solubilisation, in presence of 2 mM DTT
Teo *et al.* (2019)	188	FtsA	*E.coli*	SMA 2:1 (Polyscience)	2.5% *(w/v)*	8	300 mM	'Until clear'	4°C	-
Teo *et al.* (2019)	188	PgpB	*E.coli*	SMA 2:1 (Polyscience)	2.5% *(w/v)*	8	300 mM	'Until clear'	4°C	-
Prakash *et al.* (2019)	342	G12-KRAS	BHK cells	SMA 3:1 (Malvern)	2% *(w/v)*	7.4	137 mM	1 hr	RT	-
Hardy *et al.* (2019)	229	MRP4	Sf9 cells	SMA 2:1 (Polyscience)	2.5% *(w/v)*	7.5	-	2 hrs	4°C	250 mM sucrose
Dutta *et al.* (2019)	[**Erum2018**]	1	*P.pastoris*	SMA 2:1 (Polyscience)	2.5% *(w/v)*	8	200mM	3 hrs	RT	10% glycerol

In three words I can sum up everything I've learned about life: it goes on.

— Robert Frost

B

Appendix for Chapter 3

Contents

B.1 EM particle eccentricity **187**
B.2 Aligned TEMPO spectra **188**
B.3 5-PCSL spectra **188**

B.1 EM particle eccentricity

Table B.1: Comparison of particle eccentricity from TEM using measurements of major/minor axis per particle. Samples were generated in 20 mM HEPES at pH 7.4, 100 mM NaCl with no divalent cations.

Polymer	Major Axis (nm)	Std.Dev (nm)	Minor Axis (nm)	Std.Dev (nm)	Eccentricity (nm)	Std. Dev (nm)
SMA 3:1	14.10	±2.56	11.94	±2.06	0.65	±0.06
SMA 2:1	13.66	±2.43	11.68	±2.21	0.65	±0.05
DIBMA	24.49	±3.80	22.37	±3.73	0.64	±0.03
PMA	18.83	±4.24	15.45	±3.27	0.68	±0.05

Particle analysis of negative stain transmission electron microscopy images was performed by manual measurement of both the major axis of an individual particle, and the minor axis perpendicular to the major axis (See Figure B.1). The major

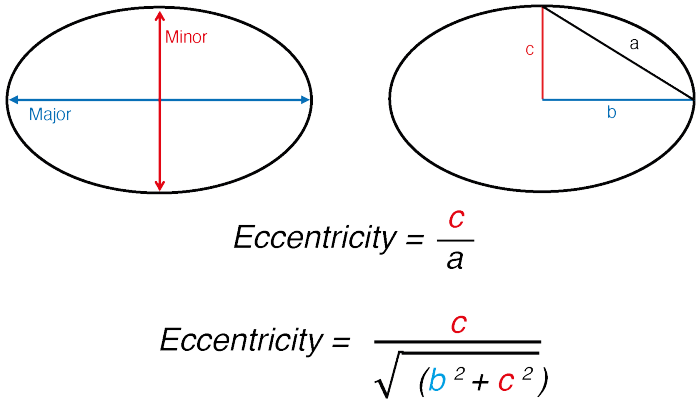


Figure B.1: Diagram showing how eccentricity was measured per TEM particle and calculated for individual polymer variants.

axis diameter was then processed and can be observed in Figure 3.2. Eccentricity of formed nanoparticles was calculated by comparing the major and minor axis per particle, as seen in the equation in Figure B.1.

There was no significant difference on average between the polymer variants in particle eccentricity (Table B.1). All particles had broadly the same eccentricity of ~0.65.

B.2 Aligned TEMPO spectra

The spectra shown in Figure B.2 is the raw (aligned) EPR spectra of TEMPO partitioning. The resulting *f*-plot of which is present as Figure 3.6 B.

B.3 5-PCSL spectra

The preliminary findings with the POPTC and SASL probes showed that it was possible to examine the lipid packing using EPR order parameters. This was combined with a desire to examine how the lipid phase behaviour changes in these nanoparticles when compared to a LUV standard. The order parameter, in conjunction with DSC enthalpic data, would allow for a robust examination on the lipid spatial and thermotropic behaviour within these systems, and allow for some insight on how different polymer association affects these properties. The

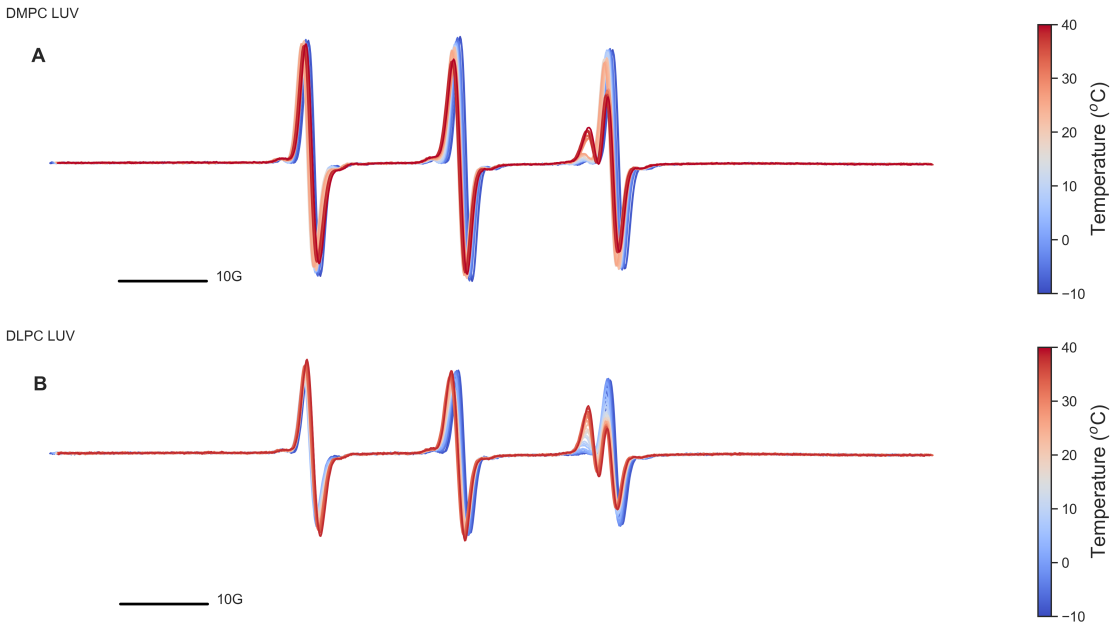


Figure B.2: TEMPO partitioning measurement of DMPC (A) and DLPC (B) LUVs from -10 to +40°C, showing hyper-fine splitting of the high field peak.

data used for the generation of Figure 3.8 is shown below, with annotations where the $A_{\perp}$ and $A_{\parallel}$ measuring points were obtained (Figure 1.14)

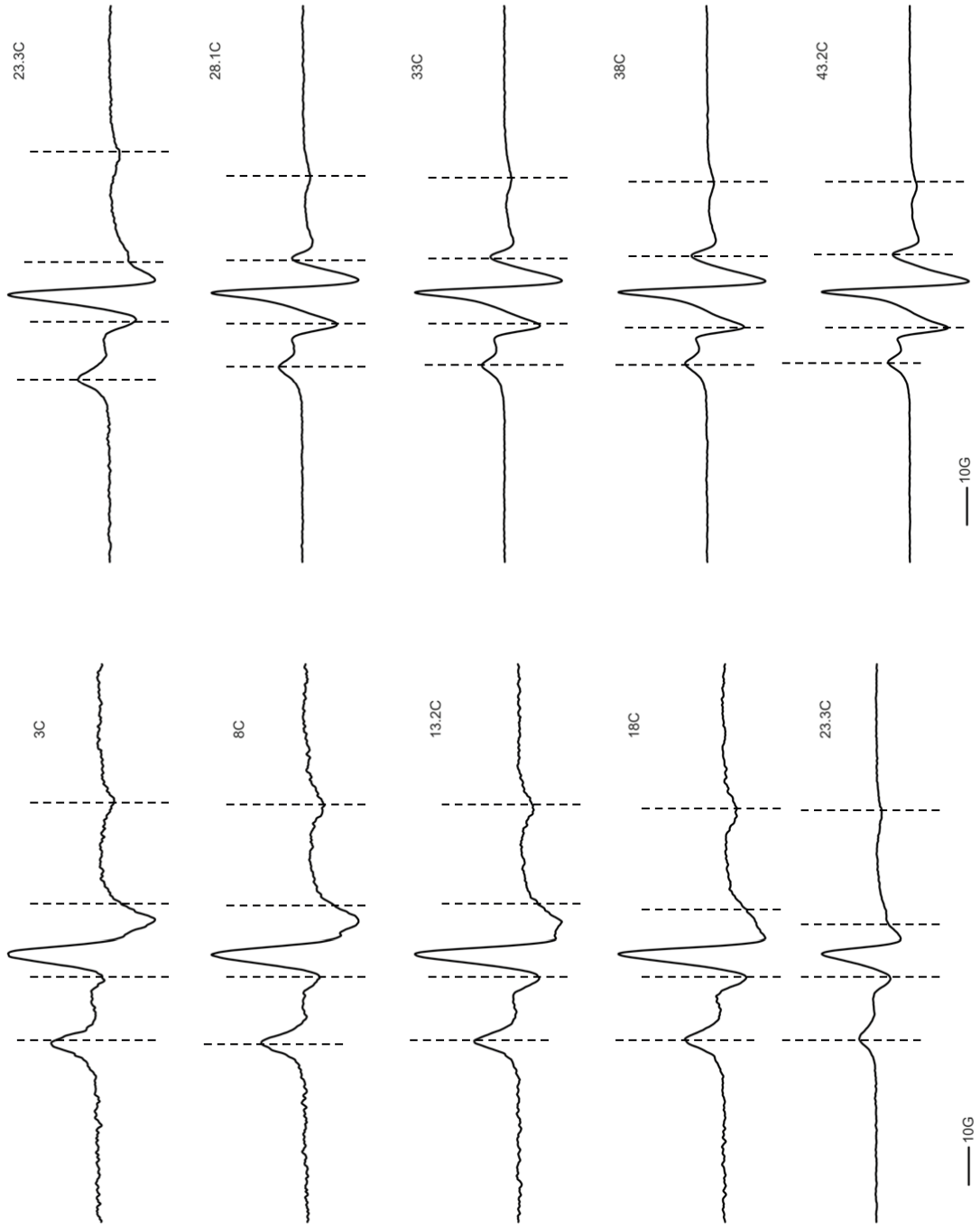


Figure B.3: Annotated EPR spectra of 1% (molar) 5-PCSL label within a 400 nm DMPC LUV. Dashed lines show $A_{\perp}$ (outer pair) and $A_{\parallel}$ (inner pair) measuring points. Temperature of measurement is also shown for each spectra.

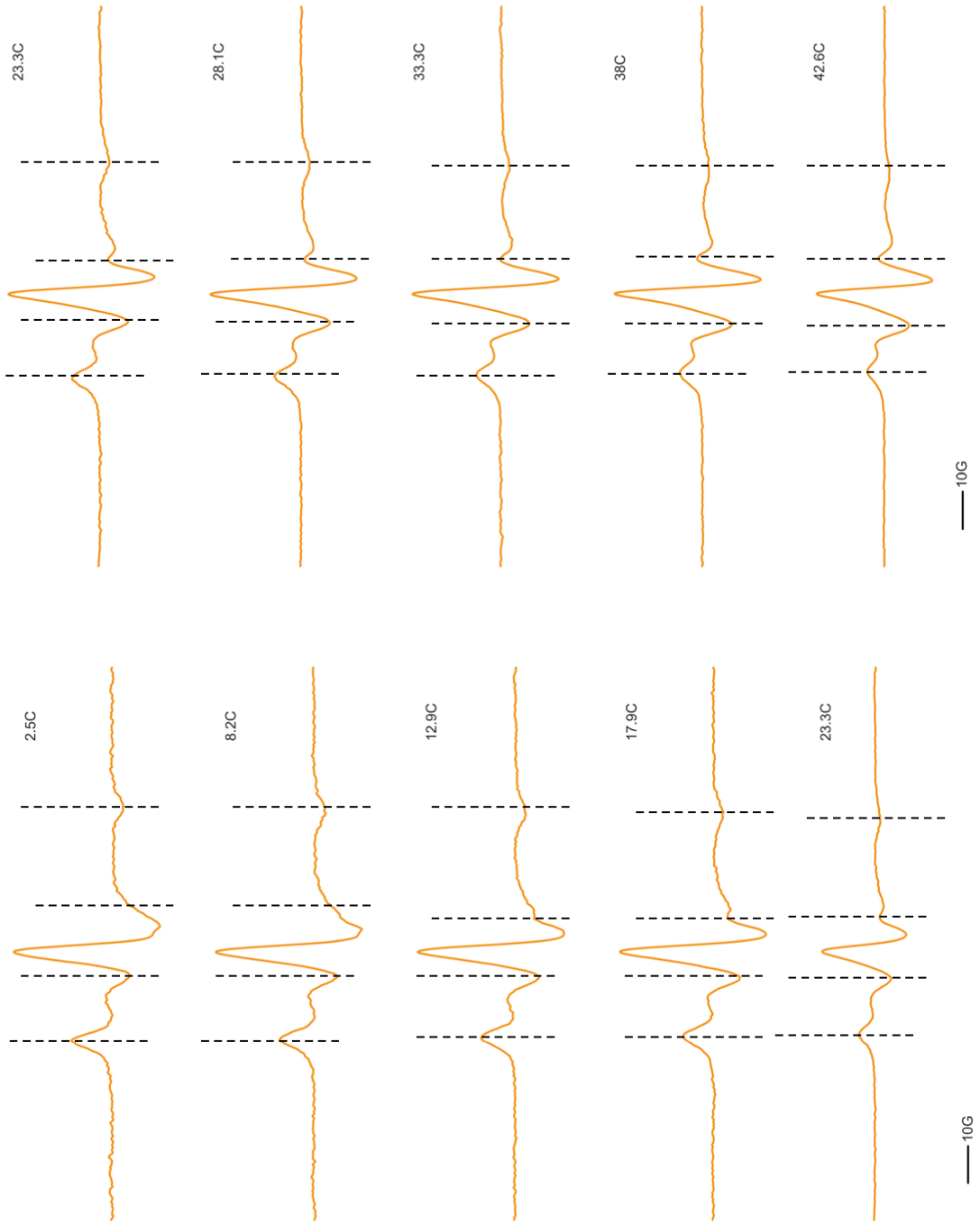


Figure B.4: Annotated EPR spectra of 1% (molar) 5-PCSL label within a SMA 3:1-DMPC nanoparticle. Dashed lines show $A_{\perp}$ (outer pair) and $A_{\parallel}$ (inner pair) measuring points. Temperature of measurement is also shown for each spectra.

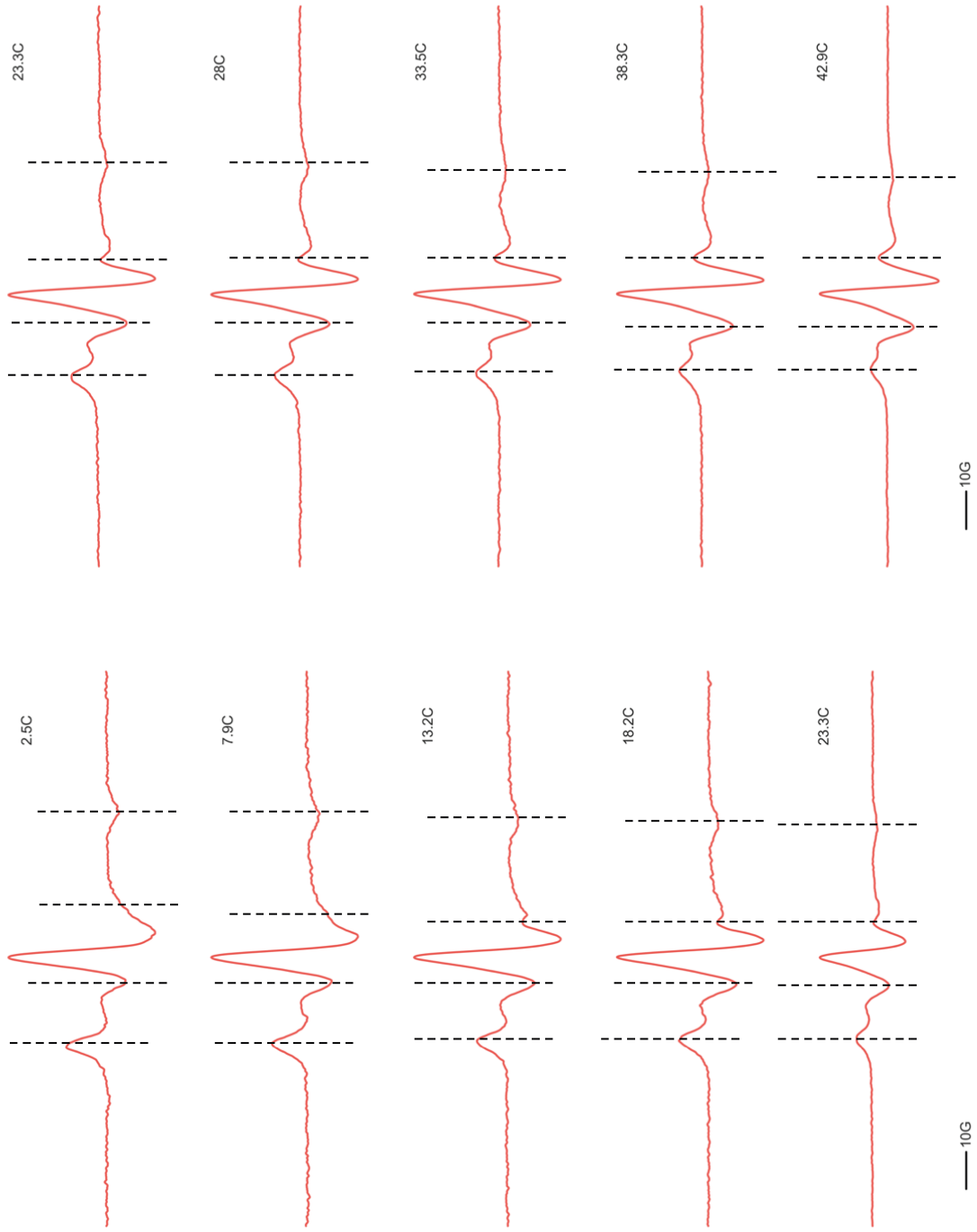


Figure B.5: Annotated EPR spectra of 1% (molar) 5-PCSL label within a SMA 2:1-DMPC nanoparticle. Dashed lines show $A_{\perp}$ (outer pair) and $A_{\parallel}$ (inner pair) measuring points. Temperature of measurement is also shown for each spectra.

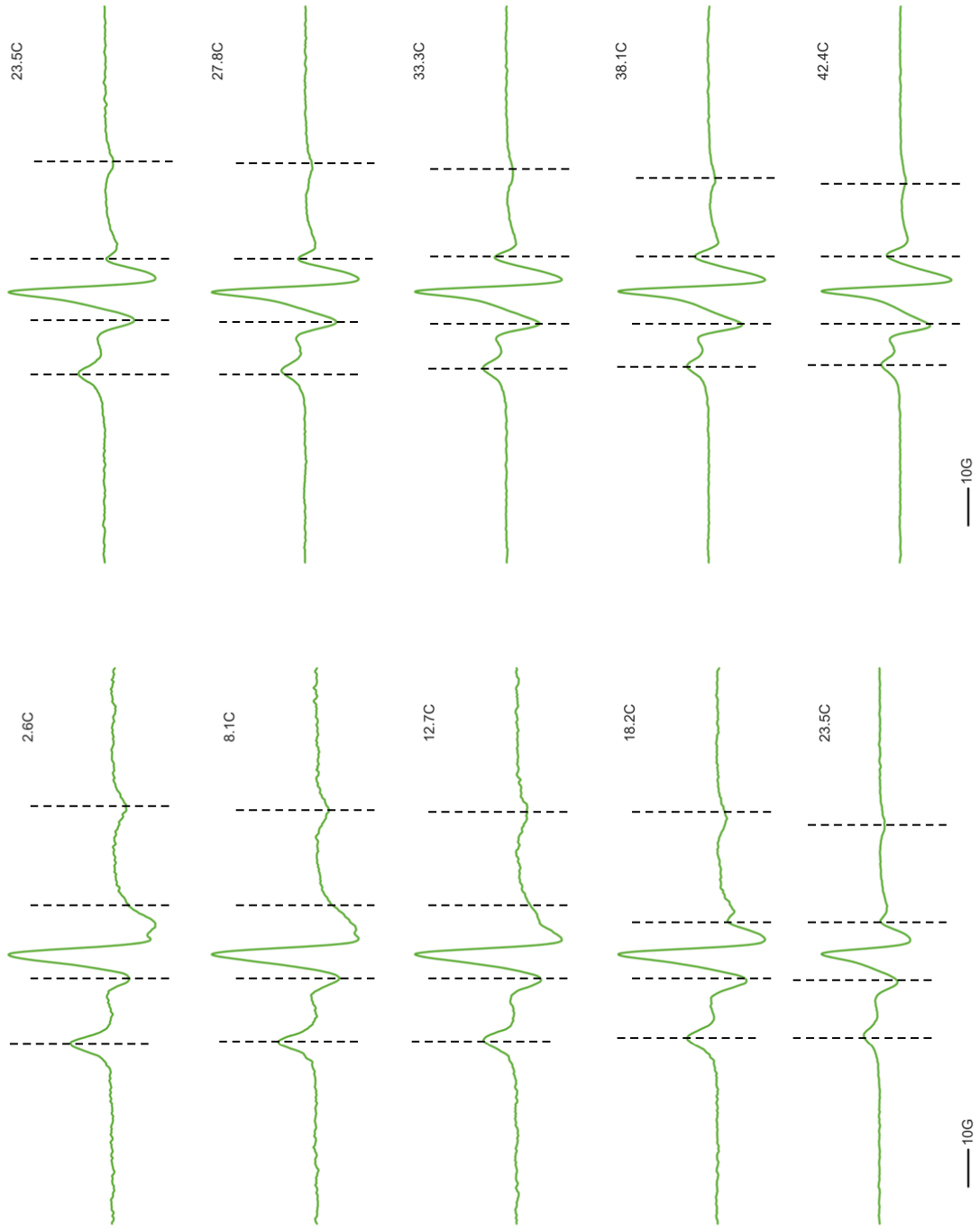


Figure B.6: Annotated EPR spectra of 1% (molar) 5-PCSL label within a DIBMA-DMPC nanoparticle. Dashed lines show $A_{\perp}$ (outer pair) and $A_{\parallel}$ (inner pair) measuring points. Temperature of measurement is also shown for each spectra.

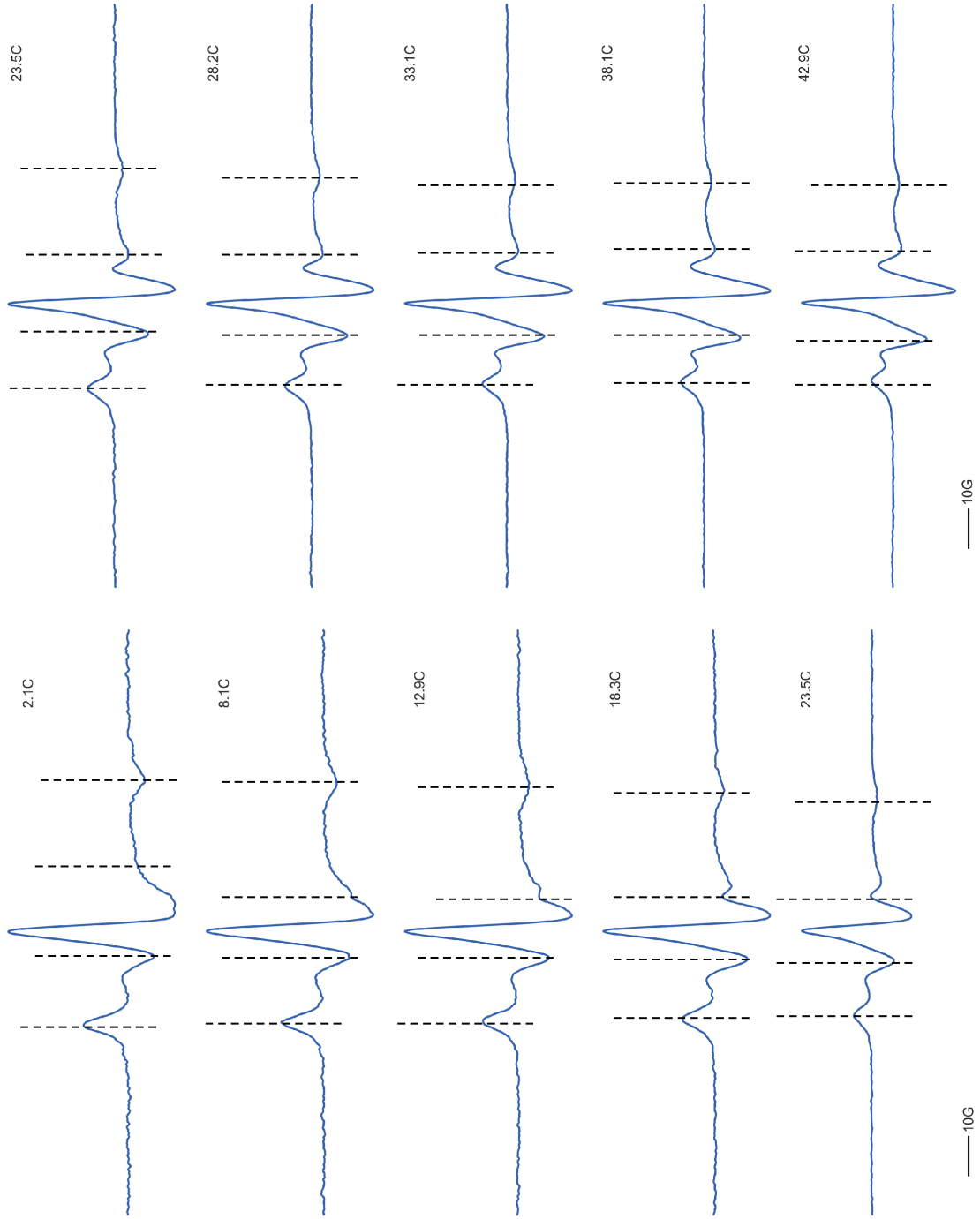


Figure B.7: Annotated EPR spectra of 1% (molar) 5-PCSL label within a PMA-DMPC nanoparticle. Dashed lines show $A_{\perp}$ (outer pair) and $A_{\parallel}$ (inner pair) measuring points. Temperature of measurement is also shown for each spectra.

I esteem his understanding and subtlety highly, but I consider that they have been put to ill use in the greater part of his work, where the author studies things of little use...

— Christiaan Huygens (Writing about Isaac Newton)

C

Appendix for Chapter 4

Contents

C.1 Development of FRET assay for aLUV and supposed aLQ 195
C.2 Development of EPR assay for aLUV and supposed aLQ 197
C.3 Development of ^{31}P NMR assay to determine level of mixing in LQ systems 201
C.4 TR-FRET data for additional polymers 205

C.1 Development of FRET assay for aLUV and supposed aLQ

Based upon preliminary data from D.Yin (2016), there was an indication that asymmetry formed in LUV membrane models could be retained in Lipodisq particles. This was initially examined through the use of asymmetric LUVs using two lipid-fluorescent dyes Cy3-DLPE and Cy5-DLPE as purchased by Avanti and later synthesised in-house, with later additional assays through the use of cw-EPR (§C.2).

The Cy5 signal generated in the LUV systems were unable to be replicated in the LQ systems. Whilst the LUV sample showed a high FRET efficiency (Figure C.1 D, solid black line), there was no excitation observed within the expected

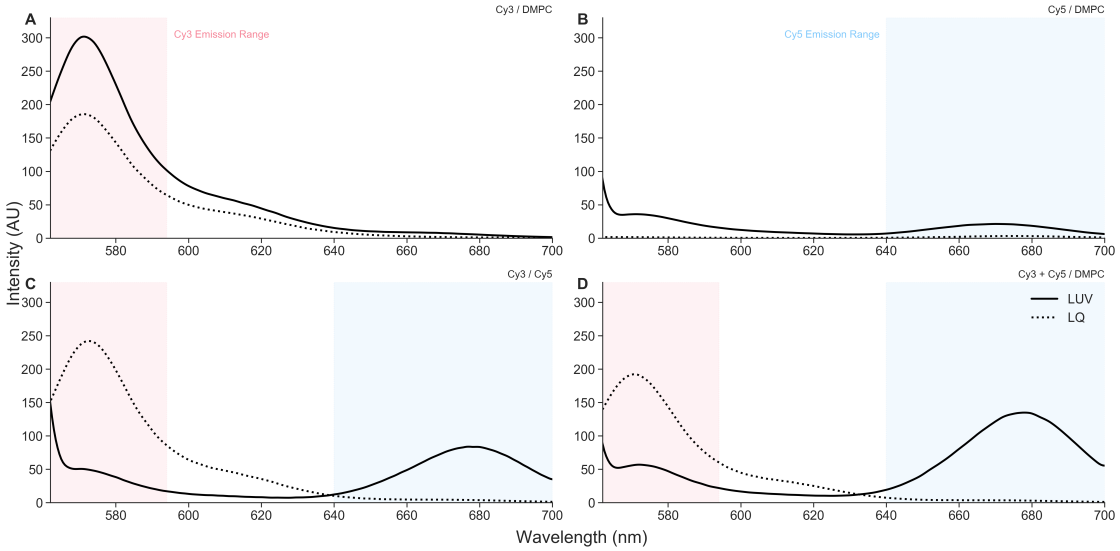


Figure C.1: Fluorescence spectra for Cy3 and Cy5 labelled lipids in aLUV and LQ systems. (A) Cy3-DLPE / DMPC. (B) Cy5-DLPE / DMPC. (C) Cy3-DLPE / Cy5-DLPE. (D) Cy3-DLPE + Cy5-DLPE / DMPC. Where / denotes change in leaflet. All samples were prepared to 1% (molar) dye-lipid to DMPC, and excited at 555 nm

region for Cy5 in any of the LQ samples. This was initially believed to be due to a concentration error affecting FRET efficiency, and an additional experiment was designed with an increased molar concentration of 2% molar (not shown) however this showed similarly disappointing results. The ability of Cy3 to fluoresce in LQ systems as well as the colouration of the Cy3-Cy5 systems in both LUVs and LQs indicate that both Cy3 and Cy5 dye were being incorporated into the LQ system from the aLUVs, however the fluorescence by Cy5 was somehow inhibited in LQ systems. Excitation at the Ex_{max} of Cy5, 650 nm, was also performed (not shown), which did not show any Cy5 fluorescence in any LQ system.

This phenomenon was eventually explained after a literature search, Gruber *et al.* showed that a large amount of mutual resonance energy transfer occurs between Cy5 dyes at high concentrations and when exposed to a high surface charge, with this self quenching found to lower fluorescence by 97%.[343] Similarly, Berlier *et al.* showed that Cy5 is liable to forming dye aggregates that also show no fluorescence upon formation.[344] It is therefore very likely that the presence of the highly charged polymer band in LQs nucleates Cy5 aggregate formation, removing fluorescent Cy5 from the lipid mixture whilst still retaining the visual colour seen.

A combination of the Cy5 difficulties and the prohibitive cost of the cyanine-lipid dye conjugates meant that the Cy3/Cy5 FRET pairing was abandoned, and replaced with a more well known NBD-PE/Rho-PE FRET pair (Figure 4.2). These were chosen as there was good literature precedent for their use in lipid FRET based assays, with the protocol developed for use with Cy3/Cy5 pairing being used, as described in §4.2.2.

C.2 Development of EPR assay for aLUV and supposed aLQ

With the initial complications with the FRET based asymmetry assay, an alternative was designed utilising the same principles of distanced dependant energy exchange. However in place of fluorescent dyes for this measurement, the alternative assay utilised nitroxide spin labels and inter-spin dipolar interactions to measure whether asymmetry is maintained in LQ systems. Electroparamagnetic resonance (EPR) methods such as this have been used extensively in membrane biophysics within the lab,[110, 204, 345] and within the literature.[70, 166, 346].

As a preliminary experiment it was decided to measure the distance by spin-spin interaction with continuous wave EPR over the more delicate and powerful pulsed techniques such as double electron-electron resonance (DEER).[347] If the there was any observable change measured between asymmetric an symmetric samples, then this technique would be looked into more closely.

The technique utilised two spin label probes: a TEMPO-PC labelled lipid (POPTC) and an MTSL-labelled protein in the form of a purified archeorhodopsin 3 (AR3) mutant M173C. This mutant, kindly supplied and purified by Javier Vinals Camallonga,[185] possesses a single cysteine residue on a solvent exposed loop of the protein, allowing for simple click chemistry to attach a spin-label probe (MTSL). Once generated, the MTSL-AR3 was inserted into two LUV mixtures. The first sample (***1***) containing only DMPC (1:100 MTSL-AR3:DMPC molar ratio) and the second (***2***) containing a 1% POPTC label (1:1:100 AR3-MTSL:POPTC:DMPC).

Table C.1: Composition of inner (*I*) and outer (*O*) leaflet lipids used for aLUV measurements by EPR

Sample Number	**Sample Name**	**Inner Leaflet** *I*	**Outer Leaflet** *O*
1	$DMPC_i$ / $POPTC_o$	DMPC	1% (molar) POPTC + DMPC
2	$POPTC_i$ / $DMPC_o$	1% (molar) POPTC + DMPC	DMPC

To ensure the MTSL-AR3 label was only present on a single leaflet side, both LUV mixtures were subjected to ascorbate quenching to selectively quench the outer leaflet of LUV samples. aLUVs were then formed from these LUV samples by a similar process described in §4.2.2, with final leaflet contents described in Table C.1. The generated aLUVs were then solubilised to form 'aLQs'. 4 samples in total were measured by cw-EPR, as shown in Figure C.2. If spin-spin exchange occurs, then an identifiable difference between symmetric spectra and asymmetric spectra would be observed, with the symmetric spectra showing deformation from the additional spin-spin exchange taking place due to the close proximity of the two labels.

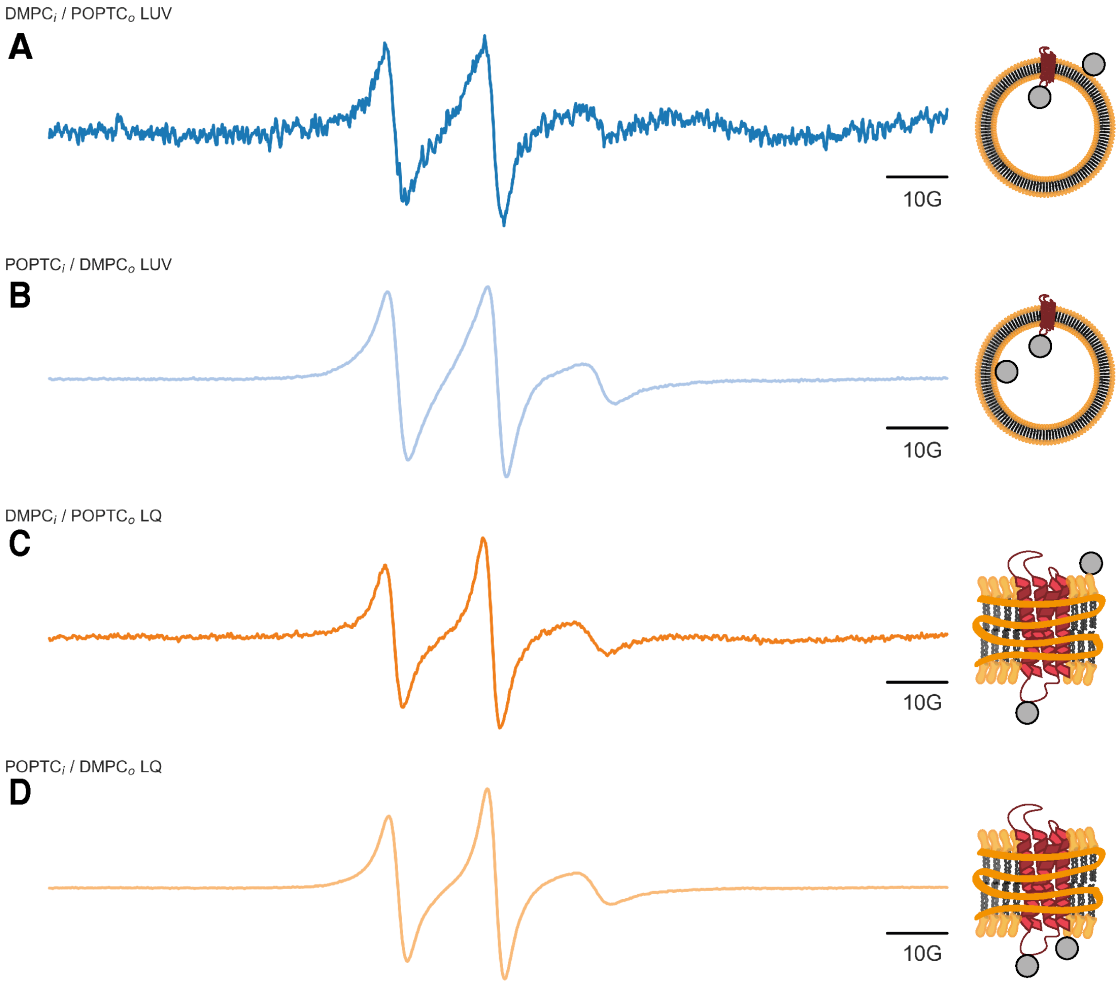


Figure C.2: EPR spectra of aLUV and supposed aLQ with leaflet-selective labelled AR3 and POPTC

As can be seen in Figure C.2, there is no obvious difference between the shape of the spectra for the LUV samples (A and B), and the LQ samples (C and D), with the slight caveat of the noise level present in the $DMPC_i$ / $POPTC_o$ most likely caused by a lower concentration due to sample loss during preparation. Due to the delicate nature of EPR spectra, the difference between the symmetric ($POPTC_i$ / $DMPC_o$) and asymmetric ($DMPC_i$ / $POPTC_o$) may not be clear visually. If spin-spin exchange is weakly present in the samples, it is possible to reveal the spectra of this exchange by subtraction of the non-exchange spectra. To this end, symmetric spectra ($POPTC_i$ / $DMPC_o$) were subtracted by asymmetric spectra ($DMPC_i$ / $POPTC_o$) in the hope of revealing the distinctive line shape of spin-spin

exchange, as seen in Figure C.3, previously described by Watts *et al.*[166]

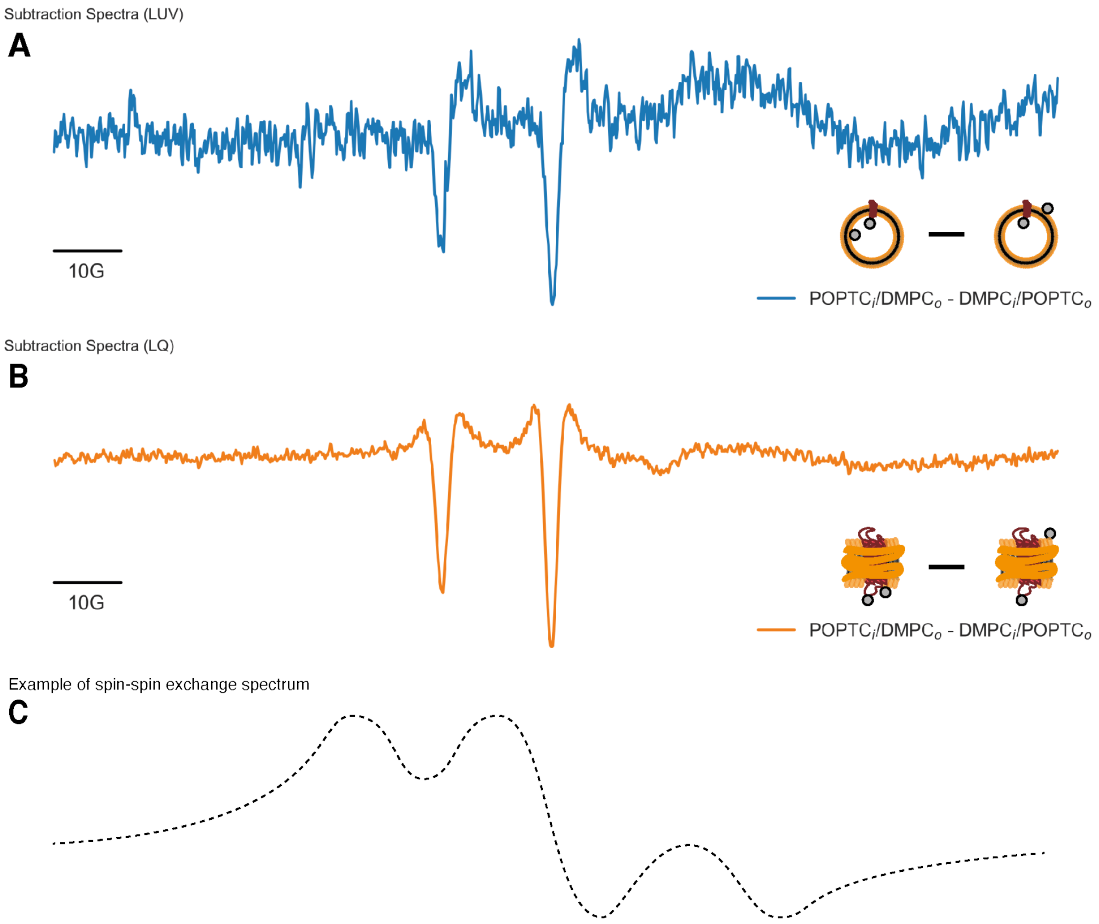


Figure C.3: EPR subtraction spectra of aLUV (A) and aLQ (B) with an example expected resultant spectra if spin-spin exchange was present (C)

The subtraction spectra does not show the distinctive line shape that would be expected if spin-spin exchange was occurring in only the symmetric sample. It is therefore likely that either the spin-spin exchange is present in both asymmetric and symmetric samples due to an insufficient difference in spin label distance, or the spin-spin exchange present in the symmetric sample is too weak to be measurable by cw-EPR methods.

Due to the data emerging from Figure 4.2 indicating that asymmetry is lost in LQ systems, and additionally data from Keller *et al.*,[262] this method was not developed any further due to time constraints of method development and the likelihood of lipid-mixing destroying leaflet asymmetry in LQ systems. In addition to this, a paper was published at around this time describing the lipid scramblase

effect of a closely related, and structurally similar, protein, bacteriorhodopsin, in model membrane systems.[348] If this property is conserved in archeorhodopsin, then the assay containing this protein would obviously not be a viable option for a method to measure leaflet asymmetry.

C.3 Development of ^{31}P NMR assay to determine level of mixing in LQ systems

Whilst developing a FRET and EPR based assay to assess whether asymmetric LQs were possible using labelled lipids, questions were raised at *how* asymmetric aLQs could be expected to be. The simplistic model for polymer solubilisation of membranes at the time was described informally as a 'cookie-cutter' like manner, however the solubilisation step involved polymer adsorption onto the membrane bilayer in a similar manner to antimicrobial peptides which have been known to scramble membrane asymmetry during this step.[349, 350] Logically, some lipid flip-flop must occur between leaflets during this solubilisation process, and this has been shown with simulations of SMA-based solubilisation.[220, 351] However the empirical measurement of this scrambling had not been attempted.

At the time of assay design it was believed that there was no lipid mixing between nanoparticles in solution. To examine the level of the mixing during solubilisation it was decided to measure the level of leaflet asymmetry by generating asymmetric nanoparticles of DMPC/DMPG lipids. Using the naturally occurring ^{31}P, it is possible to measure the change in the immediate local environment of the lipid head groups without the need for additional labelling. If the DMPC leaflet experiences the presence of more negative DMPG lipids, the excess electron density will cause a measurable shift in ppm (also known as $\Delta\delta$) of both DMPC and DMPG lipids. Similarly, if the electron density of DMPG bilayers is diluted in the presence of DMPC lipids, this too will show a measurable ppm shift. The distance at which this environmental change can occur is restricted to immediately neighbouring lipids, and therefore can only be detected if the asymmetric DMPC/DMPG leaflets are

perturbed. The exact level of asymmetry loss can be then measured by the level of shift in ppm against known titrations of lipid mixtures.

To measure the level of mixing in asymmetric samples, titration standards were prepared of 100% DMPC, 75:25 DMPC:DMPG, 50:50 DMPC:DMPG, 25:75 DMPC:DMPG and 100% DMPG lipid mixtures (Figure C.4 A-E). In addition to this, two 'asymmetric' LQ samples were prepared with inverted leaflet asymmetry of $DMPC_i$ / $DMPG_o$ and $DMPG_i$ / $DMPC_o$ (Figure C.4 F,G). This was performed as it wasn't clear whether DMPG, with it's highly charged head group, was able to be exchanged by cyclodextrin-mediated transfer to form aLUVs initially, however this has now been shown by London *et al.* that cyclodextrin-mediated exchange is not affected by head group charge.[266]

The spectra shown in Figure C.4 show that as the amount of DMPG increases within a DMPC bilayer, the DMPC ^{31}P nuclei experience a change in their local environment (due to the increased electron density of the increasing DMPG population). This causes the DMPC peak to shift from 0.060 ppm in 100% DMPC to around 0.154 ppm in 25% DMPC, 75% DMPG membranes. The linear increase in DMPC ppm is mirrored by a decrease in DMPG ppm in the presence of DMPC, shifting down from 1.230 ppm in 100% DMPG bilayers, to 1.153 ppm in 75:25 DMPC:DMPG membranes. The linear shifts for both DMPC and DMPG can be plotted (Figure C.5), and the gradient of this slope can be used to calculate the level of mixing of unknown samples, by measuring the required DMPC and DMPG peaks.

Using the standard curve generated by the titration samples, it is possible to determine the level of mixing between DMPC and DMPG leaflets in the 'asymmetric' LQ samples (Figure C.5). As this was a preliminary experiment and required a large amount of material, $DMPC_i$ / $DMPG_o$ (orange) and $DMPG_i$ / $DMPC_o$ (purple) were only measured with a single sample, and therefore have no calculated error attached. Despite this, there was a good general agreement between the asymmetric samples on the level of mixing (± 10%), and both samples indicated that approximately 30% of total lipids in the LQ systems are mixed during solubilisation, assuming that lipid mixing only occurs during solubilisation and not after this in solution.

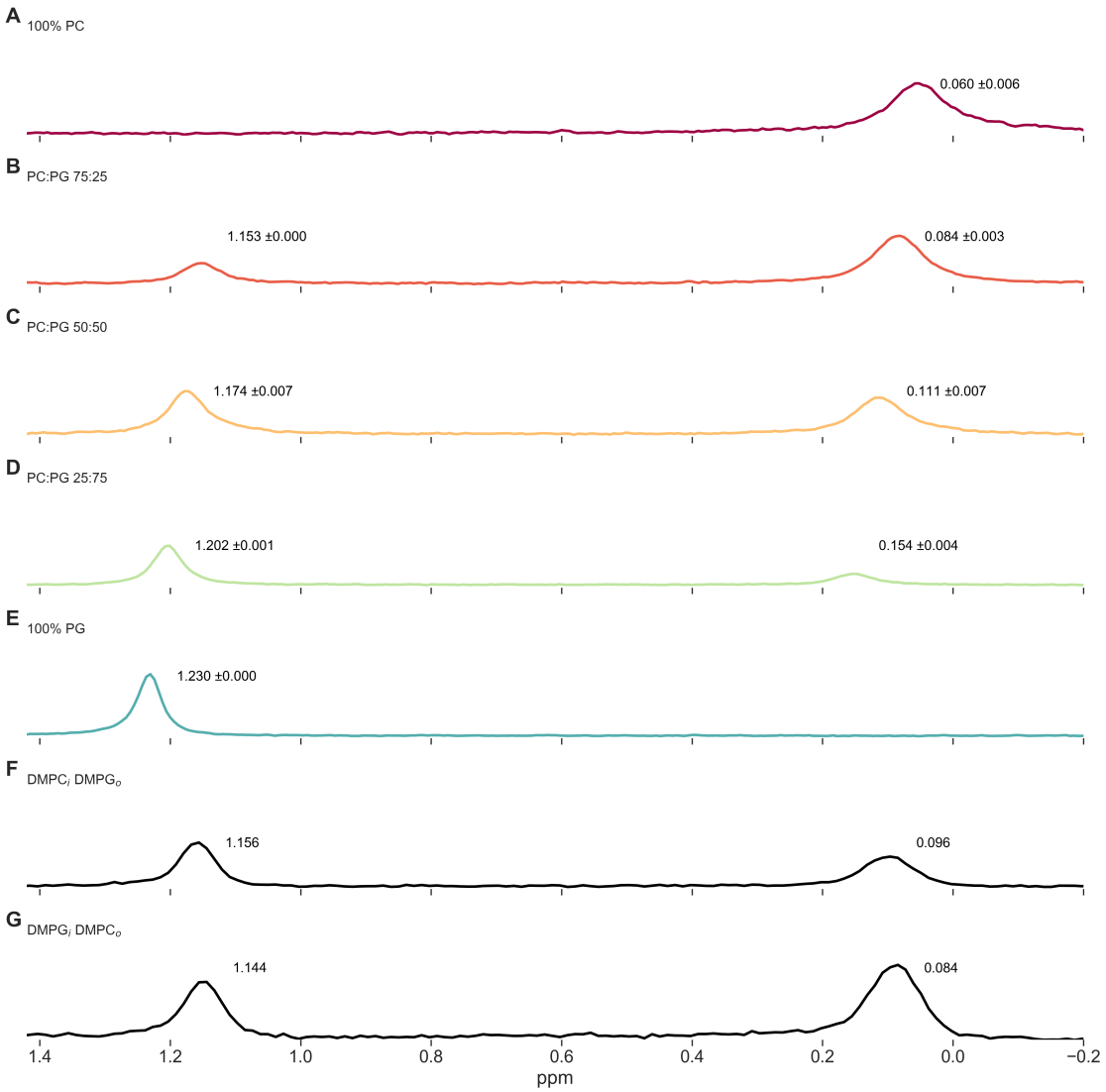


Figure C.4: ^{31}P NMR spectra for pre-mixed PC:PG standards and asymmetric DMPC /DMPG samples

However it is now known that lipid mixing in solution *does* occur in solution, from the data shown in Chapter 4, and this NMR experiment is now known to have instead captured the incomplete mixing by collisional lipid transfer (Figure 4.8). As the aLUVs were known to be unstable for long periods of time, they were immediately solubilised to form 'aLQs' for this experiment, with the time taken between solubilisation, centrifugation and sample preparation to measurement by NMR taking approximately 30 minutes, all of which was performed at 4°C.

Once it was established that lipid mixing in solution does occur, the titration standards were re-purposed and the mixing experiment shown in Figure 4.8 was

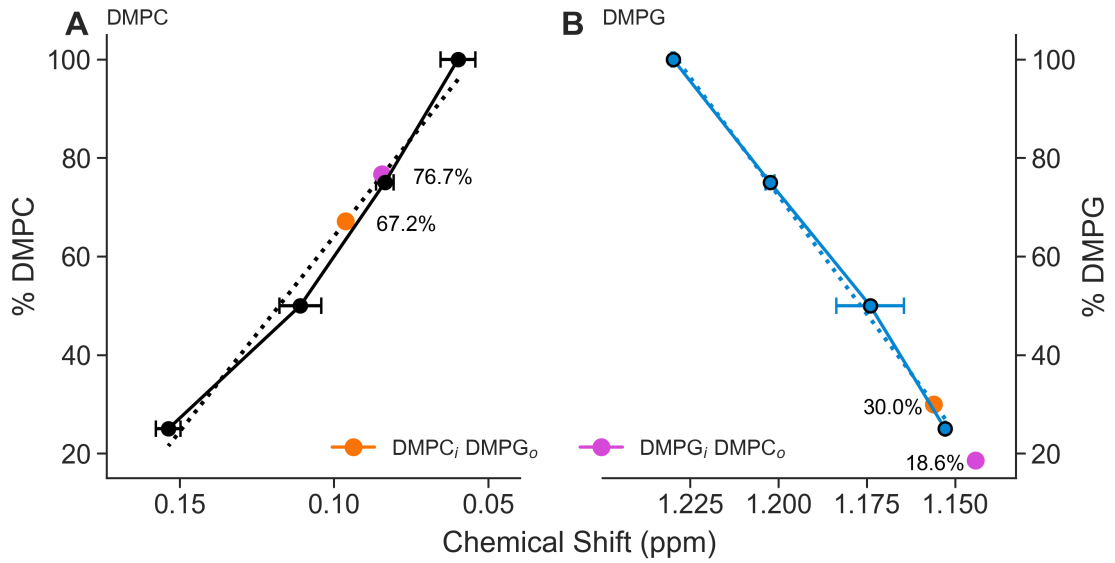


Figure C.5: Lipid mixing of SMA 3:1-DMPC and SMA 3:1-DMPG nanoparticles as measured by ^{31}P NMR, showing DMPC (A) and DMPG (B) titration curves of pre-mixed standards. Sample peak measurements are shown in orange ($DMPC_i$ / $DMPG_o$) and purple ($DMPG_i$ / $DMPC_o$)

performed. In addition to the data shown in this Figure, integrated peak heights were measured of the spectra shown in Figure 4.7, to give a rough indication of the PC:PG molar ratio of the samples (Table C.2). This was taken as it was unsure how effective solubilisation would be across the DMPC:DMPG titration by SMA 3:1. Similarly, pH readings were taken of titration standards to ascertain whether the peak shifting observed in both Figures 4.7 and C.4 was due to changes in the local environment of the lipids, or due to pH shifting by the more acidic DMPG being introduced in combination with insufficient buffering of the samples (Table C.2). For the mixing samples pH readings were measured prior to and after each mixing experiment, showing no major deviation in pH between the wholly PC or wholly PG nanoparticles. This further indicates that the shifting observed is due to a change in local environment, rather than pH variance.

Table C.2: Integrated peak ratio of DMPC:DMPG standards and mixing samples with associated pH.

Sample Name	**Sample Number**	**Normalised PC:PG Ratio**	**pH**
75:25 PC:PG	1	1 : 0.32	7.81
	2	1 : 0.30	7.79
	3	1 : 0.33	7.79
50:50 PC:PG	1	1 : 0.95	7.80
	2	1 : 0.93	7.76
	2	1 : 0.94	7.71
25:75 PC:PG	1	1 : 2.53	7.77
	2	1 : 2.71	7.77
	3	1 : 2.92	7.77
Sample prior to mixing (PC)	A	-	7.89
	B	-	7.85
	C	-	7.85
Sample prior to mixing (PG)	A	-	7.81
	B	-	7.84
	C	-	7.81
Sample	A	1 : 1.07	7.75
	B	1 : 0.97	7.77
	C	1 : 1.06	7.77

C.4 TR-FRET data for additional polymers

Whilst TR-FRET measurements were performed for all 4 polymers within this thesis, only SMA 3:1 is shown for clarity in §4.3.2. The additional plots for SMA 2:1, DIBMA, and PMA can be seen below. As for the SMA 3:1 assay (Figure 4.4), an initial recording for 5 minutes of sample A (the 'High-FRET' sample) was taken, after which an equimolar amount of sample B (DMPC-SMA 3:1 nanoparticles) were

added. The initial gradient of unpaired NBD-PE was measured after injection of sample B, and the rate calculated from this using a python script as described in §4.2.2. With the exception of SMA 3:1, all polymers showed no measurable lipid mixing at 4°C, however this is most likely due to a time limitation in the TR-FRET assay, as the mixing observed in Figure 4.3 for all polymers showed complete removal of asymmetry after incubation overnight at 4°C.

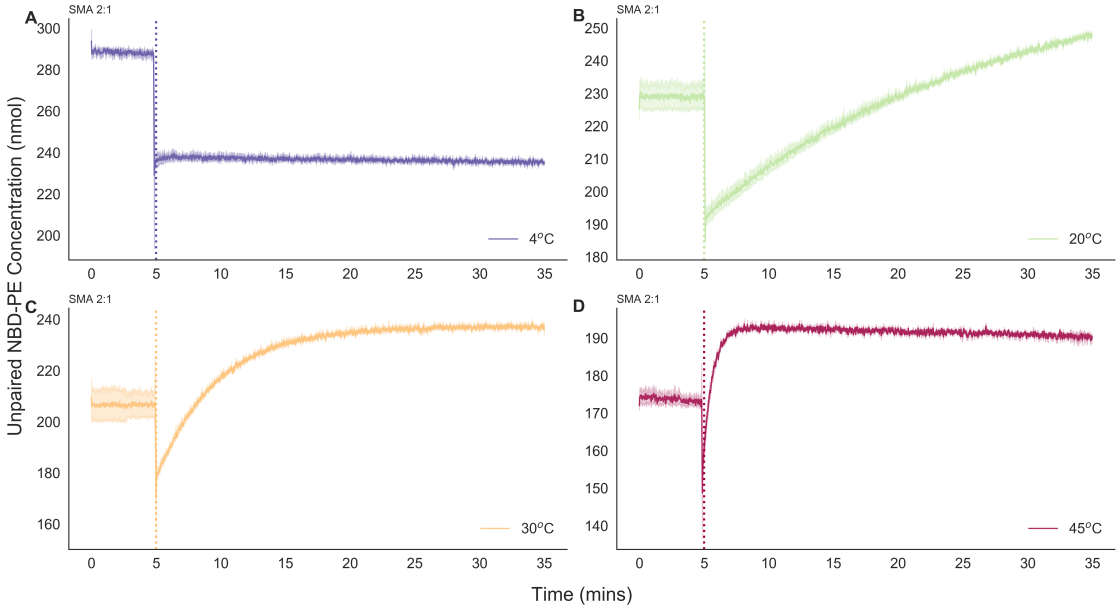


Figure C.6: Rate of lipid mixing as measured by NBD-PE emission at 510 nm for SMA 2:1 nanoparticles across a temperature range of 4°C (A), 20°C (B), 30°C (C) and 45°C (D).

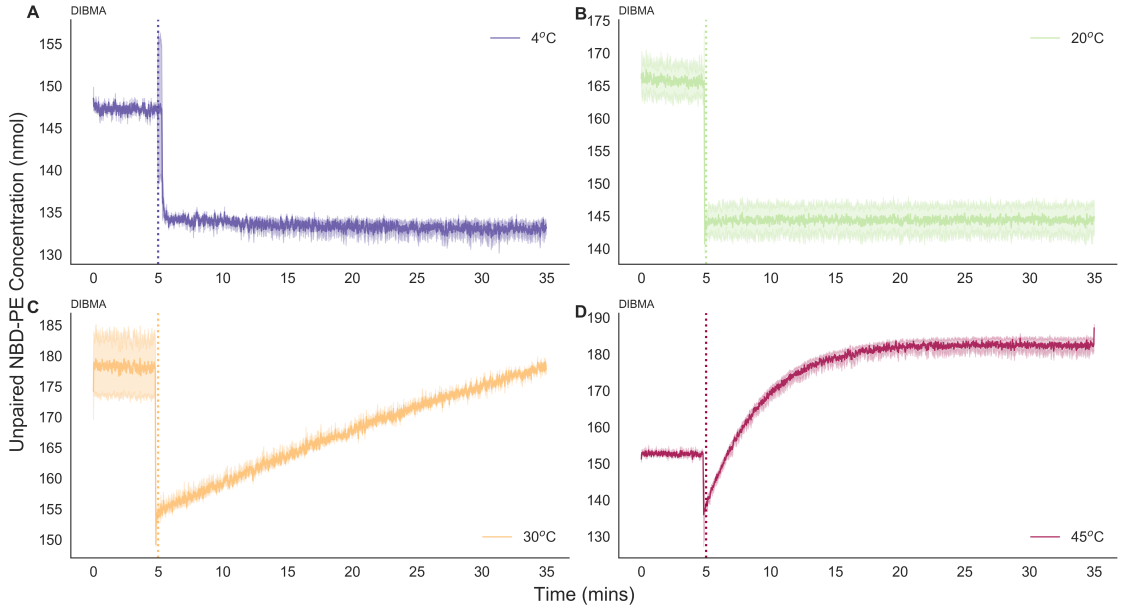


Figure C.7: Rate of lipid mixing as measured by NBD-PE emission at 510 nm for DIBMA nanoparticles across a temperature range of 4°C (A), 20°C (B), 30°C (C) and 45°C (D).

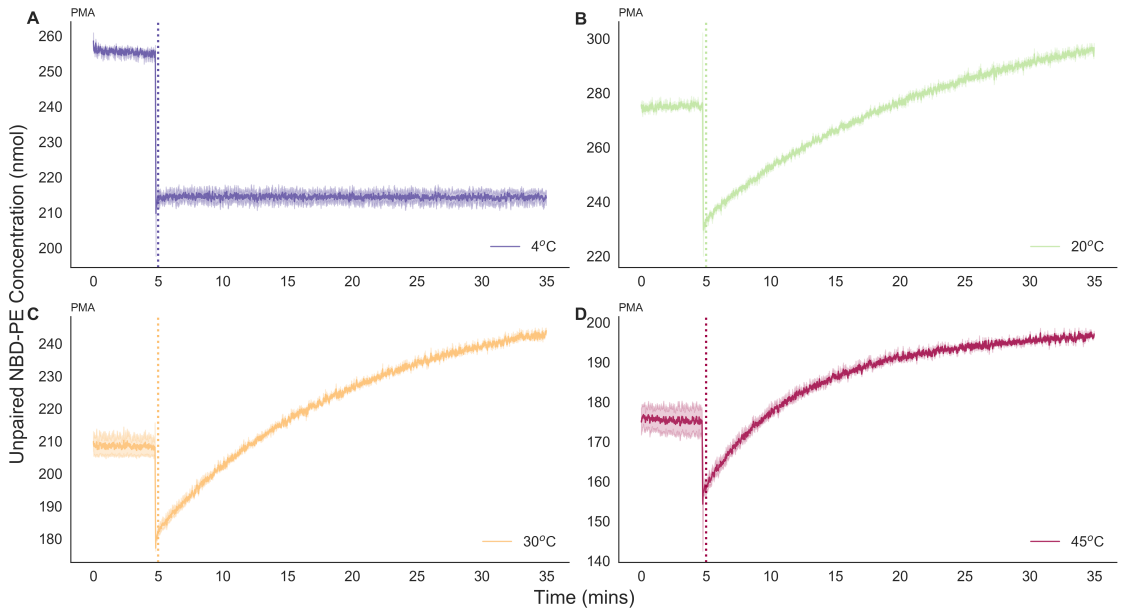


Figure C.8: Rate of lipid mixing as measured by NBD-PE emission at 510 nm for PMA nanoparticles across a temperature range of 4°C (A), 20°C (B), 30°C (C) and 45°C (D).

Can anything be sadder than work left unfinished?
Yes, work never begun.

— Christina Rossetti

D

Appendix for Chapter 5

Contents

D.1 Additional HPLC purification attempts 209
D.2 ST1-QAA T0 EM image 214
D.3 Additional characterisation assays 215
D.3.1 Dynamic light scattering (DLS) 216
D.3.2 CD melt 217

D.1 Additional HPLC purification attempts

Following the initial purification attempt using an initial scouting run (Figure 5.2, 10-70% over 20 minutes), purity was anticipated to be improved through modification of buffer B gradient. The first modification was to perform a shallower gradient of 10-40% for 20 minutes, followed by a sharper gradient of 40-70% in 5 minutes. This was done as the initial scouting gradient (Figure 5.2 A) showed that ST1-QAA was relatively hydrophilic, and appeared to elute at low % of Buffer B.

As can be seen in Figure D.1, the shallow gradient of 10-40% in 20 minutes generated a single peak containing ST1-QAA. This peak was narrower than the previous scouting run, and contained a greater yield of ST1-QAA. However, the resulting analytical and ESI-MS data (Figure D.1 B-C) indicated that no significant

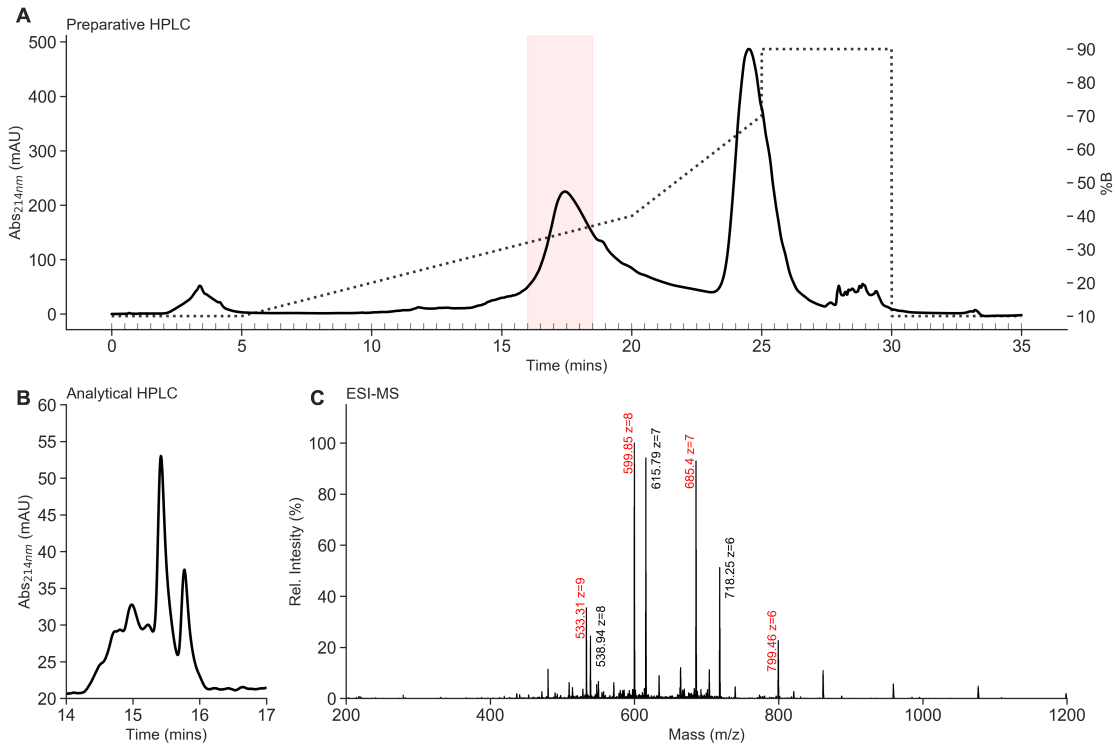


Figure D.1: Second attempt of ST1-QAA purification, showing preparative HPLC UV chromatogram (A), overlaid with a slower linear gradient of Buffer B (dotted line) used for purification attempt. Red highlighted region indicates fractions pooled for sown analytical HPLC (B) to assess purity, and ESI-MS to assess contents of fraction (C). Red annotation indicates mass/charge ratio *(m/z)* of expected M_R for ST1-QAA (4791.52 Da).

increase in purity was achieved over the scouting run. A third attempt, utilising an isocratic hold at 34% (calculated from elution time of previous attempts) was then trialed, as shown in Figure D.2.

The isocratic hold at 34% Buffer B showed and increased yield (as measured by preparative HPLC, Figure D.2 A), as well as a decrease in number of contaminants over the initial purification (Figure 5.2) as measured by ESI-MS (Figure D.2 C). However, the contamination of the truncated peptide with a mass of 4315.5 Da was still present. In addition to this, the preparative and analytical peaks appeared broader than might be expected for a two compound HPLC. This initially was thought to be due to the isocratic hold causing broadening of the preparative HPLC chromatogram. However, as the analytical HPLC showed broadening and more peaks than predicted by ESI-MS, it raised questions of aggregation affecting purification attempts. An additional attempt was made to remove any hydrophilic

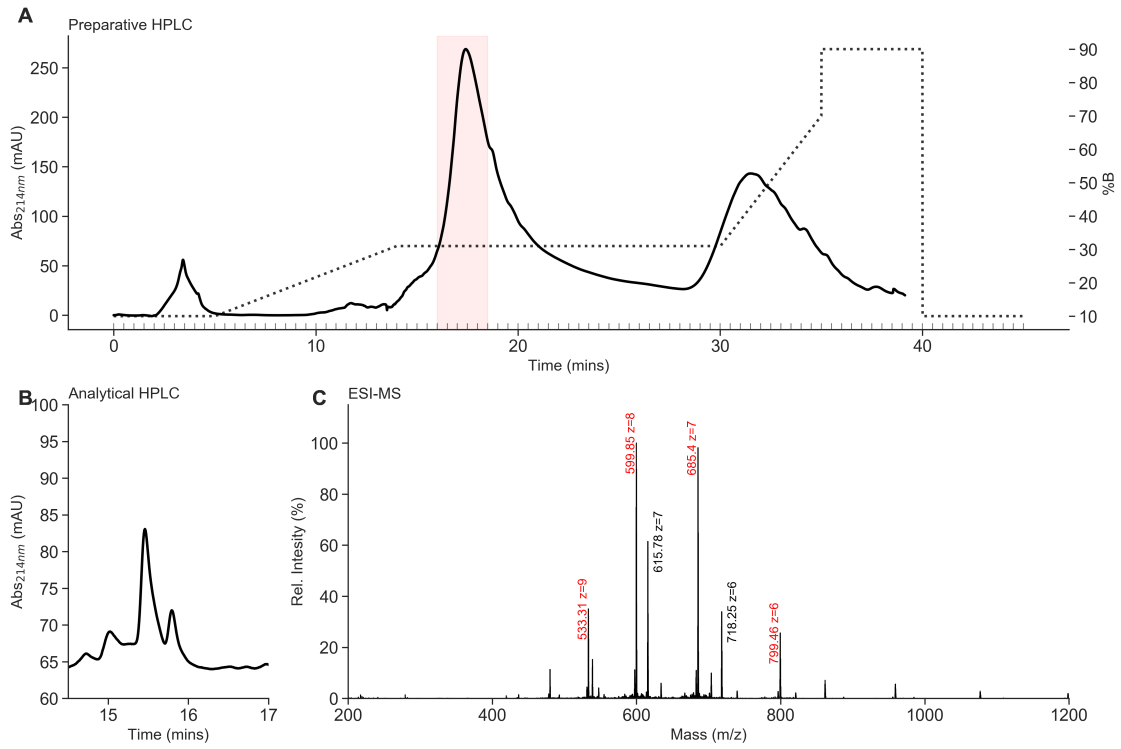


Figure D.2: Third attempt of ST1-QAA purification, showing preparative HPLC UV chromatogram (A), overlaid with modified protocol of Buffer B gradient (dotted line) used for purification attempt. Red highlighted region indicates fractions pooled for shown analytical HPLC (B) to assess purity, and ESI-MS to assess contents of fraction (C). Red annotation indicates mass/charge ratio *(m/z)* of expected M_R for ST1-QAA (4791.52 Da).

impurities through the use of an isocratic hold at 28% B, followed by a shallow gradient of 28-34% over 20 minutes. As it was known that ST1-QAA elutes around 30-34%, it was hoped that contaminants not detected by ESI-MS, but observed in the analytical HPLC may elute before ST1-QAA.

The pre-elution isocratic hold at 28% (Figure D.3 A) showed some improvement over a continuous isocratic hold at 34%, with an increased purity by analytical HPLC and ESI-MS being observed. However, the ghost peaks in the analytical HPLC (Figure D.3 B) were still observed.

Manual collection of analytical HPLC peaks of attempt 3 (Figure D.2 B) were taken, and ESI-MS was performed to ascertain which contaminant was responsible for the additional peaks. The resulting ESI-MS data (not shown) indicated that all peaks analysed were composed of the same combination of ST1-QAA and the truncated peptide, in a consistent manner across the elution. The differential elution

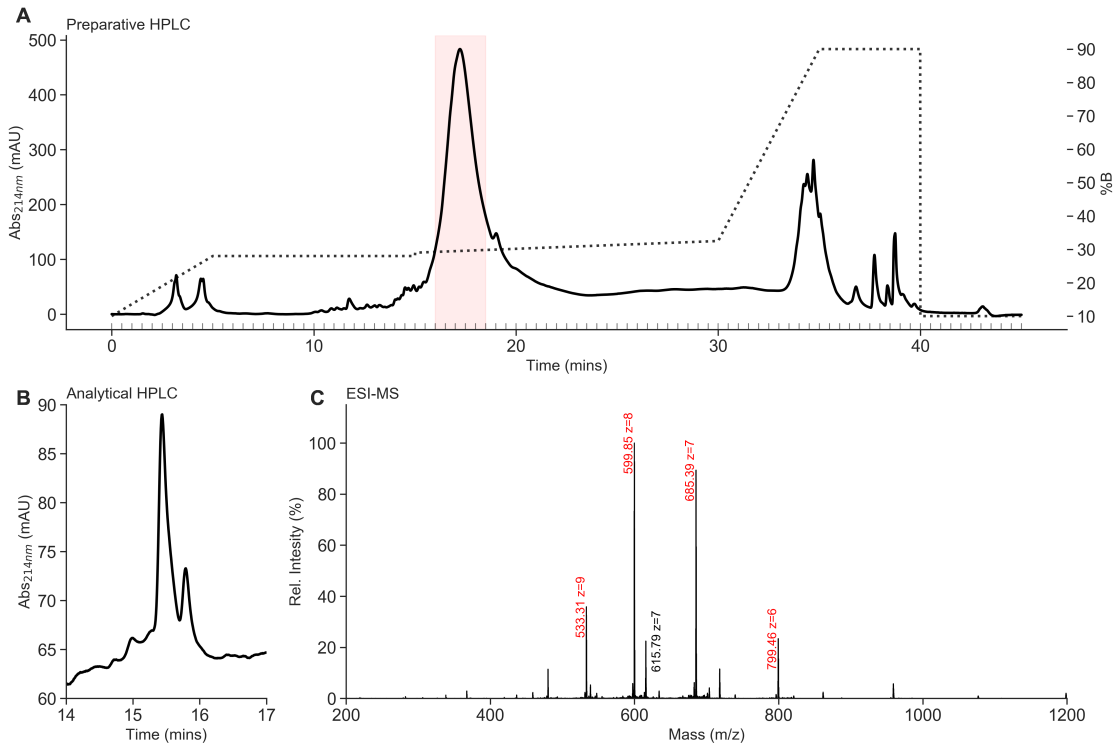


Figure D.3: Fourth attempt of ST1-QAA purification, showing preparative HPLC UV chromatogram (A), overlaid with modified protocol of Buffer B gradient (dotted line) used for purification attempt. Red highlighted region indicates fractions pooled for shown analytical HPLC (B) to assess purity, and ESI-MS to assess contents of fraction (C). Red annotation indicates mass/charge ratio *(m/z)* of expected M_R for ST1-QAA (4791.52 Da).

was therefore thought to be due to co-aggregation of ST1-QAA and the truncated peptide, either during preparative HPLC or prior to injection. This aggregation appeared to hinder full separation between the truncated contaminant and pure ST1-QAA, along with the formation of ghost peaks in the resultant analytical HPLC of pooled fractions. To improve purity and attempt to remove ghost peaks, 10% TFE (*v/v*) was added prior to future injections (Figures D.4 and 5.3). In the hope of achieving usable purity levels, all previous attempts (pooled fractions from Figures 5.2, D.1, D.2 and D.3) were pooled for a final attempt at purification (Figure D.4).

As can be observed in Figure D.4, the addition of 10% (*v/v*) prior to preparative HPLC dramatically improved peak shape. However, the improvement in UV chromatography in both preparative and analytical HPLC did not equate to an improve in purity (as measured by ESI-MS) as expected. This may be due to the presence of residual aggregation, as indicated by remaining ghost peaks in

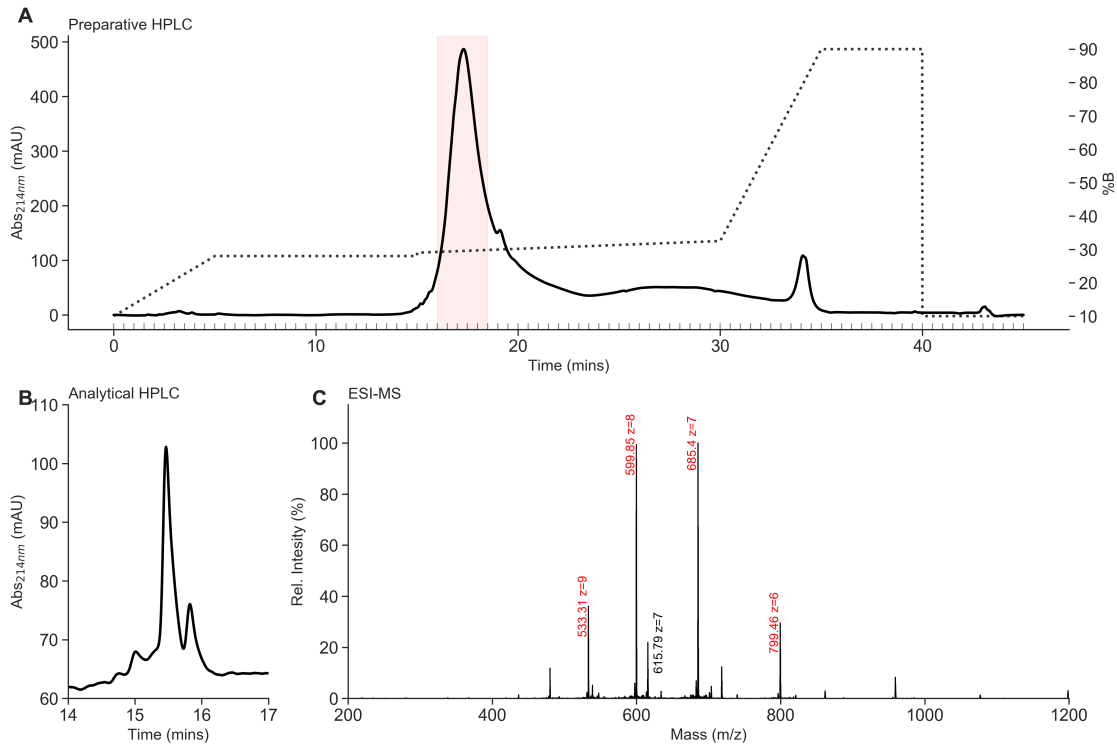


Figure D.4: Fifth attempt of ST1-QAA purification, showing preparative HPLC UV chromatogram (A), overlaid with modified protocol of Buffer B gradient (dotted line) used for purification attempt. Red highlighted region indicates fractions pooled for shown analytical HPLC (B) to assess purity, and ESI-MS to assess contents of fraction (C). Red annotation indicates mass/charge ratio *(m/z)* of expected M_R for ST1-QAA (4791.52 Da).

the analytical HPLC and the persistence of the truncated peptide throughout all fractions tested. Due to the presence of ghost peaks in the analytical HPLC, purity quantification was limited. An approximation of purity through the combination of analytical HPLC and ESI-MS intensities indicated an approximate purity of ~70%, with a final yield of 10.4 mg.

During purification attempts, and subsequent synthesis attempts, it was discovered that the peptide synthesiser had a persistent issue with the regulation of pressure of nitrogen gas. This nitrogen gas is required in the moving of reactants, products, and waste washing per reaction cycle, with the fault eventually evolving into the synthesiser breaking entirely. Due to the length of peptide (47 amino acids), it is highly likely that the yield of peptide normally expected for solid phase peptide synthesis was far lower in the synthesis batch produced in November 2019 due to this fault. In addition to this, arginine coupling is notoriously difficult so it is unsurprising

that the final arginine coupling generated a truncated form of peptide.[315]

During purification attempts, a previously undiscovered batch of crude peptide (synthesised April 2019) was uncovered, this was then purified using the optimised protocol and can be observed in Figure 5.3, and resulted in an estimated purity > 90%, and a final yield of 2.4 mg. The high purity of this crude sample using the same protocol, in addition to the lack of truncated peptide contaminant, indicated that the limiting factor in purification of ST1-QAA was the lower initial purity of ST1-QAA in the crude resin, due to a fault in the peptide synthesiser.

D.2 ST1-QAA T0 EM image

As described in Chapter 5, three time points of ST1-QAA formation were imaged (T0, T3, T24). T3 (Figure 5.4) and T24 (Figure 5.5) showed a large number of discrete particles that allowed for further analysis. However, the T0 images showed large aggregates that make discrete particle analysis challenging. Figure D.5 A and D showed the general structure of these clusters on the EM grid, while B and D present a closer look at the cluster structure in detail. As can be observed in Figure D.5, the size of these clusters was much larger than would be expected for ST1-QAA nanoparticles. In addition, the cluster structure show no semblance of regular order, implying that it was a chaotic association rather than self-assembly. When these factors are combined with the disappearance of these larger particles in the T3 and T24 images, it was assumed that these clusters are temporary aggregations of ST1-QAA monomers during solubilisation in the aqueous buffer.

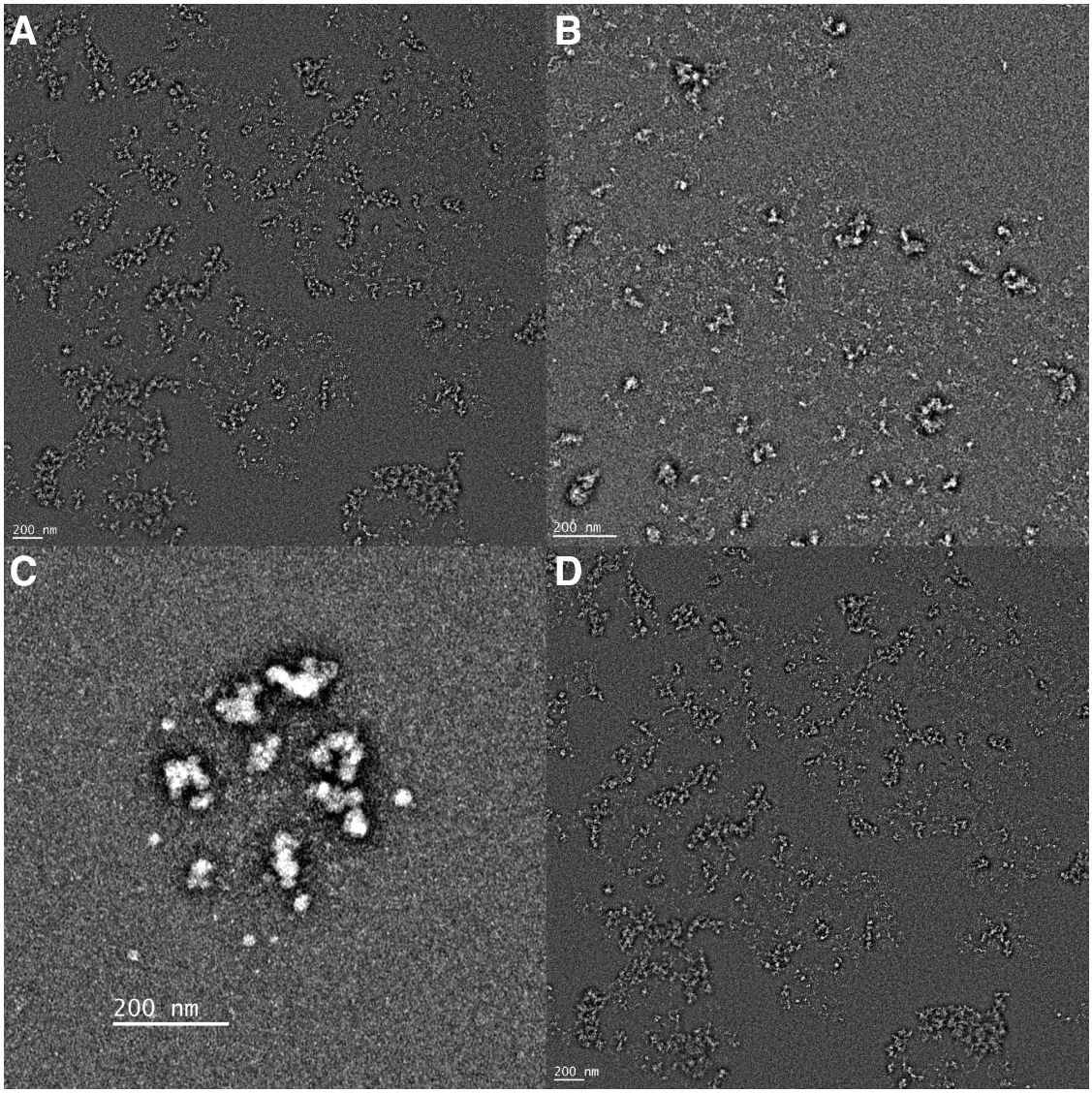


Figure D.5: Formation of ST1-QAA nanoparticles by negative stain imaging, showing severe aggregates of large size in initial stages of incubation

D.3 Additional characterisation assays

The following assays were performed as preliminary assays to aid the biophysical characterisation of ST1-QAA assembly and stability. Unfortunately due to the Covid-19 pandemic these assays were not optimised to functionality (DLS), or do not have sufficient supporting information to be relevant to the main body of work presented in Chapter 5 (CD melt).

D.3.1 Dynamic light scattering (DLS)

DLS measurements were initially designed to be performed in tandem with EM imaging to capture the formation of ST1-QAA viral like particles from monomeric peptide. DLS measurements of ST1-QAA peptide at 100 μM in 30 μL were recorded on a Malvern Zetasizer Nano-ZS using an automated protocol for measurement of 3× 10 scans (of 10 seconds each) every hour for 48 hours at 4°C. This automatic scan was hoped to provide general insight on ST1-QAA formation through particle size, as well as guide future time points for EM imaging at specific timepoints as described by DLS.

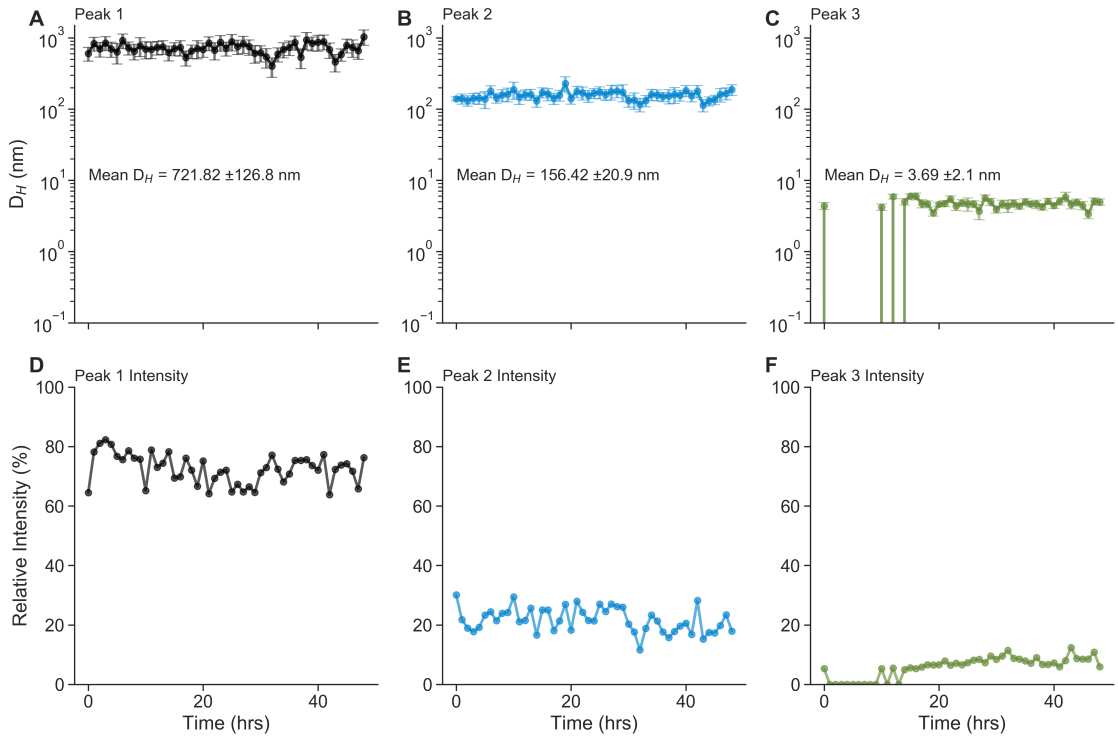


Figure D.6: Formation of ST1-QAA nanoparticles by DLS (as measured by Intensity mode). (A,D) Peak 1 hydrodynamic diameter (D_H) and associated peak intensity. (B,E) Peak 2 hydrodynamic diameter (D_H) and associated peak intensity. (C,F) Peak 3 hydrodynamic diameter (D_H) and associated peak intensity

As described by Figure D.6, the DLS measurements (calculated by the 'Intensity' mode) did not show the expected D_H of ~20 nm (as measured from the EM images) across at any point across the 48 hour measurement. The report generated by the machine also recorded a high degree of noise within the sample measurement,

and equated this to aggregation. Due to the aggregation observed in Figure D.5 for T0 of incubation, it is likely that the concentration of ST1-QAA was too high for DLS measurement under these conditions.

Due to the limited amount of purified ST1-QAA, the DLS optimisation was paused until purification was optimised, and samples were planned to be run at a lower concentration, as well as at 20°C in the hopes of mimicking the DLS measurements performed successfully for TecVir more closely. However, due to the prolonged optimisation of ST1-QAA purification and stalled synthesis of new peptide due to machine failures, this work was subsequently affected by the Covid-19 pandemic.

D.3.2 CD melt

A CD melt was performed, to give insight the purity of ST1-QAA. This method in particular was used partially due to material already being used for the CD time course assay, as well as being seen as an orthogonal method of purity analysis due to the issues with measuring purity by analytical HPLC alone. As a CD-melt has already been recorded for ST1-QAA by a previous member (80-85°C, not shown), it was hoped that this could be used to compare purity between a known purity (the previous member's) and the estimated purity (the sample used in this thesis). If a significant difference was observed between the two purified versions of ST1-QAA, this would indicate that the purified version used in this thesis is of a lower quality than estimated by analytical HPLC and ESI-MS techniques.

Additionally, previous CD melt work on TecVir showed that the tecto-dendrimeric assembly, which showed a T_m of ~55°C, in comparison to a non self-assembling control ($TecVir^{cap}$) showing a T_m of approximately 65°C

As can be seen in Figure D.7 C, the T_m of the ST1-QAA sample estimated to be 90% pure by analytical HPLC and ESI-MS showed good agreement to the previously purified ST1-QAA T_m of 80-80°C. This therefore indicates that the purity estimated by the analytical methods described previously are accurate. Additionally, the pre- and post-melt CD spectra showed good agreement with previous work (not shown),

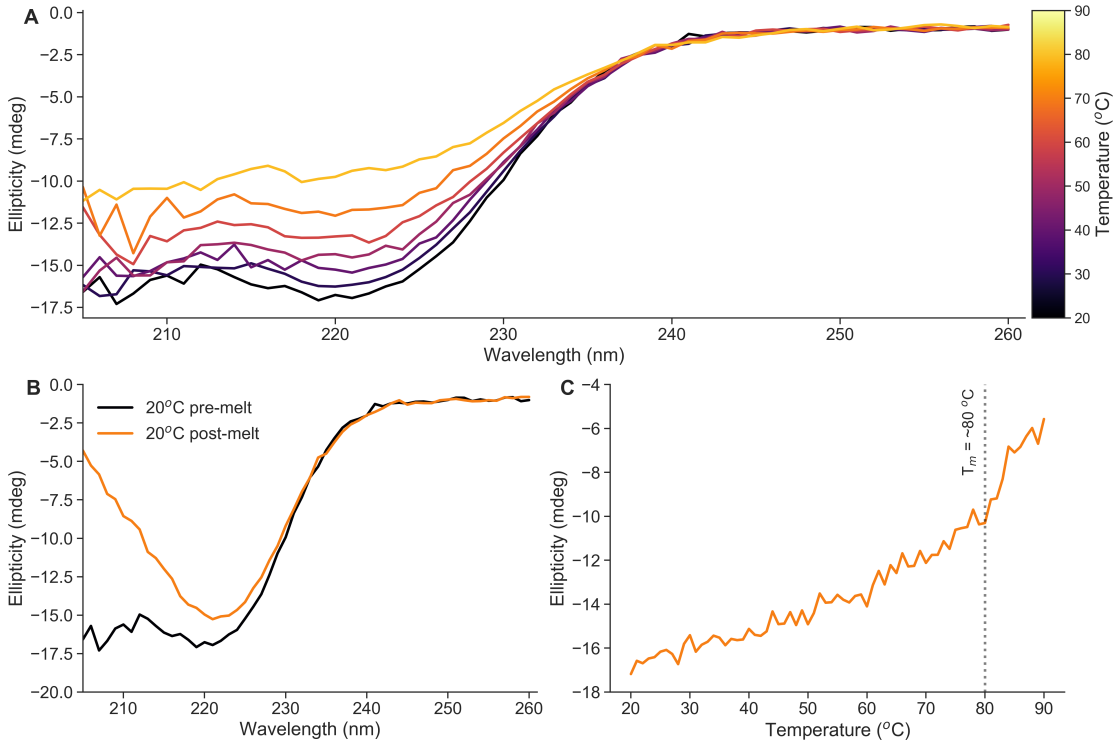


Figure D.7: Circular dichroism (CD) melt spectra of ST1-QAA from 20°C-90°C. (A) CD spectra of ST1-QAA in 10°C increments from 20-90°C (purple-yellow gradient). (B) Pre- (black) and post- (orange) melt CD spectra of ST1-QAA at 20°C. (C) Absorbance measurement of $\Delta\varepsilon$ at 222 nm over temperature in 1°C increments as indicator of secondary structure loss as temperature increases (approximate T_m annotated with black dotted line). ST1-QAA sample prepared from stock to a final peptide concentration of 100 μM in 10 mM MOPS (pH 7.4).

and implied that the modifications of the original TecVir to form ST1-QAA ablate the reversible folding observed in the original TecVir work. It is unclear however which region in particular is the cause of this re-folding failure.

If I have seen further it is by standing on the shoulders of Giants. . . .

— Isaac Newton

References

[1] Pawel L. Urban. “Compartmentalised chemistry: From studies on the origin of life to engineered biochemical systems”. In: *New J. Chem.* 38.11 (2014), pp. 5135–5141.

[2] B Alberts et al. *Molecular Biology of the Cell 4th Edition: International Student Edition*. Routledge, 2002.

[3] Manish Sud et al. “LMSD: LIPID MAPS structure database”. In: *Nucleic Acids Res.* 35.SUPPL. 1 (2007), pp. 527–532.

[4] Eoin Fahy et al. “LIPID MAPS online tools for lipid research”. In: *Nucleic Acids Res.* 35.SUPPL.2 (2007), pp. 606–612.

[5] Ann L. Robbins and David B. Savage. “The genetics of lipid storage and human lipodystrophies”. In: *Trends Mol. Med.* 21.7 (2015), pp. 433–438.

[6] Tamas Balla. “Inositol-lipid binding motifs: Signal integrators through protein-lipid and protein-protein interactions”. In: *J. Cell Sci.* 118.10 (2005), pp. 2093–2104.

[7] Gerrit Van Meer, Dennis R. Voelker, and Gerald W. Feigenson. “Membrane lipids: Where they are and how they behave”. In: *Nat. Rev. Mol. Cell Biol.* 9.2 (2008), pp. 112–124.

[8] Sven Morein et al. “Wild-type Escherichia coli cells regulate the membrane lipid composition in a "window" between gel and non-lamellar structures”. In: *J. Biol. Chem.* 271.12 (1996), pp. 6801–6809.

[9] M. E. Van der Rest et al. “The plasma membrane of Saccharomyces cerevisiae: Structure, function, and biogenesis”. In: *Microbiol. Rev.* 59.2 (1995), pp. 304–322.

[10] M. Kates, E. L. Pugh, and G. Ferrante. “Regulation of Membrane Fluidity by Lipid Desaturases”. In: *Membr. Fluidity*. Boston, MA: Springer US, 1984, pp. 379–395.

[11] Harvey T. McMahon and Emmanuel Boucrot. “Membrane curvature at a glance”. In: *J. Cell Sci.* 128.6 (2015), pp. 1065–1070.

[12] Jacob N. Israelachvili, D. John Mitchell, and Barry W. Ninham. “Theory of self-assembly of hydrocarbon amphiphiles into micelles and bilayers”. In: *J. Chem. Soc. Faraday Trans. 2 Mol. Chem. Phys.* 72 (1976), pp. 1525–1568.

[13] J. Rothman and John Lenard. “Membrane asymmetry”. In: *Science (80-.).* 195.4280 (Feb. 1977), pp. 743–753.

[14] A. J. Verkleij et al. “The asymmetric distribution of phospholipids in the human red cell membrane. A combined study using phospholipases and freeze-etch electron microscopy”. In: *BBA - Biomembr.* 323.2 (1973), pp. 178–193.

[15] Philippe F. Devaux. “Static and Dynamic Lipid Asymmetry in Cell Membranes”. In: *Biochemistry* 30.5 (1991), pp. 1163–1173.

[16] J. H. Lorent et al. “Plasma membranes are asymmetric in lipid unsaturation, packing and protein shape”. In: *Nat. Chem. Biol.* 16.June (2020).

[17] Alan J. Schroit and Robert F.A. Zwaal. “Transbilayer movement of phospholipids in red cell and platelet membranes”. In: *Biochim. Biophys. Acta - Rev. Biomembr.* 1071.3 (Nov. 1991), pp. 313–329.

[18] John S. Allhusen and John C. Conboy. “The ins and outs of lipid flip-flop”. In: *Acc. Chem. Res.* 50.1 (2017), pp. 58–65.

[19] M. Murate et al. “Transbilayer distribution of lipids at nano scale”. In: *J. Cell Sci.* 128.8 (2015), pp. 1627–1638.

[20] Philippe F. Devaux and Alain Zachowski. “Maintenance and consequences of membrane phospholipid asymmetry”. In: *Chem. Phys. Lipids* 73.1-2 (1994), pp. 107–120.

[21] R. F.A. Zwaal, P. Comfurius, and E. M. Bevers. “Surface exposure of phosphatidylserine in pathological cells”. In: *Cell. Mol. Life Sci.* 62.9 (2005), pp. 971–988.

[22] Krishnakumar Balasubramanian, Banafsheh Mirnikjoo, and Alan J. Schroit. “Regulated externalization of phosphatidylserine at the cell surface: Implications for apoptosis”. In: *J. Biol. Chem.* 282.25 (2007), pp. 18357–18364.

[23] Peter A. Leventis and Sergio Grinstein. “The Distribution and Function of Phosphatidylserine in Cellular Membranes”. In: *Annu. Rev. Biophys.* 39.1 (2010), pp. 407–427.

[24] Erwin London. “Membrane Structure-Function Insights from Asymmetric Lipid Vesicles”. In: *Acc. Chem. Res.* 52.8 (2019), pp. 2382–2391.

[25] Philip L Yeagle. *Cholesterol and the cell membrane*. 1985.

[26] Fumiyoshi Abe and Toshiki Hiraki. “Mechanistic role of ergosterol in membrane rigidity and cycloheximide resistance in Saccharomyces cerevisiae”. In: *Biochim. Biophys. Acta - Biomembr.* 1788.3 (2009), pp. 743–752.

[27] Albert Ferrer et al. *Emerging roles for conjugated sterols in plants*. 2017.

[28] E. Sackmann and Toni Feder. “Budding, fission and domain formation in mixed lipid vesicles induced by lateral phase separation and macromolecular condensation”. In: *Mol. Membr. Biol.* 12.1 (Jan. 1995), pp. 21–28.

[29] Jonathan M. Crane and Lukas K. Tamm. “Role of Cholesterol in the Formation and Nature of Lipid Rafts in Planar and Spherical Model Membranes”. In: *Biophys. J.* 86.5 (2004), pp. 2965–2979.

[30] Alex J. Laude and Ian A. Prior. “Plasma membrane microdomains: Organization, function and trafficking (Review)”. In: *Mol. Membr. Biol.* 21.3 (2004), pp. 193–205.

[31] Daniel Lingwood and Kai Simons. “Lipid rafts as a membrane-organizing principle”. In: *Science (80-.).* 327.5961 (2010), pp. 46–50.

[32] Rosie Dawaliby et al. “Allosteric regulation of G protein-coupled receptor activity by phospholipids”. In: *Nat. Chem. Biol.* 12.1 (2016), pp. 35–39.

[33] John A. Allen, Robyn A. Halverson-Tamboli, and Mark M. Rasenick. “Lipid raft microdomains and neurotransmitter signalling”. In: *Nat. Rev. Neurosci.* 8.2 (2007), pp. 128–140.

[34] George A. Robinson et al. “Transcriptional regulation of T-cell lipid metabolism: Implications for plasma membrane lipid rafts and T-cell function”. In: *Front. Immunol.* 8.NOV (2017), pp. 1–10.

[35] Kirsten A Cottrill, Carlos M Farinha, and Nael A. McCarty. “The bidirectional relationship between CFTR and lipids”. In: *Commun. Biol.* 3.1 (Dec. 2020), p. 179.

[36] Olga Wesołowska et al. “Giant unilamellar vesicles - a perfect tool to visualize phase separation and lipid rafts in model systems”. In: *Acta Biochim. Pol.* 56.1 (2009), pp. 33–39.

[37] Michael Edidin. “The state of lipid rafts: From model membranes to cells”. In: *Annu. Rev. Biophys. Biomol. Struct.* 32 (2003), pp. 257–283.

[38] Andrey S. Shaw. “Lipid rafts: Now you see them, now you don’t”. In: *Nat. Immunol.* 7.11 (2006), pp. 1139–1142.

[39] Ilya Levental, Kandice R. Levental, and Frederick A. Heberle. “Lipid Rafts: Controversies Resolved, Mysteries Remain”. In: *Trends Cell Biol.* 30.5 (2020), pp. 341–353.

[40] Matthew J. Van Hook, Scott Nawy, and Wallace B. Thoreson. “Voltage- and calcium-gated ion channels of neurons in the vertebrate retina”. In: *Prog. Retin. Eye Res.* 72.April (2019), p. 100760.

[41] J. Preben Morth et al. “A structural overview of the plasma membrane Na+,K+-ATPase and H+-ATPase ion pumps”. In: *Nat. Rev. Mol. Cell Biol.* 12.1 (Jan. 2011), pp. 60–70.

[42] Nikolaus Pfanner, Bettina Warscheid, and Nils Wiedemann. “Mitochondrial proteins: from biogenesis to functional networks”. In: *Nat. Rev. Mol. Cell Biol.* 20.5 (May 2019), pp. 267–284.

[43] Markus Sällman Almén et al. “Mapping the human membrane proteome: A majority of the human membrane proteins can be classified according to function and evolutionary origin”. In: *BMC Biol.* 7 (2009), p. 50.

[44] Andrew L. Hopkins Overington, John P. Bissan Al-Lazikani. “How many drug targets are there?” In: *Nat. Rev. Drug Discov.* 5.12 (2006), p. 10.

[45] Gunnar Von Heijne. “Membrane-protein topology”. In: *Nat. Rev. Mol. Cell Biol.* 7.12 (2006), pp. 909–918.

[46] Irina D. Pogozheva et al. “Structural adaptations of proteins to different biological membranes”. In: *Biochim. Biophys. Acta - Biomembr.* 1828.11 (2013), pp. 2592–2608.

[47] Anthony G. Lee. “How lipids affect the activities of integral membrane proteins”. In: *Biochim. Biophys. Acta - Biomembr.* 1666.1-2 (2004), pp. 62–87.

[48] Wonhwa Cho and Robert V. Stahelin. “Membrane-protein interactions in cell signaling and membrane trafficking”. In: *Annu. Rev. Biophys. Biomol. Struct.* 34 (2005), pp. 119–151.

[49] Boyan Bonev et al. “Electrostatic peptide–lipid interactions of amyloid-β peptide and pentalysine with membrane surfaces monitored by 31P MAS NMR”. In: *Phys. Chem. Chem. Phys.* 3.14 (2001), pp. 2904–2910.

[50] Björn H. Falkenburger et al. “Phosphoinositides: Lipid regulators of membrane proteins”. In: *J. Physiol.* Vol. 588. 17. 2010, pp. 3179–3185.

[51] Daniel Kerr et al. “Sensitivity of peripheral membrane proteins to the membrane context: A case study of phosphatidylserine and the TIM proteins”. In: *Biochim. Biophys. Acta - Biomembr.* 1860.10 (2018), pp. 2126–2133.

[52] Katarina Moravcevic, Camilla L. Oxley, and Mark A. Lemmon. “Conditional Peripheral Membrane Proteins: Facing up to Limited Specificity”. In: *Structure* 20.1 (Jan. 2012), pp. 15–27. arXiv: NIHMS150003.

[53] N N Nalivaeva and A J Turner. “Lipid Anchors to Proteins”. In: *Handb. Neurochem. Mol. Neurobiol. Neural Lipids*. Ed. by Abel Lajtha, Guido Tettamanti, and Gianfrancesco Goracci. Boston, MA: Springer US, 2009, pp. 353–372.

[54] Hiroh Ikezawa. “Glycosylphosphatidylinositol (GPI)-anchored proteins.” eng. In: *Biol. Pharm. Bull.* 25.4 (Apr. 2002), pp. 409–417.

[55] Michael A J Ferguson, Taroh Kinoshita, and Gerald W Hart. “Glycosylphosphatidylinositol Anchors.” eng. In: ed. by Ajit Varki et al. 2009.

[56] Chiara Zurzolo and Kai Simons. “Glycosylphosphatidylinositol-anchored proteins: Membrane organization and transport”. In: *Biochim. Biophys. Acta - Biomembr.* 1858.4 (2016), pp. 632–639.

[57] Guillermo Romero. “Inositolglycans and cellular signalling”. In: *Cell Biol. Int. Rep.* 15.9 PART 1 (Sept. 1991), pp. 827–852.

[58] T. S. van Zanten et al. “Hotspots of GPI-anchored proteins and integrin nanoclusters function as nucleation sites for cell adhesion”. In: *Proc. Natl. Acad. Sci.* 106.44 (Nov. 2009), pp. 18557–18562.

[59] Theodore G. Clark et al. “The I-antigens of Ichthyophthirius multifiliis are GPI-anchored proteins”. In: *J. Eukaryot. Microbiol.* 48.3 (May 2001), pp. 332–337.

[60] Fang L Zhang. “Protein Prenylation: Molecular Mechanisms and Functional Consequences”. In: *Annu. Rev. Biochem.* 65.1 (Jan. 1996), pp. 241–269.

[61] P J Casey. “Biochemistry of protein prenylation.” In: *J. Lipid Res.* 33.12 (Dec. 1992), pp. 1731–1740.

[62] Charuta C. Palsuledesai and Mark D. Distefano. “Protein prenylation: Enzymes, therapeutics, and biotechnology applications”. In: *ACS Chem. Biol.* 10.1 (2015), pp. 51–62.

[63] Mei Wang and Patrick J. Casey. “Protein prenylation: Unique fats make their mark on biology”. In: *Nat. Rev. Mol. Cell Biol.* 17.2 (2016), pp. 110–122.

[64] Ajit Varki et al., eds. *Essentials of Glycobiology*. eng. 2015.

[65] D A Cumming. “Physiological relevance of protein glycosylation.” eng. In: *Dev. Biol. Stand.* 76 (1992), pp. 83–94.

[66] Robert S. Haltiwanger and John B. Lowe. “Role of Glycosylation in Development”. In: *Annu. Rev. Biochem.* 73.1 (2004), pp. 491–537.

[67] Pauline M. Rudd et al. “Roles for glycosylation of cell surface receptors involved in cellular immune recognition”. In: *J. Mol. Biol.* 293.2 (1999), pp. 351–366.

[68] Kazuaki Ohtsubo and Jamey D. Marth. “Glycosylation in Cellular Mechanisms of Health and Disease”. In: *Cell* 126.5 (2006), pp. 855–867.

[69] Bobby G. Ng and Hudson H. Freeze. “Perspectives on Glycosylation and Its Congenital Disorders”. In: *Trends Genet.* 34.6 (2018), pp. 466–476.

[70] Derek Marsh. “Protein modulation of lipids, and vice-versa, in membranes”. In: *Biochim. Biophys. Acta - Biomembr.* 1778.7-8 (2008), pp. 1545–1575.

[71] Derek Marsh and László I. Horváth. “Structure, dynamics and composition of the lipid-protein interface. Perspectives from spin-labelling”. In: *Biochim. Biophys. Acta - Rev. Biomembr.* 1376.3 (1998), pp. 267–296.

[72] Gary L. Powell, Peter F. Knowles, and Derek Marsh. “Association of spin-labelled cardiolipin with dimyristoylphosphatidylcholine-substituted bovine heart cytochrome c oxidase. A generalized specificity increase rather than highly specific binding sites”. In: *BBA - Biomembr.* 816.1 (1985), pp. 191–194.

[73] Hildur Palsdottir and Carola Hunte. *Lipids in membrane protein structures.* 2004.

[74] Duncan Laverty et al. “Cryo-EM structure of the human $\alpha1\beta3\gamma2$ GABAA receptor in a lipid bilayer”. In: *Nature* 565.7740 (2019), pp. 516–520.

[75] Takanori Nakane et al. “Single-particle cryo-EM at atomic resolution”. In: *Nature* 587.7832 (2020), pp. 152–156.

[76] Germán G Sgro and Tiago R D Costa. “Cryo-EM Grid Preparation of Membrane Protein Samples for Single Particle Analysis”. In: *Front. Mol. Biosci.* 5.July (2018), pp. 1–8.

[77] Xia Yao, Xiao Fan, and Nieng Yan. “Cryo-EM analysis of a membrane protein embedded in the liposome”. In: *Proc. Natl. Acad. Sci. U. S. A.* 117.31 (2020), pp. 18497–18503.

[78] J. Antoinette Killian. “Hydrophobic mismatch between proteins and lipids in membranes”. In: *Biochim. Biophys. Acta - Rev. Biomembr.* 1376.3 (1998), pp. 401–416.

[79] Nancy K. Burgess et al. “β-Barrel proteins that reside in the Escherichia coli outer membrane in vivo demonstrate varied folding behavior in vitro”. In: *J. Biol. Chem.* 283.39 (2008), pp. 26748–26758.

[80] Ipsita Basu, Amitabha Chattopadhyay, and Chaitali Mukhopadhyay. “Ion channel stability of Gramicidin A in lipid bilayers: Effect of hydrophobic mismatch”. In: *Biochim. Biophys. Acta - Biomembr.* 1838.1 PARTB (2014), pp. 328–338.

[81] Anthony G. Lee. “Lipid-protein interactions”. In: *Biochem. Soc. Trans.* 39.3 (2011), pp. 761–766.

[82] María Florencia Pignataro et al. “Modulation of plasma membrane Ca2+-ATPase by neutral phospholipids: Effect of the micelle-vesicle transition and the bilayer thickness”. In: *J. Biol. Chem.* 290.10 (2015), pp. 6179–6190.

[83] Hayley J. Sharpe, Tim J. Stevens, and Sean Munro. “A Comprehensive Comparison of Transmembrane Domains Reveals Organelle-Specific Properties”. In: *Cell* 142.1 (2010), pp. 158–169.

[84] Theo A. Berkhout, Annie Rietveld, and Ben de Kruijff. "Preferential lipid association and mode of penetration of apocytochrome c in mixed model membranes as monitored by tryptophanyl fluorescence quenching using brominated phospholipids". In: *BBA - Biomembr.* 897.1 (1987), pp. 1–4.

[85] Steve L Reichow and Tamir Gonen. *Lipid-protein interactions probed by electron crystallography*. 2009.

[86] Jacco van Rheenen et al. "PIP2 signaling in lipid domains: a critical re-evaluation". In: *EMBO J.* 24.9 (May 2005), pp. 1664–1673.

[87] Henriette Elisabeth Autzen et al. "Regulation of the Ca2+-ATPase by cholesterol: A specific or non-specific effect?" In: *Mol. Membr. Biol.* 32.3 (2015), pp. 75–87.

[88] María Lourdes Renart et al. *Modulation of function, structure and clustering of K+ channels by lipids: Lessons learnt from KcsA*. 2020.

[89] Stefan Gahbauer and Rainer A Böckmann. *Membrane-mediated oligomerization of G protein coupled receptors and its implications for GPCR function*. 2016.

[90] Joanne Oates et al. "The role of cholesterol on the activity and stability of neurotensin receptor 1". In: *Biochim. Biophys. Acta - Biomembr.* 1818.9 (2012), pp. 2228–2233.

[91] Juan H. Bolivar et al. "Interaction of lipids with the neurotensin receptor 1". In: *Biochim. Biophys. Acta - Biomembr.* 1858.6 (2016), pp. 1278–1287.

[92] Neal C. Robinson. "Specificity and Binding Affinity of Phospholipids to the High-Affinity Cardiolipin Sites of Beef Heart Cytochrome c Oxidase". In: *Biochemistry* 21.1 (1982), pp. 184–188.

[93] Giuseppe Paradies et al. "Role of Cardiolipin in Mitochondrial Function and Dynamics in Health and Disease: Molecular and Pharmacological Aspects". In: *Cells* 8.7 (2019), p. 728.

[94] Michelle Grace Acoba, Nanami Senoo, and Steven M Claypool. "Phospholipid ebb and flow makes mitochondria go". In: *J. Cell Biol.* 219.8 (July 2020).

[95] Edward Ross Pennington et al. *The role of cardiolipin concentration and acyl chain composition on mitochondrial inner membrane molecular organization and function*. 2019.

[96] Andrej Musatov and Neal C. Robinson. "Bound cardiolipin is essential for cytochrome c oxidase proton translocation". In: *Biochimie* 105.9 (Oct. 2014), pp. 159–164. arXiv: NIHMS150003.

[97] Neal C. Robinson. "Functional binding of cardiolipin to cytochrome c oxidase". In: *J. Bioenerg. Biomembr.* 25.2 (1993), pp. 153–163.

[98] Marcella C. Orwick et al. "Detergent-free formation and physicochemical characterization of nanosized lipid-polymer complexes: Lipodisq". In: *Angew. Chemie - Int. Ed.* 51.19 (2012), pp. 4653–4657.

[99] Jani Reddy Bolla et al. "Membrane Protein–Lipid Interactions Probed Using Mass Spectrometry". In: *Annu. Rev. Biochem.* 88.1 (2019), pp. 85–111.

[100] Joseph Gault et al. "Combining native and 'omics' mass spectrometry to identify endogenous ligands bound to membrane proteins". In: *Nat. Methods* 17.5 (May 2020), pp. 505–508.

[101] Jani Reddy Bolla et al. “A Mass-Spectrometry-Based Approach to Distinguish Annular and Specific Lipid Binding to Membrane Proteins”. In: *Angew. Chemie Int. Ed.* 59.9 (Feb. 2020), pp. 3523–3528.

[102] Annela M. Seddon, Paul Curnow, and Paula J. Booth. “Membrane proteins, lipids and detergents: Not just a soap opera”. In: *Biochim. Biophys. Acta - Biomembr.* 1666.1-2 (2004), pp. 105–117.

[103] A. D. Bangham, M. W. Hill, and N. G. A. Miller. “Preparation and Use of Liposomes as Models of Biological Membranes”. In: *Methods Membr. Biol.* Boston, MA: Springer US, 1974, pp. 1–68.

[104] Thomas D Madden. “CURRENT CONCEPTS IN MEMBRANE PROTEIN RECONSTITUTION”. In: *Chem. Phys. Lipids* 40 (1986), pp. 207–222.

[105] Maria E Zoghbi and Guillermo A Altenberg. *Membrane protein reconstitution in nanodiscs for luminescence spectroscopy studies*. 2017.

[106] Ida Louise Jørgensen, Gerdi Christine Kemmer, and Thomas Günther Pomorski. *Membrane protein reconstitution into giant unilamellar vesicles: a review on current techniques*. 2017.

[107] E. Ruckenstein and R. Nagarajan. “Critical micelle concentration. A transition point for micellar size distribution”. In: *J. Phys. Chem.* 79.24 (1975), pp. 2622–2626.

[108] Abani K Bhuyan. “On the mechanism of SDS-induced protein denaturation”. In: *Biopolymers* 93.2 (2010), pp. 186–199.

[109] J.-L. Rigaud et al. “Detergent removal by non-polar polystyrene beads”. In: *Eur. Biophys. J.* 27.4 (1998), pp. 305–319.

[110] Daniel Yin. “Biophysical Investigations into Membrane-Active Peptides and Proteins”. PhD thesis. University of Oxford, 2016.

[111] Rongfu Zhang et al. “Characterizing the structure of lipodisq nanoparticles for membrane protein spectroscopic studies”. In: *Biochim. Biophys. Acta - Biomembr.* 1848.1 (2015), pp. 329–333. arXiv: NIHMS150003.

[112] Abolfazl Akbarzadeh et al. “Liposome: classification, preparation, and applications”. In: *Nanoscale Res. Lett.* 8.102 (2013), pp. 1–9.

[113] Aldo Jesorka and Owe Orwar. “Liposomes: Technologies and Analytical Applications”. In: *Annu. Rev. Anal. Chem.* 1.1 (2008), pp. 801–832.

[114] Radda Rusinova et al. “Regulation of Ion Channel Function by the Host Lipid Bilayer Examined by a Stopped-Flow Spectrofluorometric Assay”. In: *Biophys. J.* 106.5 (Mar. 2014), pp. 1070–1078.

[115] Eric R Geertsma et al. “Membrane reconstitution of ABC transporters and assays of translocator function”. In: *Nat. Protoc.* 3.2 (2008), pp. 256–266.

[116] Nelson F. Morales-Penningston et al. *GUV preparation and imaging: Minimizing artifacts*. July 2010.

[117] William L Hwang et al. “Asymmetric droplet interface bilayers”. In: *J. Am. Chem. Soc.* 130.18 (2008), pp. 5878–5879.

[118] Maria Hitrik, Ovadia Lev, and Daniel Mandler. “Formation of asymmetric membrane by deposition of a hybrid sol-gel sublayer on top of a Langmuir film skin”. In: *J. Memb. Sci.* 595.October 2019 (2020), p. 117559.

[119] Milka Doktorova et al. “Preparation of asymmetric phospholipid vesicles for use as cell membrane models”. In: *Nat. Protoc.* ().

[120] Richard M Epand and Raquel F Epand. “Liposomes as Models for Antimicrobial Peptides”. In: *Biochim. Biophys. Acta*. Vol. 11. 1462. 2003, pp. 124–133.

[121] Charles R Sanders and R Scott Prosser. “Bicelles: A model membrane system for all seasons?” In: *Structure* 6.10 (1998), pp. 1227–1234.

[122] Alexandre Arnold et al. “Cation modulation of bicelle size and magnetic alignment as revealed by solid-state NMR and electron microscopy”. In: *Biophys. J.* 83.5 (2002), pp. 2667–2680.

[123] Timothy H Bayburt and Stephen G Sligar. “Membrane protein assembly into Nanodiscs”. In: *FEBS Lett.* 584.9 (May 2010), pp. 1721–1727. arXiv: 15334406.

[124] T. K. Ritchie et al. *Chapter 11 Reconstitution of Membrane Proteins in Phospholipid Bilayer Nanodiscs*. 2009.

[125] Vito Graziano, Lisa Miller, and Lin Yang. “Interpretation of solution scattering data from lipid nanodiscs”. In: *J. Appl. Crystallogr.* 51.1 (Feb. 2018), pp. 157–166.

[126] Robbins Puthenveetil, Khiem Nguyen, and Olga Vinogradova. *Nanodiscs and solution NMR: Preparation, application and challenges*. Feb. 2017.

[127] Abhinav Nath et al. “Single-molecule fluorescence spectroscopy using phospholipid bilayer nanodiscs.” In: *Methods Enzymol.* 472.10 (2010), pp. 89–117.

[128] Christophe Tribet, Roland Audebert, and Jean Luc Popot. “Amphipols: Polymers that keep membrane proteins soluble in aqueous solutions”. In: *Proc. Natl. Acad. Sci. U. S. A.* 93.26 (1996), pp. 15047–15050.

[129] Jörg H Kleinschmidt and Jean Luc Popot. *Folding and stability of integral membrane proteins in amphipols*. 2015.

[130] Manuela Zoonens and Jean-Luc Popot. “Amphipols for Each Season”. In: *J. Membr. Biol.* 247.9-10 (Oct. 2014), pp. 759–796. arXiv: NIHMS150003.

[131] Sam M Ireland, Altin Sula, and B. A. Wallace. “Thermal melt circular dichroism spectroscopic studies for identifying stabilising amphipathic molecules for the voltage-gated sodium channel NavMs”. In: *Biopolymers* 109.8 (Aug. 2018), pp. 1–8.

[132] Noelya Planchard et al. “The Use of Amphipols for Solution NMR Studies of Membrane Proteins: Advantages and Constraints as Compared to Other Solubilizing Media”. In: *J. Membr. Biol.* 247.9-10 (2014), pp. 827–842.

[133] Jason D. Perlmutter, Jean Luc Popot, and Jonathan N Sachs. “Molecular Dynamics Simulations of a Membrane Protein/Amphipol Complex”. In: *J. Membr. Biol.* 247.9-10 (2014), pp. 883–895.

[134] Marcella Orwick-Rydmark et al. “Detergent-free incorporation of a seven-transmembrane receptor protein into nanosized bilayer lipodisq particles for functional and biophysical studies”. In: *Nano Lett.* 12.9 (2012), pp. 4687–4692.

[135] S Lee et al. “How do short chain non-ionic detergents destabilize GPCRs?” In: 138.47 (2016), pp. 15425–15433.

[136] Stephen R. Tonge. *Compositions comprising a lipid and copolymer of styrene and maleic acid*. 2006.

[137] Marcella Orwick-Rydmark et al. “Detergent-free incorporation of a seven-transmembrane receptor protein into nanosized bilayer lipodisq particles for functional and biophysical studies”. In: *Nano Lett.* 12.9 (2012), pp. 4687–4692.

[138] Timothy J. Knowles et al. “Membrane proteins solubilized intact in lipid containing nanoparticles bounded by styrene maleic acid copolymer”. In: *J. Am. Chem. Soc.* 131.22 (2009), pp. 7484–7485.

[139] David J.K. Swainsbury et al. “The effectiveness of styrene-maleic acid (SMA) copolymers for solubilisation of integral membrane proteins from SMA-accessible and SMA-resistant membranes”. In: *Biochim. Biophys. Acta - Biomembr.* 1859.10 (2017), pp. 2133–2143.

[140] Philipp S. Orekhov et al. “Styrene/Maleic Acid Copolymers Form SMALPs by Pulling Lipid Patches out of the Lipid Bilayer”. In: *Langmuir* 35.10 (2019), pp. 3748–3758.

[141] Stefan Scheidelaar et al. “Effect of Polymer Composition and pH on Membrane Solubilization by Styrene-Maleic Acid Copolymers”. In: *Biophys. J.* 111.9 (2016), pp. 1974–1986.

[142] Juan Francisco Bada Juarez et al. *From polymer chemistry to structural biology: The development of SMA and related amphipathic polymers for membrane protein extraction and solubilisation*. 2019.

[143] Abraham Olusegun Oluwole et al. “Formation of Lipid-Bilayer Nanodiscs by Diisobutylene/Maleic Acid (DIBMA) Copolymer”. In: *Langmuir* 33.50 (2017), pp. 14378–14388.

[144] Tanushree Bala et al. “Interaction of different metal ions with carboxylic acid group: A quantitative study”. In: *J. Phys. Chem. A* 111.28 (2007), pp. 6183–6190.

[145] Adrian H. Kopf et al. “Factors influencing the solubilization of membrane proteins from Escherichia coli membranes by styrene–maleic acid copolymers”. In: *Biochim. Biophys. Acta - Biomembr.* (2019), p. 183125.

[146] Thirupathi Ravula et al. “Bioinspired, Size-Tunable Self-Assembly of Polymer–Lipid Bilayer Nanodiscs”. In: *Angew. Chemie - Int. Ed.* 56.38 (2017), pp. 11466–11470.

[147] Mansoore Esmaili and Michael Overduin. *Membrane biology visualized in nanometer-sized discs formed by styrene maleic acid polymers*. 2018.

[148] Giacomo M. Di Mauro, Nathaniel Z Hardin, and Ayyalusamy Ramamoorthy. “Lipid-nanodiscs formed by paramagnetic metal chelated polymer for fast NMR data acquisition”. In: *Biochim. Biophys. Acta - Biomembr.* 1862.9 (2020), p. 183332.

[149] Simon Lindhoud et al. “SMA-SH: Modified Styrene-Maleic Acid Copolymer for Functionalization of Lipid Nanodiscs”. In: *Biomacromolecules* 17.4 (Apr. 2016), pp. 1516–1522.

[150] Victoria Schmidt and James N. Sturgis. “Modifying styrene-maleic acid co-polymer for studying lipid nanodiscs”. In: *Biochim. Biophys. Acta - Biomembr.* 1860.3 (2018), pp. 777–783.

[151] Abraham Olusegun Oluwole et al. “Solubilization of Membrane Proteins into Functional Lipid-Bilayer Nanodiscs Using a Diisobutylene/Maleic Acid Copolymer”. In: *Angew. Chemie - Int. Ed.* 56.7 (2017), pp. 1919–1924.

[152] Bartholomäus Danielczak, Annette Meister, and Sandro Keller. “Influence of Mg 2+ and Ca 2+ on nanodisc formation by diisobutylene/maleic acid (DIBMA) copolymer”. In: *Chem. Phys. Lipids* 221.November 2018 (2019), pp. 30–38.

[153] Aiman A Gulamhussein et al. “A comparison of SMA (styrene maleic acid) and DIBMA (di-isobutylene maleic acid) for membrane protein purification”. In: *Biochim. Biophys. Acta - Biomembr.* 1862.7 (2020), p. 183281.

[154] Kazuma Yasuhara et al. “Spontaneous Lipid Nanodisc Fomation by Amphiphilic Polymethacrylate Copolymers”. In: *J. Am. Chem. Soc.* 139.51 (2017), pp. 18657–18663.

[155] Irving Ozier. *Molecular spectroscopy*. eng. Oxford, 1985.

[156] E. Huber and M. Frost. “Light scattering by small particles”. eng. In: *J. Water Supply Res. Technol. - AQUA*. Structure of matter series 47.2 (1998), pp. 87–94.

[157] Keiran Stevenson et al. “General calibration of microbial growth in microplate readers”. In: *Sci. Rep.* 6.December (2016), pp. 4–10.

[158] Michael Kaszuba et al. “Measuring sub nanometre sizes using dynamic light scattering”. In: *J. Nanoparticle Res.* 10.5 (2008), pp. 823–829.

[159] Jörg Stetefeld, Sean A. McKenna, and Trushar R Patel. *Dynamic light scattering: a practical guide and applications in biomedical sciences*. 2016.

[160] Niko Hildebrandt and Igor L Medintz. *FRET - Förster Resonance Energy Transfer : From Theory to Applications*. Weinheim, GERMANY: John Wiley & Sons, Incorporated, 2013.

[161] Rahul Roy, Sungchul Hohng, and Taekjip Ha. *A practical guide to single-molecule FRET*. June 2008.

[162] Norbert Kucerka, Mikhail a Kiselev, and Pavol Balgavý. “Determination of bilayer thickness and lipid surface area in unilamellar dimyristoylphosphatidylcholine vesicles from small-angle neutron scattering curves: a comparison of evaluation methods.” In: *Eur. Biophys. J.* 33.4 (2004), pp. 328–334.

[163] David E. Wolf et al. “Determination of the Transbilayer Distribution of Fluorescent Lipid Analogs by Nonradiative Fluorescence Resonance Energy Transfer”. In: *Biochemistry* 31.11 (1992), pp. 2865–2873.

[164] Matthias J.N.Junk. *Assessing the Functional Structure of Molecular Transporters by EPR Spectroscopy*. Berlin, Heidelberg: Springer Berlin Heidelberg, 2012.

[165] Indra D. Sahu et al. “Characterization of KCNE1 inside Lipodisq Nanoparticles for EPR Spectroscopic Studies of Membrane Proteins”. In: *J. Phys. Chem. B* 121.21 (2017), pp. 5312–5321.

[166] D. Marsh and A. Watts. *Liposomes: From physical structure to therapeutic applications*. Ed. by C. G. Knight. 7th ed. 1981, pp. 139–189.

[167] J Wiseman. “The Spin-Labeling Technique”. In: 2.1965 (1972), pp. 242–257.

[168] Edward J. Shimshick and Harden M. Mcconnell. “Lateral Phase Separation in Phospholipid Membranes”. In: *Biochemistry* 12.12 (1973), pp. 2351–2360.

[169] R. B. Merrifield. “Solid Phase Peptide Synthesis. I. The Synthesis of a Tetrapeptide”. In: *J. Am. Chem. Soc.* 85.14 (1963), pp. 2149–2154.

[170] Da’san M.M. Jaradat. “Thirteen decades of peptide synthesis: key developments in solid phase peptide synthesis and amide bond formation utilized in peptide ligation”. In: *Amino Acids* 50.1 (2018), pp. 39–68.

[171] Louis A. Carpino and Grace Y. Han. “The 9-Fluorenylmethoxycarbonyl Function, a New Base-Sensitive Amino-Protecting Group”. In: *J. Am. Chem. Soc.* 92.19 (1970), pp. 5748–5749.

[172] Raymond Behrendt, Peter White, and John Offer. “Advances in Fmoc solid-phase peptide synthesis”. In: *J. Pept. Sci.* 22.1 (2016), pp. 4–27.

[173] Sangbae Lee et al. “How Do Short Chain Nonionic Detergents Destabilize G-Protein-Coupled Receptors?” In: *J. Am. Chem. Soc.* 138.47 (2016), pp. 15425–15433.

[174] Aldona Jelinska et al. “Denaturation of proteins by surfactants studied by the taylor dispersion analysis”. In: *PLoS One* 12.4 (2017), pp. 1–11.

[175] Emmanuel Nji et al. “An engineered thermal-shift screen reveals specific lipid preferences of eukaryotic and prokaryotic membrane proteins”. In: *Nat. Commun.* 9.1 (2018).

[176] Kallol Gupta et al. “The role of interfacial lipids in stabilizing membrane protein oligomers”. In: *Nature* 541.7637 (2017), pp. 421–424.

[177] Jonas M. Dörr et al. “The styrene–maleic acid copolymer: a versatile tool in membrane research”. In: *Eur. Biophys. J.* 45.1 (2016), pp. 3–21.

[178] Kailene S. Simon, Naomi L. Pollock, and Sarah C. Lee. *Membrane protein nanoparticles: The shape of things to come*. 2018.

[179] Aiman Sadaf et al. *Amphipathic agents for membrane protein study*. 1st ed. Vol. 557. Elsevier Inc., 2015, pp. 57–94.

[180] Marta G. Lete et al. “Fast and slow biomembrane solubilizing detergents: Insights into their mechanism of action”. In: *Colloids Surfaces B Biointerfaces* 183.June (2019), p. 110430.

[181] Minmin Xue et al. “Molecular Mechanism of Lipid Nanodisk Formation by Styrene-Maleic Acid Copolymers”. In: *Biophys. J.* 115.3 (2018), pp. 494–502.

[182] Ashley R. Long et al. “A detergent-free strategy for the reconstitution of active enzyme complexes from native biological membranes into nanoscale discs”. In: *BMC Biotechnol.* 13.1 (2013), p. 41.

[183] Victoria Schmidt et al. “The lipid environment of Escherichia coli Aquaporin Z”. In: *Biochim. Biophys. Acta - Biomembr.* 1861.2 (2019), pp. 431–440.

[184] Marta Barniol-Xicota and Steven H.L. Verhelst. “Stable and Functional Rhomboid Proteases in Lipid Nanodiscs by Using Diisobutylene/Maleic Acid Copolymers”. In: *J. Am. Chem. Soc.* 140.44 (2018), pp. 14557–14561.

[185] Javier Vinals Camallonga. “Biophysical studies on the structure and function of Archaerhodopsin-3”. PhD thesis. University of Oxford, 2019.

[186] Naomi L. Pollock et al. “SMA-PAGE: A new method to examine complexes of membrane proteins using SMALP nano-encapsulation and native gel electrophoresis”. In: *Biochim. Biophys. Acta - Biomembr.* 1861.8 (2019), pp. 1437–1445.

[187] Nils Hellwig et al. “Native mass spectrometry goes more native: Investigation of membrane protein complexes directly from SMALPs”. In: *Chem. Commun.* 54.97 (2018), pp. 13702–13705.

[188] Alvin C.K. Teo et al. “Analysis of SMALP co-extracted phospholipids shows distinct membrane environments for three classes of bacterial membrane protein”. In: *Sci. Rep.* 9.1 (2019), pp. 1–10.

[189] Juan F. Bada Juarez et al. “Lipodisqs for eukaryote lipidomics with retention of viability: Sensitivity and resistance to Leucobacter infection linked to C.elegans cuticle composition”. In: *Chem. Phys. Lipids* 222.February (2019), pp. 51–58.

[190] S. R. Tonge and B. J. Tighe. “Responsive hydrophobically associating polymers: A review of structure and properties”. In: *Adv. Drug Deliv. Rev.* 53.1 (2001), pp. 109–122.

[191] Stephen C.L. Hall et al. “Influence of Poly(styrene- co -maleic acid) Copolymer Structure on the Properties and Self-Assembly of SMALP Nanodiscs”. In: *Biomacromolecules* 19.3 (2018), pp. 761–772.

[192] Worth H. Rodebush and Isaac Feldman. “Ultraviolet Absorption Spectra of Organic Molecules. III. Mechanical Interference of Substituent Groups with Resonance Configurations”. In: *J. Am. Chem. Soc.* 68.5 (1946), pp. 896–899.

[193] Harold Edelhoch. “Spectroscopic Determination of Tryptophan and Tyrosine in Proteins”. In: *Biochemistry* 6.7 (1967), pp. 1948–1954.

[194] Nicholas J. Anthis and G. Marius Clore. “Sequence-specific determination of protein and peptide concentrations by absorbance at 205 nm”. In: *Protein Sci.* 22.6 (2013), pp. 851–858.

[195] Saumya Prasad et al. “Near UV-Visible electronic absorption originating from charged amino acids in a monomeric protein”. In: *Chem. Sci.* 8.8 (2017), pp. 5416–5433.

[196] Michael Overduin and Mansoore Esmaili. *Memtein: The fundamental unit of membrane-protein structure and function.* 2019.

[197] Michael F. Ryan. “The role of magnesium in clinical biochemistry: An overview”. In: *Ann. Clin. Biochem.* 28.1 (1991), pp. 19–26.

[198] Thirupathi Ravula et al. “Formation of pH-Resistant Monodispersed Polymer–Lipid Nanodiscs”. In: *Angew. Chemie - Int. Ed.* 57.5 (2018), pp. 1342–1345.

[199] Thirupathi Ravula et al. “PH Tunable and Divalent Metal Ion Tolerant Polymer Lipid Nanodiscs”. In: *Langmuir* 33.40 (2017), pp. 10655–10662.

[200] Stephen C.L. Hall et al. “An acid-compatible co-polymer for the solubilization of membranes and proteins into lipid bilayer-containing nanoparticles”. In: *Nanoscale* 10.22 (2018), pp. 10609–10619.

[201] Aiman A. Gulamhussein et al. “Examining the stability of membrane proteins within SMALPs”. In: *Eur. Polym. J.* 112.November 2018 (2019), pp. 120–125.

[202] David J.K. Swainsbury et al. “The effectiveness of styrene-maleic acid (SMA) copolymers for solubilisation of integral membrane proteins from SMA-accessible and SMA-resistant membranes”. In: *Biochim. Biophys. Acta - Biomembr.* 1859.10 (2017), pp. 2133–2143.

[203] Adrian H. Kopf et al. “Factors influencing the solubilization of membrane proteins from Escherichia coli membranes by styrene–maleic acid copolymers”. In: *Biochim. Biophys. Acta - Biomembr.* 1862.2 (2020), p. 183125.

[204] Marcella C. Orwick. “Biophysical and Magnetic Resonance Studies of Membrane Proteins”. PhD thesis. University of Oxford, 2011.

[205] Juan Francisco Bada-Juarez. “A new detergent-free approach to solubilize membrane proteins to maintain their native environment”. PhD thesis. University of Oxford, 2018.

[206] Sharon M. Kelly, Thomas J. Jess, and Nicholas C. Price. “How to study proteins by circular dichroism”. In: *Biochim. Biophys. Acta - Proteins Proteomics* 1751.2 (2005), pp. 119–139.

[207] Henry Sawczyc. *No Title*. 2020.

[208] Sonali Gulati et al. “Detergent-free purification of ABC (ATP-binding-cassette) transporters”. In: *Biochem. J.* 461.2 (2014), pp. 269–278.

[209] Tongran Zhang. “Characterisation and Comparison of Nanoparticle Formation by Amphipathic Polymers Including SMA”. PhD thesis. University of Oxford, 2019, pp. 1–57.

[210] J D Hunter. “Matplotlib: A 2D Graphics Environment”. In: *Comput. Sci. Eng.* 9.3 (May 2007), pp. 90–95.

[211] Marcella C. Orwick et al. “Detergent-free formation and physicochemical characterization of nanosized lipid-polymer complexes: Lipodisq”. In: *Angew. Chemie - Int. Ed.* 51.19 (2012), pp. 4653–4657.

[212] Stefan Scheidelaar et al. “Molecular Model for the solubilization of membranes into nanodisks by styrene maleic acid copolymers”. In: *Biophys. J.* 108.2 (2015), pp. 279–290.

[213] Stefan Scheidelaar et al. “Effect of Polymer Composition and pH on Membrane Solubilization by Styrene-Maleic Acid Copolymers”. In: *Biophys. J.* 111.9 (2016), pp. 1974–1986.

[214] Stephen C.L. Hall et al. *Influence of Poly(styrene- co -maleic acid) Copolymer Structure on the Properties and Self-Assembly of SMALP Nanodiscs*. 2018.

[215] Rodrigo Cuevas Arenas et al. “Influence of lipid bilayer properties on nanodisc formation mediated by styrene/maleic acid copolymers”. In: *Nanoscale* 8.32 (2016), pp. 15016–15026.

[216] Tongran Zhang. “Characterisation and Comparison of Nanoparticle Formation by Amphipathic Polymers Including SMA”. PhD thesis. University of Oxford, 2019.

[217] Jetse Reijenga et al. “Development of methods for the determination of pKa values”. In: *Anal. Chem. Insights* 8.1 (2013), pp. 53–71.

[218] F. A. Long and W. F. McDevit. “Activity coefficients of nonelectrolyte solutes in aqueous salt solutions”. In: *Chem. Rev.* 51.1 (1952), pp. 119–169.

[219] Rodrigo Cuevas Arenas et al. “Influence of lipid bilayer properties on nanodisc formation mediated by styrene/maleic acid copolymers”. In: *Nanoscale* 8.32 (2016), pp. 15016–15026.

[220] Minmin Xue et al. “Molecular Mechanism of Lipid Nanodisk Formation by Styrene-Maleic Acid Copolymers”. In: *Biophys. J.* 115.3 (2018), pp. 494–502.

[221] Amy Kaufman Katz et al. “Calcium ion coordination: A comparison with that of beryllium, magnesium, and zinc”. In: *J. Am. Chem. Soc.* 118.24 (1996), pp. 5752–5763.

[222] Indra D. Sahu et al. “DEER EPR measurements for membrane protein structures via bifunctional spin labels and lipodisq nanoparticles”. In: *Biochemistry* 52.38 (2013), pp. 6627–6632.

[223] Jonas M. Dörr et al. “Detergent-free isolation, characterization, and functional reconstitution of a tetrameric K+ channel: The power of native nanodiscs”. In: *Proc. Natl. Acad. Sci. U. S. A.* 111.52 (2014), pp. 18607–18612. arXiv: arXiv:1408.1149.

[224] David J.K. Swainsbury et al. “Probing the local lipid environment of the Rhodobacter sphaeroides cytochrome bc1 and Synechocystis sp. PCC 6803 cytochrome b6f complexes with styrene maleic acid”. In: *Biochim. Biophys. Acta - Bioenerg.* 1859.3 (2018), pp. 215–225.

[225] Mohammed Jamshad et al. “Structural analysis of a nanoparticle containing a lipid bilayer used for detergent-free extraction of membrane proteins”. In: *Nano Res.* 8.3 (2015), pp. 774–789.

[226] Christel Logez et al. “Detergent-free Isolation of Functional G Protein-Coupled Receptors into Nanometric Lipid Particles”. In: *Biochemistry* 55.1 (2016), pp. 38–48.

[227] Tomas Laursen et al. “Characterization of a dynamic metabolon producing the defense compound dhurrin in sorghum”. In: *Science (80-.).* 354.6314 (2016), pp. 890–893.

[228] Inge Bos et al. “Multiple LHCII antennae can transfer energy efficiently to a single Photosystem I”. In: *Biochim. Biophys. Acta - Bioenerg.* 1858.5 (2017), pp. 371–378.

[229] David Hardy et al. “Stabilization of Human Multidrug Resistance Protein 4 (MRP4/ABCC4) Using Novel Solubilization Agents”. In: *SLAS Discov. Adv. Life Sci. R&D* 00 (2019), p. 247255521986707.

[230] Vincent Postis et al. “The use of SMALPs as a novel membrane protein scaffold for structure study by negative stain electron microscopy”. In: *Biochim. Biophys. Acta - Biomembr.* 1848.2 (2015), pp. 496–501.

[231] V. Mitch Luna et al. “Generation of membrane proteins in polymer-based lipoparticles as flow cytometry antigens”. In: *Eur. Polym. J.* 109.June (2018), pp. 483–488.

[232] Eamonn Reading et al. “Interrogating Membrane Protein Conformational Dynamics within Native Lipid Compositions”. In: *Angew. Chemie - Int. Ed.* 56.49 (2017), pp. 15654–15657.

[233] Nathan G. Brady, Shuo Qian, and Barry D. Bruce. “Analysis of styrene maleic acid alternating copolymer supramolecular assemblies in solution by small angle X-ray scattering”. In: *Eur. Polym. J.* 111.November 2018 (2019), pp. 178–184.

[234] Thirupathi Ravula et al. “Effect of polymer charge on functional reconstitution of membrane proteins in polymer nanodiscs”. In: *Chem. Commun.* 54.69 (2018), pp. 9615–9618.

[235] Steven Lavington and Anthony Watts. “Detergent-free solubilisation & purification of a G protein coupled receptor using a polymethacrylate polymer.” eng. In: *Biochim. Biophys. acta. Biomembr.* 1863.1 (Aug. 2020), p. 183441.

[236] Kerrie A. Morrison et al. “Membrane protein extraction and purification using styrene-maleic acid (SMA) copolymer: Effect of variations in polymer structure”. In: *Biochem. J.* 473.23 (2016), pp. 4349–4360.

[237] Mohammed Jamshad et al. “G-protein coupled receptor solubilization and purification for biophysical analysis and functional studies, in the total absence of detergent”. In: *Biosci. Rep.* 35 (2015), pp. 1–10.

[238] Masafumi Tanaka et al. “Effects of charged lipids on the physicochemical and biological properties of lipid–styrene maleic acid copolymer discoidal particles”. In: *Biochim. Biophys. Acta - Biomembr.* 1862.5 (2020), p. 183209.

[239] J. J. Dominguez Pardo et al. “Thermotropic properties of phosphatidylcholine nanodiscs bounded by styrene-maleic acid copolymers”. In: *Chem. Phys. Lipids* 208.August (2017), pp. 58–64.

[240] Charlie Davis. “Engineering Lipid Nanoparticles for Structural Biology and Drug Delivery”. PhD thesis. University of Oxford, 2015.

[241] Faith M. Harris, Katrina B. Best, and John D. Bell. “Use of laurdan fluorescence intensity and polarization to distinguish between changes in membrane fluidity and phospholipid order”. In: *Biochim. Biophys. Acta - Biomembr.* 1565.1 (2002), pp. 123–128.

[242] Cíntia C. De Vequi-Suplicy, Carlos R. Benatti, and M. Teresa Lamy. “Laurdan in fluid bilayers: Position and structural sensitivity”. In: *J. Fluoresc.* 16.3 (2006), pp. 431–439.

[243] Andrew W. Shaw, Mark A. McLean, and Stephen G. Sligar. “Phospholipid phase transitions in homogeneous nanometer scale bilayer discs”. In: *FEBS Lett.* 556.1-3 (2004), pp. 260–264.

[244] Pavla Angelisová et al. “The use of styrene-maleic acid copolymer (SMA) for studies on T cell membrane rafts”. In: *Biochim. Biophys. Acta - Biomembr.* 1861.1 (2019), pp. 130–141.

[245] Danuta Pentak, W. W. Sułkowski, and Anna Sułkowska. “Calorimetric and EPR studies of the thermotropic phase behavior of phospholipid membranes”. In: *J. Therm. Anal. Calorim.* 93.2 (2008), pp. 471–477.

[246] Marija Raguz et al. “Using spin-label electron paramagnetic resonance (EPR) to discriminate and characterize the cholesterol bilayer domain”. In: *Chem. Phys. Lipids* 164.8 (2011), pp. 819–829.

[247] J. E. Mahaney et al. “Effects of melittin on lipid-protein interactions in sarcoplasmic reticulum membranes”. In: *Biophys. J.* 63.6 (1992), pp. 1513–1522.

[248] Vadim Kotov et al. “High-throughput stability screening for detergent-solubilized membrane proteins”. In: *Sci. Rep.* 9.1 (2019), p. 10379.

[249] Andrew F. Craig et al. “Tuning the size of styrene-maleic acid copolymer-lipid nanoparticles (SMALPs) using RAFT polymerization for biophysical studies”. In: *Biochim. Biophys. Acta - Biomembr.* 1858.11 (2016), pp. 2931–2939.

[250] Rodrigo Cuevas Arenas et al. “Fast Collisional Lipid Transfer among Polymer-Bounded Nanodiscs”. In: *Sci. Rep.* 7 (2017), pp. 1–8.

[251] Lei Zhang et al. “Morphology and structure of lipoproteins revealed by an optimized negative-staining protocol of electron microscopy”. In: *J. Lipid Res.* 52.1 (2011), pp. 175–184.

[252] Alexandr Colbasevici et al. “Lipid dynamics in nanoparticles formed by maleic acid-containing copolymers: EPR spectroscopy and molecular dynamics simulations”. In: *Biochim. Biophys. Acta - Biomembr.* 1862.5 (2020).

[253] A. G. Lee. *Lipid-protein interactions in biological membranes: A structural perspective*. Vol. 1612. 1. 2003, pp. 1–40.

[254] Rumiana Koynova and Martin Caffrey. “Phases and phase transitions of the phosphatidylcholines”. In: *Biochim. Biophys. Acta - Rev. Biomembr.* 1376.1 (1998), pp. 91–145.

[255] Ruthven N. Lewis, N. M. Nanette Mak, and Ronald N. McElhaney. “A Differential Scanning Calorimetric Study of the Thermotropic Phase Behavior of Model Membranes Composed of Phosphatidylcholines Containing Linear Saturated Fatty Acyl Chains”. In: *Biochemistry* 26.19 (1987), pp. 6118–6126.

[256] E. Anibal Disalvo, Jesus Arroyo, and Delia L. Bernik. “Interfacial Properties of Liposomes as Measured by Fluorescence and Optical Probes”. In: *Methods Enzymol.* 367 (2003), pp. 213–233.

[257] Yuanqing Ma et al. “Time-Resolved Laurdan Fluorescence Reveals Insights into Membrane Viscosity and Hydration Levels”. In: *Biophys. J.* 115.8 (2018), pp. 1498–1508.

[258] Justyna Barucha-Kraszewska, Sebastian Kraszewski, and Christophe Ramseyer. “Will C-Laurdan dethrone Laurdan in fluorescent solvent relaxation techniques for lipid membrane studies?” In: *Langmuir* 29.4 (2013), pp. 1174–1182.

[259] Silvio Osella et al. “Conformational Changes as Driving Force for Phase Recognition: The Case of Laurdan”. In: *Langmuir* 35.35 (2019), pp. 11471–11481.

[260] Heimke Krudopp, Frank D. Sönnichsen, and Anja Steffen-Heins. “Partitioning of nitroxides in dispersed systems investigated by ultrafiltration, EPR and NMR spectroscopy”. In: *J. Colloid Interface Sci.* 452 (2015), pp. 15–23.

[261] Avnika P. Bali et al. “Structural characterization of styrene-maleic acid copolymer-lipid nanoparticles (SMALPs) using EPR spectroscopy”. In: *Chem. Phys. Lipids* 220.January (2019), pp. 6–13.

[262] Rodrigo Cuevas Arenas et al. “Fast Collisional Lipid Transfer among Polymer-Bounded Nanodiscs”. In: *Sci. Rep.* 7.March (2017), pp. 1–8.

[263] Tsutomu Hamada et al. “Construction of asymmetric cell-sized lipid vesicles from lipid-coated water-in-oil microdroplets”. In: *J. Phys. Chem. B* 112.47 (2008), pp. 14678–14681.

[264] Jonathan D. Nickels, Jeremy C. Smith, and Xiaolin Cheng. “Lateral organization, bilayer asymmetry, and inter-leaflet coupling of biological membranes”. In: *Chem. Phys. Lipids* 192 (2015), pp. 87–99.

[265] Motohide Murate and Toshihide Kobayashi. “Revisiting transbilayer distribution of lipids in the plasma membrane”. In: *Chem. Phys. Lipids* 194 (2016), pp. 58–71.

[266] Zhen Huang and Erwin London. “Effect of cyclodextrin and membrane lipid structure upon cyclodextrin-lipid interaction”. In: *Langmuir* 29.47 (2013), pp. 14631–14638.

[267] Orly B. Tarun, Maksim Yu Eremchev, and Sylvie Roke. “Interaction of Oil and Lipids in Freestanding Lipid Bilayer Membranes Studied with Label-Free High-Throughput Wide-Field Second-Harmonic Microscopy”. In: *Langmuir* 34.38 (2018), pp. 11305–11310.

[268] Samuel O Grim, Edward F Davidoff, and Tobin J Marks. “Preparation and 31P Chemical Shifts of Some Quaternary Phosphonium Salts”. In: *Zeitschrift fur Naturforsch. - Sect. B J. Chem. Sci.* 26.3 (1971), pp. 184–190.

[269] Erik Sedlák and Neal C. Robinson. “Phospholipase A2 digestion of cardiolipin bound to bovine cytochrome c oxidase alters both activity and quaternary structure”. In: *Biochemistry* 38.45 (1999), pp. 14966–14972.

[270] Edward A. Berry and Bernard L. Trumpower. “Simultaneous determination of hemes a, b, and c from pyridine hemochrome spectra”. In: *Anal. Biochem.* 161.1 (Feb. 1987), pp. 1–15.

[271] Marie Markones et al. “Engineering Asymmetric Lipid Vesicles: Accurate and Convenient Control of the Outer Leaflet Lipid Composition”. In: *Langmuir* 34.5 (2018), pp. 1999–2005.

[272] Drew Marquardt et al. “1 H NMR Shows Slow Phospholipid Flip-Flop in Gel and Fluid Bilayers”. In: *Langmuir* (2017), acs.langmuir.6b04485.

[273] Theodor Förster. ““Energiewanderung und Fluoreszenz. (Translated text)”. In: *Naturwissenschaften* 33(6).1 (1946), pp. 166–175.

[274] Nicolas Di Fiori and Amit Meller. “The Effect of dye-dye interactions on the spatial resolution of single-molecule FRET measurements in nucleic acids.” In: *Biophys. J.* 98.10 (2010), pp. 2265–2272.

[275] M. Parsons, B. Vojnovic, and S. Ameer-Beg. “Imaging protein-protein interactions in cell motility using fluorescence resonance energy transfer (FRET)”. In: *Biochem. Soc. Trans.* 32.3 (2004), pp. 431–433.

[276] Jiankang Deng et al. “A ratiometric fluorescent biosensor based on cascaded amplification strategy for ultrasensitive detection of kanamycin”. In: *Sensors Actuators, B Chem.* 273.December 2017 (2018), pp. 1495–1500.

[277] Anne Grethen, David Glueck, and Sandro Keller. “Role of Coulombic Repulsion in Collisional Lipid Transfer Among SMA(2:1)-Bounded Nanodiscs”. In: *J. Membr. Biol.* 251.3 (2018), pp. 443–451.

[278] J. Wylie Nichols and Richard E. Pagano. “Kinetics of Soluble Lipid Monomer Diffusion between Vesicles”. In: *Biochemistry* 20.10 (1981), pp. 2783–2789.

[279] Michael A. Gardam, Joseph J. Itovitch, and John R. Silvius. “Partitioning of Exchangeable Fluorescent Phospholipids and Sphingolipids between Different Lipid Bilayer Environments”. In: *Biochemistry* 28.2 (1989), pp. 884–893.

[280] Frank Sixl and Anthony Watts. “Interactions between Phospholipid Head Groups at Membrane Interfaces: A Deuterium and Phosphorus Nuclear Magnetic Resonance and Spin-Label Electron Spin Resonance Study”. In: *Biochemistry* 21.25 (1982), pp. 6446–6452.

[281] Gavin Hazell et al. “Evidence of Lipid Exchange in Styrene Maleic Acid Lipid Particle (SMALP) Nanodisc Systems”. In: *Langmuir* 32.45 (2016), pp. 11845–11853.

[282] Sophie J. Hesketh et al. “Styrene maleic-acid lipid particles (SMALPs) into detergent or amphipols: An exchange protocol for membrane protein characterisation”. In: *Biochim. Biophys. Acta - Biomembr.* 1862.5 (2020), p. 183192.

[283] Michael Overduin and Mansoore Esmaili. “Native nanodiscs and the convergence of lipidomics, metabolomics, interactomics and proteomics”. In: *Appl. Sci.* 9.6 (2019), pp. 1230–1245.

[284] A. Watts, D. Marsh, and P. F. Knowles. “Lipid-substituted cytochrome oxidase: No absolute requirement of cardiolipin for activity”. In: *Biochem. Biophys. Res. Commun.* 81.2 (1978), pp. 403–409.

[285] Ivano Bertini, Gabriele Cavallaro, and Antonio Rosato. “Cytochrome c: Occurrence and functions”. In: *Chem. Rev.* 106.1 (2006), pp. 90–115.

[286] Maik Hüttemann et al. “The multiple functions of cytochrome c and their regulation in life and death decisions of the mammalian cell: From respiration to apoptosis”. In: *Mitochondrion* 11.3 (2011), pp. 369–381.

[287] W. D. Butt and D. Keilin. “Absorption spectra and some other properties of cytochrome c and of its compounds with ligands.” In: *Proc. R. Soc. Lond. B. Biol. Sci.* 156.November (1962), pp. 429–458.

[288] Bartholomäus Danielczak and Sandro Keller. “Collisional lipid exchange among DIBMA-encapsulated nanodiscs (DIBMALPs)”. In: *Eur. Polym. J.* 109.August (2018), pp. 206–213.

[289] Daniela Krüger et al. “Measuring Protein Binding to Lipid Vesicles by Fluorescence Cross-Correlation Spectroscopy”. In: *Biophys. J.* 113.6 (2017), pp. 1311–1320.

[290] I. Triano et al. “Occupancy of Nonannular Lipid Binding Sites on KcsA Greatly Increases the Stability of the Tetrameric Protein”. In: *Biochemistry* 49.25 (June 2010), pp. 5397–5404.

[291] Robin A. Corey et al. “Insights into Membrane Protein–Lipid Interactions from Free Energy Calculations”. In: *J. Chem. Theory Comput.* 15.10 (Oct. 2019), pp. 5727–5736.

[292] Emiliana De Santis et al. “Antimicrobial peptide capsids of de novo design”. In: *Nat. Commun.* 8.1 (2017).

[293] James E. Noble et al. “A de Novo Virus-Like Topology for Synthetic Virions”. In: *J. Am. Chem. Soc.* 138.37 (2016), pp. 12202–12210.

[294] Emiliana De Santis and Maxim G. Ryadnov. “Peptide self-assembly for nanomaterials: The old new kid on the block”. In: *Chem. Soc. Rev.* 44.22 (2015), pp. 8288–8300.

[295] Eleanor F. Banwell et al. “Rational design and application of responsive α-helical peptide hydrogels”. In: *Nat. Mater.* 8.7 (2009), pp. 596–600.

[296] Ying Li, Bin Xue, and Yi Cao. “100th Anniversary of Macromolecular Science Viewpoint: Synthetic Protein Hydrogels”. In: *ACS Macro Lett.* 9.4 (2020), pp. 512–524.

[297] Jia Kong et al. “Rationally Designed Peptidyl Virus-Like Particles Enable Targeted Delivery of Genetic Cargo”. In: *Angew. Chemie - Int. Ed.* 57.43 (2018), pp. 14032–14036.

[298] Joseph L. Beesley et al. “Modifying Self-Assembled Peptide Cages to Control Internalization into Mammalian Cells”. In: *Nano Lett.* 18.9 (2018), pp. 5933–5937.

[299] Valeria Castelletto et al. “Structurally plastic peptide capsules for synthetic antimicrobial viruses”. In: *Chem. Sci.* 7.3 (2016), pp. 1707–1711.

[300] Noel A. Roberts et al. “Rational design of peptide-based HIV proteinase inhibitors”. In: *Science (80-.).* 248.4953 (1990), pp. 358–361.

[301] M. T. Pisabarro and L. Serrano. “Rational design of specific high-affinity peptide ligands for the Abl- SH3 domain”. In: *Biochemistry* 35.33 (1996), pp. 10634–10640.

[302] Yuxin Chen et al. “Rational Design of α-Helical Antimicrobial Peptides with Enhanced Activities and Specificity/Therapeutic Index”. In: *J. Biol. Chem.* 280.13 (Apr. 2005), pp. 12316–12329.

[303] Randal Eckert et al. “Adding selectivity to antimicrobial peptides: Rational design of a multidomain peptide against Pseudomonas spp.” In: *Antimicrob. Agents Chemother.* 50.4 (2006), pp. 1480–1488.

[304] Lijuan Zhang and Timothy J Falla. “Antimicrobial peptides: therapeutic potential”. In: *Expert Opin. Pharmacother.* 7.6 (2006), pp. 653–663.

[305] Yuri Zimenkov et al. “Rational design of a reversible pH-responsive switch for peptide self-assembly”. In: *J. Am. Chem. Soc.* 128.21 (2006), pp. 6770–6771.

[306] Jordan M. Fletcher et al. “A basis set of de novo coiled-Coil peptide oligomers for rational protein design and synthetic biology”. In: *ACS Synth. Biol.* 1.6 (2012), pp. 240–250.

[307] Valeria Castelletto et al. “Structurally plastic peptide capsules for synthetic antimicrobial viruses”. In: *Chem. Sci.* 7.3 (2016), pp. 1707–1711.

[308] Derek N. Woolfson. “The Design of Coiled-Coil Structures and Assemblies”. In: 2005, pp. 79–112.

[309] By Peter Greil. “Advanced Materials Progress Report on Microporous and Mesoporous Material”. In: *Adv. Mater.* 14.10 (2002), pp. 709–716.

[310] Omar Z. Fisher et al. “Bioinspired materials for controlling stem cell fate”. In: *Acc. Chem. Res.* 43.3 (2010), pp. 419–428.

[311] Sun Young Wang et al. “Development of Biocompatible HA Hydrogels Embedded with a New Synthetic Peptide Promoting Cellular Migration for Advanced Wound Care Management”. In: *Adv. Sci.* 5.11 (2018).

[312] Kyriakos G. Varnava and Vijayalekshmi Sarojini. “Making Solid-Phase Peptide Synthesis Greener: A Review of the Literature”. In: *Chem. - An Asian J.* 14.8 (2019), pp. 1088–1097.

[313] Sascha Knauer et al. “Sustainable Peptide Synthesis Enabled by a Transient Protecting Group”. In: *Angew. Chemie Int. Ed.* (2020).

[314] Edward F. Plow et al. “Ligand binding to integrins”. In: *J. Biol. Chem.* 275.29 (2000), pp. 21785–21788.

[315] Barbara Rzeszotarska and Elzbieta Masiukiewicz. “Arginine, histidine and tryptophan in peptide synthesis. The guanidino function of arginine”. In: *Org. Prep. Proced. Int.* 20.5 (1988), pp. 427–464.

[316] Toshiaki Hara et al. “Trifluoroethanol-containing RP-HPLC mobile phases for the separation of transmembrane peptides human glycophorin-A, integrin alpha-1, and p24: Analysis and prevention of potential side reactions due to formic acid”. In: *J. Pept. Sci.* 21.2 (2015), pp. 61–70.

[317] Jilie Kong and Shaoning Yu. “Fourier transform infrared spectroscopic analysis of protein secondary structures”. In: *Acta Biochim. Biophys. Sin. (Shanghai).* 39.8 (2007), pp. 549–559.

[318] Andreas Barth and Christian Zscherp. “What vibrations tell us about proteins”. In: *Q. Rev. Biophys.* 35.4 (2002), pp. 369–430.

[319] Thomas Heimburg et al. “Specific recognition of coiled coils by infrared spectroscopy: Analysis of the three structural domains of type III intermediate filament proteins”. In: *Biochemistry* 35.5 (1996), pp. 1375–1382.

[320] V. Frecer, B. Ho, and J. L. Ding. “De novo design of potent antimicrobial peptides”. In: *Antimicrob. Agents Chemother.* 48.9 (2004), pp. 3349–3357.

[321] Francesca Grisoni et al. “De novo design of anticancer peptides by ensemble artificial neural networks”. In: *J. Mol. Model.* 25.5 (2019), pp. 1–10.

[322] Jordan M. Fletcher et al. “Self-assembling cages from coiled-coil peptide modules”. In: *Science (80-.).* 340.6132 (2013), pp. 595–599.

[323] Naomi L. Pollock et al. *Structure and function of membrane proteins encapsulated in a polymer-bound lipid bilayer.* 2018.

[324] Juan J. Dominguez Pardo et al. “Solubilization of lipids and lipid phases by the styrene–maleic acid copolymer”. In: *Eur. Biophys. J.* 46.1 (2017), pp. 91–101.

[325] Masafumi Tanaka et al. “Preparation and Characterization of Reconstituted Lipid-Synthetic Polymer Discoidal Particles”. In: *Langmuir* 31.46 (2015), pp. 12719–12726.

[326] Bartholomäus Danielczak, Annette Meister, and Sandro Keller. “Influence of Mg 2+ and Ca 2+ on nanodisc formation by diisobutylene/maleic acid (DIBMA) copolymer”. In: *Chem. Phys. Lipids* 221 (2019), pp. 30–38.

[327] Jesper V Møller, Birte Juul, and Marc le Maire. “Structural organization, ion transport, and energy transduction of P-type ATPases”. In: *Biochim. Biophys. Acta - Rev. Biomembr.* 1286.1 (May 1996), pp. 1–51.

[328] David J.K. Swainsbury et al. “Bacterial reaction centers purified with styrene maleic acid copolymer retain native membrane functional properties and display enhanced stability”. In: *Angew. Chemie - Int. Ed.* 53.44 (2014), pp. 11803–11807.

[329] Sarah Paulin et al. “Surfactant-free purification of membrane protein complexes from bacteria: Application to the staphylococcal penicillin-binding protein complex PBP2/PBP2a”. In: *Nanotechnology* 25.28 (2014).

[330] Adam J. Bell, Laurie K. Frankel, and Terry M. Bricker. “High yield non-detergent isolation of photosystem I-light-harvesting chlorophyll II membranes from spinach thylakoids: Implications for the organization of the PS I antennae in higher plants”. In: *J. Biol. Chem.* 290.30 (2015), pp. 18429–18437.

[331] Irfan Prabudiansyah et al. “Characterization of the annular lipid shell of the Sec translocon”. In: *Biochim. Biophys. Acta - Biomembr.* 1848.10 (2015), pp. 2050–2056.

[332] Joanna Komar et al. “Membrane protein insertion and assembly by the bacterial holo-Translocon SecYEG-SecDF-YajC-YidC”. In: *Biochem. J.* 473.19 (2016), pp. 3341–32354.

[333] N. Voskoboynikova et al. “Characterization of an archaeal photoreceptor/transducer complex from: Natronomonas pharaonis assembled within styrene-maleic acid lipid particles”. In: *RSC Adv.* 7.81 (2017), pp. 51324–51334.

[334] Jana Broecker, Bryan T. Eger, and Oliver P. Ernst. “Crystallogenesis of Membrane Proteins Mediated by Polymer-Bounded Lipid Nanodiscs”. In: *Structure* 25.2 (2017), pp. 384–392.

[335] Shahid Rehan, Ville O. Paavilainen, and Veli Pekka Jaakola. “Functional reconstitution of human equilibrative nucleoside transporter-1 into styrene maleic acid co-polymer lipid particles”. In: *Biochim. Biophys. Acta - Biomembr.* 1859.5 (2017), pp. 1059–1065.

[336] Beate Bersch et al. “Proton-Detected Solid-State NMR Spectroscopy of a Zinc Diffusion Facilitator Protein in Native Nanodiscs”. In: *Angew. Chemie - Int. Ed.* 56.9 (2017), pp. 2508–2512.

[337] Marjorie Damian et al. “GHSR-D2R heteromerization modulates dopamine signaling through an effect on G protein conformation”. In: *Proc. Natl. Acad. Sci. U. S. A.* 115.17 (2018), pp. 4501–4506.

[338] Chang Sun et al. “Structure of the alternative complex III in a supercomplex with cytochrome oxidase”. In: *Nature* 557.7703 (2018), pp. 123–126.

[339] Yao Liu et al. “Bacillus subtilis MraY in detergent-free system of nanodiscs wrapped by styrene-maleic acid copolymers”. In: *PLoS One* 13.11 (2018), pp. 1–18.

[340] Marta Barniol-Xicota and Steven H.L. Verhelst. “Stable and Functional Rhomboid Proteases in Lipid Nanodiscs by Using Diisobutylene/Maleic Acid Copolymers”. In: *J. Am. Chem. Soc.* 140.44 (2018), pp. 14557–14561.

[341] M. G. Karlova et al. “Detergent-free solubilization of human Kv channels expressed in mammalian cells”. In: *Chem. Phys. Lipids* 219.January (2019), pp. 50–57.

[342] Priyanka Prakash et al. “Dynamics of Membrane-Bound G12V-KRAS from Simulations and Single-Molecule FRET in Native Nanodiscs”. In: *Biophys. J.* 116.2 (2019), pp. 179–183.

[343] H. J. Gruber et al. “Anomalous fluorescence enhancement of Cy3 and Cy3.5 versus anomalous fluorescence loss of Cy5 and Cy7 upon covalent linking to IgG and noncovalent binding to avidin”. In: *Bioconjug. Chem.* 11.5 (2000), pp. 696–704.

[344] JE Berlier et al. “Quantitative comparison of long-wavelength Alexa Fluor dyes to Cy dyes: fluorescence of the dyes and their bioconjugates”. In: *Histochem. ...* 51.12 (2003), pp. 1699–1712.

[345] Patricia M Dijkman. “Biophysical Studies of Membrane Protein Structure and Function”. In: (2014).

[346] James A. Cooke and Louise J. Brown. “Distance Measurements by Continuous Wave EPR Spectroscopy to Monitor Protein Folding”. In: 2011, pp. 73–96.

[347] Gunnar Jeschke. “DEER Distance Measurements on Proteins”. In: *Annu. Rev. Phys. Chem.* 63.1 (2012), pp. 419–446.

[348] Alice Verchère et al. “Light-independent phospholipid scramblase activity of bacteriorhodopsin from Halobacterium salinarum”. In: *Sci. Rep.* 7.1 (2017), pp. 1–10.

[349] Katsumi Matsuzaki et al. “An antimicrobial peptide, magainin 2, induced rapid flip-flop of phospholipids coupled with pore formation and peptide translocation”. In: *Biochemistry* 35.35 (1996), pp. 11361–11368.

[350] Hari Leontiadou, Alan E Mark, and Siewert J Marrink. “Antimicrobial Peptides in Action”. In: *J. Am. Chem. Soc.* 128.37 (Sept. 2006), pp. 12156–12161.

[351] Bikash R. Sahoo et al. “Self-Assembly of Polymer-Encased Lipid Nanodiscs and Membrane Protein Reconstitution”. In: *J. Phys. Chem. B* 123.21 (2019), pp. 4562–4570.